

Sustainable Aviation

T. Hikmet Karakoc
Can Ozgur Colpan
Alper Dalkiran *Editors*

New Frontiers in Sustainable Aviation



 **SARES**
INTERNATIONAL SUSTAINABLE AVIATION
AND ENERGY RESEARCH SOCIETY



Springer

Sustainable Aviation

Series Editors

T. Hikmet Karakoc, Faculty of Aeronautics and Astronautics, Eskisehir Technical University, Eskisehir, Turkey

C. Ozgur Colpan, Department of Mechanical Engineering, Dokuz Eylül University, Buca, Izmir, Turkey

Alper Dalkiran, School of Aviation, Süleyman Demirel University, Isparta, Turkey

The Sustainable Aviation book series focuses on sustainability in aviation considering all aspects of the field. The books are developed in partnership with the International Sustainable Aviation Research Society (SARES), and include contributed volumes consisting of select contributions to SARES international symposiums and conferences, as well as cutting edge monographs and professional books focused on all aspects of sustainable aviation. The series aims at publishing state-of-the-art research and development in areas including, but not limited to:

Green and renewable energy resources and aviation technologies
Aircraft engine, control systems, production, storage, efficiency and planning
Exploring the potential of integrating renewables within airports
Sustainable infrastructure development under a changing climate
Training and awareness facilities with aviation sector and social levels
Teaching and professional development in renewable energy technologies and sustainability


More information about this series at <http://www.springer.com/series/16670>

T. Hikmet Karakoc • Can Ozgur Colpan
Alper Dalkiran
Editors

New Frontiers in Sustainable Aviation

 Springer

Editors

T. Hikmet Karakoc 
Faculty of Aeronautics and Astronautics
Eskisehir Technical University
Eskisehir, Turkey

Can Ozgur Colpan 
Department of Mechanical Engineering
Dokuz Eylul University
Buca, Izmir, Turkey

Alper Dalkiran 
School of Aviation
Süleyman Demirel University
Isparta, Turkey

ISSN 2730-7778

ISSN 2730-7786 (electronic)

Sustainable Aviation

ISBN 978-3-030-80778-8

ISBN 978-3-030-80779-5 (eBook)

<https://doi.org/10.1007/978-3-030-80779-5>

© The Editor(s) (if applicable) and The Author(s), under exclusive license to Springer Nature Switzerland AG 2022

This work is subject to copyright. All rights are solely and exclusively licensed by the Publisher, whether the whole or part of the material is concerned, specifically the rights of translation, reprinting, reuse of illustrations, recitation, broadcasting, reproduction on microfilms or in any other physical way, and transmission or information storage and retrieval, electronic adaptation, computer software, or by similar or dissimilar methodology now known or hereafter developed.

The use of general descriptive names, registered names, trademarks, service marks, etc. in this publication does not imply, even in the absence of a specific statement, that such names are exempt from the relevant protective laws and regulations and therefore free for general use.

The publisher, the authors and the editors are safe to assume that the advice and information in this book are believed to be true and accurate at the date of publication. Neither the publisher nor the authors or the editors give a warranty, expressed or implied, with respect to the material contained herein or for any errors or omissions that may have been made. The publisher remains neutral with regard to jurisdictional claims in published maps and institutional affiliations.

This Springer imprint is published by the registered company Springer Nature Switzerland AG
The registered company address is: Gewerbestrasse 11, 6330 Cham, Switzerland

Preface

The negative effects of air pollution and climate change are the main driving factors behind sustainable solutions for aircrafts and airport operations. The design of aircrafts based on electric power systems; the use of various sustainable fuels, obtained either from biomass or the utilization of electrically generated hydrogen and carbon dioxide; the development of effective flow-control methods; the improvement of aerodynamic performance of existing aircrafts; and the modification of buildings and runways in an airport are all important topics in this regard.

This book includes ten chapters on various subjects of sustainable aviation, including green airports, aircraft operations, control techniques, power, and propulsion or materials. Novel methods and advanced approaches are also presented to achieve sustainability in aviation applications. Electric aviation seems to be one of the most popular topics in this area. This book summarizes aircraft electric power systems and discusses battery performance in different conditions through numerical studies. Airports are one of the essential parts of the aviation industry where it is important to achieve sustainability. A chapter has been dedicated to the sustainability practices in airports. This book also presents an analysis on the wind speed and direction distribution model of a runway in an airport. It is also essential to sustain the airports in terms of reducing energy consumptions in the terminal buildings. The use of life cycle energy assessment for airport terminal glass facades is also discussed. Life cycle cost methodology is also applied for replacement decisions of aging aircrafts. The dynamic air vehicle design is still in the spotlight of science. Active and passive flow control methods over airfoils for improvement in aerodynamic performance are covered in this book. Another chapter which complements this study, that is, the structural stability of air vehicles' aerodynamic airfoils, is included. Exergy analysis has been one of the commonly used tools to assess the thermodynamic performance of aeroengines. This analysis is conducted for an air cycle machine for different flight conditions in this book. Finally, this book also includes the presentation of a wind tunnel study on the aerodynamic characteristics of an unmanned aerial vehicle.

We would like to thank Springer's editorial team for their support towards the preparation of this book, and chapter authors and reviewers for all their great contributions.

Eskisehir, Turkey
Buca, Izmir, Turkey
Isparta, Turkey

T. Hikmet Karakoc
Can Ozgur Colpan
Alper Dalkiran

Contents

| | | |
|----------|---|------------|
| 1 | A Numerical Study on Thermal and Electrical Performance of Prismatic Li-Ion Batteries and Estimation on Artificial Neural Networks | 1 |
| | Ozge Yetik | |
| 2 | Active and Passive Flow Control Methods Over Airfoils for Improvement in Aerodynamic Performance. | 19 |
| | Musa Özkan | |
| 3 | An Analysis on the Wind Speed and Direction Distribution Model of a Runway | 35 |
| | Aziz Kaba | |
| 4 | Optimization of Control Surfaces Using Different Corrugated Design to Minimize the Vibration and Flutter in the Wing | 51 |
| | N. G. Hareesha and M. Rudresh | |
| 5 | Exergy Analysis of an Air Cycle Machine for Different Flight Conditions | 71 |
| | M. Zeki Yilmazoglu and Cem Gulseven | |
| 6 | Life Cycle Energy Assessment of European Airport Terminal Buildings According to Glass Facades | 101 |
| | Okan Kon and Ismail Caner | |
| 7 | An Overview of Aircraft Electric Power System for Sustainable Aviation | 113 |
| | Halime Hizarci, Onur Demirel, Kemal Kalayci, and Ugur Arifoglu | |
| 8 | Life Cycle Cost Methodology for Replacement Decisions of Aging Aircraft. | 147 |
| | Zeliha Akça | |

| | |
|--|-----|
| 9 Numerical and Experimental Investigation of Aerodynamic Characteristics of an Unmanned Aerial Vehicle in a Low Subsonic Wind Tunnel | 167 |
| Furkan Dilbaz, Adnan Burak Incedal, Talha Batuhan Korkut, Yasemin Nur Aydın, Seda Kırmacı Arabacı, and Aytaç Gören | |
| 10 Sustainability Practices in Airport | 191 |
| Hakan Rodoplu and Serap Gürsel | |
| Index | 203 |

Chapter 1

A Numerical Study on Thermal and Electrical Performance of Prismatic Li-Ion Batteries and Estimation on Artificial Neural Networks



Ozge Yetik

Nomenclature

| | |
|-------------|--|
| ANN | Artificial neural networks |
| BR | Bayesian regularization |
| CGP | Pola-Ribiere conjugate gradient |
| CoV | Covariation |
| C_p | Heat capability |
| E | Open circuit voltage |
| F | Faraday stable |
| j_{ECh} | Volumetrically current transfer ratio |
| j_{short} | Current transfer ratio |
| j_{ECh} | Resource term |
| k | Thermic conductivity |
| LM | Levenberg-Marquardt |
| n | Size of electrons |
| NTGK | Newman, Tiedemann, Gu and Kim |
| p | Pressure |
| ρ | Density |
| RMSE | Root mean square error |
| SCG | Scaled conjugate gradient |
| SIMPLE | Semi-implicit method for pressure-linked equations |
| Q_{gen} | Heat generation |
| Q_j | Joule heat |
| Q_r | Electrochemical reaction heat |
| t | Time |
| T | Temperature |

O. Yetik (✉)

Eskişehir Osmangazi University, Eskişehir, Turkey

| | |
|--------------------|---|
| T_{inlet} | Air inlet temperature |
| T_{max} | Max of temperature |
| u | Velocity |
| V | Operational voltage |
| V_{inlet} | Air inlet speed |
| μ | Viscosity |
| $\sigma+$ | Effective electric conductivities for the positive electrodes |
| $\sigma-$ | Effective electric conductivities for the negative electrodes |
| $\varphi+$ | Phase potentials for the positive electrodes |
| $\varphi-$ | Phase potentials for the negative electrodes |

1.1 Introduction

Batteries with electrochemical energy are used in electric vehicle technologies, aviation vehicles, important weapon systems and renewable energy integrated lighting systems. Energy storage systems also stand out as electronic devices. The performances of these devices are important for all areas.

Temperature analysis of batteries is an important research area for researchers. The cooling of the batteries is very important for the performer. Battery cooling generally consists of air cooling (Sun and Dixon 2014; Cicconi et al. 2017; Weixiong et al. 2018; Lu et al. 2016), liquid cooling (Rao et al. 2017; Tong et al. 2015; Zhao et al. 2018; Bai et al. 2019), phase change material cooling (Rao et al. 2017; Tong et al. 2015; Zhao et al. 2018; Bai et al. 2019) and heat pipe cooling (Kshetrimayum et al. 2019). Wang et al. (2017b) evaluated the thermal state of cylindrical batteries with composite paraffin and fin. They used experimental and other thermal management techniques in their studies. Batteries are model batteries made of aluminium and have wings. Temperature changes and instantaneous Nusselt numbers of the batteries were measured. The heat state with phase change material-fin was evaluated experimentally, and the logarithmic dependence of the average Nusselt number was associated with the heat transfer area ratio. As a result, it was found that the composite phase change material-fin group had the benefits of long thermal life and good thermal success. Jilte et al. (2019) studied two different types of battery refrigerating. These are fluid-loaded battery refrigerating systems and fluid-roamed battery refrigerating systems. The air refrigerating element of an electric vehicle was combined with the battery cooling element. The study was carried out at the discharge ratios of 2C and 4C. The air needed for two coolings was provided at two conditions: first, if the ambient temperature is around 35C and air refrigerating is 'close' in an electric transport. Second, air refrigerating is 'open', and recirculated air from transport cabin exists at 30C to be supplied to the battery refrigerating system. The conclusion indicates the feasibility of similar battery systems for the secure processing of electric transport. Martín-Martín et al. (2019) examined a simple battery thermal management system with CFD modelling and numerical optimization methods. A new heat generation model, called misconnected, was obtained

to check the heat density produced in each cell of the battery module in simulation with thermal communication and accuracy. In order to determine the heat distribution, the best placement of the temperature sensors was decided on the basis of the CFD model results. Jilte et al. (2019) covered all the batteries with single phase change material. They said that the cells in the corners radiated heat better than the cells in the middle. In this study, they examined the active and passive cooling of a classic battery module. The battery module is lined up as 1S6P, and the gap between them is taken as 4 mm. Thermal analysis was carried out at a discharge rate of 2C and 4C and an ambient temperature of 27 °C, 35 °C and 40 °C. It was found that the materials around the batteries emitted better heat than the phase change material. Wang et al. (2017a) proposed gas and liquid cooling to solve the thermal problems of li-ion batteries. They studied numerically the effects of gas density and liquid cooling on temperature control in different sequences. They used the computational fluid dynamics method in their studies. Compared to traditional methods, the maximum temperature and overall temperature difference were found to be reduced by 3.45K and 3.88K. Numerical results contribute to the new process that can develop the performance and reliability of the battery module very well. An et al. (2019) proposed a liquid-cooled thermal management system with paraffin/expanded graphite composite material to keep the temperature rise and difference of lithium-ion batteries at the desired discharge rate of 3C. The conclusion shows that the heat distribution of the battery module increases with increased flow rate, but when the flow rate is higher than 0.08 m/s, increasing the flow rate has small effect on the development heat distribution performance.

There are only two studies involving batteries and artificial neural networks. Panchal et al. (2016) examined the thermal modelling of the temperature rise in lithium-ion batteries. They used artificial neural networks to develop the model. Temperature and voltage conclusions obtained from the design were checked with experimental data. In the study, the cooling temperature in the 2C and 4C discharge state was chosen as 5 °C, 15 °C, 25 °C and 35 °C. As a result, increased discharge rates were found to rise the surface temperature of the battery. Xuan et al. (Qian et al. 2019) examined the optimization of the heat distribution of the batteries with ANN. They considered the maximum temperature and temperature difference as the outputs. They used the Bayesian regularization algorithm as a training algorithm.

Although there are many studies on thermal analysis of batteries, there are only two studies in which thermal analysis of batteries and estimation with ANN are made including several deficiencies. In our study, more training algorithms (1, Levenberg-Marquardt (LM); 2, Bayesian regularization (BR); 3, scaled conjugate gradient (SCG); and 4, Pola-Ribiere conjugate gradient (CGP)) were used. More data (3132 pattern) were used, whereas not only temperature values but also area-weighted average potential values were evaluated as the outputs. The more data we use, the closer we will be to the correct guess. The analysis of the batteries is a long, time-consuming work, and artificial neural networks are modules that save us time with high-rate estimation ability. The operating range of the battery module is kept wider (0.5C–1.0C–1.5C–2.0C–2.5C). Two different speeds are discussed for battery cooling (0.5 m/s–1.0 m/s). Three different air inlet temperatures are discussed

(289K, 292K and 295K). Also the through three different statistical analysis have the most correct result (R2, RMSE, CoV).

Secondly, as can be seen from the literature, while conducting thermal or electrical analysis of the batteries, the effect of busbar (the elements connecting the batteries) was not considered in any study. Busbars are important elements of the module, which warms up as much as the batteries. In our study, we discussed the busbars and evaluated the results together.

1.2 The Battery Pack Model

The battery module with air cooling is given in Figure 1.1. The battery module consists of ten li-ion prismatic batteries with cathode material LiMn_2O_4 . In the module, nine busbars were added to connect the batteries together.

1.2.1 Numerical Solution

The numerical calculation was made in FLUENT 18.1. The Laminar model was chosen. The numerical solution was studied in FLUENT 18.1. The Newman, Tiedemann, Gu and Kim (NTGK) empirical model was selected. SIMPLE (semi-implicit method for pressure-linked equations) was used in this study as a solution method. For spatial discretization, ‘least squares cell based’ was chosen as the gradient discretization method because it has advanced calculation accuracy. ‘Second order’ was applied as the pressure, momentum and energy discretization method. The velocity inlet was selected for the inlet boundary situation, and the pressure outlet was selected for the output boundary situation. The convection heat transfer

Fig. 1.1 The battery module with air cooling

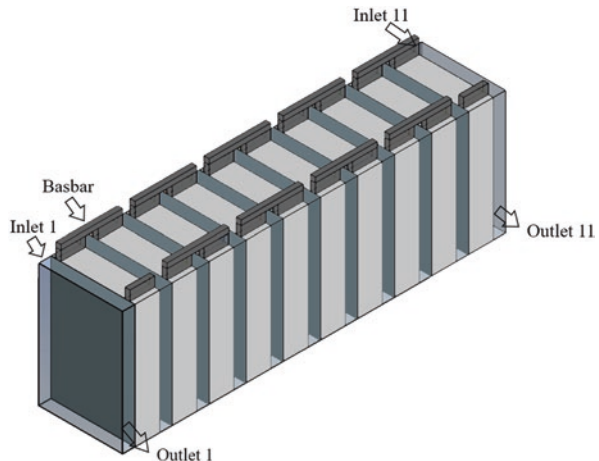
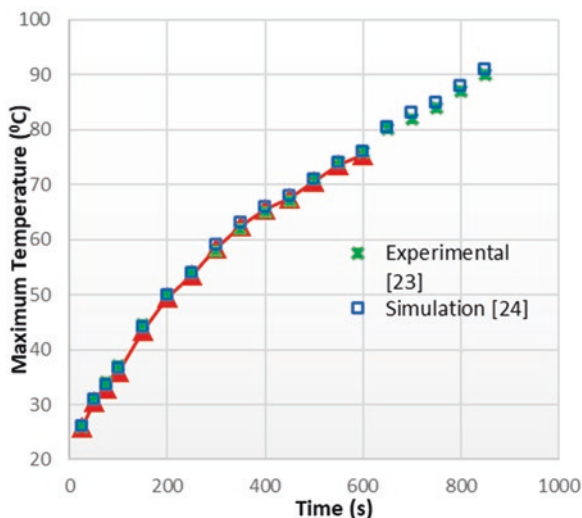


Fig. 1.2 Compared results of our study and the literature for one battery



coefficient of whole surfaces of the module was received as $5W/(mK)$, and the convection boundary situation was taken for whole surfaces. The inlet air temperatures were chosen as 289K, 292K and 295K, and inlet velocities are chosen as 0.5 m/s and 1.0 m/s. An independency testing of the size of grids was done to ensure the accuracy of calculations. The number of nodes has been increased from 78750 to 992540. When the size of nodes increased from 622400 to 762899, the change in the maximum temperature was seen to be 0.5 %. The grid size chosen was 622400 because this had the best conclusion in a short period. Mesh size function is curvature, and max face size is 0.0008.

In Figure 1.2, we compared our study with the literature for one battery. The close evaluation demonstrates the accuracy of our study. Comparisons were done at a discharge ratio of 5C. It was shown that the relative error didn't exceed 1.62% (Qian et al. 2016; Rao et al. 2015)

1.2.2 Governing Equations

The temperature of single battery was estimated with the energy conservation equation (Amiribavandpour et al. 2015):

$$\frac{\partial}{\partial t}(\rho_b C_{pb} T) = \nabla \cdot (k_b \nabla T) + Q_{gen} \quad (1.1)$$

In Equation (1.1), Q_{gen} is the heat generation of the battery, ρ_b is the density, k_b is the thermic conductivity, C_{pb} is the heat capability and T is the temperature. The battery temperature is set through Q_{gen} (Amiribavandpour et al. 2015).

$$Q_{gen} = Q_r + Q_j \quad (1.2)$$

The resource Q_{gen} forms electrochemical reaction heat Q_r and joule heat Q_j . Electrochemical reaction heat forms in consequence of chemical reactions. The calculation of the Q_r is set in Equation (1.3) (Karimi and Li 2013).

$$Q_r = -T \Delta S \frac{I}{nF} \quad (1.3)$$

In Equation (1.3), I is the discharge current, n is the size of electrons, F is the Faraday stable, ΔS is the entropy alteration and T is the temperature.

Joule heat forms in consequence of current transfer. The calculation of the Q_j is dedicated in Equation (1.4).

$$Q_j = I(E - V) \quad (1.4)$$

In Equation (1.4), E is the open circuit voltage and V is the operational voltage. That's why Q_{gen} is identified in Equation (1.5).

$$Q_{gen} = I(E - V) - T \Delta S \frac{I}{nF} \quad (1.5)$$

The continuity, momentum and energy conservation equations are given as follows:

Continuity equation:

$$\frac{\partial \rho}{\partial t} + \nabla \cdot (\rho \vec{u}) = 0 \quad (1.6)$$

Momentum conservation equation:

$$\frac{\partial \vec{u}}{\partial t} + (\vec{u} \nabla) \vec{u} = -\frac{\nabla p}{\rho} + \frac{\mu}{\rho} \nabla^2 \vec{u} \quad (1.7)$$

Energy conservation equation:

$$\rho c_p \left(\frac{\partial e}{\partial t} + u_x \frac{\partial e}{\partial x} + u_y \frac{\partial e}{\partial y} + u_z \frac{\partial e}{\partial z} \right) = k \left(\frac{\partial^2 e}{\partial x^2} + \frac{\partial^2 e}{\partial y^2} + \frac{\partial^2 e}{\partial z^2} \right) \quad (1.8)$$

The Newman, Tiedemann, Gu and Kim (NTGK) model was selected in this study. NTGK model is a simple semi-empirical electrochemical model. The model equality are dedicated in Equations (1.9), (1.10) and (1.11) (ANSYS FLUENT Tutorial Guide 18 2017)

$$\nabla \cdot (\sigma_+ \nabla \varphi_+) = -(j_{ECh} - j_{short}) \quad (1.9)$$

$$\nabla \cdot (\sigma_- \nabla \varphi_-) = j_{ECh} - j_{short} \quad (1.10)$$

$$j_{ECh} = \alpha Y [U - (\varphi_+ - \varphi_-)] \quad (1.11)$$

In the equation, σ_+ and σ_- are the effective electric conductivities for the positive and negative electrodes, while φ_+ and φ_- are the phase potentials for the positive and negative electrodes, j_{ECh} is the volumetric current transfer ratio and j_{short} is the current transfer ratio. The resource term, j_{ECh} , was calculated using an electrochemical sub-model (ANSYS FLUENT Tutorial Guide 18 [2017](#)).

1.3 ANN Modelling of Li-Ion Battery

Artificial neural network is a knowledge technology improved by inspiring the knowledge working technique of the humanistic brain. ANN simulates the way the simple biological nervous system works. Fake nerve cells store neurons, and these neurons are attracted to each other in different ways to shape the network. These networks are able to understand, store and explain the relation between information. In other words, ANNs provide solution to the question that generally requires an individual's native capability to contemplate and observe. The primary cause why a person can produce solutions for questions that imply contemplation and observation skills is the ability of the human brain, and hence the ability to understand by seeing or trying. ANNs are numerical systems comprising several operation units (neurons) that are weighted together. A working unit is actually an equality frequently applied to as the transfer function. This working unit takes marks from other neurons; it associates, reduces and produces a numerical conclusion. Usually, the working units communicate to real neurons approximately and are connected in a network; this construction also forms neural networks.

Many learning algorithms are present to achieve the relation between the inputs and the outputs. The most common preferred algorithm is the feedforward back-propagation learning algorithm. It is a gradient descent algorithm. The most common preferred algorithms in the field of energy and battery are Bayesian regularization (BR), Levenberg-Marquardt (LM), Pola-Ribiere conjugate gradient (CGP) and scaled conjugate gradient (SCG). LM and BR algorithms appear to be the fastest method for feedforward neural networks (Qian et al. [2019](#); Arslan and Yetik [2011](#); Arslan and Yetik [2014](#)). The construction of the created model is decided by considering certain statistical techniques, for example, the coefficient of multiple determinations (R^2), the root mean square error ($RMSE$) and covariation (CoV). These statistical conclusions are marked by output value (y_{output}), average of output (\bar{y}_{output}), actual value (y_{real}), average of actual (\bar{y}_{real}) and pattern number (n) as follows:

$$R^2 = \left[\frac{\sum_{m=1}^n (y_{output} - \bar{y}_{output})(y_{real} - \bar{y}_{real})}{\sqrt{\sum_{m=1}^n (y_{output} - \bar{y}_{output})^2 \sum_{m=1}^n (y_{real} - \bar{y}_{real})^2}} \right] \quad (1.12)$$

$$RMSE = \sqrt{\frac{\sum_{n=1}^n \left(\frac{y_{output} - \bar{y}_{real}}{y_{output}} \right)^2}{n}} \times 100 \quad (1.13)$$

$$CoV = \frac{\sum_{m=1}^n (y_{output} - \bar{y}_{output})(y_{real} - \bar{y}_{real})}{n} \times 100 \quad (1.14)$$

Inputs and outputs are standardized in the 0–1 range and rely on the non-linear transfer function, where the logarithmic sigmoid (logsig) is preferred:

$$f(ze) = \frac{1}{1 + e^{-ze}} \quad (1.15)$$

ze is the weighted sum. Equation (1.16) is given in ze . w is weight, y is output and b is bias.

$$ze_j = \sum_{i=1}^n w_{ij} y_i + b_j \quad (1.16)$$

1.3.1 Thermal and Electrical Result and Discussion of the Battery Module

In the study, ten prismatic batteries were connected in series to each other. The capacities of the batteries are 14.6 Ah and LiMn_2O_4 cathode. A three-dimensional thermal and electrical examination was done. The simulation study was carried out under forced transport (V_{inlet} : 0.5–1.0 m/s). While evaluating five different C ratios (0.5-1.0-1.5-2.0-2.5), the inlet temperature of air was handled in three different ways (295-292-289K). Consequently, the maximum temperature, minimum temperature and average of potential ϕ of the battery module were evaluated. In Figure 1.3, the maximum temperature distribution of the battery module is given when the air inlet speed is 0.5 m/s, C ratios are 0.5-1.0-1.5-2.0-2.5 and the air inlet temperatures are 289-292 and 295K. In Figure 1.4, the maximum temperature distribution of the battery module is given when the air inlet speed is 1.0 m/s, C ratios are 0.5-1.0-1.5-2.0-2.5 and the air inlet temperatures are 289-292 and 295K. In Figure 1.5, the minimum temperature distribution of the battery module is given

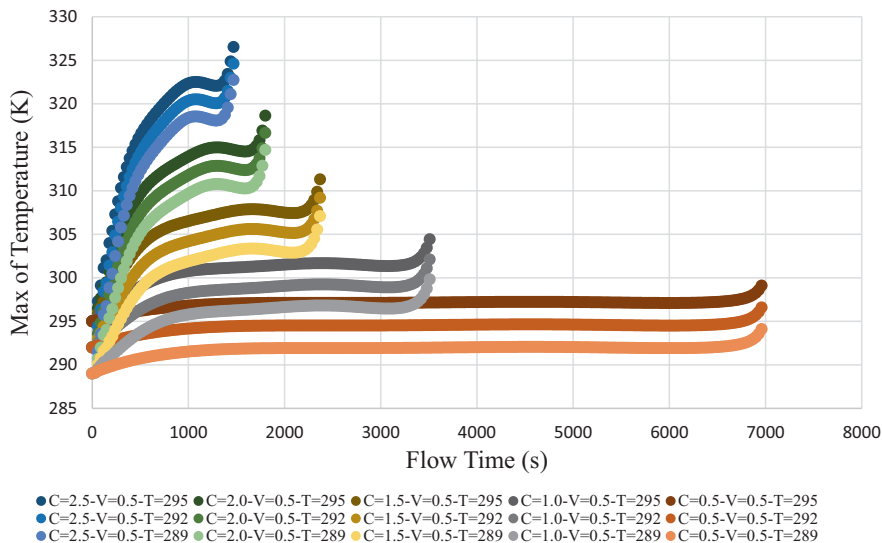


Fig. 1.3 The max temperature changes at different flow rates, and the inlet temperature under inlet velocity is 0.5 m/s

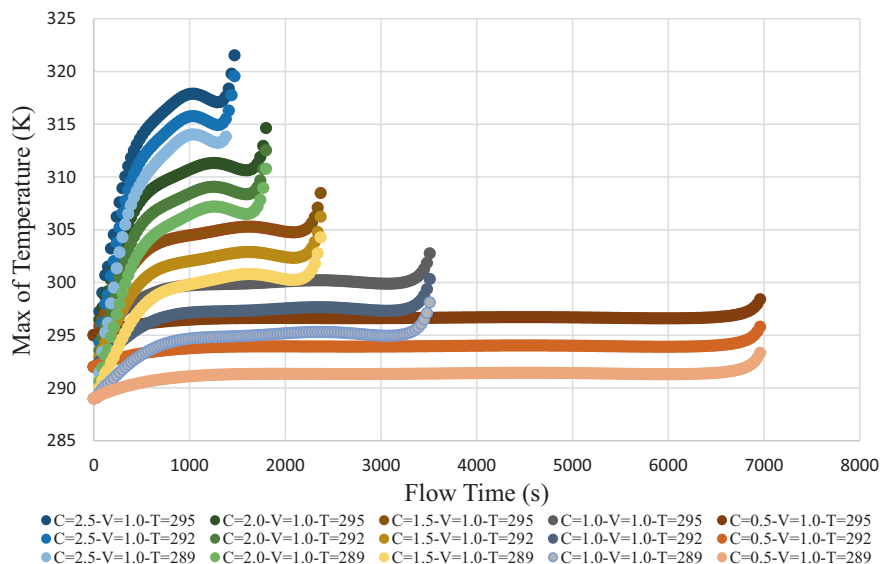


Fig. 1.4 The max temperature changes at different flow rates, and the inlet temperature under inlet velocity is 1.0

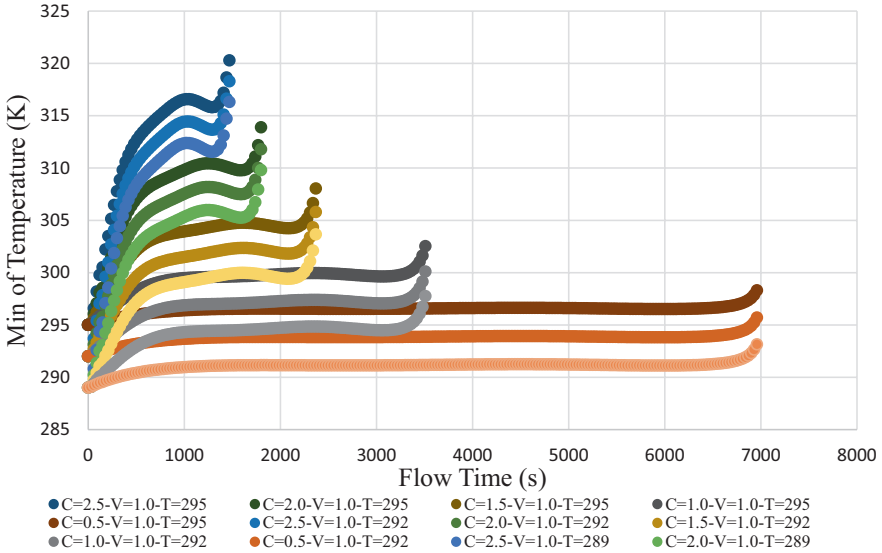


Fig. 1.5 The min temperature changes at different flow rates, and the inlet temperature under inlet velocity is 1.0 m/s

when the air inlet speed is 1.0 m/s, C ratios are 0.5-1.0-1.5-2.0-2.5 and the air inlet temperatures are 289-292 and 295K.

According to Figures 1.3–1.4 and 1.5, it was observed that the temperature of the battery module increased as the C ratio increased. It was observed that the temperature of the battery module decreased when the air inlet temperature decreased. The temperature of the module decreased as the air inlet speed increased. The temperature of 313K should not be exceeded to ensure the ideal advantage from batteries. The temperatures of the battery module were observed to be very high under velocity inlet 0.5 m/s in the case of a discharge rate of 2.5C and 2.0C under temperature inlet 295K (Fig. 1.3). The temperatures of the battery module were observed to be very high under velocity inlet 1.0 m/s and in the case of a discharge rate of 2.5C (Fig. 1.4). Figure 1.6 shows the discharge curve, and it demonstrates a control between the discharge curves at different discharge ratios variation from 0.5C to 2.5C. The figure indicates a reducing tendency for all discharge ratios, but the decrease ratio is suitable for the discharge ratio. Consequently, the area average potential will decrease instantly in the top part of the discharge ratio. For example, the discharge ratio of 2.5C has the maximum decrease tendency when compared to another discharge ratios.

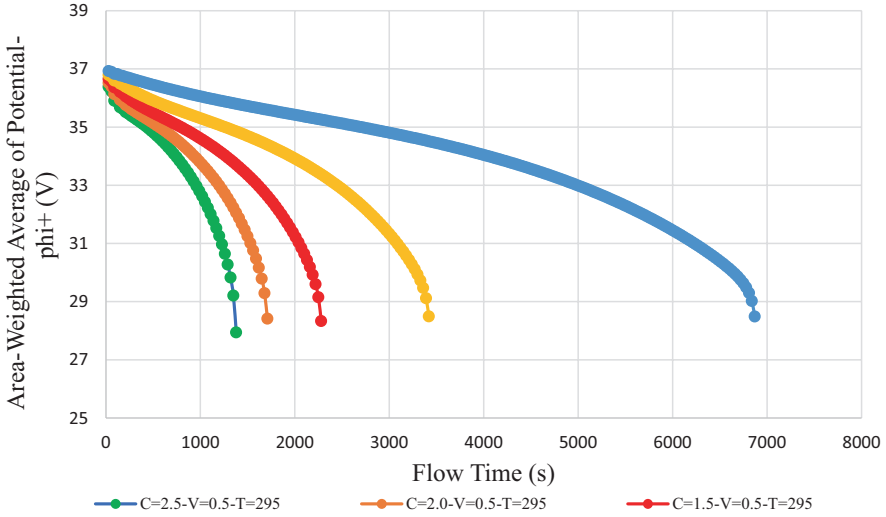


Fig. 1.6 Discharge curves at different flow rates (Vinlet, 0.5 m/s; Tinlet, 295K)

1.4 Estimation of the Result of the Battery Module with ANN and Discussion

In the ANN modelling of the ten prismatic battery module, there are three inputs: C ratio, temperature of the inlet boundary condition and velocity of the inlet boundary condition. Maximum temperature of the battery module, minimum temperature of the battery module and average of potential ϕ_+ were achieved as the outputs. Varying models were applied using the software MATLAB. These models were set using a data series including 3132 patterns. In the training step, 2505 (80%) of this pattern was used. A raised number of neurons (from 6 to 26) were tested to describe the output for 3000 epochs for BR and LM algorithms, because these algorithms are the most widely used ones and give the best accuracy. CGP and SCG training algorithms with the best neuron numbers were also compared. The results of the LM and BR training algorithm of the output of the maximum temperature value of the battery module are given in Tables 1.1 and 1.2. According to Tables 1.1 and 1.2, both LM and BR algorithms are very close and give good results, while the BR algorithm provided a little better results. Therefore, BR18 and CGP18 and SCG18 were compared in three output results and are given in Table 1.3.

Table 1.1 Comparison of BR algorithm for the maximum temperature of the battery module

| Algorithm | Testing step | | | |
|-----------------|-----------------|----------|-------------|-----------------|
| | R2 | RMSE | CoV | BR6 |
| 0.995044 | 0.013310 | 0.006822 | BR8 | 0.995359 |
| 0.013130 | 0.006737 | BR10 | 0.996811 | 0.010972 |
| 0.006750 | BR12 | 0.997148 | 0.011217 | 0.006751 |
| BR14 | 0.997876 | 0.009258 | 0.006756 | BR16 |
| 0.998227 | 0.008417 | 0.006762 | BR18 | 0.998985 |
| 0.006460 | 0.007024 | BR20 | 0.998861 | 0.006836 |
| 0.006781 | BR22 | 0.998760 | 0.007922 | 0.006749 |
| BR24 | 0.988566 | 0.007641 | 0.006752 | BR26 |
| 0.998480 | 0.007264 | 0.006762 | | |

Table 1.2 Comparison of LM algorithm for the maximum temperature of the battery module

| Algorithm | Testing step | | |
|--------------|-----------------|-----------------|-----------------|
| | R2 | RMSE | CoV |
| LM-6 | 0.994805 | 0.014021 | 0.006743 |
| LM-8 | 0.995449 | 0.013295 | 0.006738 |
| LM-10 | 0.996253 | 0.012064 | 0.006750 |
| LM-12 | 0.996267 | 0.012067 | 0.006765 |
| LM-14 | 0.997281 | 0.010235 | 0.006767 |
| LM-16 | 0.998828 | 0.010751 | 0.007176 |
| LM-18 | 0.998211 | 0.011655 | 0.006767 |
| LM-20 | 0.997964 | 0.011416 | 0.006793 |
| LM-22 | 0.997260 | 0.012477 | 0.006735 |
| LM-24 | 0.996895 | 0.012682 | 0.006772 |
| LM-26 | 0.996158 | 0.013578 | 0.006785 |

Table 1.3 Comparison of CGP, BR and SCG algorithms for three output results

| Algorithm | Training step | | | Testing step | | | R2 |
|-----------------|-----------------|------------------------|-----------------|------------------------|-----------------|------------------------|-----------------|
| | RMSE | CoV | R2 | RMSE | CoV | For the parameter Tmax | CGP18 |
| 0.966915 | 0.034270 | 0.006512 | 0.97164 | 0.032357 | 0.006799 | BR18 | 0.998895 |
| 0.006587 | 0.006780 | 0.998985 | 0.006460 | 0.007024 | SCG18 | 0.852686 | 0.06706 |
| 0.005879 | 0.854946 | 0.068302 | 0.006052 | For the parameter Tmin | CGP18 | 0.970225 | 0.032299 |
| 0.006405 | 0.974348 | 0.030572 | 0.006689 | BR18 | 0.998778 | 0.006863 | 0.00667 |
| 0.998877 | 0.006739 | 0.006936 | SCG18 | 0.843671 | 0.068844 | 0.005733 | 0.84645 |
| 0.069952 | 0.005910 | For the parameter phi+ | CGP18 | 0.939339 | 0.048633 | 0.008047 | 0.936935 |
| 0.05207 | 0.008524 | BR18 | 0.998389 | 0.008832 | 0.008242 | 0.997856 | 0.01109 |
| 0.008902 | SCG18 | 0.881022 | 0.064699 | 0.007828 | 0.884015 | 0.067085 | 0.008239 |

Fig. 1.7 Structure of the best ANN topologies for the battery module

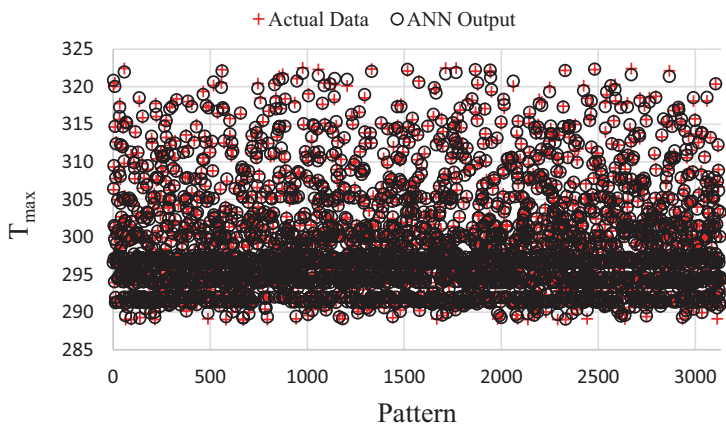
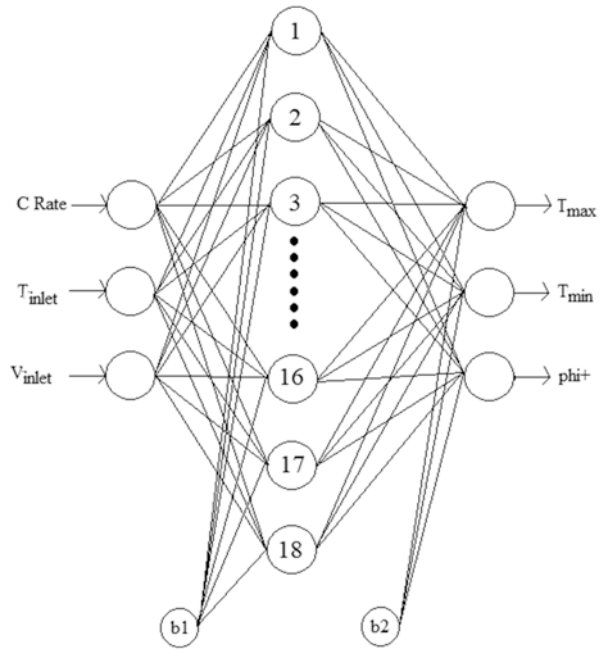


Fig. 1.8a The comparison of ANN estimate and real design results for T_{max}

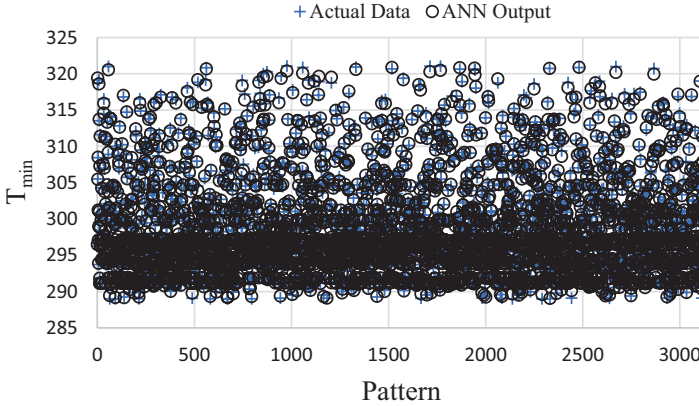


Fig. 1.8b The comparison of ANN estimate and real design results for T_{min}

According to Table 1.3, the best algorithm among the three output results is BR18 algorithm. According to Tables 1.1, 1.2 and 1.3, each ANN model was highly satisfactory and could be used for the applicability of a battery module with an acceptable level of accuracy. The ideal ANN topology was found to be BR18. The structure of the ideal topologies is indicated in Figure 1.7.

The value of R^2 was obtained to be 0.998895 when the values of RMSE and CoV were determined to be 0.006587 and 0.00678, respectively, for the outputs of T_{max} in the training step. These values were, respectively, 0.998985, 0.006460 and 0.007024 in the testing step. The comparison of the actual and the ANN outputs is given in Figure 1.8a for the maximum temperature of the battery module. The value of R^2 was obtained to be 0.998778 when the values of RMSE and CoV were determined to be 0.006863 and 0.00667, respectively, for the outputs of T_{min} in the training step. These values were, respectively, 0.998877, 0.006739 and 0.006936 in the testing step. The comparison of the actual and the ANN outputs is given in Figure 1.8b for the minimum temperature of the battery module. The value of R^2 was obtained to be 0.998389 when the values of RMSE and CoV were determined to be 0.008832 and 0.008242 for the output of ϕ_{+} in the training step. These values were, respectively, 0.997856, 0.01109 and 0.008902 in the testing step. The comparison of the actual and the ANN outputs is given in Figure 1.8c for average of potential ϕ_{+} of the battery module.

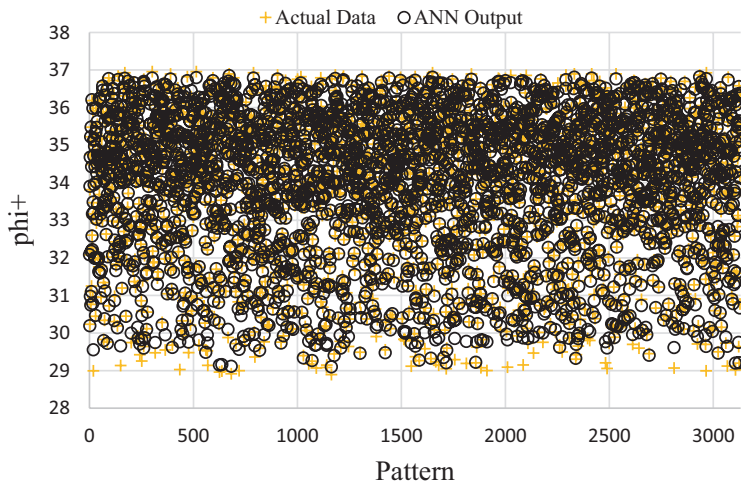


Fig. 1.8c The comparison of ANN estimate and real design results for $\phi+$

1.5 Conclusion

Due to air pollution, increase in greenhouse gases and reduction of fossil energy sources, the need for electric vehicles in both land and air transportation is increasing every day. The most important element in designing electric vehicles is the storage of energy. For this reason, batteries are of great importance today. In this study, the temperature and electrical analyses of the battery modules were examined. These temperature and electrical analysis results require lengthy studies, so ANN was proposed for reliable results in a short time.

The temperature and electrical results of the battery modules were evaluated with ANN's perfectly matched alloys because ANN is a non-linear neural network. The best-performing algorithms BR, LM, SCG and CGP were evaluated in the study. Algorithms were evaluated by some statistical methods, such as R^2 , RMSE and CoV. Although the results of the BR and LM algorithms are both very close to each other and very good, the BR algorithm provided a little better result than the LM algorithm for our three output results. R^2 values were 0.998895 for T_{max} output, 0.998778 for T_{min} output and 0.998389 for $\phi+$ output.

As the temperature of the batteries increases, its electrical conductivity decreases. In addition, temperature increase causes irreversible damage and explosions in the batteries. Therefore, it is requested that the batteries do not exceed 313K, which is the optimum operating temperature. In the case of air inlet speed of both 0.5 and 1.0 m/s and three different air inlet temperatures, our battery module was found to exceed the optimum temperature at 2.5C. At the same time, in the case of air inlet speed of 0.5 m/s and air inlet temperature of 295K, our battery module exceeded the optimum temperature at 2C. If it is necessary to work at these C ratios, lower air inlet temperature or bigger air inlet speeds may be preferred.

References

- Amiribavandpour, P., Shen, W., Mu, D., Kapoor, A.: An improved theoretical electrochemical-thermal modelling of lithium-ion battery packs in electric vehicles. *J. Power Sources*. **284**, 328–338 (2015)
- An, Z., Chen, X., Zhao, L., Gao, Z.: Numerical investigation on integrated thermal management for a lithium-ion battery module with a composite phase change material and liquid cooling. *Appl. Therm. Eng.* **163**, 114345 (2019)
- ANSYS, Inc. and ANSYS Europe, Ltd. are UL registered ISO 9001: 2008 companies, Ansys fluent tutorial guide 18 (2017).
- Arslan, O., Yetik, O.: ANN based optimization of supercritical ORC-Binary geothermal power plant: Simav case study. *Appl. Therm. Eng.* **31**, 3922–3928 (2011)
- Arslan, O., Yetik, O.: ANN Modeling of an ORC-binary geothermal power plant: Simav case study. *Energy Sources, A: Recovery, Util. Environ. Eff.* **36**, 418–428 (2014)
- Bai, F., Chen, M., Song, W., Yu, Q., Li, Y., Feng, Z., Ding, Y.: Investigation of thermal management for lithium-ion pouch battery module based on phase change slurry and mini channel cooling plate. *Energy*. **167**, 561–574 (2019)
- Cicconi, P., Landi, D., Germani, M.: Thermal analysis and simulation of a Li-ion battery pack for a lightweight commercial EV. *Appl. Energy*. **192**, 159–177 (2017)
- Jilte, R.D., Kumar, R., Ahmadi, H.: Cooling performance of nanofluid submerged vs. nanofluid circulated battery thermal management systems. *J. Clean. Prod.* **240**, 118131 (2019)
- Jilte, R.D., Kumara, R., Ahmadi, M.H., Chenc, L.: Battery thermal management system employing phase change material with cell-to-cell air cooling. *Appl. Therm. Eng.* **161**, 114199 (2019)
- Karimi, G., Li, X.: Thermal management of lithium-ion batteries for electric vehicles. *Int. J. Energy Res.* **37**, 13–24 (2013)
- Kshetrimayum, K.S., Yoon, Y., Gye, H., Lee, C.: Preventing heat propagation and thermal runaway in electric vehicle battery modules using integrated PCM and microchannel plate cooling system. *J. Appl. Therm. Eng.* **159**, 113797 (2019)
- Lu, Z., Meng, Z., Wei, C., Hu, Y., Zhang, Y., Jin, W.: Thermal management of densely-packed EV battery with forced air cooling strategies. *Energy Procedia*. **88**, 682–688 (2016)
- Martín-Martína, L., Gastellurrutíaa, J., Larraonab, G.S., Antónb, R., Portillo-Valdés, L., Gild, I.: Optimization of thermal management systems for vertical elevation applications powered by lithium-ion batteries. *Appl. Therm. Eng.* **147**, 155–166 (2019)
- Panchalal, S., Dincer, I., Agelin-Chaab, M., Fraser, R., Fowler, M.: Thermal modeling and validation of temperature distributions in a prismatic lithium-ion battery at different discharge rates and varying boundary conditions. *Appl. Therm. Eng.* **96**, 190–199 (2016)
- Qian, Z., Li, Y., Rao, Z.: Thermal performance of lithium-ion battery thermal management system by using mini-channel cooling. *Energy Convers. Manag.* **126**, 622–631 (2016)
- Qian, X., Xuan, D., Zhao, X., Shi, Z.: Heat dissipation optimization of lithium-ion battery pack based on neural networks. *Appl. Therm. Eng.* **162**, 114289 (2019)
- Rao, Z., Huo, Y., Liu, X., Zhang, G.: Experimental investigation of battery thermal management system for electric vehicle based on paraffin/copper foam. *J. Energy Inst.* **88**, 241–246 (2015)
- Rao, Z., Qian, Z., Kuang, Y., Li, Y.: Thermal performance of liquid cooling based thermal management system for cylindrical lithium-ion-ion battery module with variable contact surface. *J. Appl. Therm. Eng.* **123**, 1514–1522 (2017)
- Sun, H., Dixon, R.: Development of cooling strategy for an air cooled lithium-ion battery pack. *J. Power Sour.* **272**, 404–414 (2014)
- Tong, W., Somasundaram, K., Birgenesson, E., Mujumdar, S., Yap, C.: Numerical investigation of water cooling for a lithium-ion-ion bipolar battery pack. *J. Int. J. Therm. Sci.* **94**, 259–269 (2015)
- Wang, S., Li, Y., Li, Y., Mao, Y., Zhang, Y., Guo, W., Zhong, M.: A forced gas cooling circle packaging with liquid cooling plate for the thermal management of Li-ion batteries under space environment. *Appl. Therm. Eng.* **123**, 929–939 (2017a)

- Wang, Z., Zhang, H., Xia, X.: Experimental investigation on the thermal behavior of cylindrical battery with composite paraffin and fin structure. *Int. J. Heat Mass Transf.* **109**, 958–970 (2017b)
- Weixiong, W., Wei, W., Shuangfeng, W.: Thermal management optimization of a prismatic battery with shape-stabilized phase change material. *Int. J. Heat Mass Transf.* **121**, 967–977 (2018)
- Zhao, C., Cao, W., Dong, T., Jiang, F.: Thermal behavior study of discharging/charging cylindrical lithium-ion-ion battery module cooled by channeled liquid flow. *J. Int. J. Heat Mass Transf.* **120**, 751–762 (2018)

Chapter 2

Active and Passive Flow Control Methods Over Airfoils for Improvement in Aerodynamic Performance



Musa Özkan

Nomenclature

| | |
|-----------------|---|
| CFI: | Cross-Flow Instability |
| LES: | Large-Eddy Simulation |
| NACA: | National Advisory Committee for Aeronautics |
| NASA: | National Aeronautics and Space Administration |
| TSI: | Tollmien-Schlichting Instability |
| A_p : | Planform Area |
| b : | Length of the Span |
| c : | Chord Length |
| $C_{D,press}$: | Pressure Drag |
| $C_{D,fric}$: | Friction Drag |
| C_D : | Drag Coefficient |
| C_L : | Lift Coefficient |
| F_D : | Drag Force |
| F_L : | Lift Force |
| V : | Free Stream velocity |
| α : | Angle of Attack |
| ρ : | Density of the Fluid |

2.1 Introduction

An airfoil is a two-dimensional cross-sectional view of blade or wing profiles, which are surely the main part of an aircraft. Fundamentally, three-dimensional boundary layer flows are usually encountered over the wings of an airplane or rotor

M. Özkan (✉)
Bilecik Seyh Edebali University, Bilecik, Turkey
e-mail: musa.ozkan@bilecik.edu.tr

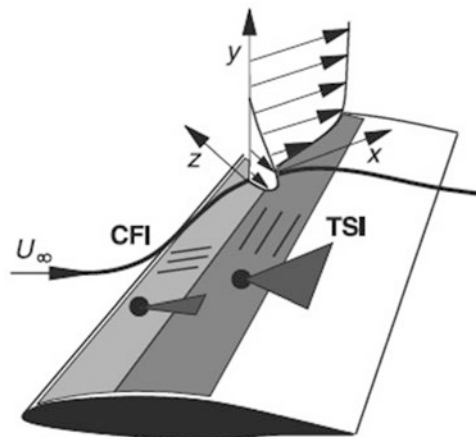
blades of a helicopter. A cross-flow component occurs at the tip of the blades and wings as a result of the pressure difference between the upper and lower surfaces of these geometries. This component affects the two-dimensional flow over the profile and creates a three-dimensional boundary layer.

Three-dimensional boundary layers are one of the most complex flow phenomena in fluid dynamics to conduct experiments and perform computational analyses. This is due to the fact that the transition mechanism from laminar to turbulent flow for three-dimensional boundary layers is completely different from the one exists for two-dimensional boundary layers. Two-dimensional boundary layers, which occur in most engineering applications and natural events such as the atmospheric boundary layer, are prone to Tollmien-Schlichting instability (White 1974). On the other hand, cross-flow instability occurs in three-dimensional boundary layers (Gregory et al. 1955; Kohama 1987).

The cross-flow effect and thus the three-dimensional boundary layer substantially occupy the whole region over the wing profile when the wing is designed as highly swept and also the flight is in the transonic or supersonic regions. Nevertheless, highly swept design of wings is not always encountered at every type of aircraft in aviation industry. Some unmanned aerial vehicles and rotor blades of helicopters, for instance, do not demonstrate a sweep angle. Moreover, the three-dimensional boundary layer does not completely occupy the suction side of the swept wing for flights in the subsonic region. Figure 2.1 demonstrates the different instability mechanisms encountered over a swept wing at the subsonic region (Schlichting and Gersten 2017).

Although the flow over the wing or the blade of an aircraft is three-dimensional, examination of this flow with a two-dimensional simplification can still provide valuable results (Erkan et al. 2020) since not all wing profiles of aircrafts have a sweep angle and besides flights in the subsonic region still establish a two-dimensional velocity profile over a large part of the wing that is far away from the tip (Ge et al. 2019). By this means, the investigation of two-dimensional flows over airfoils can both simplify the complexity of the problem and contribute to the aerodynamic performance characteristics of the wings and blades of aircrafts.

Fig. 2.1 Demonstration of instability regions in the three-dimensional boundary layer over a swept-wing profile. (*CFI* cross-flow instability; *TSI* Tollmien-Schlichting instability; Cooper et al. 2015)



By means of this simplification of the flow over wing profiles, aerodynamic forces acting on the airfoils and the effects of the boundary layer flow control mechanisms on these forces are greatly studied in literature. The objective of this chapter is to provide theoretical description of different flow control mechanisms and to summarize some of the recent studies concerning these engineering applications.

2.2 Aerodynamics of Airfoils

A solid body with any geometrical shape located inside a fluid flow will undergo aerodynamic forces. In the aviation industry, the most important ones of these forces are the lift and the drag forces. The lift force is the beneficial one that balances the weight of the aircraft against the gravitational force and carries the total mass of the flying object during the flight. The drag force, on the contrary, acts in the opposite direction of the thrust force that is provided by the engines of aircrafts. Therefore, to obtain an optimal flight condition, one needs to increase the lift force and decrease the drag force acting on the solid body immersed in a fluid flow.

An airfoil has a geometrical shape of which is known to be the most effective structure aerodynamically. These bodies are aimed to produce big lift forces, which are perpendicular to the flow direction and drag forces as small as possible. Many different airfoil profiles are modeled to obtain the most efficient ones to cover various flow conditions; see for instance, the list of airfoils provided by the National Advisory Committee for Aeronautics (NACA) or newly known as the National Aeronautics and Space Administration (NASA) (NACA Airfoil Tools 2020).

A schematic view of an airfoil is shown in Fig. 2.2, which also indicates the directions of the lift and the drag forces acting on this airfoil. This airfoil has constant chord length, c , in the span wise direction where the length of the span is

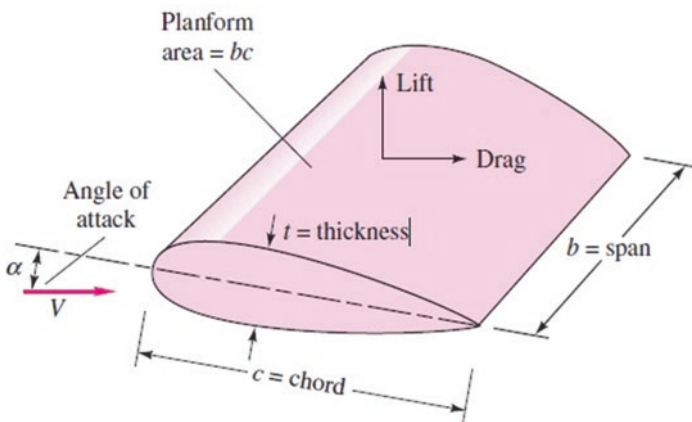


Fig. 2.2 A schematic view of an airfoil with the directions of lift and drag forces (White 2011) defined with respect to the planform area (Erkan and Ozkan 2020).

represented by b . Therefore, the planform area of this airfoil becomes $A_p = bc$. The most important parameter of the aerodynamic flows over airfoils is probably the angle of attack, α , which is the angle between the direction of the fluid flow and the chord line.

Considering the forces applied to an airfoil in their dimensional form is inappropriate, since these forces are obtained from the pressure distribution over the airfoil and obviously directly affected by the area of the airfoil. Nondimensional forms of these forces need to be considered for better evaluation of the aerodynamic characteristics, because it allows a direct comparison between different profiles of airfoils (Gölcük and Kurtuluş 2017). When the lift and the drag forces are represented by F_L and F_D , respectively, the nondimensional force coefficients C_L and C_D can be.

$$C_L = \frac{F_L}{\frac{1}{2}\rho V^2 A_p} \quad (2.1)$$

$$C_D = \frac{F_D}{\frac{1}{2}\rho V^2 A_p} \quad (2.2)$$

In Eqs. 2.1–2.2, V is the free stream velocity and ρ is the density of the fluid. When the chord is not constant along the span wise direction, then the planform area needs to be obtained by the integration of c with respect to b as, $A_p = \int c db$.

The upper surface of the airfoil is called the suction side, and the lower part is known as the pressure side. The edge that the fluid faces first is the leading edge, and from the trailing edge, the flow leaves the airfoil. The curved shape of the leading edge helps the airfoil to penetrate smoothly through the fluid and prevents the flow separation. The leading edge otherwise has a sharp form which deflects the flow and thus creates the lift force.

Figure 2.3 illustrates the time-dependent development of the lift force, where firstly the flow in downstream after the leading edge is irrotational and inviscid, seen in Fig. 2.3a. Then, in Fig. 2.3b, leading edge results in a flow separation and small vortex structures starts to form. In Fig. 2.3c, the formed vortex structures are discarded by means of the viscosity of the fluid, and the streamlines are started to be smooth again in the trailing edge at this stage. Lastly, Fig. 2.3d shows the vortex structures far behind the airfoil, and the flow at the trailing edge is very smooth where the lift force is considered to be fully developed at this final stage.

Figure 2.3 represents a flow over an airfoil at a small angle of attack. Although vortex structures and an adverse pressure gradient exist near the trailing edge, viscous effects at this angle of attack is strong enough to retain the flow attached to the surface of the airfoil, and thus a notable flow separation does not occur in the boundary layer. If the angle of attack is increased, the adverse pressure gradient at the suction side starts to be more powerful, and eventually a separation bubble forms and moves toward the leading edge (von Kármán 1921). At a particular angle $\alpha = 15^\circ$ to 20° , the fluid can no longer retain attached to the suction surface and entirely

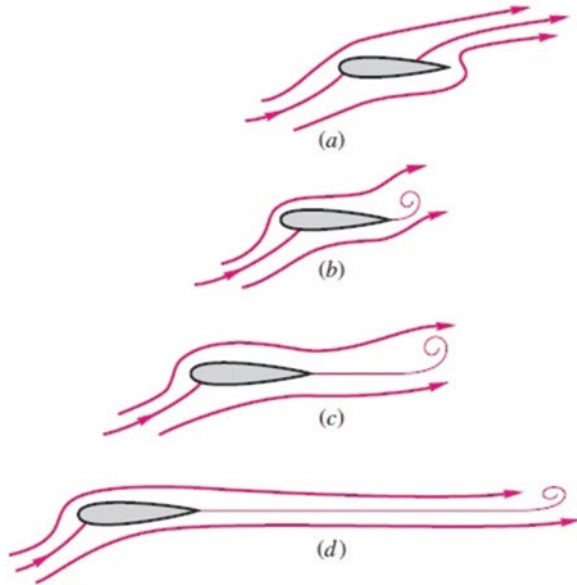
Fig. 2.3 The time-dependent stages of the development of the lift force on an airfoil:

a start-up;

b starting vortex forms;

c starting vortex is shed;

d starting vortex is shed far behind (White 2011),



separated from the airfoil. By this means, the lift force is drastically decreased, and the drag force, on the other hand, is significantly increased. As a result, the airfoil can no longer hang in the air, and the aircraft suddenly starts free fall. This flow phenomenon is called stall which needs to be carefully avoided in aviation.

2.2.1 Drag of Immersed Bodies

A drag can basically be considered as a loss of energy, which needs to be overcome by producing adequate energy from the engine to thrust the aircraft in the proposed direction of the movement. There are fundamentally two types of drag forces acting on an immersed body. One of them is resulted from the friction on the surface, i.e., the strong shear stress encountered in the vicinity of the airfoil surface due to no slip condition on the wall. The second one is formed due to the fact that the flow is separated from the surface and thus high- and low-pressure fields occur in the attached flow and the separated region, respectively. When considering the drag force on an object, the pressure drag and the friction drag need to be integrated to obtain the total drag force.

$$C_D = C_{D,press} + C_{D,fric} \quad (2.3)$$

The magnitudes of these drag forces, resulted from completely different mechanisms, totally depend on the shape of immersed body. If the flow separation is

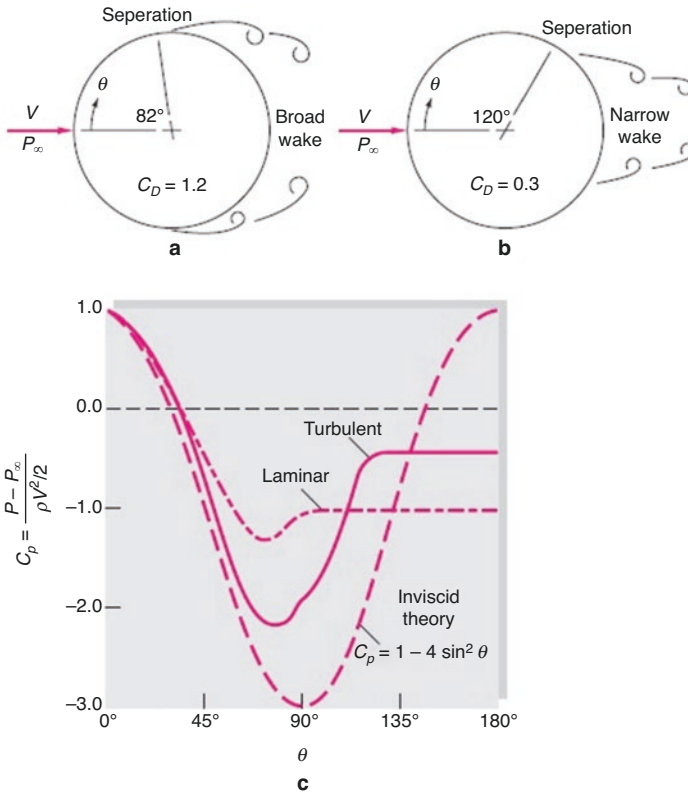


Fig. 2.4 Flow past a circular cylinder
a Laminar separation,
b Turbulent separation,
c Pressure distribution over the surface (White 2011).

strong, this causes a huge pressure drag, where in that case the friction drag can be negligible in comparison. Likewise, if there is no flow separation, then the viscous drag dominates the flow. Nevertheless, the viscous drag is unavoidable, and for an airfoil profile, it is insignificant compared to the pressure drag. Therefore, aerodynamic performance analyses focus on the reduction of pressure drag by means of flow control methods.

Figure 2.4 displays the flow past a circular cylinder as an example of an external flow over an immersed body. The theoretical solution which neglects the friction effects, i.e., inviscid theory, shows a complete symmetry, and thus the drag force does not act on the body, which is not logical, and this phenomenon is known as d’Alembert’s paradox (Young et al. 2011).

In reality, the viscous effects are significant, and according to the flow condition, boundary layer separation occurs on the cylinder. Figure 2.4a, for instance, shows the separation for a laminar boundary layer, where the flow detaches from the

surface at approximately 80° . The drag coefficient in this case is $C_D = 1.2$. When the boundary layer becomes turbulent, the flow can attach to the surface further and detaches at around 120° . This results in a reduction in the drag where the drag coefficient is decreased to $C_D = 0.3$.

The turbulent boundary layer is beneficial in terms of the boundary layer separation, since the flow separation is simply encountered when the energy of the flow inside the boundary layer is not enough to attach on the surface of the body. In the laminar boundary layer as a result of the strong shear stress near the wall, the flow loses its energy. However, strong eddies in the turbulent boundary layer can carry extra energy from the free stream flow into the boundary layer, and therefore the flow can attach to the surface further. Golf balls are typical examples of this phenomenon in real applications. The surface of a golf ball is intentionally produced with dimples, which trigger the turbulence over the golf ball. This allows the golf ball to fly longer with the same amount of the applied force.

In conclusion, flow control techniques mainly try to provide extra energy to the boundary layer, by triggering the turbulence at the right location over the surface. Consequently, the flow can attach to the surface of the airfoil longer, and thus the drag can be reduced significantly.

2.3 Boundary Layer Control Methods

The application of the boundary layer control methods on the flows over airfoils generally enhances the aerodynamic performance of aircrafts. These flow control methods can be divided into two main groups as active and passive control techniques. The main discrepancy between these methods is that for the active control approaches, an extra energy is necessary, while for passive control methods, no additional energy is required.

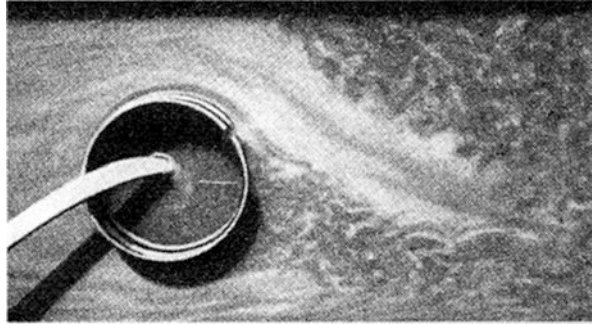
2.3.1 Active Flow Control Techniques

The main methods of active control techniques can be suction and blowing from slits located on the surfaces of airfoils. Moreover, a more recent development is using plasma actuators as active control methods. This section summarizes the principles of these two methods.

2.3.1.1 Suction and Blowing

Ludwig Prandtl was the first researcher to examine the effects of suction on the boundary layer flow over a circular cylinder in his experiments in 1904 (Prandtl 1904). Figure 2.5 illustrates this experiment, where a slit suction is located at the

Fig. 2.5 Flow past a circular cylinder with a slit suction on the upper side of the cylinder (Genc et al. 2020)



upper side of the cylinder. This illustration clearly shows that the flow over the upper side remains attached to the surface longer than the lower surface. The flow separation does not exist, and thus the drag is significantly reduced.

The placement of the suction on the surface mainly changes the flow velocity inside the boundary layer. As a result of the suction, the flow accelerates in front of the slit, and thus the flow separation is prevented. This is reasonable since the separation occurs due to the huge velocity gradient in the vicinity of the wall where no-slip boundary condition exists. Although the suction decelerates the flow downstream of the slit, the boundary layer needs to start from the zero thickness. Therefore, the flow can resist larger adverse pressure gradients, and the separation is not experienced.

The investigation of the implementation of suction as an active control method to improve the aerodynamic performance of airfoils was started even in the middle of the twentieth century (Goldstein 1948; Poppleton 1955). Even though the suction method is one of the most effective drag reduction techniques, there are significant drawbacks such as the energy required for the suction and the existence of an additional sink drag that needs to be considered for the calculation of the total drag acting on the airfoil. Nevertheless, the idea of using suction as a means of aerodynamic performance enhancer for airfoils is still an interesting research topic. A recent study, for instance, reported the efficiency of the uniform suction as a means of control method for the aerodynamic flow over NACA-4412 airfoil by means of LES and for a wide range of Reynolds numbers (Atzori et al. 2020).

Blowing, seen in Fig. 2.6, is another control mechanism, which essentially is providing extra kinetic energy to the boundary layer, where the velocity of the flow is slow. The jet of air is blown into the boundary layer from a small opening on the surface of an airfoil, and the risk of flow separation is reduced by means of the kinetic energy of this higher velocity fluid. Some aerodynamic researchers have been conducting studies concerning integrated suction and blowing to increase the aerodynamic performance (Liu et al. 2010; Pehlivanoglu et al. 2010; Goodarzi et al. 2012).

Fig. 2.6 Some active flow control methods: (a) blowing, (b) suction (Schlichting and Gersten 2017)

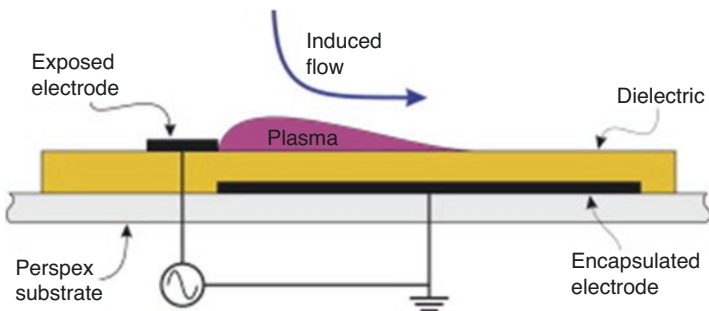
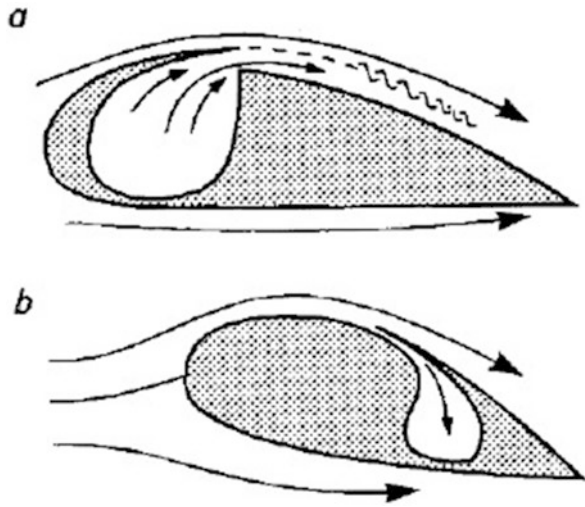


Fig. 2.7 Schematic of a single dielectric barrier discharge plasma actuator (Erfani et al. 2015; Erfani et al. 2013)

2.3.1.2 Plasma Actuators

Plasma actuators have recently been implemented for the control of aerodynamic flows over airfoils. These actuators consist of asymmetrically positioned electrodes and an alternative current voltage source. By means of the employment of a high voltage AC signal throughout the electrodes, a low-temperature plasma forms and the air around the electrodes are ionized. As a result, the ionized air molecules are speeded up via the electric field as shown in Fig. 2.7.

Due to the fact that this is a more recent development, the topic exceedingly draws the attention of aerodynamic researchers. One of the recent studies, for instance, examines the effects of plasma actuators on the flow over a wing profile of a micro-air vehicle, and the researchers reported that the plasma actuators are effective in the flow control of a flapping airfoil (Kumar and Wang 2020). Another study employed the plasma actuators as a means of flow control mechanism to improve the aerodynamic performance of wind turbine blades at low airspeeds (Omidi and Mazaheri 2020).

Similar to the suction/blowing method, this control technique requires additional energy to supply high voltages. Apart from this drawback, the control of the flow over an airfoil with the implementation of plasma actuators can be significantly beneficial.

2.3.2 *Passive Flow Control Techniques*

Although the active flow control mechanisms can effectively be used to suppress boundary layer separation, the necessity of extra energy is a crucial disadvantage. In terms of the sustainability of an aircraft, the amount of energy saved by means of the drag reduction with the application of a flow control method needs to be greater than the amount of energy required to operate the flow control unit itself. Therefore, studies investigating the efficiency of passive flow control methods are also in demand. This section outlines the mechanisms of some of the passive flow control techniques and briefly summarizes some studies conducted in literature.

2.3.2.1 **Vortex Generators**

Vortex generators, illustrated in Fig. 2.8, are one type of passive flow control methods. They can effectively be used over the blades of wind turbines with their simple implementation on the surface (Wang et al. 2017). The use of the vortex generators as a flow control technique was firstly introduced in 1947 (Taylor 1947). The employment of vortex generators is aerodynamically beneficial for the flows over not only the wind turbine blades but also the airfoils of aircrafts. Micro-vortex generators were investigated for the aerodynamic flow over high-lift airfoils (Lin et al. 1994), and an experimental research was conducted also for the airfoil performance with the application of vortex generators (Bragg and Gregorek 1987).

The principle of these vortex generators is simply that the rectangular- and/or triangular-shaped small plates are attached on the surface of the body at a desired

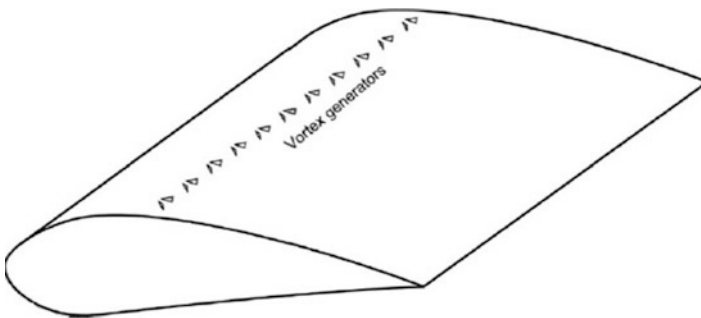


Fig. 2.8 Schematic of vortex generators placed on the surface of an airfoil (Pechlivanoglou 2012)

location. The flow over the body is disturbed when it faces these obstacles and becomes turbulent. By this means, low-velocity flow inside the laminar boundary layer can be energized in conjunction with the high velocity flow in the free stream. Thus, the flow can attach to the surface, and the boundary layer separation does not occur, which leads to a pressure drag reduction.

2.3.2.2 Airfoils with Cavity

One of the interesting passive flow control methods is installation of a cavity region on the suction surface of an airfoil. This method was originally presented in 1974 (Kasper 1974). The working principle of this method is that the flow is trapped inside a cavity geometry, which creates a suitable pressure gradient on the suction surface of an airfoil. Thus, the flow separation can be avoided, which results in a reduction in the drag (Genc et al. 2020).

A study examining the aerodynamic flow over an airfoil under various flow conditions and angles of attack revealed that the cavity on the surface could postpone the stall phenomenon that decreases the region of the flow separation (Olsman and Colonius 2011).

Another numerical study investigated the flow over NACA 0018 airfoil with a cavity structure on its suction surface in terms of aeroacoustics and reported that the cavity can provide an increased lift-to-drag ratio and also reduced noise levels (Lam and Leung 2018).

Figure 2.9 illustrates a typical example of a cavity structure positioned on the suction surface of an airfoil.

2.3.2.3 Surface Roughness

The skin friction drag that occurs in the turbulent boundary layer is greater than the one arises in the laminar boundary layer. On the other hand, the laminar flow is prone to the flow separation more than the turbulent flow, since the momentum and the energy loss in the laminar boundary layer are greater than the turbulent boundary layer. Therefore, in terms of the drag reduction, one needs to remain in the laminar region to reduce the friction drag and also needs to trigger the turbulence at the correct locations to prevent flow separation, i.e., a reduction in the pressure drag.

Until recently, the surface roughness has been considered, triggering the turbulence and thus increasing the skin friction drag (Dryden 1953). However, at the beginning of the twenty-first century, it was revealed that the flow can actually be

Fig. 2.9 The flow over an airfoil with a cavity on its suction surface (Olsman and Colonius 2011)



stabilized, and therefore the skin friction drag can be reduced by means of the application of the right sort of surface roughness (Carpenter 1997).

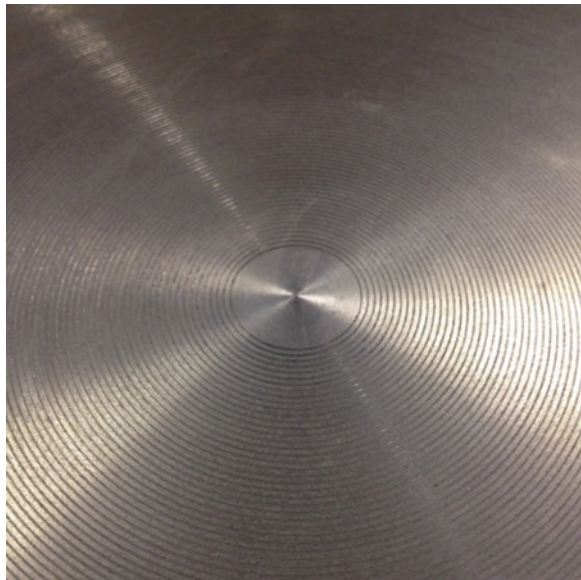
Thereafter, many researchers investigated the effects of the surface roughness on the transition process from laminar to turbulent. The main motivation of these studies is to reveal the definition of the right sort of roughness. Some numerical studies, which model the roughness as a sinusoidal surface and a partial-slip condition on the surface, have found that the distributed surface roughness can bypass the transition to turbulence and thus stabilize the three-dimensional boundary layer flows (Cooper et al. 2015; Garrett et al. 2016).

Furthermore, the examples of using roughness as a passive flow control method exist in nature. A recent study, for instance, reviews the effects of the riblet structures on the skin of sharks and reports that by means of their skin structures, sharks undergo reduced skin friction drag forces in the turbulent flow regime (Dean and Bhushan 2010).

In addition to computational studies, there are experimental investigations concerning different roughness profiles as a means of passive flow control approach. Concentrically grooved disk surfaces, shown in Fig. 2.10, for instance, are immersed in quiescent water to investigate their effects on the three-dimensional boundary layers (Ozkan 2016).

There are also studies comparing the effects arise from the surface roughness and the effects resulted from geometrical limitations of the experimental facilities. One of these studies, for instance, compared the effects of surface roughness and the confinement of a rotor-stator cavity flow configuration and reported that, for the type of flow configuration discussed there, it can be difficult to distinguish between these effects in experiments (Ozkan et al. 2017). In addition to the distributed

Fig. 2.10 Surface of a disk intentionally manufactured with concentric grooves having different roughness depths and profiles (Ozkan 2016)



roughness, single and/or dynamic roughness elements can also be employed for the control of the flow separation (Servini et al. 2018).

2.4 Conclusion

This chapter briefly reviews the active and passive flow control methods employed for the flows over airfoils to improve the aerodynamic performance of aircrafts. The main purpose of these two fundamentally different control techniques is to prevent the flow separation over the surface and thus reduce the pressure drag. A possible reduction in the drag is significantly important in the context of the sustainable aviation, since this is directly related with a reduction in the fuel consumption.

Although this review in the related literature revealed that both active and passive methods can efficiently be used as means of flow control mechanisms, there are some discrepancies between these two approaches.

The active methods are stronger than the passive methods due to fact that the control of the flow is adaptable based on the flow conditions. However, these control methods require additional energy to operate the control system itself. In terms of the sustainability, one can expect that the extra energy needed to power the system needs to be lower than the energy saved by means of the drag reduction.

The passive control techniques, on the other hand, do not require additional energy. However, the efficiency of these control mechanisms in comparison with the active ones can be questionable, since there is no chance of adjusting the control parameters according to the dynamic flow conditions during the flight.

In conclusion, this chapter provides practical guidance on the aerodynamic performance of aircrafts and the flow control techniques for the drag reduction. The information provided here might be beneficial for the aerodynamic researchers in the aviation industry.

References

- Atzori, M., Vinuesa, V., Fahland, G., Stroh, A., Gatti, D., Frohnapfel, B., Schlatter, P.: Aerodynamic effects of uniform blowing and suction on a NACA4412 airfoil. *Flow Turbul. Combust.* **105**(3), 735–759 (2020). <https://doi.org/10.1007/s10494-020-00135-z>
- Bragg, M.B., Gregorek, G.M.: Experimental study of airfoil performance with vortex generators. *J. Aircr.* **24**(5), 305–309 (1987). <https://doi.org/10.2514/3.45445>
- Carpenter, P.W.: The right sort of roughness. *Nature.* **388**, 713–714 (1997). <https://doi.org/10.1038/41870>
- Cooper, A.J., Harris, J.H., Garrett, S.J., Ozkan, M., Thomas, P.J.: The effect of anisotropic and isotropic roughness on the convective stability of the rotating disk boundary layer. *Phys. Fluids.* **27**(014107) (2015). <https://doi.org/10.1063/1.4906091>
- Dean, B., Bhushan, B.: Shark-skin surfaces for fluid-drag reduction in turbulent flow: a review. *Phil. Trans. R. Soc. A.* **368**, 4775–4806 (2010). <https://doi.org/10.1098/rsta.2010.0201>

- Dryden, H.L.: The review of published data on the effect of roughness on transition from laminar to turbulent flow. *J. Aeronaut. Sci.* **20**(7), 477–482 (1953)
- Erfani, R., Erfani, T., Utyuzhnikov, S.V., Kontis, K.: Optimisation of multiple encapsulated electrode plasma actuator. *Aerosp. Sci. Technol.* **26**, 120–127 (2013). <https://doi.org/10.1016/j.ast.2012.02.020>
- Erfani, R., Zare-Behtash, H., Hale, C., Kontis, K.: Development of DBD plasma actuators: the double encapsulated electrode. *Acta Astronaut.* **109**, 132–143 (2015). <https://doi.org/10.1016/j.actaastro.2014.12.016>
- Erkan, O., Ozkan, M.: Investigation of the flow over NACA 63–415 airfoil. *BSJ. Eng. Sci.* **3**(2), 50–56 (2020). <https://doi.org/10.34248/bsengineering.643916>
- Erkan, O., Ozkan, M., Karakoc, T.H., Garrett, S., Thomas, P.J.: Investigation of aerodynamic performance characteristics of a wind-turbine-blade profile using the finite-volume method. *Renew. Energy.* (2020). <https://doi.org/10.1016/j.renene.2020.07.138>
- Garrett, S.J., Cooper, A.J., Harris, J.H., Ozkan, M., Segalini, A., Thomas, P.J.: On the stability of von Kármán rotating-disk boundary layers with radial anisotropic surface roughness. *Phys. Fluids.* **28**(014106) (2016). <https://doi.org/10.1063/1.4939793>
- Ge, M., Zhang, H., Wu, Y., Li, Y.: Effects of leading edge defects on aerodynamic performance of the S809 airfoil. *Energy Convers. Manag.* **195**, 466–479 (2019). <https://doi.org/10.1016/j.encoman.2019.05.026>
- Genc, M.S., Koca, K., Demir, H., Acikel, H.H.: Traditional and new types of passive flow control techniques to pave the way for high maneuverability and low structural weight for UAVs and MAVs. Autonomous vehicles. *Doi:10.5772/intechopen.90552*Goldstein S (1948) low-drag and suction airfoils. *J. Aeronaut. Sci.* **15**, 189–220 (2020)
- Gölcük, A.I., Kurtuluş, D.F.: Winglet design and analysis for low-altitude solar-powered UAV. *Int. J. Sustain. Aviat.* **3**(1), 64–86 (2017). <https://doi.org/10.1504/IJSA.2017.085325>
- Goldstein, S.: Low-drag and suction airfoils. *J. Aeronaut. Sci.* **15**, 189–220 (1948)
- Goodarzi, M., Rahimi, M., Fereidouni, R.: Investigation of active flow control over NACA0015 airfoil via blowing. *Int. J. Aerosp. Sci.* **1**(4), 57–63 (2012)
- Gregory, N., Stuart, J.T., Walker, W.S.: On the stability of three-dimensional boundary layers with applications to the flow due to a rotating disk. *Philos. Trans. Roy. Soc London A.* **248**, 155–199 (1955)
- Kasper, W.: Aircraft Wing With Vortex Generation. US Patent 3,831,885 (1974)
- Kohama, Y.: Some expectations on the mechanism of cross-flow instability in a swept wing flow. *Acta Mech.* **66**, 21–38 (1987)
- Kumar, V.M., Wang, C.C.: Active flow control of flapping airfoil using Openfoam. *J. Mech.* **36**(3), 361–372 (2020). <https://doi.org/10.1017/jmech.2019.46>
- Lam, G.C., Leung, R.C.: Aeroacoustics of NACA 0018 airfoil with a cavity. *AIAA J.* **56**(3), 1–12 (2018). <https://doi.org/10.2514/1.J056389>
- Lin, J.C., Robinson, S.K., McGhee, R.J., Valarezo, W.O.: Separation control on high-lift airfoils via micro-vortex generators. *J. Aircr.* **31**(6), 1317–1323 (1994). <https://doi.org/10.2514/3.46653>
- Liu, P.Q., Duan, H.S., Chen, J.Z., He, Y.W.: Numerical study of suction-blowing flow control technology for an airfoil. *J. Aircr.* **47**(1), 229–239 (2010)
- NACA Airfoil Tools (2020) US. <http://airfoiltools.com/search/airfoils?m=a>. Accessed 29 Aug 2020
- Olsman, W.F.J., Colonius, T.: Numerical simulation of flow over an airfoil with a cavity. *AIAA J.* **49**(1), 143–149 (2011). <https://doi.org/10.2514/1.J050542>
- Omidi, J., Mazaheri, K.: Micro-plasma actuator mechanisms in interaction with fluid flow for wind energy applications: physical parameters. *Phys. Fluids.* **32**(7), 077107 (2020). <https://doi.org/10.1063/5.0011884>
- Ozkan, M.: Boundary Layer Transition Over Rotating Disks. Dissertation, University of Warwick (2016)
- Ozkan, M., Thomas, P.J., Cooper, A.J., Garrett, S.J.: Comparison of the effects of surface roughness and confinement on rotor–stator cavity flow. *Eng. Appl. Comp. Fluid.* **11**(1), 142–158 (2017). <https://doi.org/10.1080/19942060.2016.1247297>

- Pechlivanoglou, G.: Passive and Active Flow Control Solutions for Wind Turbine Blades. Dissertation, Berlin Institute of Technology (2012)
- Pehlivanoglu, Y.V., Yağız, B., Kandil, O., Baysal, O.: Particle swarm optimization of suction and blowing on airfoils at transonic speeds. *J. Aircr.* **47**(6), 1955–1965 (2010)
- Poppleton, E.D.: Boundary layer control for high lift by suction at the leading-edge of a 40 degree swept-back wing. ARC-RM-2897 (1955)
- Prandtl, L.: Über Flüssigkeitsbewegungen bei sehr kleiner Reibung. Verhandlg. III. Intern. Math. Kongr. Heidelberg, 484–491 (1904)
- Schlichting, H., Gersten, K.: *Boundary Layer Theory*, 9th edn. Springer, Berlin (2017)
- Servini, P., Smith, F.T., Rothmayer, A.P.: The impact of dynamic roughness elements on marginally separated boundary layers. *J. Fluid Mech.* **855**, 351–370 (2018). <https://doi.org/10.1017/jfm.2018.589>
- Taylor, H.D.: The elimination of diffuser separation by vortex generators. Technical Report No 4012. United Aircraft Corporation (1947)
- von Kármán, T.: On laminar and turbulent friction. *Z. Angew. Math. Mech.* **1**, 235–236 (1921)
- Wang, H., Zhang, B., Qiu, Q., Xu, X.: Flow control on the NREL S809 wind turbine airfoil using vortex generators. *Energy*. **118**, 1210–1221 (2017). <https://doi.org/10.1016/j.energy.2016.11.003>
- White, F.M.: *Viscous Fluid Flow*. McGraw-Hill, New-York (1974)
- White, F.M.: *Fluid Mechanics*, 7th edn. McGraw-Hill, New-York (2011)
- Young, D.F., Munson, B.R., Okiishi, T.H., Huebsch, W.W.: *A Brief Introduction to Fluid Mechanics*, 5th edn. Wiley, New York (2011)

Chapter 3

An Analysis on the Wind Speed and Direction Distribution Model of a Runway



Aziz Kaba

Nomenclature

| | |
|-------|---|
| ACC: | Allowable Crosswind Component |
| CDF: | Cumulative Distribution Function |
| FAA: | Federal Aviation Administration |
| ICAO | International Civil Aviation Organization |
| MADE: | Maximum Absolute Density Error |
| RDC: | Runway Design Code |
| RMSE: | Root Mean Square Error |
| R2: | R Squared |
| PDF: | Probability Density Function |
| WMM: | World Magnetic Model |

3.1 Introduction

Airport design is a multi-objective engineering optimization problem, where the configuration of its runway has the major effect on the design process. While the main issues regarding runway configuration are the number of runways and their layout with dimensional parameters, such as width and length, another variables are environmental impacts, shape of the airport land, surrounding buildings and operational prerequisites of the authorities. One of the main factors on runway design is the wind coverage, which comprises wind speed and direction, since runway configuration must be changed according to the properties of the wind (Chang 2015).

Wind is a very important measurement element in operational meteorology and aviation forecasting. Wind speed and direction have stochastic behaviour since the

A. Kaba (✉)

Faculty of Aeronautics and Astronautics, Eskisehir Technical University, Eskisehir, Turkey
e-mail: azizkaba@eskisehir.edu.tr

wind is considered as the most variable figure amongst the weather elements. In short term, it is possible to observe that the wind can increase or decrease its speed with a factor of two or more within seconds and can change its direction up to 180 degrees within a minute. Due to aforementioned nondeterministic characteristics, wind properties are measured with a time sample order of seconds, and their mean values are used in calculation (Burt 2012). But in order to preserve the marginal effects of the wind speed, peak values (both minimum and maximum) should be recorded within the given time frame of observations.

According to the angle between the runway and wind direction, wind terminology is changed. Wind is called as crosswind if the direction is perpendicular to the runway and called tailwind if the direction is the same with the course of movement of the aircraft but blows from aft of the aircraft. Also, wind is called as gust if a rapid fluctuation in wind speed is observed within a short period of time. Lastly, wind shear occurs both in vertical and horizontal plane, when the direction and speed properties are fluctuated rapidly. Crosswind not only depends on the configuration of the runway, but it also depends on the size of the aircraft. The maximum allowable crosswind limit for the aircrafts is obtained through the flight tests. Crosswind limit is proportional to the size of the aircraft (Bellasio 2014). During landing and take-off phases, if the crosswind with gusts exceeds limit of 20 knots, the risk of an accident is increased exponentially (Bellasio 2014; van Es and Karwal 2001). Also, if the tailwind passes the safety limit, possible overrun accidents are most likely to occur in landing phase (Bellasio 2014; van der Geest et al. 2001; van Es and Karwal 2001).

The orientation of the runways is designed in such a way that the usability factor of the airport must be more than 95% of all time. In order to satisfy this limit, runways are oriented throughout the direction of the prevailing winds. Thus, most of the time, the expected value of the wind direction will not be perpendicular to the runway, which decreases the probability of undesired crosswind in landing and take-off phases of the flight. The assessment of the direction of the prevailing wind must be based on the historical wind data for at least 5 years. Wind data should be tested for the reliability and completeness. Recorded dataset of the wind must contain speed, direction and time for at least eight measurements/day. The dataset is divided into segments by 10° wind direction with total of 36 direction segments. The dataset is plotted on a two-dimensional radial plane, which is known as wind rose. The resultant graph of wind rose can be used to obtain the prevailing wind direction, which determines the orientation of the runway (Bellasio 2014; Oktal and Yildirim 2014; Ashford et al. 2011).

Since the air traffic demand is growing exponentially, effective usage of the capacity of a runway is an important but a challenging factor (Tee and Zhong 2018). Runway and air traffic must be controlled under full potential so as to prevent the possible delays and minimize costs and incidents (Sahin 2019). Since wind coverage is a key figure in airport usability and also limit-exceeding speeds and undesired directions may cause go-around or other operational disruptions (Iijima et al. 2020), it is necessary to analyse the wind speed and direction distribution model of the runways.

Based on the above discussion, the motivation behind this paper covers the following aspects:

- Analysis of monthly wind speed histograms.
- Determination of wind speed models.
- Proposition of three-dimensional seasonal wind speed analysis with hourly and daily distributions.
- Derivation of yearly wind rose chart for the Eskisehir Hasan Polatkan Airport with more than 8800 samples/year.

The organization of the remainder is as follows: In Sect. 3.2, the properties of wind dataset is given. Section 3.3 covers the monthly wind speed histogram analysis and derivation of wind speed models with statistical analysis. In Sect. 3.4, seasonal analysis with hourly and daily distributions for three-dimensional space is conducted. In Sect. 3.5, wind rose comprising wind speed and direction distributions of the runway is derived for yearly dataset to determine the crosswind and prevailing wind direction of the airport. Lastly, discussions and conclusions are given in Section 3.6.

3.2 Wind Data

The proposed models, related coefficients, analyses and wind rose are based on and validated for the Eskisehir Hasan Polatkan Airport. The latitude and longitude of the meteorological station are 39.8133 N and 30.5284 E, respectively. The elevation of the field is 787 [m], and the station tower is 10 [m] above the field. Wind data is taken for a 1-year period with 24 samples/day (hourly) and a total of 8871 samples. A sample format of the dataset is given in Table 3.1. The calculated monthly mean wind speed and standard deviation values of the wind dataset (without null velocities) are given in Table 3.2. Time series distribution of the whole dataset is given in Fig. 3.1.

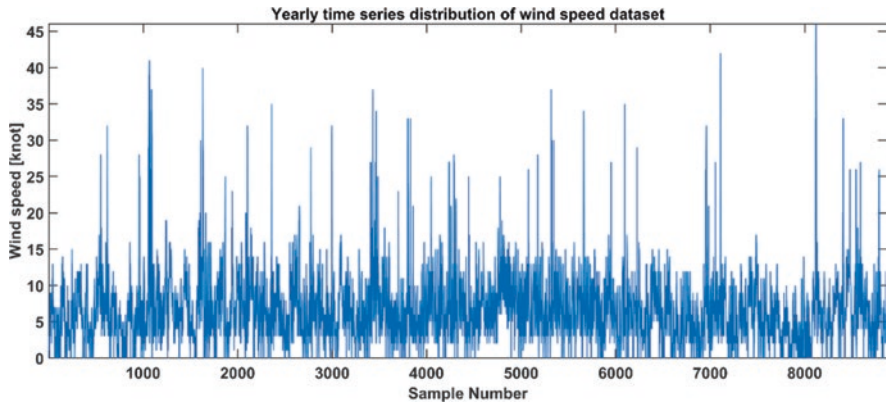
According to Table 3.2, it is seen that the monthly minimum mean wind speed value is no more than 5.86 [knot] with mean peak value of 8.06 [knot]. Standard deviations of the monthly mean wind speed values are relatively high in comparison

Table 3.1 Format of the wind dataset

| Datetime | Direction | Speed | Gust |
|---------------------|-----------|-------|------|
| Day/month/year/hour | 120 | 9 | 0 |
| Day/month/year/hour | 100 | 11 | 0 |
| Day/month/year/hour | 100 | 11 | 3 |
| Day/month/year/hour | 90 | 10 | 0 |
| Day/month/year/hour | 90 | 12 | 0 |
| Day/month/year/hour | 80 | 9 | 0 |
| Day/month/year/hour | 90 | 8 | 0 |

Table 3.2 Monthly mean wind speed and standard deviation values

| Month | Mean wind speed [knot] | Standard deviation [knot] |
|-----------|------------------------|---------------------------|
| January | 6.607194 | 3.679087 |
| February | 7.861027 | 5.769031 |
| March | 7.831293 | 4.879066 |
| April | 6.822254 | 3.979895 |
| May | 7.275766 | 5.145769 |
| June | 7.277620 | 4.778733 |
| July | 8.063309 | 4.059928 |
| August | 7.675141 | 4.369963 |
| September | 6.784946 | 3.774386 |
| October | 6.212077 | 4.184791 |
| November | 5.867596 | 3.122272 |
| December | 7.529086 | 4.938160 |

**Fig. 3.1** Yearly time series distribution of the wind speed dataset

to the mean wind speed values, which shows the random nature of the wind. It is observed that the value of the standard deviations is in the range of 3.12 [knot]–5.14 [knot].

Figure 3.1 shows that the maximum value of 46 [knot] is observed during the year, whereas general occurrence is between 5 and 15 [knot]. It is worth to mention that, in the following analysis, some missing data values are replaced with null parameters for seasonal analysis and also null velocities are disregarded for wind speed model distribution analysis to prevent the divergence of the pdf.

3.3 Wind Speed Model

In order to extract information from the dataset of the wind speed, a transformation is needed from time domain to probability domain. Firstly, wind speed values must be grouped according to the number of occurrences or frequencies. Then, occurrences must be normalized such that the sum of all the frequencies must be equal to 1. By doing so, the wind speed time series dataset is converted into the probability domain that all elements satisfy the following equation:

$$P = \{p_i \mid p_i \in [0,1], \sum_{i=1}^N p_i = 1\} \quad (3.1)$$

where p_i denotes the probability of wind speed.

Domain transformation is conducted for every set of data that are separated monthly. As a result, 12 wind speed histograms are obtained. In order to model the wind speed histograms, some known pdfs may be used. Amongst many, Rayleigh, Weibull, exponential and logistic distributions are used for wind speed modelling. But the widely used and accepted model for the wind speed distribution is Weibull (Akdag and Dinler 2009). Rayleigh distribution is a special case of the Weibull pdf, which has only one parameter. Also, Weibull distribution has two other variations that are two-parameter and three-parameter Weibull distributions. In this work, modelling of the wind speed histograms is achieved via two-parameter Weibull distribution since it is the widely used one. The pdf of Weibull distribution is given in Eq. (3.2).

$$f(v) = \left(\frac{k}{c}\right) \left(\frac{v}{c}\right)^{k-1} \exp\left(-\left(\frac{v}{c}\right)^k\right) \quad (3.2)$$

where v is the wind speed, $f(v)$ is the pdf, k is the shape parameter and c is the scale parameter. The cdf of the Weibull distribution is given in Eq. (3.3).

$$F(v) = 1 - \exp\left(-\left(\frac{v}{c}\right)^k\right) \quad (3.3)$$

where $F(v)$ is the cdf of the Weibull distribution. The monthly wind speed histograms and the proposed models are given in Figs. 3.2, 3.3 and 3.4. Shape and scale values for the pdf and cdf of the obtained models are given in Table 3.3.

Goodness-of-fit evaluation of the proposed pdf models for the monthly wind speed histograms of the runway is based on the maximum absolute pdf error, root mean square error and R-squared value. MADE metric is calculated according to Eq. (3.4).

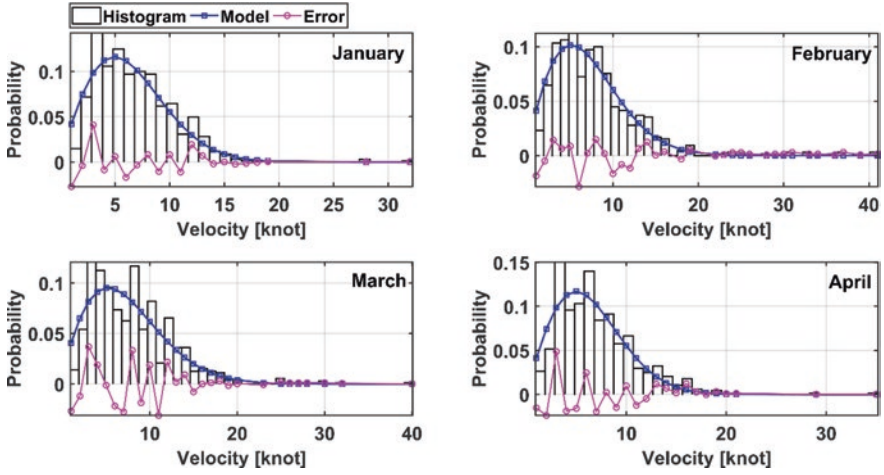


Fig. 3.2 Wind speed histogram, the proposed model and modelling error: January–April

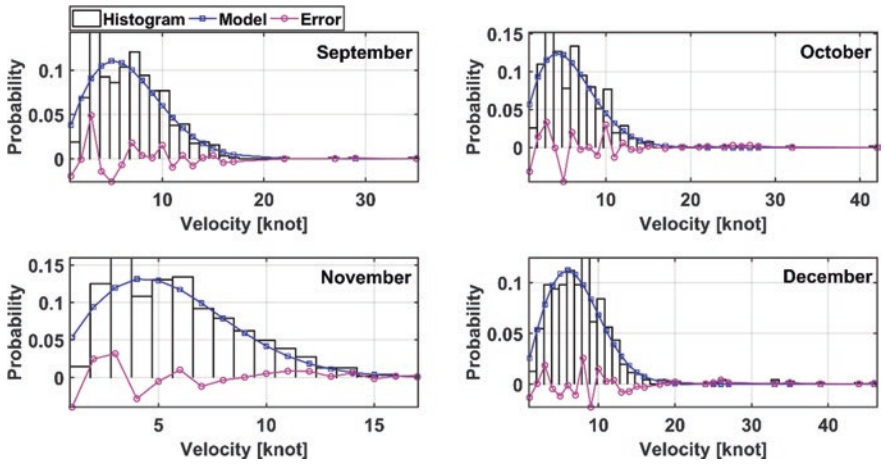


Fig. 3.3 Wind speed histogram, the proposed model and modelling error: May–August

$$MADE = \max(\|\varepsilon_{pdf}\|) \tag{3.4}$$

where \max is the maximum element of the set, $\|$ is the absolute value of the set and ε_{pdf} is the set of the modelling errors for the proposed models. RMSE metric is calculated by using Eq. (3.5) as follows:

$$RMSE = \sqrt{\frac{1}{N} \sum_{k=1}^N (y_k - \hat{y}_k)^2} \tag{3.5}$$

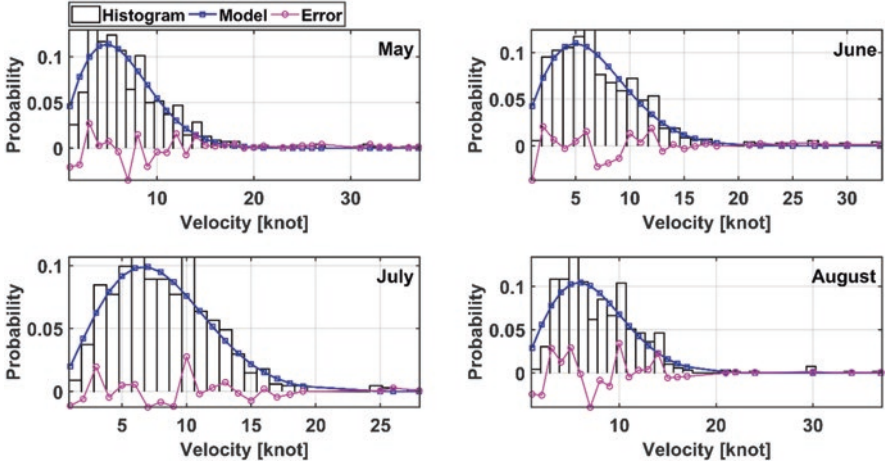


Fig. 3.4 Wind speed histogram, the proposed model and modelling error: September–December

Table 3.3 Parameters of the proposed wind speed models

| Month | k | c |
|-----------|----------|----------|
| January | 1.930629 | 7.20907 |
| February | 1.813647 | 7.953842 |
| March | 1.767624 | 8.372943 |
| April | 1.941637 | 7.194031 |
| May | 1.863537 | 7.203354 |
| June | 1.868342 | 7.479995 |
| July | 2.120383 | 9 |
| August | 2.0048 | 8.216008 |
| September | 1.929772 | 7.587462 |
| October | 1.83437 | 6.530539 |
| November | 1.921247 | 6.34236 |
| December | 2.122248 | 7.971803 |

where N is the number of observations, y_k is the measured values and \hat{y}_k is the proposed model values. R^2 metric for the goodness-of-fit test is given in Eq. (3.6).

$$R^2 = 1 - \frac{\sum_{k=1}^N (y_k - \hat{y}_k)^2}{\sum_{k=1}^N (y_k - \bar{y})^2} \tag{3.6}$$

where \bar{y} is the mean value.

Performance metrics for the proposed monthly wind speed model are close to 0 as desired for RMSE and MADE statistics. Also, the same convergence is observed with R^2 statistics since the best fit that can be obtained through the R^2 metric is 1.

The calculated error values of the proposed wind speed model are 0.0410 MADE, 0.0132 RMSE and 0.9143 R^2 for January; 0.0285 MADE, 0.0087 RMSE and 0.9440 R^2 for February; 0.0368 MADE, 0.0161 RMSE and 0.8269 R^2 for March; 0.0488 MADE, 0.0156 RMSE and 0.8755 R^2 for April; 0.0351 MADE, 0.0113 RMSE and 0.9207 R^2 for May; 0.0369 MADE, 0.0120 RMSE and 0.9157 R^2 for June; 0.0277 MADE, 0.0093 RMSE and 0.9369 R^2 for July; 0.0398 MADE, 0.0172 RMSE and 0.8375 R^2 for August; 0.0489 MADE, 0.0146 RMSE and 0.8890 R^2 for September; 0.0452 MADE, 0.0152 RMSE and 0.8975 R^2 for October; 0.0397 MADE, 0.0162 RMSE and 0.8924 R^2 for November; and, lastly, 0.0257 MADE, 0.0092 RMSE and 0.9510 R^2 for December.

3.4 Three-Dimensional Seasonal Models

The duration for the knowledge of the wind speed and direction data can be as important as the data itself. For example, to define the prevailing wind direction of a runway, a dataset with minimum of 5 years is needed. Also, the optimal minimum time frame between two samples can be taken hourly for runway operations, while an interval of 10 minutes is more appropriate for the wind energy potential determination of a site. Between short- and long-term calculations, it is also important to derive and determine the intermediate time frames, such as monthly and seasonal. While monthly models may be used to predict the flight schedules, seasonal models may be used to determine the impacts of the random wind effects so as to prevent delays or minimize costs during high seasons, such as summer or winter. So, it can be considered as important to get those informations out of the historical dataset. Some applications on the seasonal wind property determination can be found in (Kumaraswamy et al. 2011; Prema and Rao 2015; Soukissian et al. 2017; Jaramillo and Borja 2004; Zeng et al. 2020; Lledo et al. 2019).

Since airport is located on the northern hemisphere, yearly dataset is divided into the seasonal subsets as follows (Karatepe and Corscadden 2013):

- Winter: December, January and February.
- Spring: March, April and May.
- Summer: June, July and August.
- Autumn: September, October and December.

Since the sample time of the dataset is provided as hourly, it is also possible to propose the seasonal wind speed model in three-dimensional space rather than just two-dimensional plane with an additional axis information of the hour of the day. Thus, seasonal analysis can be further improved regarding days and hours with respect to the wind speed. With the proposed three-dimensional model, windy and calm days of the season can be investigated. Also, calm and windy hours of the days of the season can be determined, too. Three-dimensional models are given in Figs. 3.5, 3.6, 3.7 and 3.8 for winter, spring, summer and autumn, respectively. Also, contour planes of the proposed models are given in Figs. 3.9, 3.10, 3.11

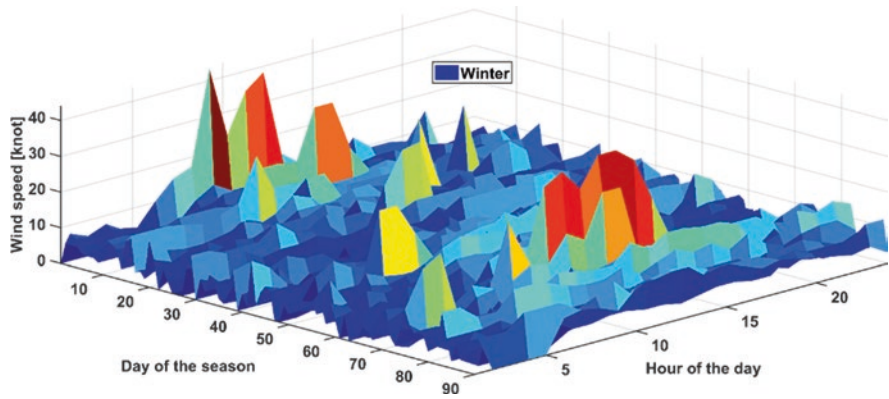


Fig. 3.5 Three-dimensional model of runway wind speed: Winter

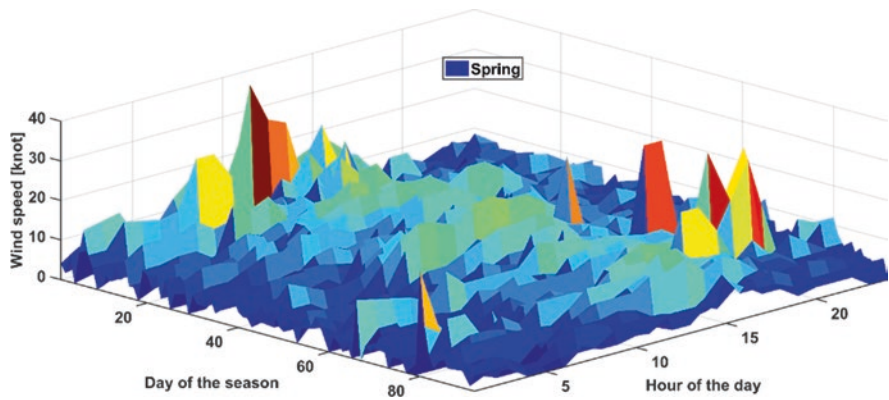


Fig. 3.6 Three-dimensional model of runway wind speed: Spring

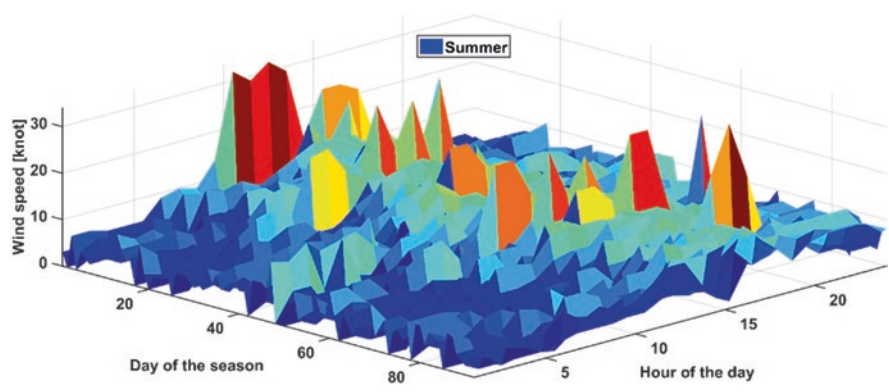


Fig. 3.7 Three-dimensional model of runway wind speed: Summer

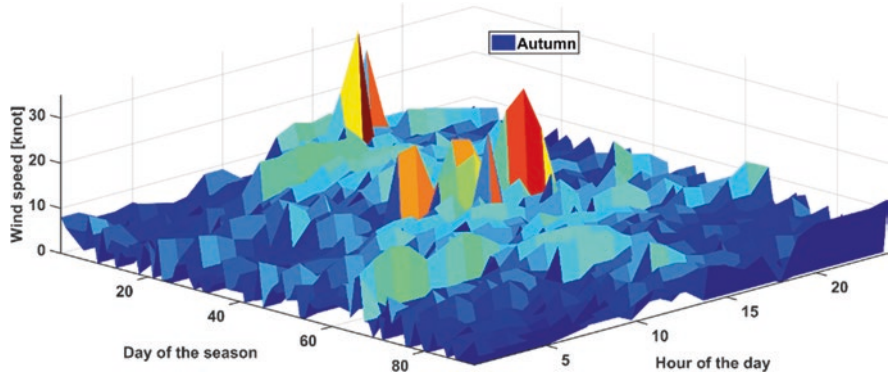


Fig. 3.8 Three-dimensional model of runway wind speed: Autumn

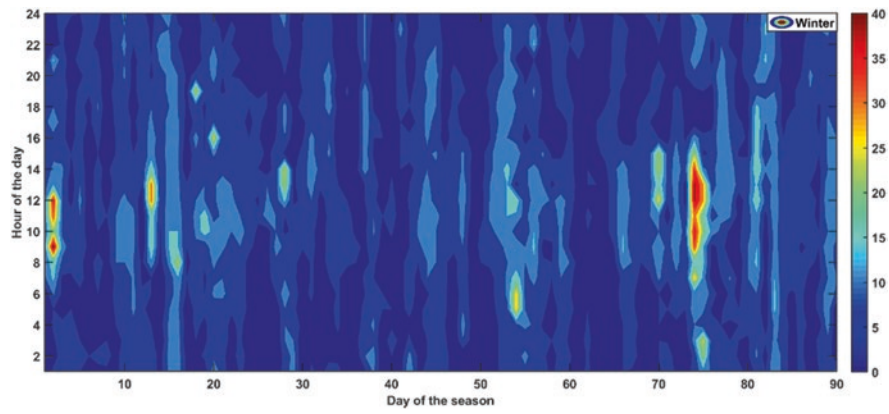


Fig. 3.9 Contour model of runway wind speed: Winter

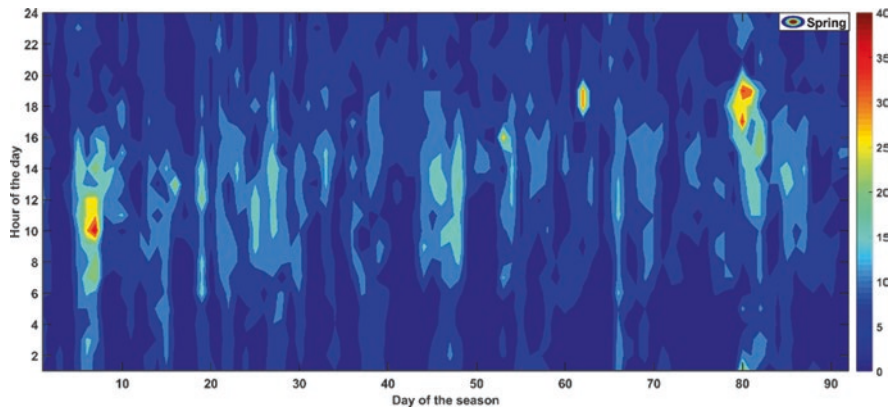


Fig. 3.10 Contour model of runway wind speed: Spring

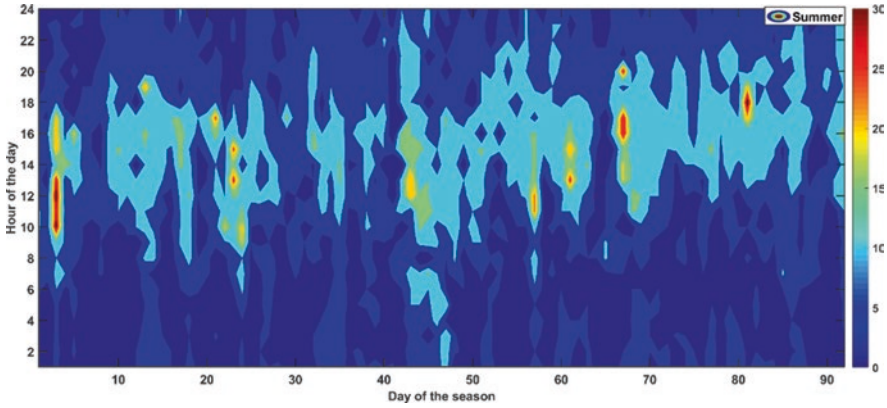


Fig. 3.11 Contour model of runway wind speed: Summer

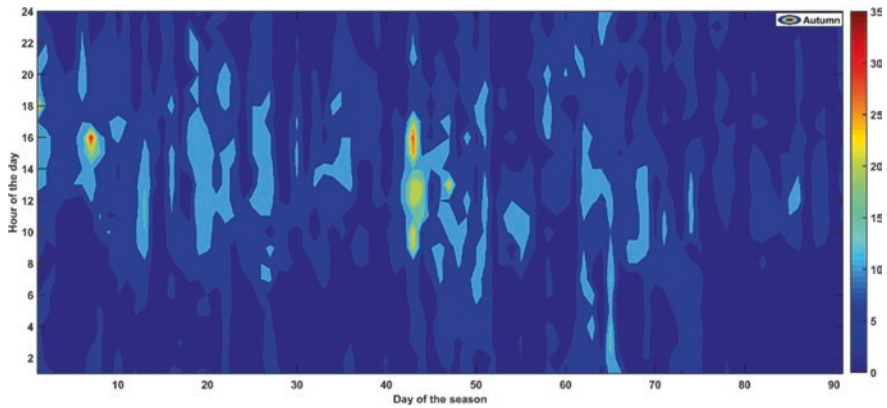


Fig. 3.12 Contour model of runway wind speed: Autumn

and 3.12. While, with the three-dimensional models, peak values and calm days can be easily observed, with the help of the contour planes, windy hours of the day can be easily determined.

According to the results, the maximum wind speed value is 44 [knot] for winter, 40 [knot] for spring, 34 [knot] for summer and 35 [knot] for autumn. The expected values are 6.6287 [knot] for winter, 6.7541 [knot] for spring, 7.0978 [knot] for summer and 5.3407 [knot] for autumn. The minimum wind speed values are 0 for all seasons. However, it must be noted that the threshold value of the measurement device determines the calm wind values. So, different sensors and systems may consider the threshold independently.

Further analysis of the contour models shows that high wind speeds are observed from 6 am to 4 pm for winter season, while sometimes windy time frame extends from 2 am to 8 pm. High wind activity can be observed on the first and last days of the spring season, while there is a trend on active time frame from 6 am–4 pm to

12 pm–8 pm. High-speed winds are observed through the summer season on the daytime, while a trend is observed for the time frame from 8 am–6 pm to 2 pm–10 pm through the last days of the summer. Lastly, high wind speed activities are observed with a trend from 2 pm–6 pm to 8 am–6 pm through the autumn season.

3.5 Wind Rose

Wind rose is a two-dimensional radial plane that shows the wind speed, wind direction and occurrence frequencies. Wind direction is separated as 10° intervals with a total of 36 direction segments. On a typical wind rose, circles depict the wind speed, while radial lines depict the wind direction (Ashford et al. 2011). The main purpose of the wind rose is to determine the runway orientation regarding the prevailing wind direction. Runway orientation is indicated with direction numbers that are given in 01–36. The numbers show the heading of the runway regarding the north. So, the relation between the runway orientation and its heading is one-tenth. For example, the numbers of 11–29 correspond to 110° – 290° orientation of the runway with respect to the north. Both sides of the runway can be used for take-off and landing. So, runway 11 becomes runway 29 when it is used in opposite direction with an addition or subtraction of 18, depending on the orientation. It must be noted that the tailwinds become headwinds and right crosswinds become left crosswinds, according to the runway direction (Bellasio 2014). The runway orientation of the Eskisehir Hasan Polatkan Airport is 09–27, where the aerial view of the airport and runway is given in Fig. 3.13. According to the WMM 2020, there is about 5.4° (east) deviation due to the magnetic inclination between true north and magnetic north for the runway.

The main reason behind coinciding the orientation of the runway with the prevailing wind is to eliminate the crosswinds on take-off and landing phases. The aviation authorities established an ACC based on the RDC. RDC consists of a letter for aircraft approach speed and a Roman numeral for wingspan or tail height of the aircraft. ACC changes according to the length of the take-off field. For dry runway surface, ACC is given as follows (Bellasio 2014; ICAO 2012; EASA 2011):

$$f(x) = \begin{cases} 10[\text{knot}], & x < 1200[m] \\ 13[\text{knot}], & 1200 < x < 1500[m] \\ 20[\text{knot}], & x > 1500[m] \end{cases} \quad (3.7)$$

where x is the length of the field and $f(x)$ is the allowable crosswind component.

Wind coverage of a runway in an airport must be equal to or greater than 95% (FAA 2012). Wind coverage means that the crosswind through the runway must be less than the ACC for 95% of the time. If it is not possible to satisfy the coverage with a single runway, then additional runways must be installed, such as crosswind runways, in combination with the main runway to serve and satisfy the above criteria. It is also worth to mention that the wind coverage is also called as a usability factor.



Fig. 3.13 Aerial view of the Eskisehir Hasan Polatkan Airport. (Source: Google)

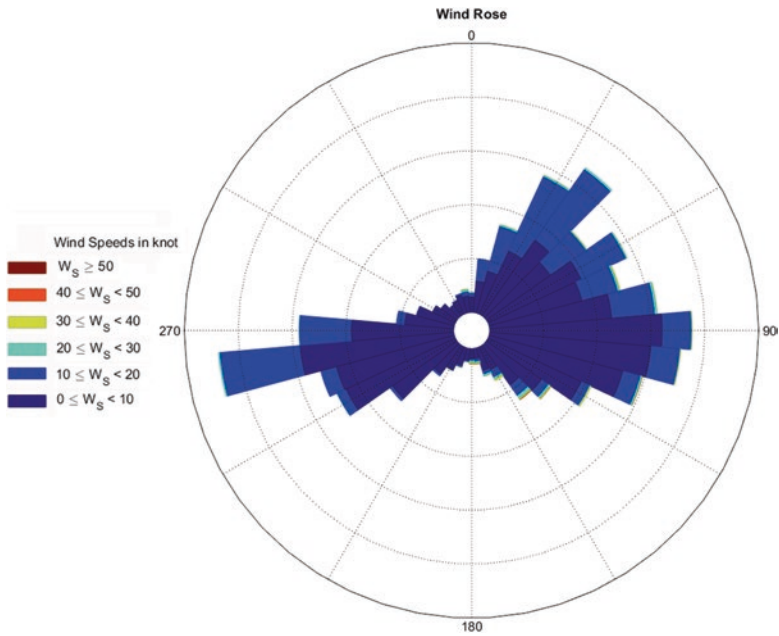


Fig. 3.14 Yearly wind rose model of the runway

The wind rose model of the airport with a data of 1 year long is given in Fig. 3.14. Wind speed values are separated by 10 [knot]. However, since the majority of the wind speed occurrences lies inside the 0–20 [knot], the effects of the upper wind speed values (> 20 [knot]) have little impact on the modelled chart. The prevailing

wind direction is in the east-west line with a deviation of about 5° . So, the orientation of the runway and the prevailing wind distribution of the year coincide with a small deviation. But, as mentioned earlier, the magnetic inclination of the runway is about 5.4° E for the year of 2020, which shows a match between the orientation and prevailing wind direction. The direction of the crosswind elements is also near to the prevailing wind direction, which ensures low crosswind components due to smaller angle. The expected value of the wind speed is observed up to 20 [knot], whereas some outliers can be detected up to 45 [knot] with a very small frequency of occurrence.

3.6 Conclusions

In this paper, analysis of the wind speed distribution and derivation of the monthly wind speed models are developed. According to the results, the proposed wind speed models have high goodness-of-fit values regarding RMSE, MADE and R^2 . MADE of the proposed models are no more than 0.0489 with 0.0378 mean and 0.0078 standard deviation values. The lowest MADE value is 0.0257. RMSE of the proposed models are between 0.0172 and 0.0087 with a mean value of 0.0132 and standard deviation of 0.003. R^2 values for the models are as high as 0.951 with an expected value of 0.9001 and a standard deviation of 0.0391.

The hourly and daily wind speed distributions regarding seasons are also derived. Results show that the autumn season has the lowest mean wind speed value of 5.43 [knot], where winter is following with a mean value of 6.62 [knot], spring is following with a mean value of 6.75 [knot] and summer season has the highest mean value of 7.09 [knot]. Hourly distributions show that the high activity regions are shifted throughout the season, where the maximum of the hourly mean wind speed value is observed at the winter.

Lastly, yearly wind rose chart is derived to assess the prevailing wind direction of the runway and to determine the alignment. Results show that the prevailing wind direction is on the east-west line, which aligns with the orientation of the 09–27 runway. Thus, crosswinds can be eliminated, and flight safety is increased with the orientation of the runway.

References

- Akdag, S., Dinler, A.: A new method to estimate Weibull parameters for wind energy applications. *Energy Convers. Manag.* **50**(7), 1761–1766 (2009)
- Ashford, N., Mumayiz, S.A., Wright, P.H.: *Airport Engineering: Planning, Design, and Development of 21st-Century Airports*. Wiley-Interscience Publications, New York (2011)
- Bellasio, R.: Analysis of wind data for airport runway design. *J. Air Airport Manag.* **4**(2), 97–116 (2014)

- Burt, S.: Measuring wind speed and direction. In: *The Weather Observer's Handbook*, pp. 192–221. Cambridge University Press, Cambridge (2012)
- Chang, S.-W.: Crosswind-based optimization of multiple runway orientations. *J. Adv. Transp.* **49**, 1–9 (2015)
- EASA. Authority, Organisation and Operations Requirements for Aerodromes. NPA 2011–20 (B.III) (2011)
- FAA. Advisory Circular AC 150/5300-13A. U.S. Department of Transportation, Federal Aviation Administration (2012)
- ICAO. Cir 329/AN/191, Runway Surface Condition Assessment, Measurement and Reporting (2012)
- Iijima, T., Matayoshi, N., Ueda, S.: Operational concept and validation of a new airport low-level wind information system. *Aeronaut. J.* **124**(1277), 1–41 (2020)
- Jaramillo, O., Borja, M.: Wind speed analysis in La Ventosa, Mexico: a bimodal probability distribution case. *Renew. Energy.* **29**, 1613–1630 (2004)
- Karatepe, S. Corscadden, K. W.: “Wind Speed Estimation: Incorporating Seasonal Data Using Markov Chain Models,” ISRN Renewable Energy (2013)
- Kumaraswamy, B. G., Keshavan, B. K., Ravikiran, Y. T.: Analysis of seasonal wind speed and wind power density distribution in Aimangala wind farm at Chitradurga Karnataka using two parameter Weibull distribution function. In: *IEEE Power and Energy Society General Meeting*, Detroit (2011)
- Lledo, L., Torralba, V., Soret, A., Ramon, J., Doblas-Reyes, F.: Seasonal forecasts of wind power generation. *Renew. Energy.* **143**, 91–100 (2019)
- Oktal, H., Yildirim, N.: New model for the optimization of runway orientation. *J. Transp. Eng.* **140**(3) (2014)
- Prema, V., Rao, K.: Time series decomposition model for accurate wind speed forecast. *Renewables.* **2**(18) (2015)
- Sahin, O.: A proposed solution for airborne delays: linear holding. *Aeronaut. J.* **123**, 1840–1856 (2019)
- Soukissian, T., Papadopoulos, A., Skrimizeas, P., Karathanasi, F., Axaopoulos, P., Avgoustoglou, E., Kyriakidou, H., Tsalis, C., Voudouri, A., Gofa, F., Katsafados, P.: Assessment of offshore wind power potential in the Aegean and Ionian seas based on high-resolution hindcast model results. *AIMS Energy.* **5**(2), 268–289 (2017)
- Tee, Y.Y., Zhong, Z.W.: Modelling and simulation studies of the runway capacity of Changi airport. *Aeronaut. J.* **122**, 1022–1037 (2018)
- van der Geest, P.J., van Es, G.W.H., Nieuwpoort, T.M.H.: Safety aspects of aircraft operations in crosswinds. Flight Safety Foundation FSF, 11th Annual European Aviation Safety Seminar, Amsterdam March 8–10, 1999. NLR-TP-2001-217 (2001)
- van Es, H.G.W., Karwal, K.A.: Safety aspects of tailwind operations. Flight Safety Foundation Annual European Aviation Safety Seminar, Amsterdam, The Netherlands on 12–14 March, 2001. NLR-TP-2001-003 (2001)
- Zeng, P., Sun, X., Farnham, D.: Skillful statistical models to predict seasonal wind speed and solar radiation in a Yangtze River estuary case study. *Sci. Rep.* **10** (2020)

Chapter 4

Optimization of Control Surfaces Using Different Corrugated Design to Minimize the Vibration and Flutter in the Wing



N. G. Hareesha and M. Rudresh

Nomenclature

- σ : Density of structural material
- ω : Circular frequency
- λ : Eigenvalue

4.1 Introduction

When a body is disturbed from its mean position, it is set to vibrate. This same phenomenon is also observed in aircraft during the flight, known as flutter. Flutter is an unstable oscillatory aerodynamic condition with high frequency and high amplitude. This phenomenon results in a catastrophic failure of structure at faster rate. It will also lead to aerodynamic instability, reduction of life of an aircraft wing and its components. Therefore, it is of a great concern to any pilot, since extreme flutter has instigated a number of aircraft to lose control and eventually crash in the history of aviation.

Even though any surface on an aircraft which is exposed to airflow can experience flutter, the most common type of flutter involves the control surfaces, such as ailerons, elevators and rudders, which are the primary aerodynamic devices allowing the pilot to adjust and control the aircraft flight's attitude.

In an aircraft, as the speed of the wind increases, there may be a point at which the structural damping is insufficient to damp out the motions which are increasing due to aerodynamic energy being added to the structure. So one of the methods to suppress the fluttering phenomenon is by increasing the stiffness of the wing structure by using corrugated design. The mass properties of these control surfaces are

N. G. Hareesha · M. Rudresh (✉)
Department of Aeronautical Engineering, Dayananda Sagar College of Engineering,
Bengaluru, Karnataka, India
e-mail: hareesha-ae@dayanandasagar.edu; rudresh-ae@dayanandasagar.edu

precarious and have to be measured with great precaution to minimize the flutter. The shape of corrugated panel is the key to its durable, yet lightweight characteristics, which make it the perfect choice for many applications.

A control surface experiences flutter in-flight when its natural frequency matches the exciting frequency of gust loads acting on it. This needs to be corrected; hence, different corrugated surfaces are being used to bring flutter within limits. Amongst various corrugated surfaces, the best design needs to be analysed, considering stiffness-to-weight ratio. This shifts its natural frequency to safer values. Configuration of the corrugation is to be decided based on the analysis made by varying the height and width of corrugation, distance between corrugation and number of corrugation.

This chapter deals with the design and analysis of an optimized control surface for a small aircraft and unmanned aerial vehicles (UAVs) against occurrence of flutter and other dynamic instabilities. Unmanned aerial vehicles are widely in use for various applications across the world, which include military and non-military applications. The absence of active flutter suppression techniques on-board, such as flying machines, makes them prone to get affected by flutter mid-flight.

4.2 Flutter and Corrugation Design

The signature shape of corrugated panel is the key to its durable, yet lightweight characteristics, which make it the perfect choice for many applications. In the same way that the paper that makes up a cardboard box is strengthened by the sheet of wavy paper sandwiched between two flat layers, sheets of metal can be made stronger by corrugating or folding the material to make ridges and grooves. The wavy construction leads to increased strength over a shorter surface area. Scientists and engineers studied flutter and developed theories for the cause of and mathematical tools to analyse the behaviour.

J.K.S. Dillinger and T. Klimmek stimulated the research to use the anisotropy property of composite material for more efficient aircraft structures by stiffness optimization of the upper and lower skin of composite wings (Dillinger and Klimmek 2013). The optimizer was shown to yield efficient convergence behaviour for mass and aileron effectiveness. The advantage of unbalanced over balanced laminates was elaborated, demonstrated by considerable savings when minimizing the mass or aileron effectiveness benefits when constraining mass. The optimized designs showed a simultaneous use of strength and buckling constraints in a majority of the optimized panels.

H. Mohammadi, S. Ziaei-Rad and I. Dayyani analysed the trapezoidal corrugation plates. It showed that plates with corrugated profiles show higher stiffness-to-mass ratio in the transverse to the corrugation direction in comparison to flat plates. This enables them to withstand the aerodynamic and inertial loads. They are also flexible in the corrugation direction, which allows the shape changes. They observed that as the thickness of the plate increases, the elastic and shear moduli also increase.

They also revealed that in-plane moduli of the plate were decreased by increasing the corrugation height.

Bruce Ralphin Rose J and Jinu G R proposed an Active flutter Suppression technique. To overcome the instabilities in a cruising airplane when the wing is subject to intense dynamic pressure which will cause the redundant vibrations by flutter effect which influences the airplane performance and its structural life to a large extend. Mass balancing and stiffness enhancement with control systems are the different methods available. Their research revealed various possibilities and modifications in AFS techniques using advanced feedback control systems (Ralphin et al. 2014) (Fig. 4.1).

Jie Zeng introduced a flutter-boundary prediction technique for an aeroelastic/aeroservoelastic structure, which uses time-series flight/wind-tunnel flutter test data to compute an accurate estimate of the flutter speed. This approach is especially developed to deal with the cases where the aeroelastic/aeroservoelastic structure is subjected to the atmospheric turbulence excitation during the flight/wind-tunnel flutter tests and internal excitation from the on-board excitation system. Application of the proposed flutter-boundary prediction method reveals that it is an efficient tool for flutter-boundary prediction of aeroelastic structure (Zeng 2013).

Y. Xia, M.I. Friswell and E.I. Saavedra Flores presented a homogenization-based analytical model, which is suitable for any corrugation shape. The coupling stiffness is considered in the proposed method. The stiffness of the equivalent corrugated panel is obtained from the geometry of a unit cell and the stiffness properties of the original sheet, which is convenient for the optimal design of morphing skins. The panel has been treated both as an original corrugated model and as an equivalent orthotropic model (Xia et al. 2012a).

Julio Cesar Molina, Juliano Fiorelli and Holmer Savastano Jr. presented different numerical models for the evaluation of the stresses in corrugated sheets under bending. The sheets with larger spans present larger stresses for the same applied load.

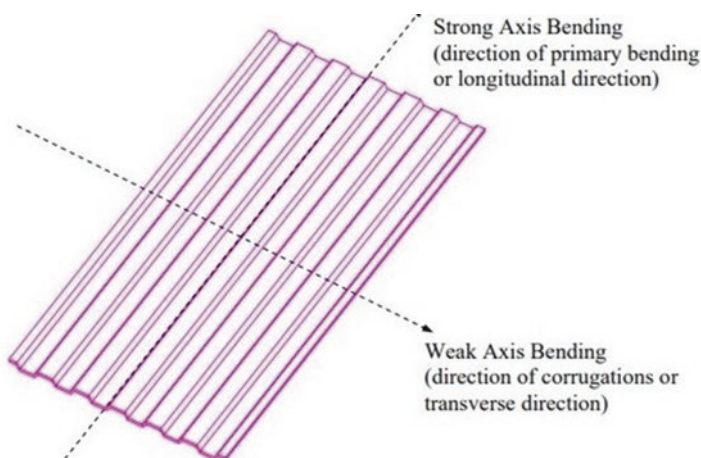


Fig. 4.1 Effects of corrugation in mutually perpendicular directions. (Mohammadi et al. 2015)

The most intense values of tension occur in the troughs of the sheets, on the lower surface, while the most intense values of compression occur in the crests, on the upper surface of the sheet. The flanks, which are the parts amongst the troughs and crests of the sheets, are submitted to low levels of stresses (Molina et al. 2014).

Yuying Xia, Rafic M. Ajajv and Michael I. Friswell optimized the geometry of the corrugated skin to minimize the axial stiffness, with constraints of material strength limits and out-of-plane deformations due to the aerodynamics (Yuying, Xia et al. 2014).

M. Winkler and G. Kress investigated the influence of the corrugation pattern of corrugated structures by using a generalized plane-strain Finite Element (FE) model. The substitute stiffness matrix is influenced by changing the geometry. Triangular, rectangular, circular and trapezoidal shapes were also studied. The increase or decrease of the stiffness due to the change from a triangular to the trapezoidal geometry is independent of the material. The absolute values of the stiffness are strongly dependent on the material configuration. The results showed that the geometry pattern can be used to tailor the stiffness and anisotropy of a corrugated structure (Winkler and Kress 2012).

C. Thurnherr, L. Ruppen, S. Brandli, C.M. Francheschi, G. Kress and P. Ermanni investigated the geometric non-linear behaviour of corrugated laminates in six different loading conditions. They observed that the qualitative non-linear stiffness response mainly depends on the corrugation amplitude. These results can be used in design processes where large deformations might occur, such as morphing wings. They concluded that non-linearities have to be taken into account for structural materials (Thurnherr et al. 2017).

Matthew Kampner and Joachim L. Grenestedt studied the use of corrugated skin in a sandwich beam using a simplified approach (Kampner and Grenestedt 2008). Corrugated skin was modelled as a conventional material with a homogenized stiffness. Analytically optimized ordinary flat sandwich beams were compared to numerically optimized corrugated sandwich beams. The corrugated sandwich beams showed weight savings on the order of 10–20% over their plain counterparts.

Y. Xia, M.I. Friswell and E.I. Saavedra Flores proposed a homogenization-based analytical model, which is suitable for any corrugation shape (Xia et al. 2012a). The earlier models required the original sheet material to be isotropic or treated as isotropic; in contrast, this method has no limitations. This approach was demonstrated on two common geometries, namely, trapezoidal and round corrugations. The stiffness of an equivalent corrugated was obtained from the geometry of a unit cell and the stiffness properties of the original sheet. It gives explicit expressions to calculate the equivalent material properties. They also studied the effects of corrugation geometry, ply angles, laminate thickness and fibre volume fraction.

Kyle Hord and Yongsheng Lian performed numerical simulations to understand the aerodynamic and structural characteristics of a corrugated aerofoil (Hord and Lian 2012). They noticed that the corrugated aerofoil produces similar lift as a flat plate, but, at peak gliding ratios, it produces more drag. This increase in drag is due to higher pressure drag, resulting from the thicker virtual streamlined profile. Overall, the aerodynamic analysis revealed that the selected corrugated profile provides no advantages in terms of stall delay or lift generation. The study showed that

corrugated wing can reduce deflection and stress on the wing by use of corrugations; it is shown that increase in structural rigidity can be obtained with minimum materials.

Denis B. Kholodar, Jeffrey P. Thomas, Earl H. Dowell and Kenneth C. Hall studied how structural and aerodynamic parameters, such as free-stream Mach number, affect flutter and Limit Cycle Oscillations (LCO) characteristics of a typical two-DOF aerofoil configuration using Euler-based time-linearized aerodynamic code (Kholodar et al. 2003).

They concluded that flutter variables, such as velocity, frequency and structural eigenmode, vary little with mass ratio for subsonic Mach numbers; they also demonstrated that solutions of flutter are very sensitive to Mach numbers in the transonic range and also the effect of ratio of uncoupled natural frequencies determined that flutter velocity has a minimum when uncoupled natural frequency is almost equal to 1.

Mayuresh J. Patil's investigation was based on conservation of energy for understanding the flutter and flapping flight (Patil 2003). Energy produced, energy lost and work done due to structural vibration, aerodynamic wake and propulsion were taken into account. It is shown that there exist three types of modes in an aeroelastic system, namely, unstable mode producing drag, stable mode producing drag and stable mode producing thrust. The type of mode can be determined from the mode shape for a given reduced frequency. The flutter region decreases with reduced frequency, whereas thrust-producing region increases. Flutter always leads to drag, and thrust-producing modes are always stable. The actual modes of an aeroelastic system move relative to the energy curves and may change from one type of mode to another.

Dominique Poirel, Shane Dunn and Jay Porter used Zimmerman and Wiesenberger's method to capture more effectively the inherent uncertainty present in the test data (Poirel et al. 2005). Two approaches were proposed such that all "good" measured values of the modal parameters are used to construct either flutter margin or flutter speed histograms. It was found that flutter margin and flutter speed probability density functions are not symmetrical. Different flutter margin and flutter speed statistics are investigated. Related to the flutter margin, the mode is considered to be the most relevant estimation of the flutter margin. Consistent conservative predictions are obtained and found that predicted flutter speed based on this criterion is generally conservative compared with the prediction based on the mean modal parameters, which is the essence of the conventional method.

4.3 Modelling and Analysis

The corrugated plate has protuberances at regular intervals. These are called the corrugations. To model these corrugated protrusions on a plate, a designing software CATIA V5 is used. The dimensions used for the corrugated plate is shown in Fig. 4.2.

Geometric details of design (all in mm)

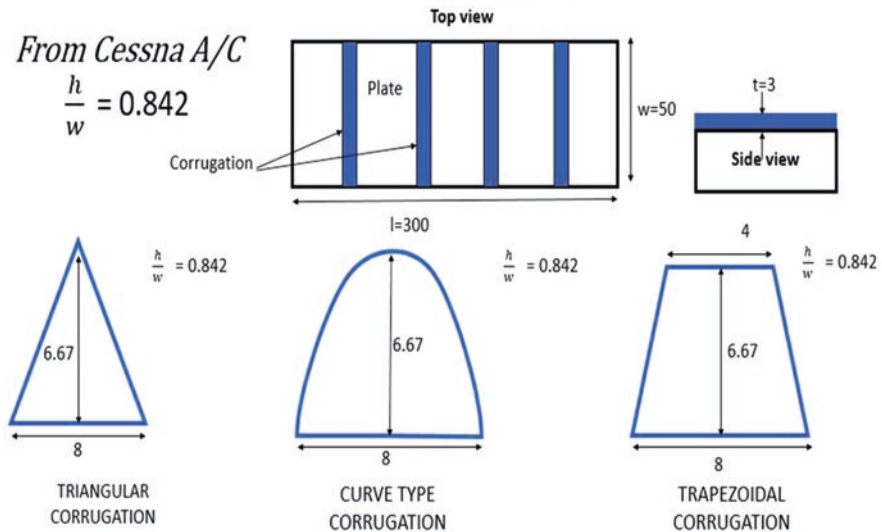


Fig. 4.2 Design values of various corrugation types used (all dimensions in mm)

Dimensions obtained from real Cessna 172-Skyhawk aircraft control surface (Cessna aircrafts have control surface with corrugations):

Length of control surface plate (L) = 1645 MM.

Width of control surface plate (W) = 127 MM.

Height of corrugation (H) = 8 MM.

Width of corrugation (w) = 9.5 MM.

Distance between each corrugation (D) = 75 MM.

The three-dimensional corrugated plate is modelled. Depending on the type of corrugation profile, fibre option in pad definition may be selected to avoid any thickness overlaps.

The number of corrugation strips per plate is kept at 4 with equal spacing maintained between each for preliminary analysis. In further analysis, this spacing is varied each time in the design phase and analysed for variations to obtain the most optimum design for flutter control. Hypermesh is the software used for meshing the model. To catch the variations made by the corrugation more accurately, volume tetra option with second order of elements is selected. The element size opted for ranges from 04 to 08, to keep the mesh quality as fine as possible. The solid is then selected to be meshed. Material definition is created to input the material constant values such as the elastic modulus and Poisson's ratio. MAT 1 is selected as the card for the material, since isotropic behaviour is regarded. The elastic modulus value of 71,700 MPa and Poisson's ratio of 0.33 is fed corresponding to aluminium. The density for the alloy considered, aluminium-7075, is 2.8×10^{-06} Kg/mm³. The solver

employed in the analysis is OptiStruct HyperWorks, which is a highly parallelized solver for NVH analysis. OptiStruct is an industry proven, modern structural analysis solver for linear and non-linear problems under static and dynamic loadings.

4.4 Results and Discussions

4.4.1 Shape Optimization (Mesh Independent)

Modal analysis for different shaped corrugation is carried out, and the frequency and stiffness plot for the first five modes is extracted. Figure 4.3 shows the model of simple plate. The extracted frequency and stiffness values are shown in Tables 4.1 and 4.2 for different mesh sizes.

Figure 4.4 shows the model of triangular corrugation. The extracted frequency and stiffness values are shown in Tables 4.3 and 4.4 for different mesh sizes.

Figure 4.5 shows the model of trapezoidal corrugation. The extracted frequency and stiffness values are shown in Tables 4.5 and 4.6 for different mesh sizes.

Figure 4.6 shows the model of trapezoidal corrugation. The extracted frequency and stiffness values are shown in Tables 4.7 and 4.8 for different mesh sizes.

We see that, as we go for higher modes, the frequency will be higher, which can be clearly seen from the graphs (Fig. 4.7). Similarly stiffness also increases with the number of modes for one particular plate (Fig. 4.8). From the graph we can say that

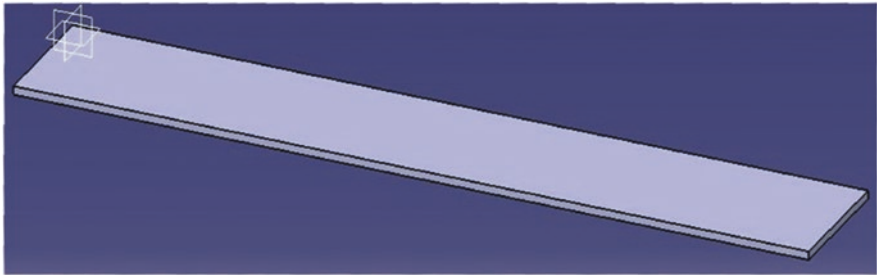


Fig. 4.3 Simple plate

Table 4.1 Result for simple plate (mesh size 05)

| Mode | Frequency (Hz) | Stiffness (N/mm) |
|------|----------------|------------------|
| 1 | 32.69 | 42201.39 |
| 2 | 34.69 | 47522.16 |
| 3 | 40.85 | 65904.24 |
| 4 | 50.94 | 102452.5 |
| 5 | 65.05 | 167059.2 |

Table 4.2 Result for simple plate (mesh size 15)

| Mode | Frequency (Hz) | Stiffness (N/mm) |
|------|----------------|------------------|
| 1 | 33.11 | 43288.43 |
| 2 | 35.51 | 49786.57 |
| 3 | 42.58 | 71588.30 |
| 4 | 54.11 | 115607.5 |
| 5 | 70.11 | 194087.6 |

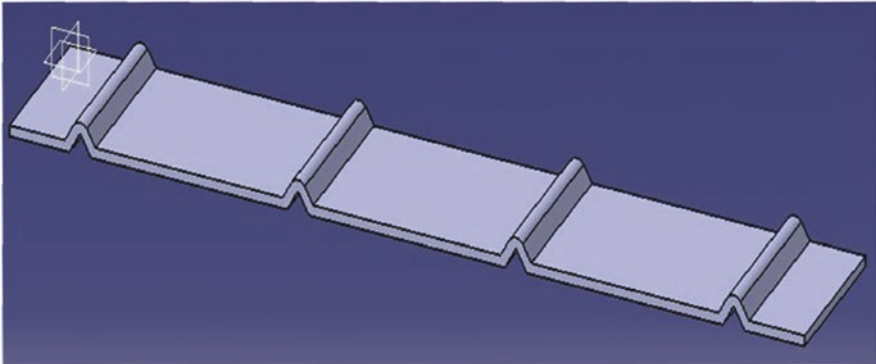


Fig. 4.4 Triangular corrugation

Table 4.3 Result for triangular corrugation (mesh size 05)

| Mode | Frequency (Hz) | Stiffness (N/mm) |
|------|----------------|------------------|
| 1 | 54.27 | 116314.5 |
| 2 | 56.25 | 124945.9 |
| 3 | 60.63 | 145167.2 |
| 4 | 67.76 | 181278.7 |
| 5 | 72.60 | 208133.1 |

Table 4.4 Result for triangular corrugation (mesh size 15)

| Mode | Frequency (Hz) | Stiffness (N/mm) |
|------|----------------|------------------|
| 1 | 55.83 | 123068.8 |
| 2 | 58.92 | 137089.9 |
| 3 | 65.03 | 167001.6 |
| 4 | 74.11 | 216839.3 |
| 5 | 82.92 | 271483.3 |

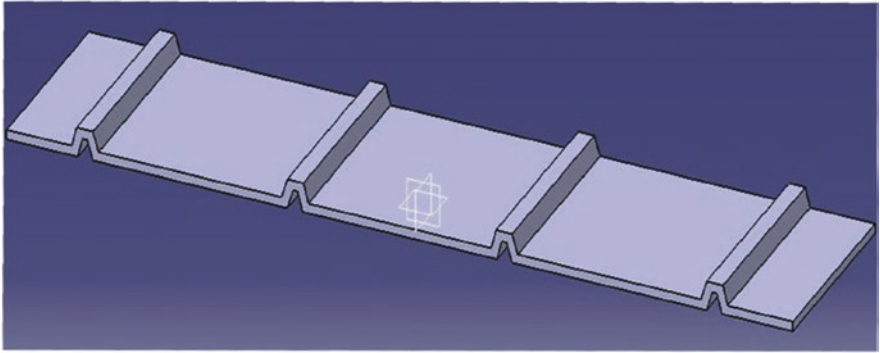


Fig. 4.5 Trapezoidal type corrugation

Table 4.5 Result for trapezoidal corrugation (mesh size 05)

| Mode | Frequency (Hz) | Stiffness (N/mm) |
|------|----------------|------------------|
| 1 | 63.46 | 159010.5 |
| 2 | 65.06 | 167105.3 |
| 3 | 68.81 | 186931.4 |
| 4 | 74.88 | 221389.1 |
| 5 | 77.81 | 239061.1 |

Table 4.6 Result for trapezoidal corrugation (mesh size 15)

| Mode | Frequency (Hz) | Stiffness (N/mm) |
|------|----------------|------------------|
| 1 | 66.37 | 173907.6 |
| 2 | 68.40 | 184717.5 |
| 3 | 73.39 | 212678.9 |
| 4 | 80.95 | 258726.8 |
| 5 | 87.13 | 299728.6 |

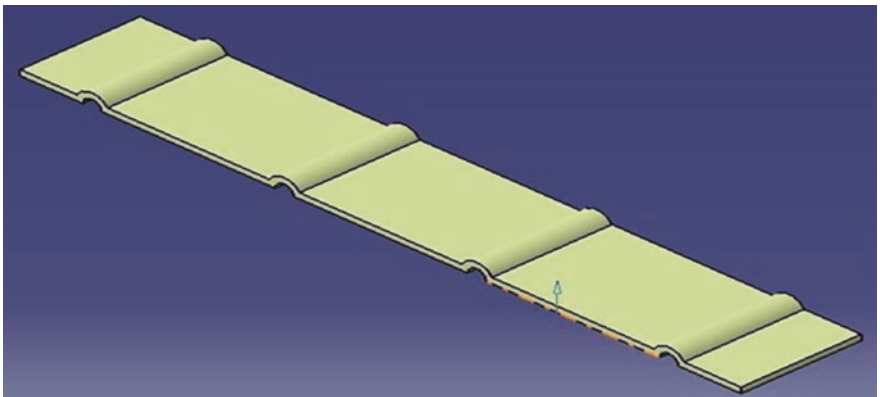


Fig. 4.6 Curve-type corrugation

Table 4.7 Result for curve-type corrugation (mesh size 05)

| Mode | Frequency (Hz) | Stiffness (N/mm) |
|------|----------------|------------------|
| 1 | 44.80 | 79258.73 |
| 2 | 46.90 | 86866.16 |
| 3 | 52.17 | 107450.0 |
| 4 | 60.89 | 146385.7 |
| 5 | 70.07 | 193869.8 |

Table 4.8 Result for curve-type corrugation (mesh size 15)

| Mode | Frequency (Hz) | Stiffness (N/mm) |
|------|----------------|------------------|
| 1 | 45.13 | 80428.30 |
| 2 | 47.26 | 88192.52 |
| 3 | 52.54 | 109017.6 |
| 4 | 61.31 | 148431.9 |
| 5 | 70.56 | 196558.8 |

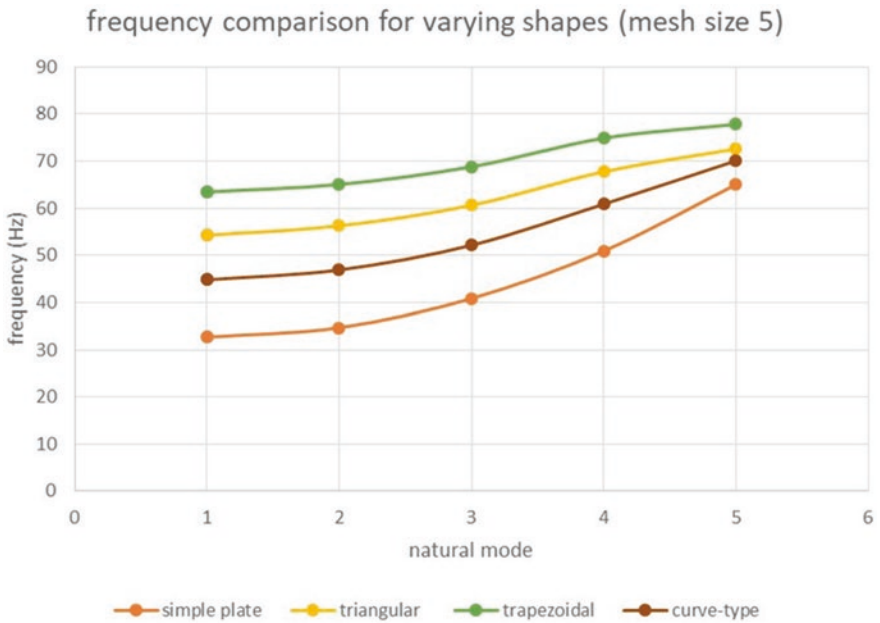


Fig. 4.7 Natural frequency comparisons for different shapes

giving particular corrugation design (triangular, trapezoidal, curve type) shifts the natural frequency to a higher extent. For example, fundamental frequency of simple plate is 18 Hz, which can be shifted to 42 Hz by using curve-type corrugation. It can also be noticed that with minimum increment in weight by using corrugation design,

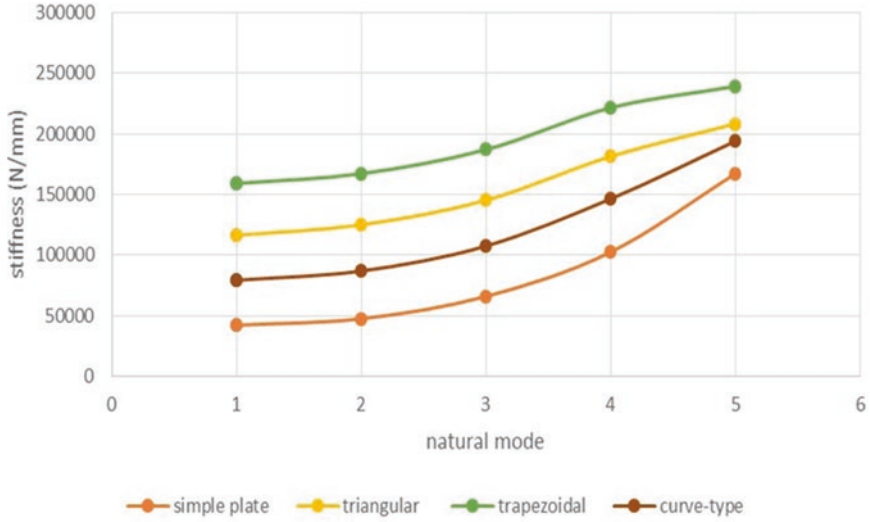


Fig. 4.8 Stiffness variations for different shapes

a very high stiffness value can be achieved. Most of the corrugated plate gives higher frequency and stiffness value compared to flat plate at all modes of vibration. The height of the corrugation also matters as it can be seen from the graph; for the semicircle corrugated plate, which has the half corrugation height compared to other designs, it gives lower values of stiffness and frequency.

4.4.2 Corrugation Height Optimization

Specifications *Shapes: Triangular type corrugation and trapezoidal type corrugation*

No. of corrugation: 4

Height variation: 4, 6 and 8 (mm)

Triangular shape width: 8 (mm)

Trapezoidal shape base width: 8 (mm)

Trapezoidal shape top width: 4 (mm)

From Figs. 4.9 and 4.10, it can be seen that the increase in the corrugation height in both triangular and trapezoidal corrugation shapes yields an increase in the natural frequency. The initial modes are quite different when compared to the last mode frequencies, which are closer in value, indicating that there is lesser effect of height as we approach higher modes.

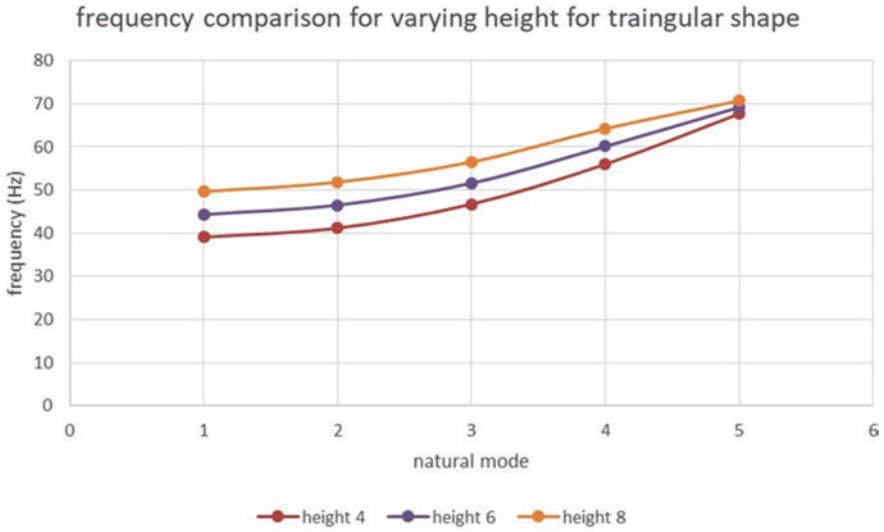


Fig. 4.9 Natural frequency comparison for different heights of corrugation (triangular)

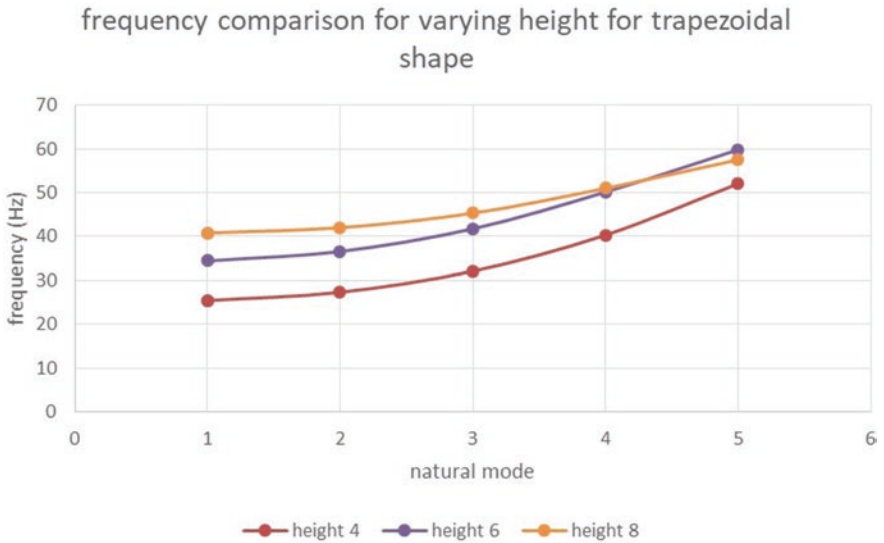


Fig. 4.10 Natural frequency comparison for different heights of corrugation (trapezoidal)

4.4.3 Corrugation Width Optimization

Specifications Shapes: *Triangular type corrugation and trapezoidal type corrugation*

No. of corrugation: 4

Triangular width variation: 6,8 and 10 (mm)

Trapezoidal width variation: 8 and 12 (mm)

Trapezoidal shape corresponding top width: 4 and 6 (mm)

Triangular shape height: 8 (mm)

Trapezoidal shape height: 8 (mm)

Width variations do present a different scenario. As shown in Fig. 4.11, triangular type corrugation with an increase in height from 6 mm to 8 mm, there is an increase in frequency values, whereas further increase in width gives frequency values which are closer to 6 mm width values. A similar trend is observed in trapezoidal type corrugation as shown in Fig. 4.12. This implies that there is an optimum width for corrugation to increase the natural frequency at which flutter might occur.

4.4.4 Corrugation Distance Optimization

Specifications Shapes: *Curve-type corrugation*

No. of corrugation: 4

Distance variation: 60, 70, 80 and 90 (mm)

Figures 4.13 and 4.14 give the values of the frequency and stiffness for the first five modes of curve-type corrugated plate. Here, the number of corrugation is kept

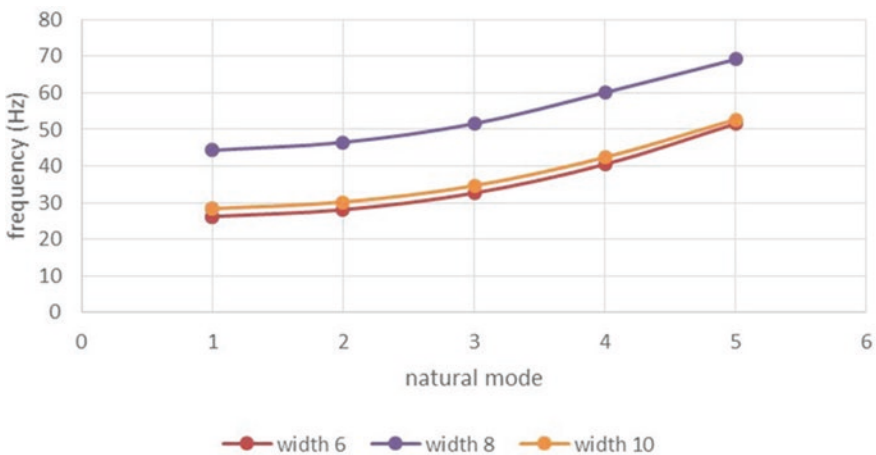


Fig. 4.11 Natural frequency comparison for different widths of corrugation (triangular)

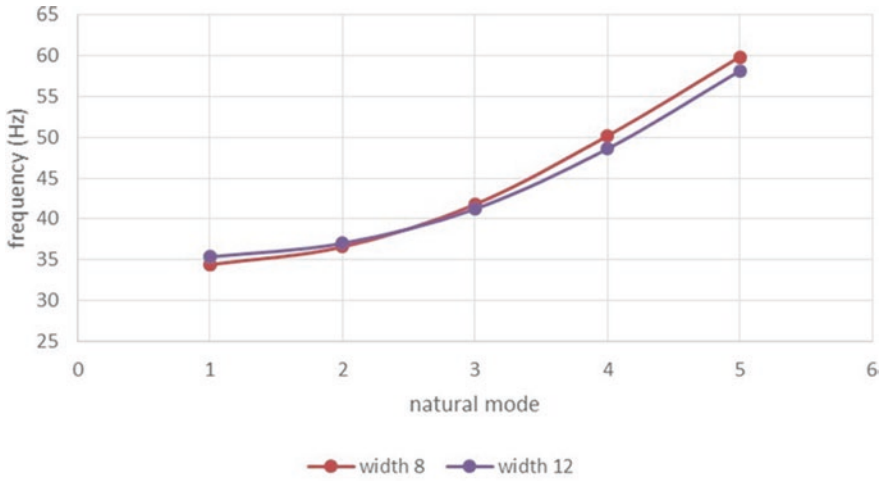


Fig. 4.12 Natural frequency comparison for different widths of corrugation (trapezoidal)

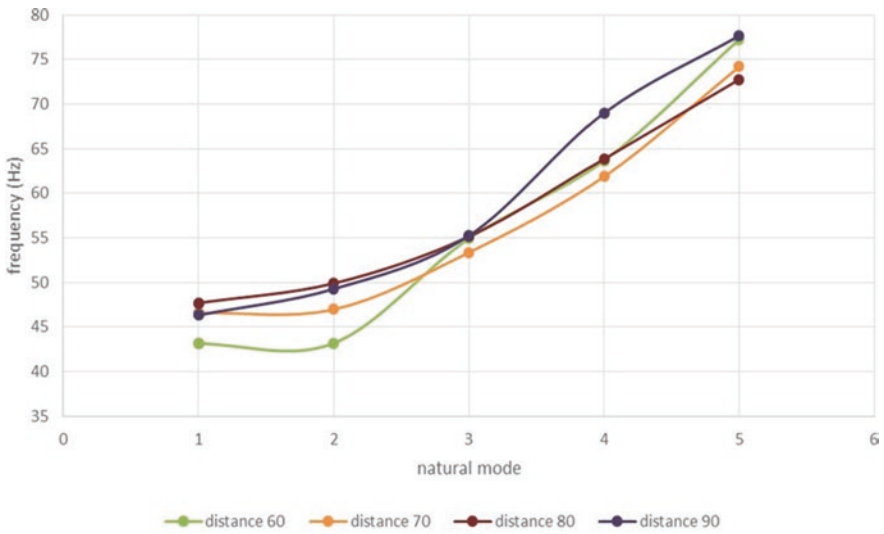


Fig. 4.13 Natural frequency comparison for varying distances of corrugation

constant with varying the distance between corrugations. The frequency and stiffness graphs are almost similar. Both graphs show similar variation with modes of vibration of a particular plate. From the graph we can say that varying the distance between corrugations affects the natural frequency of the plate. This effect is not similar for all modes of vibration of the plate. Since varying the distance does not have much effect on the frequency and stiffness, we can use appropriate design based on the requirements.

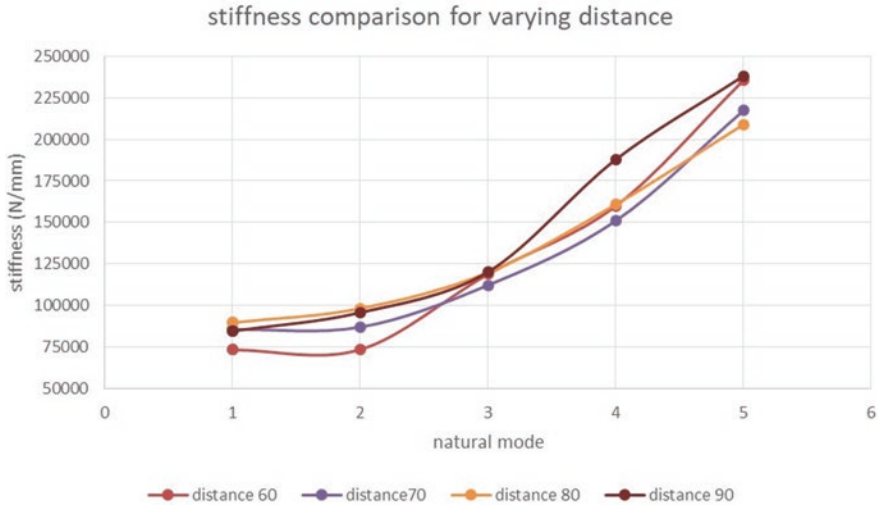


Fig. 4.14 Stiffness variations for varying distances of corrugation

4.4.5 Number of Corrugation Optimization

Specifications *Shapes: Curve-type corrugation equally spaced*
No. of corrugation: 3, 4, 5 and 6 (varying distance)

Figures 4.15 and 4.16 show the variation in the frequency and stiffness values of the plate having different numbers of corrugation. Providing more number of corrugations to a particular plate gives higher stiffness values as well as higher natural frequency. This can be clearly seen from the graph. As we go for higher modes of vibration, the effect of the number of corrugation on the frequency and stiffness becomes less effective compared to the first mode. However, highly corrugated plate gives better stiffness, and it also includes the weight penalty. Hence, based on the application of the plate, we can use the appropriate number of corrugation.

4.4.6 Static Analysis

From the static analysis results, stress distribution and displacement variation in simple plate follows a uniform path along the width and length of plate. Since the cantilever-type simple plate (without corrugation) is subjected to a static load at free end, the displacement will be maximum at free end (along the length of plate). Whereas due to constraints at the other end, the stress generated will be maximum near to the constrained portion along the length of the plate. Considering the case for corrugated plate, variation of stress distribution and displacement will no longer

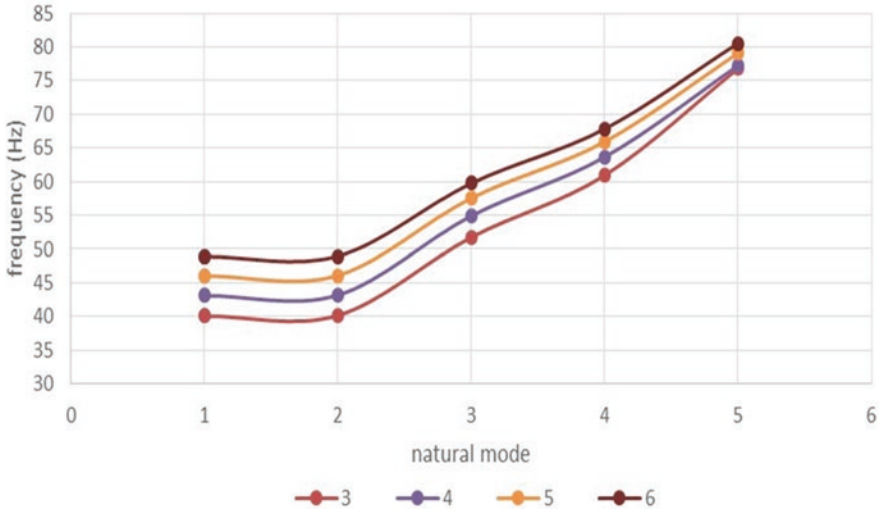


Fig. 4.15 Natural frequency comparisons for varying numbers of corrugation

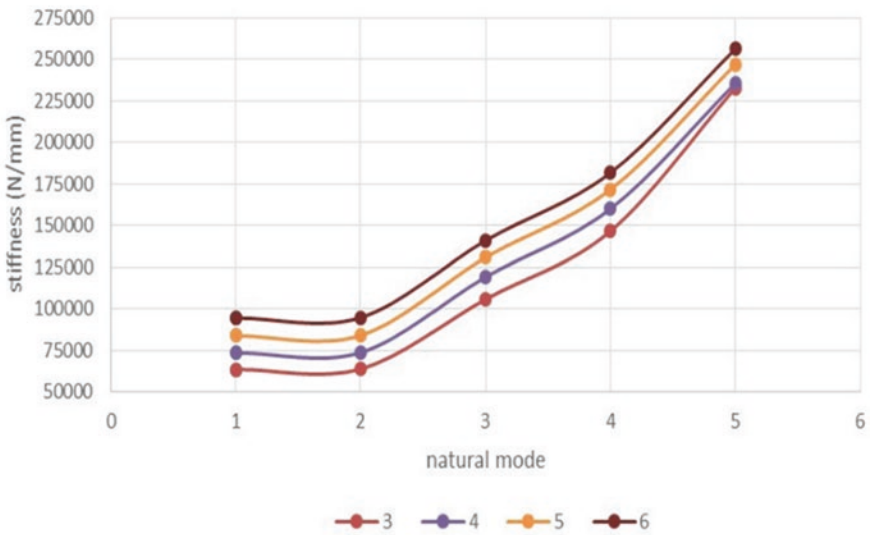


Fig. 4.16 Stiffness variations for varying numbers of corrugation

be uniform as in the case of simple plate (Fig. 4.17, 4.18, 4.19, 4.20, 4.21, 4.22, 4.23, 4.24).

The load of 100 N has deflected the plates along the free end and produced stresses along the fixed end as expected. These stress and displacement are not evenly distributed and vary from plate to plate. From the analysis of corrugated plate, we can say that the majority area in a corrugated plate is free from maximum

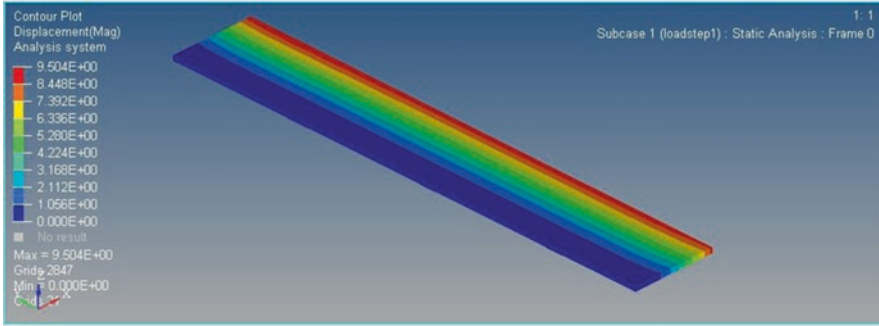


Fig. 4.17 Displacement contour for simple plate with load of 100 N

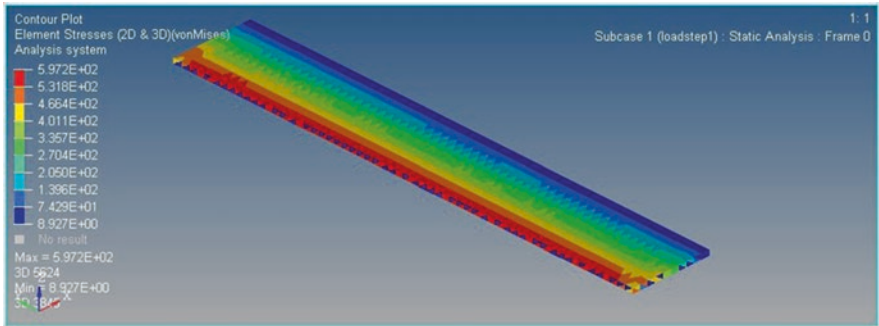


Fig. 4.18 Stress contour for simple plate with load of 100 N

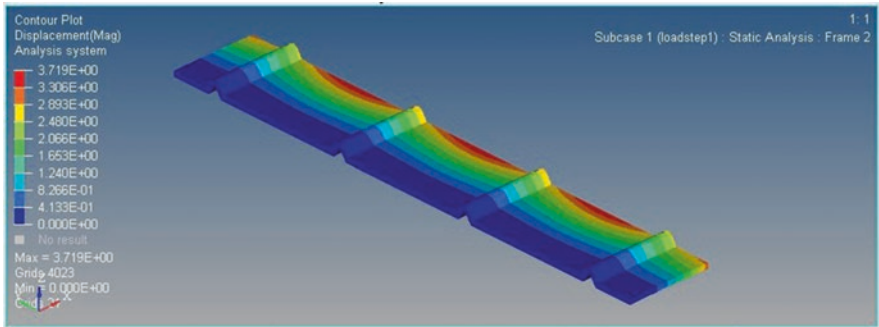


Fig. 4.19 Displacement contour for triangular corrugation with load of 100 N

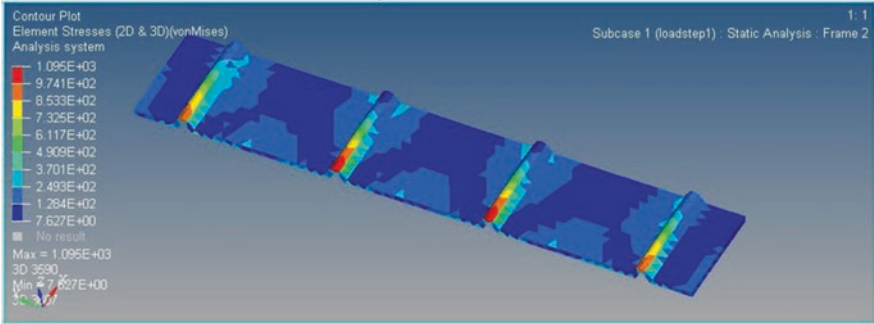


Fig. 4.20 Stress contour for triangular corrugation with load of 100 N

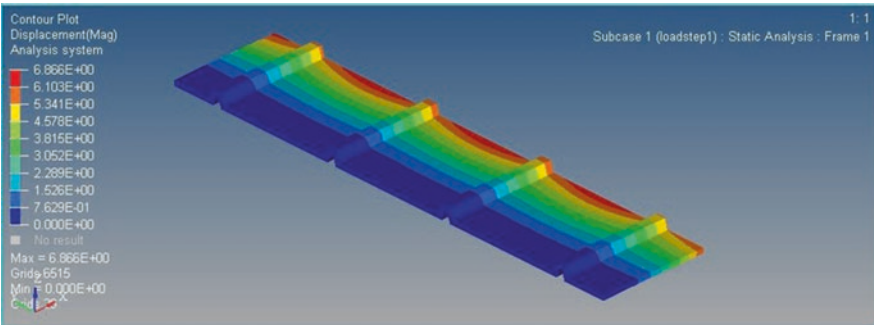


Fig. 4.21 Displacement contour for trapezoidal corrugation with load of 100 N

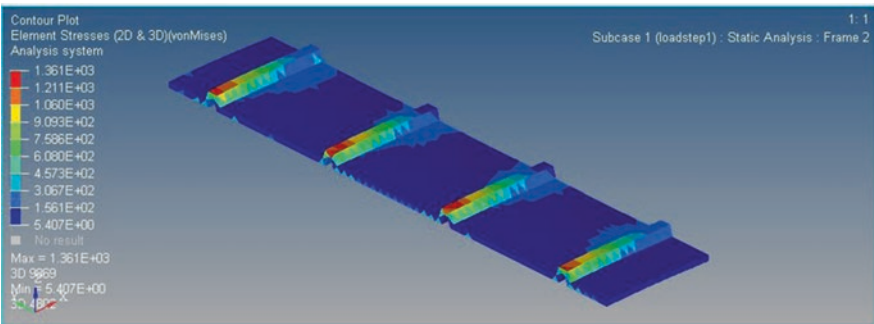


Fig. 4.22 Stress contour for trapezoidal corrugation with load of 100 N

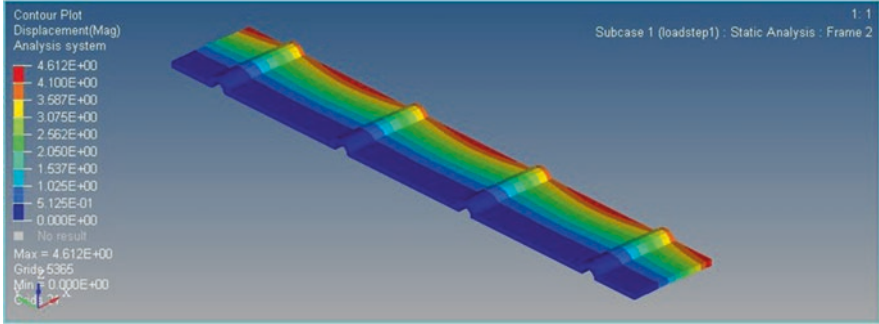


Fig. 4.23 Displacement contour for curve-type corrugation with load of 100 N

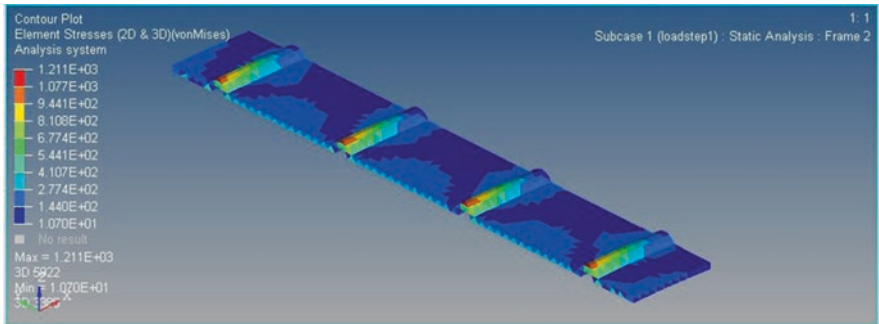


Fig. 4.24 Stress contour for curve-type corrugation with load of 100 N

stress. Due to corrugated area, higher values of stress will be resisted by the corrugated portion, and other areas of the plate will be under least stress value. Hence, the overall stress generated on the corrugated plate will be less compared to the simple plate. As we know in the case of cantilever beam, higher displacement will indicate low stiffness of the plate. This can be clearly justified from the comparison of displacement values of the corrugated plate and simple plate. All corrugated plates yield less displacement values at any point on the plate when compared to the simple plate, which, in turn, shows high stiffness property of corrugated plate.

4.5 Conclusions

The dynamic analysis is carried out for various corrugation designs with varying shapes. It is seen that the trapezoidal shape corrugation has good dynamic characteristics followed by the triangular and curve-type corrugation, which is widely in use. Height optimization is linear in nature, with the upper bound being limited by

the definition of corrugation. According to the width optimization analysis, there is an optimum width which presents the best frequency values for a given design type.

The results, from the third type of design criteria, showed that varying the distance does not have much effect on the frequency and stiffness. We can use appropriate design based on the requirements and application.

In the final type of design variable considered, it is seen that providing more number of corrugation to a particular plate gives higher stiffness values as well as higher natural frequency. Therefore, for a plate to have sufficient vibration (flutter) damping, it should have large number of corrugations. This indirectly shifts its natural frequency, at which flutter occurs to a larger value by increasing its stiffness. But having very high number of corrugation may deteriorate the aerodynamic characteristics of the control surface and will also increase its weight to an extent. Therefore, it is advised to have discontinuous corrugation pattern with constant distance between each corrugation.

References

- Bruce Ralphin Rose J and Jinu G R "A Study on Aeroelastic Flutter Suppression & its Control Measures –Past and Future" *International Journal of Engineering and Technology (IJET)*, Vol. 6, No. 2, Apr-May 2014, ISSN : 0975–4024
- Dillinger, J.K.S., Klimmek, T.: Stiffness optimization of composite wings with aeroelastic constraints. *J. Aircr.* **50**(4), 220–224 (2013)
- Dominique Poirel, Shane Dunn and Jay Porter. "Flutter-margin method for modal parameter uncertainties". *Journal of aircraft* vol. 42, no. 5, September- October 2005
- Jie, Zeng Sunil L., Kukreja (2013) Flutter Prediction for Flight/Wind-Tunnel Flutter Test Under Atmospheric Turbulence Excitation. *Journal of Aircraft* 50(6) 1696–1709 10.2514/1.C031710
- Kholodar, D.B., Thomas, J.P., Dowell, E.H., Hall, K.C.: Parametric study of flutter for an airfoil in in viscid transonic flow. *J. Aircr.* **40**(2), 269–276 (2003)
- Kyle Hord and Yongsheng Lian." Numerical investigation of the aerodynamic & structural characteristics of a corrugated airfoil". *Journal of aircraft*, vol. 49, no. 3, may-June 2012
- Matthew Kampner, Joachim L. Grenestedt." On using corrugated skins to carry shear in sandwich beams", *composite structure* 85 (2008) 139–148
- Mohammadi, H., Ziaei-Rad, S., Dayyani, I.: An equivalent model for trapezoidal corrugated cores based on homogenization method. *Compos. Struct.* **131**(2), 160–170 (2015)
- Patil, M.J.: From fluttering wings to flapping the energy connection. *J. Aircr.* **40**(2), 364–376 (2003)
- Winkler, M., Kress, G.: Influence of corrugation geometry on the substitute stiffness matrix of corrugated laminates. *Compos. Struct.* **94**(4), 2827–2833 (2012)
- Xia, Y., Friswell, M.I., Saavedra Flores, E.I.: Equivalent models of corrugated panels. *Int. J. Solids Struct.* **49**(5), 1453–1462 (2012a)
- Yuying, X., Ajajv, R.M., Friswell, M.I.: Design and optimization of composite corrugated skin for a span morphing wing. *AIAA.* **42**(2), 744–762 (2014)

Chapter 5

Exergy Analysis of an Air Cycle Machine for Different Flight Conditions



M. Zeki Yilmazoglu and Cem Gulseven

Nomenclature

| | |
|-------------|--|
| c | Specific Heat, J/(kg·K) |
| \bar{c}_p | Specific Heat in Constant Pressure, J/(kg·K) |
| E | Exergy, kW |
| \dot{E} | Exergy Flow, kW/s |
| e | Specific Exergy, kW/kg |
| \bar{e} | Molar Exergy, kW/mol |
| h | Enthalpy |
| \dot{m} | Mass Flow Rate |
| P | Pressure |
| R | Universal Gas Constant |
| \bar{R} | Molar Universal Gas Constant |
| s | Specific Entropy |
| T | Temperature |
| \dot{W} | Work Flow |
| x | Molar Fraction |

Subscripts

| | |
|-----|-----------------|
| a | Dry Air |
| D | Destroyed |
| F | Fuel |
| i | ith Flow Stream |

M. Z. Yilmazoglu (✉) · C. Gulseven
Department of Mechanical Engineering, Gazi University, Maltepe, Ankara, Turkey
e-mail: zekiyilmazoglu@gazi.edu.tr

| | |
|-----|------------------------------|
| k | kth Substance of Gas Mixture |
| L | Loss |
| p | Constant Pressure |
| P | Product |
| r | rth Component |
| v | Water Vapor |
| 0 | Reference State |

Superscripts

| | |
|------|------------|
| CH | Chemical |
| M | Mechanical |
| PH | Physical |
| T | Thermal |

Greek Letters

| | |
|-------------|--|
| η | Exergetic Efficiency |
| φ | Rate of Exergy Destroyed Related to Total Exergy of Fuel |
| φ^* | Rate of Exergy Destroyed Related to Total Exergy Destruction |

Acronyms

| | |
|--------|-------------------------|
| BPV | Bypass Valve |
| CON | Condenser |
| $COMP$ | Compressor |
| CR | Cruise |
| HUM | Humidifier |
| LA | Landing |
| MHX | Main Heat Exchanger |
| PHX | Primary Heat Exchanger |
| RHX | Reheater Heat Exchanger |
| TO | Takeoff |
| $TURB$ | Turbine |
| TX | Taxi |
| WS | Water Separator |

5.1 Introduction

Aircraft needs conditioned air for passengers and crew and should overcome various challenges during operation by utilizing the air. Conditioned air is required for various operations to operate flawlessly as the operating environment of an aircraft changes. With differing climate conditions and altitude, operating aircraft needs to be protected from various effects, such as icing on windshields, the amount of ozone present on the current position of aircraft in the atmosphere, etc. Distracting ozone, providing oxygen, and regulating carbon dioxide levels of ventilation air are crucial for a healthy and comfortable flight for passengers and crew. These applications are controlled by environmental control systems (ECS) for an aircraft. ECS controls the air-conditioning system, consists of an air cycle machine (ACM), and several heat exchangers, depending on the design and control valves. Every dynamic component of an aircraft needs energy, and it is obtained by the aircraft fuel, since it is the only source of energy for such a system with limited boundaries. Since the fuel is the limited and only source of power, consequently, to make flight operation more efficient with lesser cost, it is necessary to examine the efficiencies of components during the changing operating conditions. Exergy analysis is a widely accepted approach to examine mechanical systems' efficiency on the system basis and component level. This chapter presents an overview of the corresponding system, the thermodynamic analysis of the air refrigeration cycle, the exergy analysis of the system for various flight operations, the analysis results by exergetic efficiency, and the exergy destruction on the component level, along with the exergetic improvement potential for every single component.

5.1.1 *Environmental Control System (ECS)*

Environmental control system (ECS) is a generic term used in the aircraft industry for the systems and equipment associated with ventilation, heating, cooling, humidity/contamination control, and pressurization in the occupied compartments, cargo compartments, and electronic equipment bays. The term ECS not only encompasses these objectives but also covers windshield defog, airfoil anti-ice, oxygen systems, and other pneumatic demands (ASHRAE Handbook 2015). The main concerns while designing an ECS are the necessity to provide essentially survivable but also a comfortable condition suitable for work and relaxation, for passengers during the flight, as well as for the flight crew. During a typical flight, the environment of the aircraft evolves into a hostile medium, consequently requiring the control of several independent factors for the aim of ECS (Dechow and Nurcombe 2005). Design conditions under independent factors might be listed as ambient temperature, humidity, pressure, heating/air-conditioning load determination, airspeed during flight, heat transfer coefficients of external surfaces contacting the air, occupants' metabolic heat rate, and internal heat sources and vice versa. Also, aircraft systems

must be light, accessible for quick inspection and servicing, highly reliable, tolerant of a wide range of environmental conditions, able to withstand aircraft vibratory and maneuver loads, and able to accommodate failures occurring during flight. Under the consideration of these factors, flight operation creates cooling, heating, pressurization, air filtration, controlling ozone and carbon dioxide levels, and temperature control requirements while considering air velocity in the cabinet by ventilation to provide secure and comfortable flight (ASHRAE Handbook 2015).

ECS is divided into six main categories such as the following: bleed air system, anti-icing system, mixing manifold system, air distribution system, air package unit (consists of heat exchangers, ACM, check valves, and water separator), and cabin pressure control system. These systems are inspected by sensors to monitor in real time to track any changes of system parameters within and surroundings, send required input to the electronic control system of ECS to carry out the requirements properly during the operation (Jennions et al. n.d.) (Fig. 5.1).

Air drawn from the compressor section of the jet engine is called bleed air (also known as the outside air, fresh air, outdoor air, or ambient air). Supplied air into the aircraft cabin is extracted from the gas turbine engine compressor stages after conditioned by air-conditioning packs located under the wing center section. Compressed ambient air is used as the refrigerant in the air cycle cooling by the air-conditioning packs. The pneumatic system, or engine bleed air system, utilizes air to pressurize and ventilate the aircraft compartments, which is a small amount of the jet engine compressor air. During climb and cruise, bleed air is usually taken from the mid-stage engine bleed port for minimum-horsepower extraction (bleed

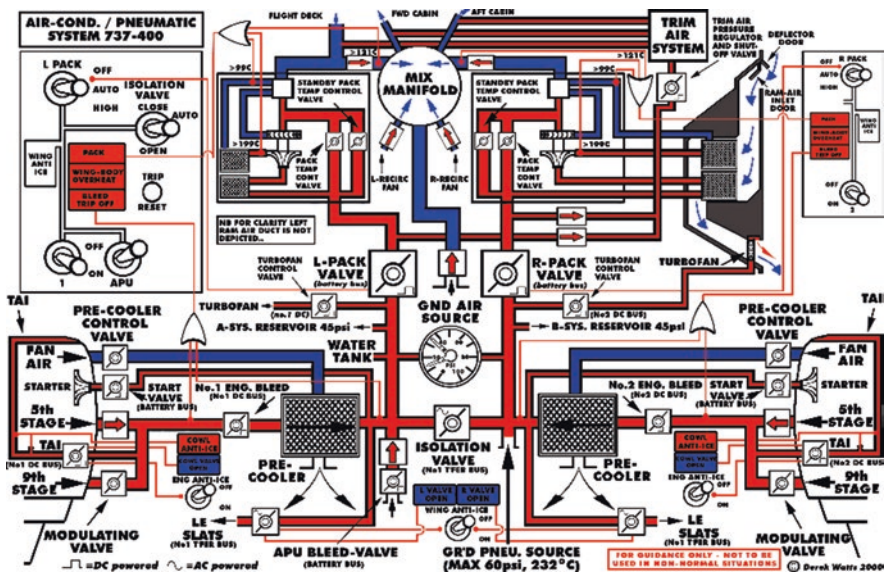


Fig. 5.1 Air-conditioning system schematic diagram Boeing 737-400 (The Boeing 737 Technical Site 1999)

penalty) (ASHRAE Handbook 2015). Bleed air extraction causes engine thrust to decrease and increases aircraft specific fuel consumption and engine turbine temperatures as a penalty (Alison 1991). During idle descent, bleed air is taken from the high-stage engine bleed port, where the maximum available pressure is required to maintain the cabin pressure and ventilation. The auxiliary power unit (APU) is also capable of providing air on the ground and during flight (ASHRAE Handbook 2015).

The auxiliary power unit is a small gas turbine engine mounted in the tail cone of an aircraft. It provides a self-governing electrical and mechanical power for various purposes, such as power for the main engine start, pneumatic power for cabin air-conditioning systems, and shaft power required for other pneumatic and hydraulic systems. The APU also provides power during in-flight emergencies and operations for the electrical and pneumatic systems. While engines are shut down on the ground, it is the source of electric and pneumatic power (Sforza 2014).

Bleed air temperature should be limited for safety requirements; therefore, bleed air is supplied under pressure control to satisfy the conditions of the system using it. In the air refrigeration system, which includes fan jet, engine fan air is used as a heat sink for bleed air, utilized by an air-to-air heat exchanger called a precooler heat exchanger. For turboprop engines, ram air is used by using an ejector or fan for static operations. The pneumatic system also includes bleed shutoff and modulating valves, a fan-air-modulating valve, sensors, controllers, and ozone converters. The pneumatic system is also used intermittently for airfoil and engine cowl anti-icing, engine start, and several other pneumatic functions. The bleed air used for airfoil anti-icing is controlled by valves feeding piccolo tubes extending along the wing leading edge. Similar arrangements are being used for anti-icing the engine cowl and tail section (ASHRAE Handbook 2015).

Pressurization is another crucial requirement for aircraft to operate safely, since the environmental pressure decreases to a point below 25 kPa in a typical flight, subjecting the aircraft body to a large amount of pressure force as well as creating a necessity to pressurize the cabin for occupant comfort and survivability. The cabin pressure is maintained at the desired level by modulating airflow discharged from the pressurized cabin through only one or several cabin outflow valves. The cabin pressure control includes the outflow valves, controller, selector panel, and redundant positive-pressure relief valves. The system controls the cabin to acceptable comfort levels according to the ascending and descending rates of aircraft to maintain the cabin pressure altitude in accordance parallel to the pressure difference schedule between the cabin and the ambient. The flight management system (FMS) is generally used for monitoring the environment and its response to requirements, but if not available, an air data computer (ADC) is used to minimize the cabin pressure altitude and rate of change (ASHRAE Handbook 2015).

As the altitude changes, the amount of ozone present in the air varies. While flying at 11900 m, several ozone plumes are encountered. The ozone concentration varies between 0,8 ppm and 0,62 ppm at that altitude. If this concentration of ozone processes through the cabin without ozone protection, passengers and crew could experience chest pain, coughing, shortness of breath, fatigue, headache, nasal congestion, and eye irritation. Atmospheric ozone dissociation occurs when ozone goes

through the compressor stages of the engine, the ozone catalytic converter which is on aircraft with a route structure that can encounter high ozone concentrations, and the air-conditioning packs. The ozone further dissociates when contacting the ducts, the interior surfaces, and the recirculation system. The ozone converter dissociates the ozone to oxygen molecules by using a noble catalyst such as palladium (ASHRAE Handbook 2015).

5.1.1.1 Aircraft Refrigeration Cycle

Air cycle refrigeration works on the reverse Brayton or Joule cycle. Air is compressed by a compressor with work input, and then heat is removed for heating purposes or further cooling of the air; this air is then expanded to a lower temperature than before it was compressed. Air then can be used to extract heat from a heat sink to provide useful cooling, resulting in the air to return its original state in a closed cycle. Turbine work occurs with the thermal energy of air converted to mechanical energy by the turbine blades, causing air to expand. Expansion of air removes the energy of air by blades; blades are driven round and reduction in air temperature occurs. This work can be used to provide work input for various equipment, such as generators and fans. It often is utilized for helping the compressor power, such as in the air cycle machine compressor of aircraft. Sometimes a separate compressor, called a “bootstrap” compressor, is powered by the expander, giving two stages of compression. Doubling the compression on the hot stream further elevates the temperature, making the air cycle system available to produce a larger heat source reservoir for heating. The cold air after the expansion stage may be used as a refrigerant, directly or indirectly in open and close cycles, respectively. For a closed cycle, heat exchangers may be used. The efficiency of such systems is limited to a great extent under the effect of compression and expansion efficiencies, as well as those of the heat exchangers, employed (Hundy et al. 2000). For aircraft refrigeration cycles, even though it is an open cycle, heat exchangers are utilized for the desired heat balance (Fig. 5.2).

The main purpose of air cycle refrigeration is to maintain air-conditioning for commercial and military aircraft. The reverse Brayton cycle or Brayton refrigeration cycle is used, as opposed to the Brayton power cycle that is used in gas turbine engines. The difference between the two cycles is that, in the power cycle, fuel in a combustion chamber adds heat and, in the refrigeration cycle, a ram air heat exchanger removes heat. The vapor compression cycle for refrigeration is another cycle that is used in military aircraft for galley cooling and is used for larger commercial transports as well as used in building and automotive air-conditioning and both domestic and commercial means (ASHRAE Handbook 2015). Air refrigeration is carried out by the surrounding air, cooling the bleed air extracted from compressor stages, conditioning it with an air cycle machine, and processing it through the mixing manifold for required use. The extracted bleed air is conditioned by several heat exchangers, and moisture is extracted with a condenser before the entrance of the turbine to prevent water droplets damage for the equipment. The

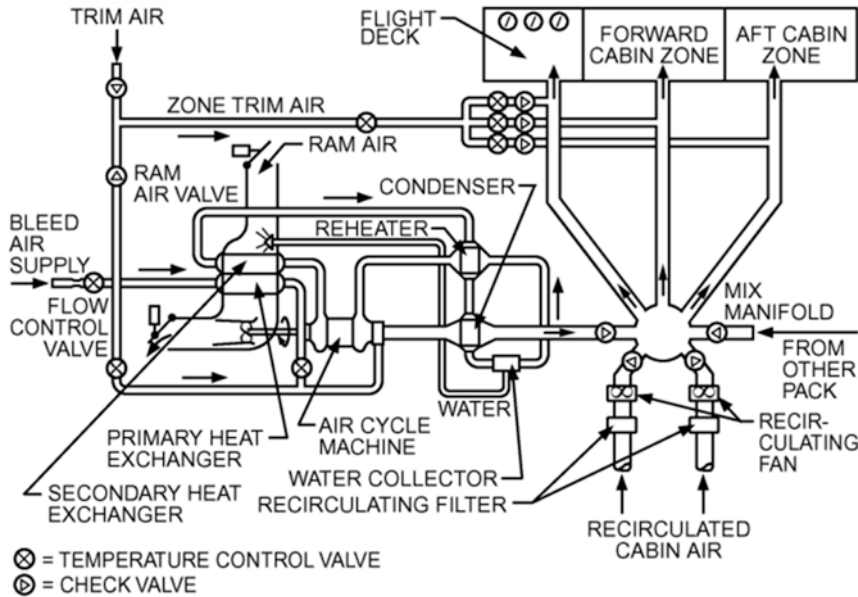


Fig. 5.2 Aircraft air-conditioning schematic (ASHRAE Handbook, HVAC Applications, American Society of Heating, Refrigerating and Air-Conditioning Engineers, Inc. © 2015)

extracted water droplets are injected into the ram air line to increase the efficiency of cooling by increasing the humidity of cooling air.

Air Cycle Machine

In an air cycle, compression of the ambient air by the gas turbine engine compressor provides the power input. The heat of compression is removed in a heat exchanger using ambient air as the heat sink. This cooled air is refrigerated by expansion across a turbine powered by the compressed bleed air. The turbine energy resulting from the isentropic expansion is absorbed by a second rotor, which is either a ram air fan, bleed air compressor, or both. This assembly is called an air cycle machine (ACM) (ASHRAE Handbook 2015).

Commercial and military aircraft has its components generally operating in an open-loop cycle. Commonly, commercial aircraft uses recirculating cabin air to prevent bleed penalty where the amount of recirculating air used is depending on the cabin comfort limits such as the carbon dioxide level and humidity. There are several different systems for air-conditioning. Essentially, the difference occurs by the air cycle machines that are used and means of water separation (ASHRAE Handbook 2015) (Fig. 5.3).

The bootstrap ACM is the most common one in air cycle machines that are in use. It consists of a turbine, a compressor, the three-wheel ones consist of a turbine,

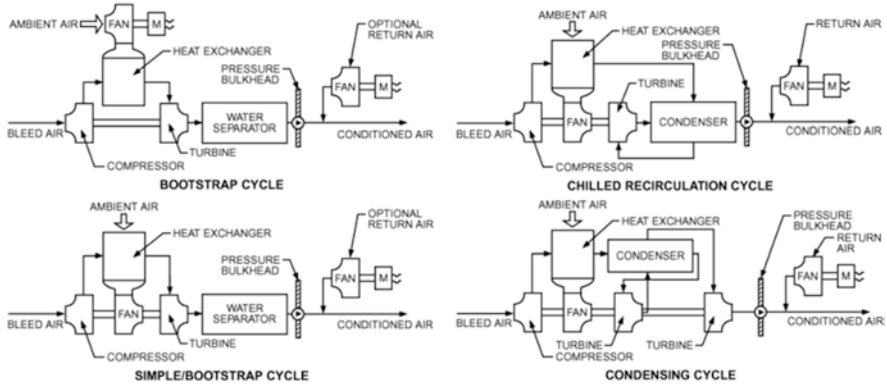


Fig. 5.3 Some aircraft refrigeration cycles (ASHRAE Handbook, HVAC Applications, American Society of Heating, Refrigerating and Air-Conditioning Engineers, Inc. © 2015)

a compressor, and a fan. The four-wheel ACM consists of two turbines, a compressor, and a fan. In military applications, the bootstrap ACM is widely used, which is a simple bootstrap cycle, and older commercial aircraft models also use this type of ACM. The three-wheel bootstrap ACM is mostly used on newer commercial, commuter, and business aircraft. The four-wheel ACM, which consists of the condensing cycle, was first introduced in the 777 aircraft model. Mixing ram-cooled bleed air with the refrigerated air is another way of controlling the air temperature supplied to the compartment, which satisfies the range of desired cooling and heating. Ram air modulation, various bypass schemes in the air-conditioning pack, and downstream controls that add heat for individual zone temperature control are other types of temperature control that are often used (ASHRAE Handbook 2015).

The early version of the Boeing 747 had the low-pressure design bootstrap cycle. Airbus A320 and A330/A340 families, Boeing 757, 737NG, the later version of the Boeing 747, and the early versions of the 767 had high-pressure water separation bootstrap air cycle machines for air-conditioning. The four-wheel bootstrap cycle has earmarks of the three-wheel one but has a turbine stage connected on the shaft also. With this construction, requirements concerning humidity control are reached for ground and cruising conditions at high altitudes. The four-wheel cycle is used in Airbus A380, Boeing 777, the later version of 767, and the Embraer EMB 170/190 family (Bender 2016).

Most aircraft use two or three air cycle packs working in parallel to ensure the secure flight operation due to failures which might avert air-conditioning, allowing the aircraft to be dispatched with certain failures. Despite the advantage of using several packs, many businesses and commuter aircraft use a single pack. However, high-altitude aircraft that have a single pack also have emergency pressurization equipment that uses ram-cooled bleed air. Concerning the pressurization in aircraft, the bleed airstream is regulated at the inlet section of the air-conditioning pack, leading through the aircraft cabin by a flow control valve. The regulation is required for ventilation and re-pressurization during descent (ASHRAE Handbook 2015).

Varying altitudes and humidity levels require a water separation unit for occasions where the cycle machine temperature goes below the dew point temperature and leads to water ingestion. For such cases, water separation prevents water spray into the cabin. Low- or high-pressure water separation might be used for this purpose. A low-pressure water separator is located downstream from the turbine and has a cloth lining integrating fine water particles entrapped in the turbine discharge air into water droplets. These droplets are collected, drained, and sprayed into ram airstream with bleed air powered ejector to increase the cooling capacity of the coolant air, enlarging the heat sink reservoir for heat transfer. The high-pressure water separator condenses the water at the outlet of the turbine section and removes the moisture. A heat exchanger uses turbine discharge air to cool the high-pressure air sufficiently to condense most of the moisture present in the bleed air supply. The moisture is collected and sprayed into the ram airstream (ASHRAE Handbook 2015).

The significant difference of the condensing cycle is that it is capable of eliminating condenser freezing problems since the condensing heat exchanger will work above the freezing conditions with the help of two turbines. One of these turbines removes the high-pressure water and the second one expands the air to a subfreezing point of temperature where it will be mixed with filtered recirculation air. The condensing cycle has higher efficiency due to the recovery of heat during the condensation phase (ASHRAE Handbook 2015).

Reverse Brayton Cycle (RBC)

In 1844, the American physician John Gorrie (1803–1855) designed and built an air-cooling apparatus in Florida to provide air-conditioning for the yellow fever patients. The machine had a piston-cylinder apparatus that compressed air that was cooled back to ambient temperature by circulating water. The cooled compressed air was then expanded in a second piston-cylinder apparatus that caused the air to drop to a sufficiently low temperature to produce ice and satisfy other cooling needs. The expanded air was then drawn back into the compressor and the cycle began again. The two piston-cylinder devices were connected, so that the expansion work was used to offset the compression work. This was an early invention of RBC (Balmer 2011).

Air or many other gases can be used as a refrigerant by expanding them to a low temperature using a gas turbine. Work obtained from the turbine is also used to maintain some parts of the compressor work. Turbine exhaust is the coldest stream on the cycle and can be employed as the coolant in a heat exchanger. The difference occurs with the vapor compression refrigeration cycle on the heat exchanger, since it replaces the evaporator in the gas refrigeration cycle. A gas refrigeration cycle is shown in Fig. 5.4 and comprises the following processes: 1–2 isentropic compression in a compressor, 2–3 cooling at constant pressure in a heat exchanger, 3–4 isentropic expansion of the gas to a lower temperature in a gas turbine, and 4–1 constant pressure heating of the cold air in a heat exchanger, thus producing refrigeration. A steady-state energy analysis of the heat exchanger as a control volume

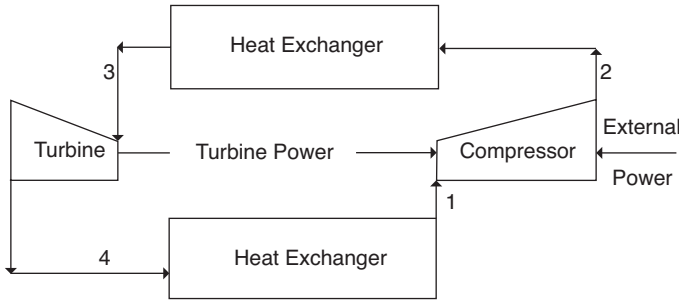


Fig. 5.4 Equipment for reverse Brayton cycle (Logan 1999)

shows that the refrigeration is the change of enthalpy occurring during processes 4–1. The compressor work done during processes 1–2 may be used by the gas turbine for expansion and to provide power for an external device, if they are connected to the compressor mechanically (Logan 1999).

The ideal gas refrigeration cycle comprises two isobaric and two isentropic processes; it is like the Brayton cycle for gas turbine power units. As the name of the cycle indicates, it is a reversed cycle, i.e., the state point rotation sustained with the opposite direction of the process occurring in the cycle (Logan 1999) (Fig. 5.5).

The focus for this cycle will be on the essential difference between the two permanent gas machines investigated. Unlike the Stirling machine, which uses a thermal (unsteady) regenerator, the Joule machine involves a recuperative heat exchanger. A simple reverse Brayton cycle consists of a parallel flow heat exchanger where the hot and cold stream mass flow rates are nearly identical. Reverse Brayton cycle is subjected to a limitation of cycled fluid temperature variation in contact with the heat sink. Nevertheless, this configuration is used in airliners' air-conditioning (Feidt 2017).

5.1.2 Literature

Throughout the aircraft improvements, the environmental control system, air cycle machine, and reverse Brayton cycle have been important aspects of flight operation to be considered by the effects on optimization and efficiency revisions of systems. Besides this application area, the reverse Brayton cycle is an important governing cycle of many refrigeration utilities, especially in cryogenic applications.

A thermo-economic analysis of a commercial aircraft environmental control system is demonstrated by Leo and Grande (Leo and Pérez-Grande 2005); since it is crucial to optimize the cost efficiency of aircraft components, a cost balance has been applied to the ECS of an aircraft as a component, and the unit cost of the conditioning stream entering the cabin has been obtained for a range of the aircraft engine bleed pressure values, pointing out the importance of cost optimization since

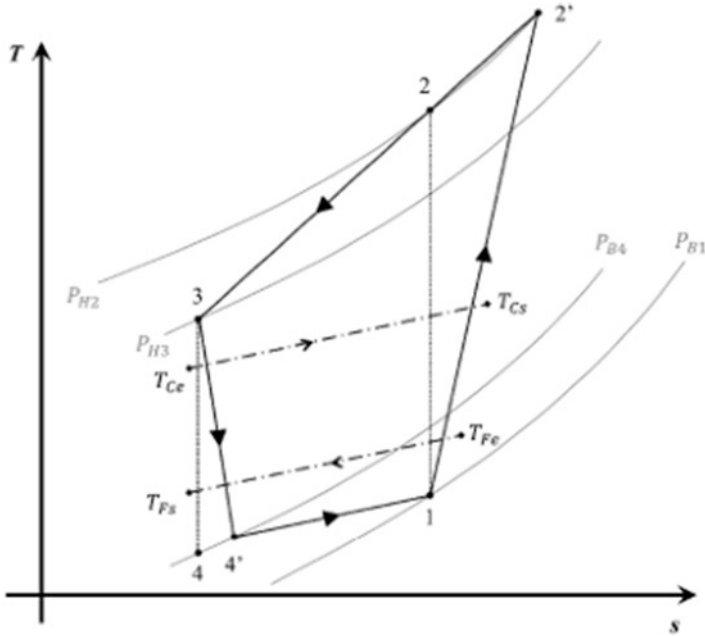


Fig. 5.5 Joule reverse cycle with imperfect heat recovery, heat gradients at contact with source and heat sink of finite heat capacities, and internal irreversibilities, including pressure losses (Feidt 2017)

the system is a transporting one while carrying its operational components within. Ma et al. (Ma et al. 2015) proposed a closed simulation ground-test method of the ram air basing on the equivalent heat transfer capacity to show that it can provide the ram air's test condition for deriving the performance of commercial airliners' aircraft environmental control system (ECS). By analyzing the key factors in the method, it was shown that altitudes and ACM characteristics can influence the power consumption and other conformance. Wright et al. (Wright et al. 2018) addressed the failures of the ECS due to fouling and identified the potential sources of fouling and operational measures that may affect the operation of the safety-critical system. Fouling collected from large commercial aircraft is analyzed using different techniques to identify the potential source emission and composition. Sun et al. proposed a novel health indicator extraction method based on the available sensor parameters for the health monitoring of the air-conditioning system (ACS) of a legacy commercial aircraft model. The corresponding health indicator can effectively characterize the degradation state of the ACS, which can provide valuable information for proactive maintenance plan in advance. Considering limited built-in sensing devices on the legacy aircraft model, one of the challenges for airborne system health monitoring is to find an appropriate health indicator that is highly related to the actual degradation state of the system (Sun et al. 2018). Chen et al. (2017) proposed a new synthesized humidification system based on the traditional

environmental control systems to prevent the low amount of humidity in aircraft cabin where occupants present, since the amount of humidity in the cabin is drier than a typical desert, which can cause dehydration in the cabin passengers. Yuan et al. (2015) conducted a simulation study of a novel aircraft environmental control system based on membrane dehumidification (MD-ECS) and compared the system with the up-to-date four-wheel high-pressure dewater system (4WHPDW-ECS). The effects of the sweep ratio of the membrane dehumidifier on the dehumidification and cooling performance of the system were also investigated. Santos et al. (2014) studied the ACM by focusing on a thermodynamic study of an air cycle machine (ACM) for aircraft air-conditioning purposes. The results showed that the computational tool implemented to solve the ACM mathematical model allows an understanding of the air cycle machine performance when flight aircraft and cabin human comfort parameters are changed to attain an optimized aircraft environmental control system (ECS) design. A work of the experimental study on the off-design performance and dynamic response of an aircraft environmental control system is done by Zhao et al. (2009). The corresponding system was subjected to a test of work and found that it meets the requirements of the ECS. This work also presented that some parameters, including outlet pressure, turbine efficiency, and rotational speed, might vary obviously when the operation conditions changed; thus, it is necessary to consider the off-design performance and the transient performance in the design of ECS. ECS and ACM improvement is a crucial research area on overcoming the inefficiencies that occur during the flight operation, and still, there is more to overcome through the future of the aircraft technologies by conducting analysis and optimization research and studies.

Reverse Brayton cycle is the working principle of many refrigeration systems such as cryogenic applications, food freezing, domestic use, air-conditioning systems, mine refrigeration systems, and aircraft ventilation with the ACM. Many researchers have been working to improve, examine, optimize, and discuss the efficiency of this cycle, along with the mechanisms which it drives.

Goodarzi presented a study of a consistent methodology incorporating the usefulness of the regenerator and heat exchanger for the alternative forms of Brayton and reverse Brayton cycle compared to the basic Brayton and regenerative Brayton cycles and performed an analytical study to explain why regenerator and heat exchanger might be useless at particular operating conditions for various types of refrigeration cycle arrangements consisting of heat exchangers along with cycles' primary components which are turbine and compressor (Goodarzi 2016). Agnew et al. performed an optimization study of combined Brayton and reverse Brayton cycles, which indicated that optimum results can be obtained when the inlet pressure to the bottom cycle is above atmospheric pressure (Agnew et al. 2003). Using reasonable assumptions for turbomachinery efficiencies and heat exchanger effectiveness, the coefficient of performance (COP) and specific heating effect (SHE) of the regenerated and unregenerated cycles are computed and optimized by Sisto in 1979 (Sisto 1979). A thermodynamic model, for open combined Brayton and reverse Brayton cycles, is established which considers the pressure drops of the working fluid along with the flow processes. The size constraints of the real power

plant using finite-time thermodynamics considered and pointed out the conditions affecting the optimization of the cycle (Wanli et al. 2009). Kumar et al. presented an exergetic analysis of reverse Brayton cryocooler for different cooling loads at 65 K for high-temperature superconductor cables (Dhillon et al. 2017).

Exergy analysis is performed to calculate the obtainable work of a system and determine the improvement potential on the performance of each system component. It also presents the effect of irreversibilities and the recoverable amount of work potential that is lost and gives a result which indicates the points that must be considered during optimization and design. The output of the analysis is progressed by performing advanced exergy analysis to obtain avoidable and unavoidable exergy destructions occurring in the component operation. During a design process, the system boundaries and requirements must be considered as well as the desired efficiency of the system. The surrounding environment consists of many aspects and limits properties which cause irreversibilities and obtained work loss. To determine restrictions and create a solution to overcome losses and inefficiencies, the exergy analysis is a widely used and useful way. With this regard, many exergy analyses are performed on various engineering systems, especially on power plant systems, as well as air-conditioning systems, etc.

As Bejan and Siems stated, there is a need for exergy analysis and optimization in the aircraft industry. It was also stated that the existing approaches about the design and optimization stages of a system require a new approach to fulfill its purpose within the economic concerns, since these methods are inadequate for thermodynamic optimization of aircraft power and cooling systems due to practice issues. Even though the need for another approach exists, characterizing the irreversibilities by exergy analysis can readily identify the predominant irreversibilities and target the optimization effort and also serves as a very useful figure of merit for measuring the degree of improvement provided by system alterations that are considered for optimizing it (Bejan and Siems 2001). With the same approach and considering the benefits of exergy analysis, this study will demonstrate an exergy analysis of an aircraft air cycle machine to obtain the exergetic improvement potential and the amount of the irreversibilities on the component level and show where the optimization effort may be made to improve efficiency and reduce fuel consumption, by examining the components consisting in the corresponding system which will be presented further in this text.

Several exergy analyses are performed on similar systems for the same purposes. Ayaz et al. performed an exergy and energy analysis on an aircraft air cycle machine at a designated altitude. The work presented the amount of exergy and entropy in each to examine the work potential on each stage (Ayaz et al. 2018). Bender performed a conventional exergy analysis of a conventional air generation unit of a commercial aircraft to integrate the analysis into the model-based design. This study also presents an evaluation of the aircraft's environmental control system. The equation-based, object-oriented modeling language Modelica was used to set up the model of a three-wheel bootstrap cycle and used Dymola as a modeling and simulation environment. It showed the exergy destruction rates of each component of the air refrigeration system of aircraft, by simulating the air generation unit under four

different flight segments of a typical flight mission. The “more electric aircraft” exergy analysis was also carried out in this study (Bender 2017).

The aviation industry accounts for 2% of the total human-induced carbon dioxide production (915 million tons of a total of 43 billion tons of carbon dioxide in 2019). A great improvement has been made in the last 40 years in fuels, airport operations, and even airport designs to ensure sustainability and reduce emissions. However, achieving a reduction of 50% of the 2005 value in carbon emissions in 2050 is one of the main sustainability targets. Exergy analysis is of great importance in analyzing sustainability and environmental impacts (Morosuk and Tsatsaronis 2013; Kaya et al. 2016), evaluating the potential of alternative fuels (Coban et al. 2017; Ekici et al. 2016), researching and developing the performance of engines (Söhret et al. 2016; Ekici et al. 2017), examining the environmental effects of emissions (Ekici et al. 2013; Altuntas et al. 2012), and analyzing airport buildings (Acikkalp et al. 2015). For this reason, in this study, the performance analysis of the air cycle machine in varying external conditions is discussed with the exergy analysis, and the components with high improvement potential are determined.

5.1.3 Exergy Analysis

5.1.3.1 System Description and Boundary Conditions

The air cycle machine in this exergy analysis consists of a turbine (TURB), a compressor (COMP), a bypass valve (BPV) for flow regulation and temperature control, a water separator (WS), a humidifier (HUM), and four heat exchangers, where two of them are working as a condenser (CON) and a reheater (RHX) heat exchanger where the warmer and colder streaming fluid are both bleed air. The primary (PHX) and secondary (MHX) heat exchangers utilize the ram air as coolant. The water is separated after the condenser outlet is injected into the ram airstream before it enters the main heat exchanger. Bypass valve works as a temperature adjusting device, since it regulates or increases the flow of bleed air through the compressor for the desired output temperature, and as such, it increases the temperature of the turbine outlet flow. The system layout of the air refrigeration cycle is presented in Fig. 5.6, a common type of a bootstrap air cycle machine-driven system. In this system, the bleed air is extracted from the various compressor stages of the aircraft gas turbine engine and conditioned by the preheating heat exchanger before proceeding through the compressor. After the compression, the bleed air is cooled by the main heat exchanger and moves through the condenser after passing through the reheater heat exchanger. During this process, bleed air contains a small amount of water vapor. Water separation is an important factor due to the harmful effects on the turbine blades. Separated water is utilized by the humidifier to increase the cooling capacity of the ram air by spraying it to the airstream. The turbine expands the dehumidified air to a very low temperature; therefore, it works as a cooling fluid for condensing purpose in the condenser. Bleed air goes through the condenser again and moves

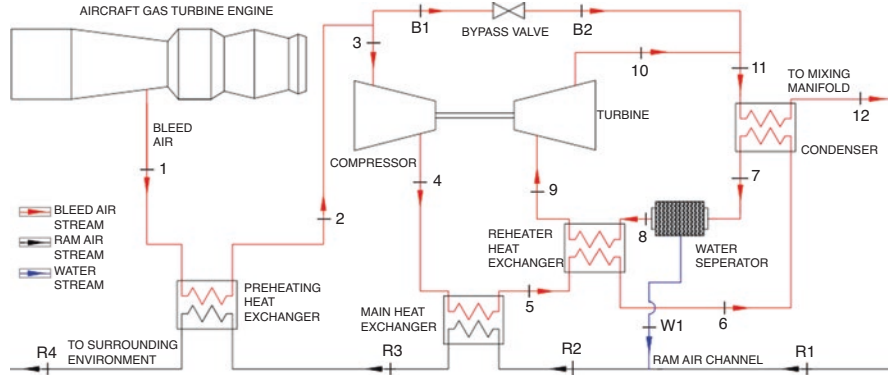


Fig. 5.6 System layout of ACM used in the simulations

through the mixing manifold, where it is going to be mixed with recirculation air coming from the aircraft cabinet. The driving force of this type of system is usually a fan, sharing the same shaft with the turbine and the compressor, where it is driven by the ram airflow. Therefore, the fan work is the input for shaft work depending on the flight operation whether it is on the ground or not. For ground operations, air package unit is used to sustain ventilation for the aircraft; besides, the fan is used to sustain work input during the flight operation on air.

The fan that drives the turbine and compressor is neglected in this study, since its effect on exergy is negligible due to small values compared to the other components and ineffective on heat transfer that occurs during the operation of the air refrigeration system.

Four initial state parameters are considered to be the parameters of the surrounding environment, which are determined for the takeoff, cruise, landing, and taxi phases of the aircraft flight operation. Ram air is obtained from ambient air and is used for various objectives of aircraft, primarily working as the cooling fluid in this system. Thermodynamic properties of the environmental parameters affect the ram air pressure, humidity, and temperature values, which affect the cooling stream of the aircraft air refrigeration system. Because of this, intensive and extensive properties of ram air are important and must be determined under the consideration of the lowest and highest possible altitude due to environmental properties of the flight operation, including the effects of climate and aircraft speed as well. The determined parameters for each flight operation are shown in Table 5.1 and used as the ram air parameters for exergy analysis.

Since the temperature and pressure changes by altitude, there is also the uncertainty of parameters at the specific point where the aircraft is physically moving; thus, these parameters are considered to be an average and estimated one to perform exergy analysis. For this study, the altitude of each flight operation is set to be 1000 m, 11,250 m, 6000 m, and 0 m from the sea level above for takeoff, cruise, landing, and taxi flight missions, respectively.

Table 5.1 Ram air parameters for different flight operations

| Flight mission | Temperature (K) | Pressure (kPa) | Relative hum. (%) |
|----------------|-----------------|----------------|-------------------|
| Takeoff | 281,75 | 89,88 | 60 |
| Cruise | 216,85 | 21,7 | 0 |
| Landing | 249,25 | 47,22 | 60 |
| Taxi | 288,15 | 101,325 | 60 |

Table 5.2 Dead state (reference) values for each flight mission

| Flight mission | Temperature (K) | Pressure (kPa) | Relative hum. (%) |
|----------------|-----------------|----------------|-------------------|
| Takeoff | 219,15 | 21,4 | 60 |
| Cruise | 219,15 | 21,4 | 0 |
| Landing | 219,15 | 21,4 | 60 |
| Taxi | 219,15 | 21,4 | 60 |

Table 5.3 Bleed air initial state parameters

| Flight mission | Temperature (K) | Pressure (kPa) | Relative hum. (%) |
|----------------|-----------------|----------------|-------------------|
| Takeoff | 498,75 | 171,6 | 60 |
| Cruise | 498,75 | 187 | 0 |
| Landing | 498,75 | 164,4 | 60 |
| Taxi | 498,75 | 171,6 | 60 |

Reference values or dead state values are crucial for the exergy analysis output since they designate the value of obtained performance from a system according to a specified reference point. The amount of obtainable work differs if the reference environment changes. For the reference point, any working system's exergy value will differ in this regard. Here, the reference values for each condition are shown in Table 5.2. The international standard atmosphere (ISA) is used to identify the ambient parameters, which is the same as the ram air properties used in the analysis.

Bleed air is primarily important for the air refrigeration system as mentioned before, since it is the source of ventilation air of cabinets for passengers and flight crew. Bleed air is conventionally taken from various compressor stages of the aircraft gas turbine engine. As altitudes and engine workload change, bleed air temperature and pressure may vary, depending on the design of the air refrigeration system. Air is taken from different stages of the compressor, depending on the desired property as the initial condition of bleed air feed. Assumed initial state parameters for bleed air are shown in Table 5.3. Heat exchangers are estimated to have a 3% pressure loss for each flow path passing through it.

5.1.3.2 Method

For this study, a three-wheel bootstrap air cycle machine of a conventional air refrigeration cycle of an aircraft with a condenser is taken, and exergy analysis is done on the corresponding system. To obtain stream parameters, the governing open

cycle is simulated for steady-state conditions with a thermodynamic and heat transfer analysis. Several assumptions are made before practicing the exergy analysis and mentioned below.

General Assumptions

Moist air is considered as an ideal gas as well as the air itself. Air is composed of many different gases, and each gas is assumed to be in a non-reacting form and at a homogenous state. These constituents are also regarded as an ideal gas. Under the condensing point of water, water moisture is considered as a gas at this stage, and its effect on the stream is neglected such as icing or solubility; therefore, these phenomena are neglected. Even though ambient temperature and pressure are the dead state reference point for exergy applications, it is set to the lowest altitude thermodynamic properties of the flight mission. The molar composition of air in the cycle is shown in Table 5.4. It is also assumed that components are not interacting with the ambient.

Exergy Analysis

The exergy of a stream consists of three main components: thermal exergy, mechanical exergy, and chemical exergy. The total flow exergy of each fluid stream “*i*” can be expressed as:

$$\dot{E}_{tot,i} = \dot{E}_{Physical,i} + \dot{E}_{Chemical,i} \quad (5.1)$$

Physical exergy is the sum of two exergy quantities, one is mechanical and the other is thermal exergy of the stream. Physical exergy flow can be expressed as:

$$\dot{E}_{Physical,i} = \dot{m}_i \left[h_i - h_0 - T_0 (s_i - s_0) \right] \quad (5.2)$$

where \dot{m}_i is the mass flow of the fluid stream and h and s represent the specific enthalpy and entropy, respectively. The subscripts i and 0 represent the flow i and reference state point 0 . The part which consisted of the enthalpy difference expresses the mechanical hand of the exergy, where the multiplication of dead state temperature with entropy difference expresses the thermal exergy of the stream.

Table 5.4 The molar composition of air

| Standard air | | | | | | |
|------------------|----------------|-----------------|------------------------|------------------------|---------|-----------------|
| Mole composition | | | | | | |
| N ₂ | O ₂ | C _{O2} | H ₂ O(vap.) | H ₂ O(liq.) | Ar | SO ₂ |
| 0,78,084 | 0,20,947 | 0,00035 | 0 | 0 | 0,00934 | 0 |

Thermal, mechanical, and chemical exergy for moist air on the molar basis can be expressed as:

$$\text{Molar thermal exergy : } \bar{e}_i^T = \left(x_a \bar{c}_{P,a} + x_v \bar{c}_{P,v} \right) \left(\frac{T}{T_0} - 1 - \ln \frac{T}{T_0} \right) \quad (5.3)$$

$$\text{Molar mechanical exergy : } \bar{e}_i^M = \bar{R}T_0 \ln \frac{P}{P_0} \quad (5.4)$$

$$\text{Molar chemical exergy : } \bar{e}_i^{CH} = \sum x_{k,i} \bar{e}_{k,i}^{CH} + \bar{R}T_0 \sum x_{k,i} \ln x_{k,i} \quad (5.5)$$

where x is the molar fraction, \bar{R} is the molar universal gas constant, P is the pressure, and \bar{c}_p is the molar heat capacity. The subscript k indicates the mole of gas, which is the constituents of air. The molar chemical exergy for the corresponding gas used in the calculation can be selected from the table of standard chemical exergy on a molar basis, as shown in Table 5.5. The molar composition of air used in this analysis is shown in Table 5.6. The chemical exergy of the liquid water extracted from the flow stream after the condenser stage is calculated using Eq. (5.1), and for the physical exergy of liquid water, Eq. (5.5) is used. The difference

Table 5.5 Chemical exergy of gases on the molar basis (Ertesvåg 2007; Bejan et al. 1996)

| Model 298,15 K 1019 Bar | | |
|-------------------------|------------------------|--------|
| Model I(kJ/kmol) | N ₂ | 639 |
| | O ₂ | 3951 |
| | CO ₂ | 14,176 |
| | H ₂ O(vap.) | 8638 |
| | H ₂ O(liq.) | 45 |
| | Ar | 11,690 |
| Model II(kJ/kmol) | N ₂ | 720 |
| | O ₂ | 3970 |
| | CO ₂ | 19,870 |
| | H ₂ O(vap.) | 9500 |
| | H ₂ O(liq.) | 900 |
| | Ar | 11,690 |

Table 5.6 The molar composition of bleed air

| | Mole composition | | | | | | |
|---------|------------------|----------------|-----------------|------------------------|------------------------|--------|-----------------|
| | N ₂ | O ₂ | CO ₂ | H ₂ O(vap.) | H ₂ O(liq.) | Ar | SO ₂ |
| Takeoff | 0,76,413 | 0,21 | 0,0003 | 0,0174 | 0 | 0,0082 | 0 |
| Cruise | 0,7808 | 0,2095 | 0,0003 | 0 | 0 | 0,0094 | 0 |
| Landing | 0,76,413 | 0,21 | 0,0003 | 0,0174 | 0 | 0,0082 | 0 |
| Taxi | 0,76,413 | 0,21 | 0,0003 | 0,0174 | 0 | 0,0082 | 0 |

between dead state molar chemical exergy and flow stream molar chemical exergy is the molar chemical exergy of the stream itself, each of them is calculated for the dead state point. For the moist air calculations, equations based on molar exergy are the governing equations for this analysis.

The molar specific exergy of a fluid stream can be calculated using the following expression and can be derived to obtain the specific exergy flow by using the mass flow rate, molecular weight, and molar composition of the stream:

$$\begin{aligned} \bar{e}_{i,total} = & \left(x_a \bar{c}_{p,a} + x_v \bar{c}_{p,v} \right) \left(\frac{T}{T_0} - 1 - \ln \frac{T}{T_0} \right) + \bar{R} T_0 \ln \frac{P}{P_0} + \sum x_{k,i} \bar{e}_{k,i}^{CH} \\ & + \bar{R} T_0 \sum x_{k,i} \ln x_{k,i} - \sum x_{k,0} \bar{e}_{k,0}^{CH} + \bar{R} T_0 \sum x_{k,0} \ln x_{k,0} \end{aligned} \quad (5.6)$$

For the calculation of chemical exergy, two models are present. Model I is chosen for the exergy analysis, since it is much suitable for the varying environmental parameters.

The thermal capacity used in molar thermal exergy is calculated for different temperatures of the flow stream. The temperature-dependent thermal capacity is used and expressed as:

$$\bar{c}_p = a + bT + cT^2 + dT^3 \quad (5.7)$$

To calculate exergy destruction for each component, fuel and product exergies are obtained, where exergy balance over for r^{th} component is expressed as:

$$\dot{E}_{F,r} = \dot{E}_{P,r} + \dot{E}_{D,r} \quad (5.8)$$

where the subscripts F , P , and D represent the fuel exergy, product exergy, and destroyed exergy of the r^{th} component, respectively. For the total system, exergy balance can be written as:

$$\dot{E}_{F,total} = \dot{E}_{P,r} + \sum_r \dot{E}_{D,r} + \dot{E}_{L,r} \quad (5.9)$$

Subscript L represents the exergy loss and r represents the component.

The exergetic efficiency is η_r of the r^{th} component that is defined by the following equation:

$$\eta_r = \frac{\dot{E}_{P,r}}{\dot{E}_{F,r}} = 1 - \frac{\dot{E}_{D,r}}{\dot{E}_{F,r}} \quad (5.10)$$

For overall system efficiency:

$$\eta_{total} = \frac{\dot{E}_{P,total}}{\dot{E}_{F,total}} = 1 - \frac{\dot{E}_{D,total} + \dot{E}_{L,total}}{\dot{E}_{F,total}} \quad (5.11)$$

The rate of exergy destroyed by the r^{th} component related to the exergy of total fuel is expressed by the exergy destruction ratio:

$$\varphi_{D,r} = \frac{\dot{E}_{D,r}}{\dot{E}_{F,total}} \quad (5.12)$$

The rate of exergy destroyed by the r^{th} component related to the exergy of total exergy destruction is expressed by the exergy destruction ratio:

$$\varphi_{D,r}^* = \frac{\dot{E}_{D,r}}{\dot{E}_{D,total}} \quad (5.13)$$

Exergy balances of each component depending on the reference state are generated as such:

$$PHX \dot{E}_{Fuel} = \dot{E}_{hot in}^{PH} - \dot{E}_{hot out}^{PH} + \dot{E}_{cold in}^M - \dot{E}_{cold out}^M + \dot{E}_{cold in}^{CH} - \dot{E}_{cold out}^{CH} \quad (5.14)$$

$$\dot{E}_{Prod} = \dot{E}_{cold out}^{TH} - \dot{E}_{cold in}^{TH} + \dot{E}_{hot out}^{CH} - \dot{E}_{hot in}^{CH} \quad (5.15)$$

$$MHX \dot{E}_{Fuel} = \dot{E}_{hot in}^{PH} - \dot{E}_{hot out}^{PH} + \dot{E}_{cold in}^M - \dot{E}_{cold out}^M + \dot{E}_{cold in}^{CH} - \dot{E}_{cold out}^{CH} \quad (5.16)$$

$$\dot{E}_{Prod} = \dot{E}_{cold out}^{TH} - \dot{E}_{cold in}^{TH} + \dot{E}_{hot out}^{CH} - \dot{E}_{hot in}^{CH} \quad (5.17)$$

$$MHX_{cruise} \dot{E}_{Fuel} = \dot{E}_{hot in}^{PH} - \dot{E}_{hot out}^{PH} + \dot{E}_{cold in}^{TOTAL} - \dot{E}_{cold out}^M - \dot{E}_{cold out}^{CH} \quad (5.18)$$

$$\dot{E}_{Prod} = \dot{E}_{cold out}^{TH} + \dot{E}_{hot out}^{CH} - \dot{E}_{hot in}^{CH} \quad (5.19)$$

$$RHX \dot{E}_{Fuel} = \dot{E}_{hot in}^{PH} - \dot{E}_{hot out}^{PH} + \dot{E}_{cold in}^M - \dot{E}_{cold out}^M + \dot{E}_{cold in}^{CH} - \dot{E}_{cold out}^{CH} \quad (5.20)$$

$$\dot{E}_{Prod} = \dot{E}_{cold out}^{TH} - \dot{E}_{cold in}^{TH} + \dot{E}_{hot out}^{CH} - \dot{E}_{hot in}^{CH} \quad (5.21)$$

$$CON \dot{E}_{Fuel} = \dot{E}_{hot in}^{PH} - \dot{E}_{hot out}^{PH} + \dot{E}_{cold in}^M - \dot{E}_{cold out}^M + \dot{E}_{cold in}^{CH} - \dot{E}_{cold out}^{CH} \quad (5.22)$$

$$\dot{E}_{Prod} = \dot{E}_{cold out}^{TH} - \dot{E}_{cold in}^{TH} + \dot{E}_{hot out}^{CH} - \dot{E}_{hot in}^{CH} \quad (5.23)$$

$$BPV \dot{E}_{Fuel} = \dot{E}_{in}^{TOTAL} \quad (5.24)$$

$$\dot{E}_{Prod} = \dot{E}_{out}^{TOTAL} \quad (5.25)$$

$$\text{TURB } \dot{E}_{\text{Fuel}} = \dot{E}_{\text{in}}^{\text{PH}} - \dot{E}_{\text{out}}^{\text{PH}} \quad (5.26)$$

$$\dot{E}_{\text{Prod}} = \dot{W}_{\text{turbine}} + \dot{E}_{\text{out}}^{\text{TH}} + \dot{E}_{\text{out}}^{\text{CH}} - \dot{E}_{\text{in}}^{\text{CH}} \quad (5.27)$$

$$\text{COMP} \dot{E}_{\text{Fuel}} = \dot{W}_{\text{compressor}} + \dot{E}_{\text{in}}^{\text{CH}} - \dot{E}_{\text{out}}^{\text{CH}} \quad (5.28)$$

$$\dot{E}_{\text{Prod}} = \dot{E}_{\text{out}}^{\text{PH}} - \dot{E}_{\text{in}}^{\text{PH}} \quad (5.29)$$

$$\text{WS} \dot{E}_{\text{Fuel}} = \dot{E}_{\text{in}}^{\text{TOTAL}} \quad (5.30)$$

$$\dot{E}_{\text{Prod}} = \dot{E}_{\text{out}}^{\text{TOTAL}} + \dot{E}_{\text{water out}}^{\text{TOTAL}} \quad (5.31)$$

$$\text{HUM} \dot{E}_{\text{Fuel}} = \dot{E}_{\text{in}}^{\text{TOTAL}} + \dot{E}_{\text{water in}}^{\text{TOTAL}} \quad (5.32)$$

$$\dot{E}_{\text{Prod}} = \dot{E}_{\text{out}}^{\text{TOTAL}} \quad (5.33)$$

The governing equation for the exergy balance of the MHX on cruise mission is different than Eqs. (5.16) and (5.17), since the inlet and outlet temperatures of each fuel and product stream are positioned differently than the other cases. Ram air parameters are below the reference point parameters.

To discuss the possible potential of improvements on components, the exergetic improvement potential rate should be calculated. This potential is expressed as (Van Gool 1992) the following:

$$\text{Improvement potential} = (1 - \eta_r) (\dot{E}_{\text{fuel}} - \dot{E}_{\text{product}}) \quad (5.34)$$

All the governing equations for exergy analysis and exergy balances are constructed from references (Bejan et al. 1996; Lazzaretto and Tsatsaronis 2006; Bejan 2016; Morusuk and Tsatsaronis).

5.1.4 Results

Turbine and compressor polytropic and isentropic efficiencies of such refrigeration are calculated and given in Tables 5.7 and 5.8. The results of the thermodynamic calculation of each fluid stream, consisting of the temperature and pressure values, and mass flow rates of each stream are shown in Table 5.9.

Table 5.7 Polytropic and isentropic efficiencies of the turbine and compressor

| | Polytropic efficiencies % | | | | Isentropic efficiencies % | | | |
|-------------------|---------------------------|-----------|-----------|-----------|---------------------------|-----------|-----------|-----------|
| | <i>TO</i> | <i>CR</i> | <i>LA</i> | <i>TX</i> | <i>TO</i> | <i>CR</i> | <i>LA</i> | <i>TX</i> |
| Compressor | 90 | 90 | 90 | 90 | 89,54 | 89,72 | 89,62 | 89,54 |
| Turbine | 90 | 81,5 | 90 | 90 | 90,91 | 83,54 | 90,91 | 90,91 |

Table 5.8 Turbine and compressor net powers

| | Generator and motor power (kW) | | | | Shaft net power (kW) | | | |
|-------------------------------|--------------------------------|-----------|-----------|-----------|----------------------|-----------|-----------|-----------|
| | <i>TO</i> | <i>CR</i> | <i>LA</i> | <i>TX</i> | <i>TO</i> | <i>CR</i> | <i>LA</i> | <i>TX</i> |
| Compressor | 17,3 | 10,89 | 14,05 | 17,3 | 10,59 | -6,85 | -13,84 | 10,59 |
| Turbine | 27,98 | 17,48 | 27,98 | 27,98 | | | | |
| Spec. Total misc. aux. | 0,096 | 0,1748 | 0,1251 | 0,096 | | | | |

The turbine and compressor net power output and inputs are shown in Table 5.8.

The ambient parameters are equal with the ram air initial parameters; the source of the ram air is directly the surrounding air. The bleed air initial temperature is set to be 498,75 K, since the stability of inlet temperature is related to the position of extraction from different stages of the gas turbine compressor, where it usually ranges between the fifth and thirteenth stages of the compressor in commercial aircraft. The effect of the water extraction can be seen at the stream parameters of the R1 and R2 path. Ram air relative humidity ratio is increased with water injection, and even though liquid water has a higher temperature than the ram airstream, it increases the cooling capacity of ram air, enhancing the cooling effect in heat exchangers. The mass flow rate of the bleed airstream decreases at cruise even though the bleed air extraction stage stays the same, since the air is less dense than the other flight environment. Another important aspect of determining the initial temperature is determining the outlet temperature of the system for the ventilation air requirements. It is done with the concern of satisfying the requirements of engineering standards to satisfy thermal comfort in the cabin and the pressurization mission of the ACM. The outlet temperature of the stream, which goes to the mixing manifold, is assumed to be around 19 °C, and the pressure gage is set to 77 kPa, to satisfy the required parameters as stated in the HVAC standards (ASHRAE Handbook 2015).

After obtaining the thermodynamic properties, the total amount of exergy flow as thermal exergy, mechanical exergy, and chemical exergy is calculated for each flow path. The amount of exergy destruction rate of components, exergetic efficiency, and exergy destruction ratio of each component related to the total exergy destroyed

Table 5.9 Fluid stream temperature and pressure values

| | | Temperature (K) | | | | Pressure (kPa) | | | | Mass flow rate (kg/s) | | | |
|-----------------------|--|-----------------|--------|--------|--------|----------------|-------|-------|--------|-----------------------|-------|--------|-------|
| | | TO | CR | LA | TX | TO | CR | LA | TX | TO | CR | LA | TX |
| Flight mission | | | | | | | | | | | | | |
| Bleed air | | | | | | | | | | | | | |
| 1 | | 498,75 | 498,75 | 498,75 | 498,75 | 169,4 | 187 | 180 | 169,4 | 0,6 | 0,49 | 0,6 | 0,6 |
| 2 | | 378,15 | 388,15 | 378,15 | 378,15 | 167,7 | 178,2 | 178,2 | 167,7 | 0,6 | 0,49 | 0,6 | 0,6 |
| 3 | | 378,15 | 388,15 | 378,15 | 378,15 | 167,7 | 178,2 | 178,2 | 167,7 | 0,4 | 0,294 | 0,4 | 0,42 |
| 4 | | 420,42 | 414,78 | 412,52 | 420,42 | 235,1 | 220 | 235,1 | 235,1 | 0,4 | 0,294 | 0,4 | 0,42 |
| 5 | | 311 | 304,33 | 311 | 311 | 230,5 | 217,8 | 230,5 | 230,5 | 0,4 | 0,294 | 0,4 | 0,42 |
| 6 | | 298,45 | 297,06 | 298,45 | 298,45 | 223,1 | 215,6 | 223,1 | 223,1 | 0,4 | 0,294 | 0,4 | 0,42 |
| 7 | | 291,06 | 294,29 | 291,06 | 291,06 | 217,9 | 213,4 | 217,9 | 217,9 | 0,4 | 0,294 | 0,4 | 0,42 |
| 8 | | 291,06 | 294,29 | 291,06 | 291,06 | 217,9 | 213,4 | 217,9 | 217,9 | 0,398 | 0,294 | 0,399 | 0,418 |
| 9 | | 308,22 | 301,54 | 308,22 | 308,22 | 210,7 | 211,2 | 210,7 | 210,7 | 0,398 | 0,294 | 0,399 | 0,418 |
| 10 | | 251,8 | 240,12 | 251,8 | 251,8 | 79 | 79,2 | 79 | 79 | 0,398 | 0,294 | 0,399 | 0,418 |
| 11 | | 285,56 | 291,5 | 285,56 | 285,56 | 79 | 79,2 | 79 | 79 | 0,598 | 0,49 | 0,599 | 0,598 |
| 12 | | 295,67 | 293,31 | 295,67 | 295,67 | 77 | 77 | 77 | 77 | 0,598 | 0,49 | 0,599 | 0,598 |
| Ram air | | | | | | | | | | | | | |
| R1 | | 281,7 | 216,85 | 249,2 | 288,1 | 89,86 | 21,7 | 47,19 | 101,28 | 1,21 | 0,42 | 1,14 | 1032 |
| R2 | | 277,99 | 216,85 | 248,64 | 283,83 | 87,26 | 21,7 | 45,88 | 98,67 | 1212 | 0,42 | 1141 | 1,03 |
| R3 | | 316,09 | 301,2 | 280,98 | 322,42 | 86,4 | 19,53 | 45,43 | 97,7 | 1212 | 0,42 | 1141 | 1032 |
| R4 | | 380,38 | 431,37 | 345,59 | 386,59 | 85,54 | 19,53 | 44,98 | 96,73 | 1212 | 0,42 | 1141 | 1032 |
| Bypass valve | | | | | | | | | | | | | |
| B1 | | 378,15 | 388,15 | 378,15 | 378,15 | 167,7 | 178,2 | 178,2 | 167,7 | 0,2 | 0,196 | 0,2 | 0,18 |
| B2 | | 378,15 | 388,15 | 378,15 | 378,15 | 79 | 79,2 | 79 | 79 | 0,2 | 0,196 | 0,2 | 0,18 |
| Liquid water | | | | | | | | | | | | | |
| W1 | | 292,12 | 294,29 | 294,12 | 295,12 | 217,9 | 213,4 | 217,9 | 217,9 | 0,002 | 0 | 0,0014 | 0,001 |

is calculated, and the results are presented in Table 5.10. The total exergy flow for each component is presented in Table 5.11.

The exergy destruction ratio of each component is shown in Fig. 5.7.

The exergetic improvement potential ratio for each component is shown in Fig. 5.8

The primary heat exchanger, main heat exchanger, and the bypass valve are the greatest source of exergy destruction for air refrigeration system during flight missions. For landing operation, the primary heat exchanger creates a significant amount of exergy destruction, as is the primary source of it, followed by the main heat exchanger and bypass valve. For the cruise mission, the main heat exchanger is the greatest source of exergy destruction, followed by BPV and PHX. The bypass valve covers the second and third largest exergy destruction sources in general. The bypass valve is not working as an expansion valve, which cools the fluid by changing the pressure, but as a flow regulation valve to differentiate the temperature to the desired level during flight. The regulation effect will result in a pressure drop, so on the stream, this pressure drop is a desirable outcome of these components, but pressure drop leads to crucial amounts of exergy destruction. Further improvements on this component are not about exergy destruction, since this is a natural outcome by using the regulation valve. The main focus on exergy destruction should be on the PHX and MHX in this regard. Water separator and humidifier have full efficiency and zero exergy destruction on the cruise since there is no humidity present in the bleed airstream

Despite the exergy destruction ratio for the PHX and MHX being the two largest destruction sources to be considered, the improvement potential ratio is considerably high, concerning the PHX for taxi and landing missions. The MHX has the greatest potential for improvement and optimization, since it is the regeneration equipment for heat transfer. The MHX maintains the heat balance by the effect of both turbine and the compressor quite directly, since the pressure differences are playing the greatest role on this component to operate at the desired efficiency level. This is a result of each fuel and product streams being the bleed air but not another coolant. If the fuel stream gets affected by any kind of temperature evaluation, it directly reflects the effects on the product as well. This leads to a solution based on the pressure of streams and pressure ratios of the turbine and the compressor of the system. In this regard, their operation is crucial to improve the MHX.

Even though the BPV had the second greatest exergy destruction ratio, it is easily seen that the improvement potential is not such high as the MHX and PHX, as a result of this equipment working principle.

Compressor and turbine improvement potentials differ by flight missions, showing no similarities compared to each operation. This is because the ambient air has different conditions, leading to a heat sink with different characteristics. To be able to adapt, the system has to control the dynamic equipment such as the turbine and compressor. For various ambient conditions, these components will perform their duty to pressurize the air refrigeration system to a required level. As a consequence, the improvement potential differs by flight missions, since the operation of these components differs as well.

Table 5.10 Amount of exergy destruction rate of components, their exergetic efficiency, and exergy destruction ratio of each component related to the total exergy destroyed

| | Exergy destruction [kW] | | | | Exergetic efficiency | | | | Exergy dest. Ratio (tot. Dest.) | | | |
|------|-------------------------|--------|--------|-------|----------------------|-------|-------|-------|---------------------------------|-------|-------|-------|
| | TO | CR | LA | TX | TO | CR | LA | TX | TO | CR | LA | TX |
| PHX | 9,74 | 7931 | 16,93 | 13,21 | 0,752 | 0,737 | 0,568 | 0,662 | 0,269 | 0,219 | 0,467 | 0,364 |
| COMP | 0,712 | 3303 | 3286 | 0,145 | 0,959 | 0,697 | 0,803 | 0,992 | 0,020 | 0,091 | 0,091 | 0,004 |
| BPV | 9549 | 10,02 | 10,320 | 8594 | 0,718 | 0,711 | 0,702 | 0,718 | 0,263 | 0,276 | 0,285 | 0,237 |
| TURB | 2349 | 3800 | 2359 | 4062 | 0,920 | 0,824 | 0,920 | 0,869 | 0,065 | 0,105 | 0,065 | 0,112 |
| MHX | 10,793 | 10,657 | 14,903 | 8691 | 0,530 | 0,326 | 0,297 | 0,562 | 0,298 | 0,294 | 0,411 | 0,240 |
| RHX | 0,108 | 0,397 | 0,108 | 0,120 | 0,965 | 0,588 | 0,965 | 0,963 | 0,003 | 0,011 | 0,003 | 0,003 |
| CON | 0,992 | 1049 | 0,992 | 1078 | 0,574 | 0,175 | 0,574 | 0,551 | 0,027 | 0,029 | 0,027 | 0,030 |
| WS | 0,872 | 0,000 | 0,872 | 0,900 | 0,986 | 1000 | 0,986 | 0,986 | 0,024 | 0,000 | 0,024 | 0,025 |
| HUM | 1134 | 0,000 | 0,493 | 2844 | 0,990 | 1000 | 0,991 | 0,974 | 0,031 | 0,000 | 0,014 | 0,078 |

Table 5.11 The total amount of exergy flow as thermal exergy, mechanical exergy, chemical exergy, and total exergy for each flow path

| Σ Total mech. ex. [kW] | | | | Σ Total th. exergy [kW] | | | | Σ Total ch. ex. MD I [kW] | | | | Σ Total exergy [kW] | | | | |
|-------------------------------|---------|--------|--------|--------------------------------|--------|--------|--------|----------------------------------|--------|--------|--------|----------------------------|---------|---------|---------|---------|
| TO | CR | LA | TX | TO | CR | LA | TX | TO | CR | LA | TX | TO | CR | LA | TX | |
| <i>Bleed air</i> | | | | | | | | | | | | | | | | |
| 1 | 78,139 | 66,455 | 80,449 | 78,139 | 62,233 | 50,341 | 62,233 | 62,233 | 0,004 | -0,328 | 0,004 | -0,328 | 140,044 | 116,799 | 142,354 | 140,044 |
| 2 | 77,755 | 64,966 | 80,066 | 77,755 | 24,142 | 21,695 | 24,142 | 24,142 | 0,004 | -0,328 | 0,004 | -0,328 | 101,569 | 86,665 | 103,880 | 101,569 |
| 3 | 51,837 | 38,980 | 53,378 | 54,428 | 16,095 | 13,017 | 16,095 | 16,900 | 0,002 | -0,219 | 0,002 | -0,219 | 67,713 | 51,999 | 69,254 | 71,098 |
| 4 | 60,408 | 42,884 | 60,408 | 63,429 | 24,061 | 16,699 | 22,488 | 25,264 | 0,002 | -0,219 | 0,002 | -0,219 | 84,251 | 59,586 | 82,678 | 88,463 |
| 5 | 59,907 | 42,698 | 59,907 | 62,902 | 6089 | 3866 | 6089 | 6394 | 0,002 | -0,219 | 0,002 | -0,219 | 65,778 | 46,566 | 65,778 | 69,066 |
| 6 | 59,079 | 42,510 | 59,079 | 62,033 | 4655 | 3283 | 4655 | 4888 | 0,002 | 0,911 | 0,002 | 0,911 | 64,037 | 45,795 | 64,037 | 67,233 |
| 7 | 58,481 | 42,320 | 58,481 | 61,405 | 3884 | 3072 | 3884 | 4078 | 0,002 | 0,745 | 0,002 | 0,745 | 62,517 | 45,394 | 62,517 | 65,626 |
| 8 | 58,012 | 42,320 | 58,012 | 60,927 | 3853 | 3072 | 3853 | 4046 | 0,002 | -0,257 | 0,002 | -0,257 | 61,608 | 45,394 | 61,608 | 64,704 |
| 9 | 57,166 | 42,128 | 57,166 | 60,039 | 5705 | 3638 | 5705 | 5992 | 0,002 | -0,257 | 0,002 | -0,257 | 62,615 | 45,768 | 62,615 | 65,761 |
| 10 | 32,476 | 23,954 | 32,476 | 34,107 | 0,860 | 0,266 | 0,860 | 0,903 | 0,002 | 0,910 | 0,002 | 0,910 | 33,625 | 24,222 | 33,625 | 35,315 |
| 11 | 48,844 | 39,924 | 48,844 | 48,844 | 5002 | 4774 | 5002 | 5002 | 0,004 | -0,387 | 0,004 | -0,387 | 53,459 | 44,701 | 53,459 | 53,459 |
| 12 | 47,873 | 39,054 | 47,873 | 47,873 | 6502 | 4997 | 6502 | 6502 | 0,004 | -0,387 | 0,004 | -0,387 | 53,988 | 44,054 | 53,988 | 53,988 |
| <i>Ram air</i> | | | | | | | | | | | | | | | | |
| R1 | 108,521 | -0,049 | 55,701 | 100,459 | 9031 | 0,007 | 2090 | 9246 | -0,013 | -0,779 | -0,013 | -0,214 | 116,772 | -0,055 | 57,576 | 109,002 |
| R2 | 106,564 | -0,049 | 53,830 | 98,669 | 8079 | 0,007 | 2020 | 8207 | -0,013 | 2922 | -0,013 | 3047 | 115,675 | -0,055 | 57,120 | 106,181 |
| R3 | 105,805 | -2838 | 53,119 | 98,214 | 20,268 | 5158 | 8324 | 19,368 | -0,013 | -0,827 | -0,013 | -0,549 | 125,246 | 2307 | 60,894 | 116,887 |
| R4 | 105,038 | -2838 | 52,402 | 97,562 | 49,765 | 27,362 | 30,582 | 45,285 | -0,013 | -0,827 | -0,013 | -0,549 | 153,976 | 24,511 | 82,434 | 142,152 |
| <i>Bypass valve</i> | | | | | | | | | | | | | | | | |
| B1 | 25,918 | 25,987 | 26,689 | 23,326 | 8047 | 8678 | 8047 | 7243 | 0,001 | -0,109 | 0,001 | -0,109 | 33,856 | 34,666 | 34,627 | 30,471 |
| B2 | 16,369 | 15,970 | 16,369 | 14,732 | 8047 | 8678 | 8047 | 7243 | 0,001 | -0,109 | 0,001 | -0,109 | 24,307 | 24,649 | 24,307 | 21,876 |
| <i>Liquid water</i> | | | | | | | | | | | | | | | | |
| W1 | 0,000 | 0,000 | 0,000 | 0,000 | 0,000 | 0,000 | 0,000 | 0,000 | 0,000 | 0,010 | 0,000 | 0,010 | 0,037 | 0,000 | 0,037 | 0,022 |

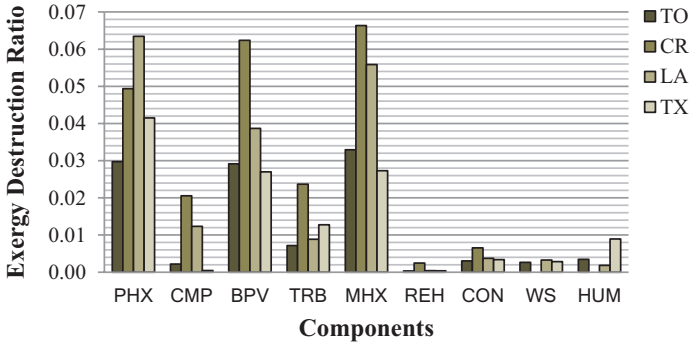


Fig. 5.7 Exergy destruction ratio of each component on four different flight missions

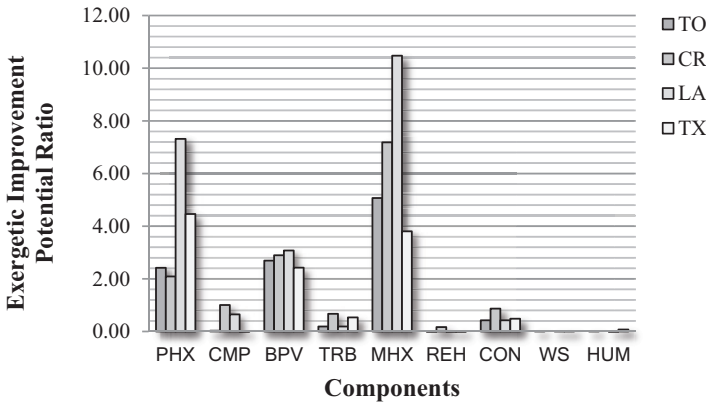


Fig. 5.8 Exergetic improvement potential ratio of each component on four different flight missions

Ayaz et al. (2018) stated that the largest exergy destruction happens to be in the secondary heat exchanger, which has identical objectives with the MHX represented here, under the same reference values.

The exergy values of each flow path are close to the cruise mission where the dead state has the same reference point with an analysis taken here (Bender 2016) and the temperature values are nearly identical. It was stated that in the cruise mode, the highest exergy destruction rate will occur in the bypass valve, main heat exchanger, turbine, and primary heat exchanger as indicated in this work. In this study, the turbine and compressor work are evaluated for the required outputs of the system. This leads to a theoretical component suitable for air refrigeration, but the performance of such a component is restricted by the system requirement restrictions, since some output parameters are strictly set to the safety and to the cause of preventing hazardous situations for passengers and cabin crew. Bypass valve inefficiency is also parallel to this work. It is always in the first third of most inefficient equipment regardless of the flight operation environmental states. Therefore, differences in the amount of exergy and exergy destruction occur because of the difference in reference state taken as the dead state point for exergy analysis.

5.1.5 Conclusion

As many scholars stated before, aircraft systems need to be a subject of optimization and improvement, since it has a limited amount of energy it carries within. This energy comes from the aircraft fuel, and fuel consumption efficiency has many effects on the overall efficiency. Higher efficiency will cause the airplane to be able to go for longer missions as it decreases the consumption of the components for its operation. In addition to these, the achievement of the aviation industry's sustainability targets is in-line with these developments.

In this regard, exergy analysis is performed on a conventional air cycle machine. To conduct this analysis, the utmost important standard requirements such as mixing manifold pressure and outlet temperature of the system are considered to be set as the objective parameters to be reached by the system operation. Component efficiencies, component effectiveness, and turbine and compressor work are evaluated values for this purpose. This leads to a possible optimized system for some components such as the turbine and compressor, since they are the driving force of the whole refrigeration cycle along with the coolant ram air. Although these are the ideal components of thermodynamic analysis and design, heat exchanger work and conditions lead to important improvement potentials. By using the exergy analysis data set, improvement potentials are calculated and compared to the exergy destruction ratio of the corresponding element. In conclusion, exergy analysis is performed to examine the inefficiencies that might occur in four different flight missions. The results are compared to some studies with similar parameters. Exergy destruction ratios and exergetic efficiencies of every single component are represented along with the exergy improvement potential ratios. The least efficient components are pointed out for optimization purposes. The ACM is a strongly dependent machine on the performance of each component, since these all affect each other intensively during the flight operation.

References

- Acikkalp, E., Hepbasli, A., Yucer, C.T., Karakoc, T.H.: Advanced exergoenvironmental assessment of a building from the primary energy transformation to the environment. *Energ. Buildings.* **89**, 1–8 (2015)
- Agnew, B., Anderson, A., Potts, I., Frost, T.H., Alabdoadaim, M.A.: Simulation of combined Brayton and inverse Brayton cycles. *Appl. Therm. Eng.* **23**(8), 953–963 (2003)
- Alison, B.: Evans, the Effects of Compressor Seventh-Stage Bleed Air Extraction on Performance of the F100-PW-220 Afterburning Turbofan Engine, NASA Contractor Report 179447. Dryden Flight Research Facility, Edwards (1991)
- Altuntas, O., Karakoc, T.H., Hepbasli, A.: Exergoenvironmental analysis of piston-prop aircrafts. *Int. J. Exergy.* **10**(3), 290–298 (2012)
- ASHRAE Handbook: HVAC Applications, American Society of Heating, Refrigerating and Air-Conditioning Engineers, Inc., Atlanta (2015)

- Ayaz, S.K., Altuntaş, Ö., Acıkkalp, E., Karakoc, T.H.: Exergy and energy analysis of an aircraft air cycle machine at designated altitude. In: Aloui, F., Dincer, I. (eds.) *Exergy for a Better Environment and Improved Sustainability 1. Green Energy and Technology*. Springer, Cham (2018)
- Balmer, R.T.: Vapor and Gas Refrigeration Cycles, pp. 535–590. *Modern Engineering Thermodynamics*, Academic Press (2011)
- Bejan, A.: *Advanced Engineering Thermodynamics*. John Wiley & Sons, Inc., Hoboken (2016)
- Bejan, A., Siems, D.L.: The need for exergy analysis and thermodynamic optimization in aircraft development. *Exergy, An Int. J.* **1**(1), 14–24 (2001)
- Bejan, A., Tsatsaronis, G., Moran, M.J.: *Thermal Design and Optimization*. A Wiley – Interscience Publication. Wiley, New York (1996)
- Bender, D.: Exergy-Based Analysis of Aircraft Environmental Control Systems – Integration into Model-Based Design and Potential for Aircraft System Evaluation, Proceedings of ECOS 2016 – The 29th International Conference on Efficiency, Cost, Optimization, Simulation and Environmental Impact of Energy Systems, June 19–23 2016
- Bender, D.: Integration of exergy analysis into model-based design and evaluation of aircraft environmental control systems. *Energy*. **137**, 739–751 (2017)
- Chen, L., Zhang, X., Wang, C., Yang, C.: A novel environmental control system facilitating humidification for commercial aircraft. *Build. Environ.* **126**, 34–41 (2017)
- Coban, K., Söhret, Y., Colpan, C.O., Karakoc, T.H.: Exergetic and exergoeconomic assessment of a small-scale turbojet fuelled with biodiesel. *Energy*. **140**, 1358–1367 (2017)
- Dechow, M., Nurcombe, C.A.H.: Aircraft environmental control systems. In: *Air Quality in Airplane Cabins and Similar Enclosed Spaces*, vol. 4H, pp. 3–24. Springer, Heidelberg (2005)
- Dhillon, A. K., Dutta, R., Ghosh, P.: Exergetic analysis of reverse brayton cryocooler for different cooling loads at 65 K for HTS cables, *Cryogenics* 2017. Proceedings of the 14th IIR International Conference: Dresden, Germany, May 15–19, 2017
- Ekici, S., Yalin, G., Altuntas, O., Karakoc, T.H.: Calculation of HC, CO and NOx from civil aviation in Turkey in 2012. *Int. J. Environ. Pollut.* **53**(3–4), 232–244 (2013)
- Ekici, S., Altuntas, O., Acıkkalp, E., Sogut, M.Z., Karakoc, T.H.: Assessment of thermodynamic performance and exergetic sustainability of turboprop engine using mixture of kerosene and methanol. *Int. J. Exergy*. **19**(3), 295–314 (2016)
- Ekici, S., Söhret, Y., Coban, K., Altuntas, O., Karakoc, T.H.: Performance evaluation of an experimental turbojet engine. *Int. J. Turbo & Jet-Engines*. **34**(4), 365–375 (2017)
- Ertesvåg, I.S.: Sensitivity of chemical exergy for atmospheric gases and gaseous fuels to variations in ambient conditions. *Energy Convers. Manag.* **48**(7), 1983–1995 (2007)
- Feidt, M.: *Finite Physical Dimensions Optimal Thermodynamics 1*, pp. 169–214. Elsevier (2017)
- Goodarzi, M.: Usefulness analysis on regenerator and heat exchanger in Brayton & inverse Brayton cycles at moderate pressure ratio operation. *Energy Convers. Manag.* **126**, 982–990 (2016)
- Hundy, G.F., Trott, A.R., Welch, T.C.: *Refrigeration and Air Conditioning*, B.H. Butterworth-Heinemann Linacre House, Jordan Hill (2000)
- Jennions, I., Ali, F., Miguez, M.E., Escobar, I.C.: Simulation of an aircraft environmental control system. *Appl. Therm. Eng.* **172**, 114925
- Kaya, N., Turan, Ö., Midilli, A., Karakoc, T.H.: Exergetic sustainability improvement potentials of a hydrogen fuelled turbofan engine UAV by heating its fuel with exhaust gasses. *Int. J. Hydrog. Energy*. **41**(19), 8307–8322 (2016). <https://doi.org/10.1016/j.ijhydene.2015.08.089>
- Lazzaretto, A., Tsatsaronis, G.: SPECO: a systematic and general methodology for calculating efficiencies and costs in thermal systems. *Energy*. **31**(8–9), 1257–1289 (2006)
- Leo, T.J., Pérez-Grande, I.: A Thermo-economic analysis of a commercial aircraft environmental control system. *Appl. Therm. Eng.* **25**(2–3), 309–325 (2005)
- Logan Jr., E.: *Thermodynamics: Processes and Applications*. Marcel Dekker, Inc., New York (1999)
- Ma, Z., Zhang, X., Wang, C., Yang, H., Yang, C.: Study on ground-test simulation method of the ram air for commercial airliners' environmental control system. *Procedia Eng.* **121**, 325–332 (2015)

- Morosuk, T., Tsatsaronis, G.: Strengths and Limitations of Advanced Exergetic Analyses. In: ASME 2013 International Mechanical Engineering Congress and Exposition; 2013
- Santos, A., Andrade, C., Zaparoli, E.: A thermodynamic study of air cycle machine for aeronautical applications. *Int. J. Thermodyn.* **17**, 117–125 (2014)
- Sforza, P.: Refined Weight and Balance Estimate. *Commercial Airplane Design Principles*. (2014), pp. 301–347. doi:<https://doi.org/10.1016/b978-0-12-419953-8.00008-5>
- Sisto, F.: The reversed Brayton cycle heat pump – a natural open cycle for HVAC application. *ASME. J. Eng. Power.* **101**(1), 162–167 (1979, January 1)
- Söhret, Y., Sogut, M.Z., Karakoc, T.H., Turan, O.: Customised application of exergy analysis method to PW120A turboprop engine for performance evaluation. *Int. J. Exergy.* **20**(1), 48–65 (2016)
- Sun, J., et al.: A data-driven health indicator extraction method for aircraft air conditioning system health monitoring. *Chin. J. Aeronaut.* (2018)
- The Boeing 737 Technical Site – 737-400 Air Conditioning System Schematic Diagram, <http://www.b737.org.uk/schematic-ac400.htm>, Chris Brady, 1999 (Currently Available: 17.10.2020)
- Van Gool, W.: Exergy analysis of industrial processes. *Energy.* **17**(8), 791–803 (1992)
- Wanli, Z., Lingen, C., Fengrui, S.: Power and efficiency optimization for combined Brayton and inverse Brayton cycles. *Appl. Therm. Eng.* **29**(14–15), 2885–2894 (2009)
- Wright, S.J., Dixon-Hardy, D., Heggs, P.J.: Aircraft air conditioning heat exchangers and atmospheric fouling. *Therm Sci Eng Prog.* (2018)
- Yuan, W., Yang, B., Guo, B., Li, X., Zuo, Y., Hu, W.: A novel environmental control system based on membrane dehumidification. *Chin. J. Aeronaut.* **28**(3), 712–719 (2015)
- Zhao, H., Yu, H., Zhu, Y., Liang, C., Chen, S.: Experimental study on the performance of an aircraft environmental control system. *Appl. Therm. Eng.* **29**(16) (2009)

Chapter 6

Life Cycle Energy Assessment of European Airport Terminal Buildings According to Glass Facades



Okan Kon and Ismail Caner

Nomenclature

| | |
|------|--------------------------------------|
| HDD | Heating Degree-Day |
| CDD | Cooling Degree-Day |
| g | Gravitational acceleration |
| T | Temperature |
| Gr | Grasshof number |
| Ra | Raleigh number |
| Pr | Prandatl number |
| Nu | Nusselt Number |
| h | Convection heat transfer coefficient |
| U | Heat transfer coefficient |
| s | Air gap thickness |
| A | Surface area |
| c | Glass thickness |
| n | Number of glass layer |
| F | Radiation view factor |
| E | Energy load |
| COP | Coefficient of Performance |
| r | Real interest rate |
| g | Inflation rate |
| i | Interest rate |
| N | Life |
| PWF | Present Worth Factor |
| C | Price |
| LCET | Life Cycle Energy Total Cost |

O. Kon (✉) · I. Caner
Engineering Faculty Department of Mechanical Engineering, Balikesir University,
Balikesir, Turkey
e-mail: okan@balikesir.edu.tr; ismail@balikesir.edu.tr

Subscripts

| | |
|-----|---------------------|
| sr | surface |
| 0 | outdoor |
| i | indoor |
| H | heat |
| C | cool |
| ng | natural gas |
| e | electricity |
| ij | radiation surfaces |
| 2,3 | 2nd and 3rd surface |

Greek Symbols

| | |
|---------------|-----------------------------|
| ϑ | kinematic viscosity |
| β | film temperature |
| ε | emissivity |
| σ | stefan-boltzman constant |
| Φ | angle |
| λ | heat conduction coefficient |

6.1 Introduction

In addition to its aesthetics and economy, other functions expected from glass are precipitation, wind, dust, etc., protection against weather conditions, saving on energy costs by providing insulation against heat transfer, solar control, maximum utilization of daylight, and sound control. In the glass to be used in glass facade systems, attention should be paid to the climatic balance of the building, heating and cooling costs, light transmittance, solar energy transfer, heat transfer value, shading, and sound control (Atalay 2006).

In airport terminal buildings, it is important to create transparent and clear spaces, where the passenger can clearly understand where he/she is at all times by optimizing the daylight with a flexible and expandable structure, also easily understand the point to go, and therefore feel comfortable. Thus, the glass facade of the airport terminal buildings is an important feature (Ekoyapı dergisi 2019).

The aim of the study is to examine the life cycle energy assessment connected to the glazed facade of the airport terminal buildings in ten different cities in Europe. For this purpose, the overall heat transfer coefficient of the double-glazed facade has been calculated for 90°, 60°, and 30° angles. For these ten cities, heating degree-days and cooling degree-days were determined based on the indoor temperature values recommended in ASHRAE for the heating and cooling periods of the airport buildings. Fuel prices, such as natural gas and electricity, and economic parameters, such as inflation and interest, were taken from the European Union Statistics Office (Eurostat).

6.2 Methodology of the Study

6.2.1 Meteorological and Geographical Features of Selected European Cities

In Table 6.1, the heating and cooling degree-day, outdoor dry bulb temperature, and indoor temperature values of the cities in Europe taken from the ASHRAE standard are given. In Table 6.1, the geographical features of the selected European cities in the study taken from the ASHRAE standard are shown.

As seen in Table 6.1, the highest heating degree-day value for Helsinki was found to be 5643 when the indoor temperature was 22 °C for the airport buildings in ASHRAE among the ten selected cities in Europe. Helsinki is also the city with the highest outdoor dry bulb temperature (−22.8) °C. Athens, on the other hand, was identified as the city with the lowest heating degree-day value. For Athens, heating degree-day value is 1731, and outdoor dry bulb temperature is the lowest value with (1.6) °C. When the indoor temperature is taken as 24 °C for the cooling period in the airport buildings according to ASHRAE, the cooling degree-day value is determined as 471 for Athens. The lowest was found as 2 for Dublin. The change of degree-day values for heating and cooling is related to the geographical locations of the airport buildings given in Table 6.1.

6.2.2 Heat Transfer Coefficient Calculation for Glazed Facade

There is an air gap of 16 mm thickness between the two glasses in glass facade. The glass thickness on the outdoor side is 10 mm, and the glass thickness on the indoor side is 6 mm. This glass facade system is taken as an example of Izmir Adnan

Table 6.1 The heating and cooling degree-day, outdoor dry bulb temperature, and indoor temperature values of European cities (<https://www.degreedays.net/>, ASHRAE 2006, 2009, 2019)

| City | Heating degree-day (HDD ₂₂) | Cooling degree-day (CDD ₂₄) | Outdoor dry bulb temperature (°C) | Heating indoor temperature (°C) | Cooling indoor temperature (°C) |
|-----------|---|---|-----------------------------------|---------------------------------|---------------------------------|
| Zagreb | 3516 | 151 | −11.0 | 22 | 24 |
| Helsinki | 5643 | 42 | −22.8 | | |
| Athens | 1731 | 471 | 1.6 | | |
| Rome | 2449 | 274 | −1.2 | | |
| Madrid | 3182 | 393 | −4.2 | | |
| London | 3732 | 53 | −3.1 | | |
| Dublin | 4420 | 2 | −1.9 | | |
| Berlin | 4104 | 112 | −13.8 | | |
| Amsterdam | 3940 | 38 | −7.3 | | |
| Istanbul | 2289 | 261 | −2.6 | | |

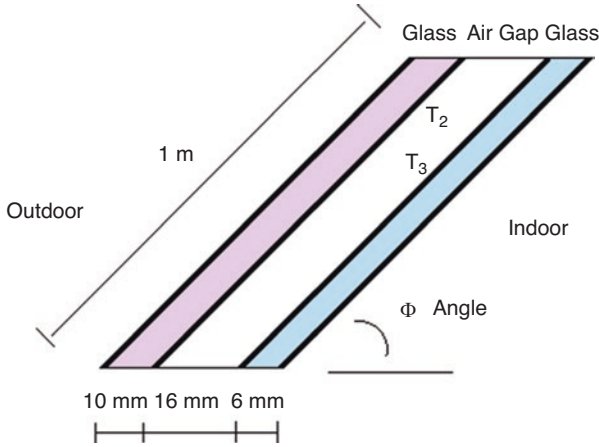


Fig. 6.1 Schematic representation of the glass facade

Menderes Airport Terminal Building in Turkey (Zeren 2010). The glass facade is shown schematically in Fig. 6.1.

The equations given below are used to find the convection heat transfer coefficient of the air gap for facades with multiple glasses (Al-Sibai et al. 2013; Çengel 2011).

Grashof number:

$$Gr = \frac{g \cdot s^3 \cdot \beta \cdot (T_{sr} - T_0)}{\nu^2} \tag{6.1}$$

Here, g is the gravitational acceleration, T_{sr} is the surface temperature, T_0 is the outdoor air temperature, ν is the kinematic viscosity, β is the film temperature, and s is the air gap thickness.

Rayleigh number:

$$Ra = Gr \cdot Pr \tag{6.2}$$

Here, Gr is the Grashof number and Pr is the Prandtl number. Table 6.2 shows the change of the Nusselt number, depending on the Rayleigh number used for heat transfer calculations in the glazed facade.

Convection heat transfer coefficient:

$$h = \frac{Nu \cdot \lambda_a}{s} \tag{6.3}$$

Overall heat transfer coefficient for multi-glazed facade (Arıcı and Kan 2015) (Karabay and Arıcı 2012):

Table 6.2 Nusselt number depending on the Rayleigh number used in calculations (Al-Sibai et al. 2013; Çengel 2011)

| Angle (Φ) | Rayleigh number | Nusselt number |
|------------------|--|---|
| 90 ° | $Ra < 10^3$ | $Nu = 1$ |
| | $10^3 < Ra < 10^4$ and $\frac{H}{s} < 83$ | $Nu = 0.38 Ra^{0.25} \left(\frac{H}{s}\right)^{-0.25}$ |
| | $10^4 < Ra < 10^7$ and $\frac{H}{s} < 83$ | $Nu = 0.42 Pr^{0.012} Ra^{0.25} \left(\frac{H}{s}\right)^{-0.25}$ |
| | $10^7 < Ra < 10^9$ | $Nu = 0.049 Ra^{0.33}$ |
| 30 °–60 ° | $Ra \cos \Phi < 2.5 \cdot 10^3$ | $Nu = 1$ |
| | $2.5 \cdot 10^3 < Ra \cos \Phi < 6 \cdot 10^3$ | $Nu = 1 + 1.21 \left[1 - \frac{2500}{Ra \cos \Phi} \right]$ |
| | $6 \cdot 10^3 < Ra \cos \Phi < 4 \cdot 10^5$ | $Nu = 0.199 (Ra \cos \Phi)^{0.258}$ |
| | $Ra \cos \Phi > 4 \cdot 10^5$ | $Nu = 0.0785 (Ra \cos \Phi)^{0.33}$ |

$$U_{GF} = \frac{1}{\frac{1}{h_i A} + \frac{c}{\lambda_{\text{glass}} A} + \frac{1}{(U_{2-3,\text{cond}} + U_{2-3,\text{conv}} + U_{2-3,\text{rad}}) + \frac{c}{\lambda_{\text{glass}} A} + \frac{1}{h_o A}}} \quad (6.4)$$

Here, $U_{2-3,\text{cond}}$ is the conduction heat transfer coefficient, $U_{2-3,\text{conv}}$ is the convection heat transfer coefficient, and $U_{2-3,\text{rad}}$ is the radiation heat coefficient between the inner surfaces of the outdoor glass (Arıcı and Kan 2015) (Karabay and Arıcı 2012):

$$U_{2-3,\text{cond}} = \frac{1}{\frac{s}{A\lambda_a} + (n-2) \left(\frac{c}{A\lambda_{\text{glass}}} + \frac{s}{A\lambda_a} \right)} \quad (6.5)$$

$$U_{2-3,\text{conv}} = \frac{1}{\frac{1}{h_o A} + (n-2) \left(\frac{1}{h_o A} \right)} \quad (6.6)$$

$$U_{2-3,\text{rad}} = \frac{1}{\frac{2(1-\varepsilon)}{(A\varepsilon)} + \frac{2(n-2)(1-\varepsilon)}{(A\varepsilon)} + \frac{(n-1)}{(F_{ij}A)}}} \cdot \frac{\sigma(T_2^4 - T_3^4)}{(T_2 - T_3)} \quad (6.7)$$

Here, n is the number of glass layer, s is the air gap thickness, A is the surface area, ε (taken as 0.84) is the emissivity, σ ($5.67 \cdot 10^{-8}$) is the Stefan-Boltzmann constant for uncoated glass window, and h_o is taken as $34 \text{ W/m}^2\cdot\text{K}$ and h_i is taken as $8.29 \text{ W/m}^2\cdot\text{K}$ for indoor and outdoor convection heat transfer coefficients, respectively. λ_{glass} is the heat conduction coefficient of glazed windows and taken as

$0.92 \text{ W/m}^2\cdot\text{K}$, $(1-\varepsilon)/(\varepsilon A)$ and $1/F_{ij}$ are the surface and radiation resistance, and F_{ij} is taken as 1. T_2 and T_3 are air gap surface temperatures, c is glass thickness, and λ_a is air's conduction heat transfer coefficient (Arıcı and Kan 2015; Karabay and Arıcı 2012; ASHRAE 2009).

6.2.3 Calculation of Energy Load and Life Cycle Energy Total Cost (LCET)

Annual heat energy load for the heating period (Samah et al. 2016; Kon and Caner 2020; Jraida et al. 2017):

$$E_H = \frac{0.024 \text{ U HDD}}{\eta} \quad (6.8)$$

Annual cool energy load for the cooling period:

$$E_C = \frac{0.024 \cdot \text{U} \cdot \text{CDD}}{\text{COP}} \quad (6.9)$$

Here, U-glass is the facade heat transfer coefficient, HDD is the heating degree-day, CDD is the cooling degree-day, η is the heating system efficiency (taken as 0.93), and COP (coefficient of performance; taken as 2.5) shows the cooling system performance value.

Calculation of present worth factor (PWF) (Dombayci et al. 2006):

If $i > g$ real interest rate,

$$r = \frac{i - g}{1 + g} \quad (6.10)$$

If $i < g$ real interest rate,

$$r = \frac{g - i}{1 + i} \quad (6.11)$$

Present worth factor:

$$\text{PWF} = \frac{(1+r)^N - 1}{r \cdot (1+r)^N} \quad (6.12)$$

where g is the inflation rate, i is the interest rate, and N (taken as 10 years) is the life.

Life cycle energy total cost equation (Samah et al. 2016; Kon and Caner 2020; Jraida et al. 2017):

$$LCET = (C_{ng} \cdot E_H + C_e \cdot E_C) \cdot PWF \tag{6.13}$$

6.3 Results and Discussion

As seen in Fig. 6.2, the highest heat transfer coefficient values are calculated as 3.029 W/m².K for 90° angled glazed facade and 3.166 W/m².K for 60° and 3.288 W/m².K for 30° angles. The lowest heat transfer coefficient values are calculated as 3.008 W/m².K for a 90° glazed facade, 3.052 W/m².K for 60°, and 3.208 W/m².K for 30°. The highest heat transfer coefficients for a glazed facade with an angle of 90°, 60°, and 30° are calculated for Helsinki. The lowest is calculated in Athens. The most important reason for this is that the outdoor dry bulb temperature value is the lowest for Helsinki and the highest outdoor dry bulb temperature value for Athens.

As given in Fig. 6.3, the highest values of heating energy load are calculated as 444.2 kWh/m² for 90° angled glazed facades, 464.3 kWh/m² for 60°, and 480.3 kWh/m² for 30°. Heating energy load minimum values are calculated as 134.4 kWh/m² for 90° glazed facades, 136.3 kWh/m² for 60°, and 143.3 kWh/m² for 30°. The highest heating energy load is calculated in Helsinki for 90°, 60°, and 30° angled glazed facades. The lowest is calculated in Athens.

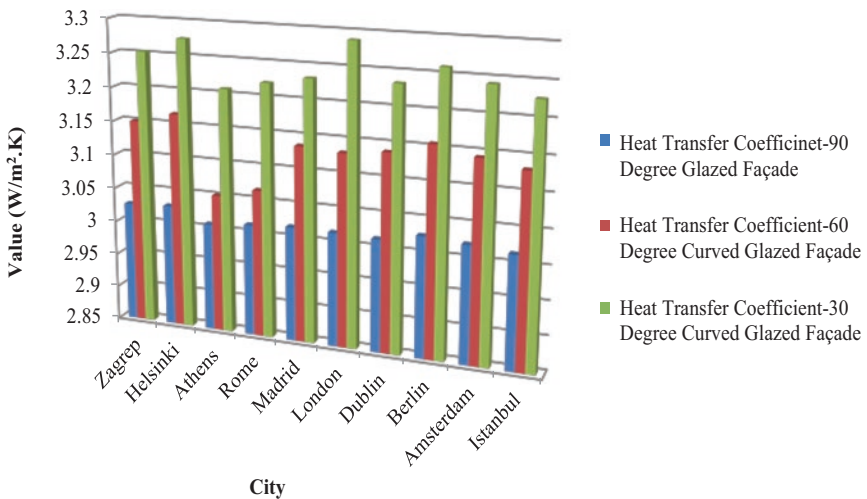


Fig. 6.2 Heat transfer coefficients in glass facades with different angles for European cities

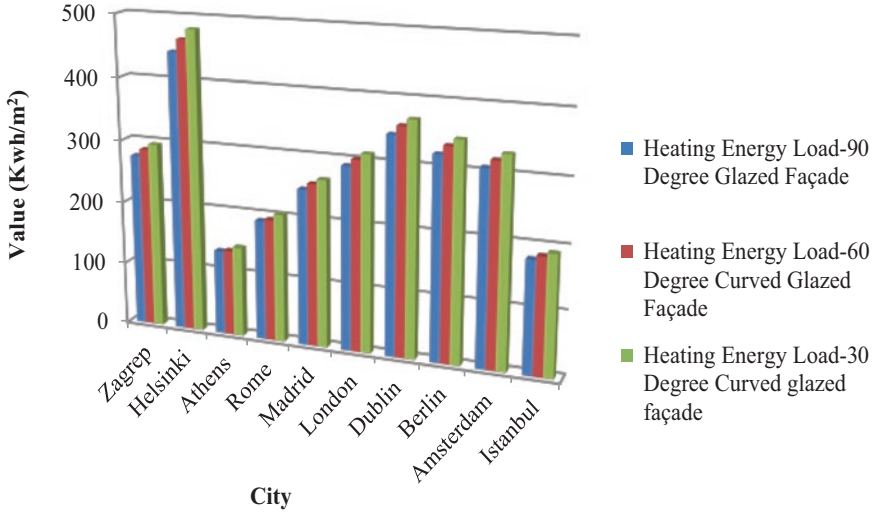


Fig. 6.3 Heating energy load on glass facades with different angles for European cities

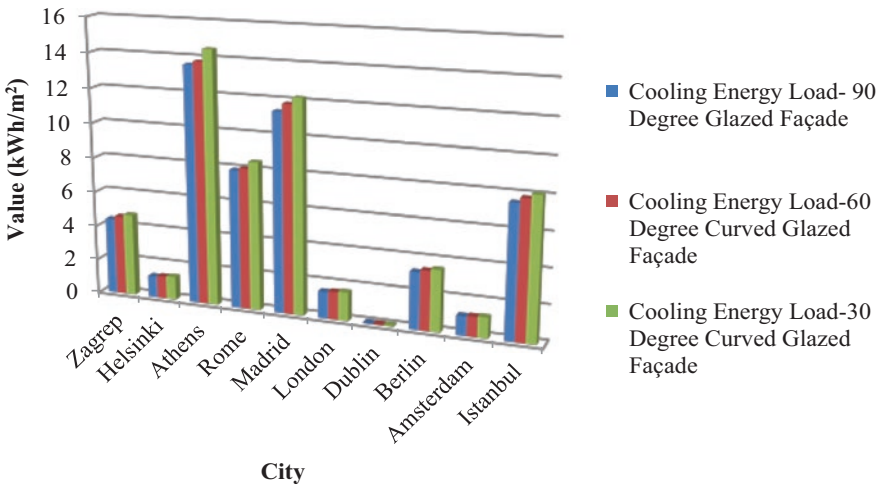


Fig. 6.4 Cooling energy load on glass facades with different angles for European cities

As seen in Fig. 6.4, the cooling energy load peak values are calculated as 13.6 kWh/m² for 90° angled glazed facades, 13.8 kWh/m² for 60°, and 14.5 kWh/m² for 30°. The cooling energy load minimum values are calculated as 0.058 kWh/m² for 90° glazed facades, 0.061 kWh/m² for 60°, and 0.062 kWh/m² for 30°. In contrast to the heating energy load, the highest cooling energy load is calculated in Athens for the 90°, 60°, and 30° glazed facades. The lowest is calculated in Helsinki.

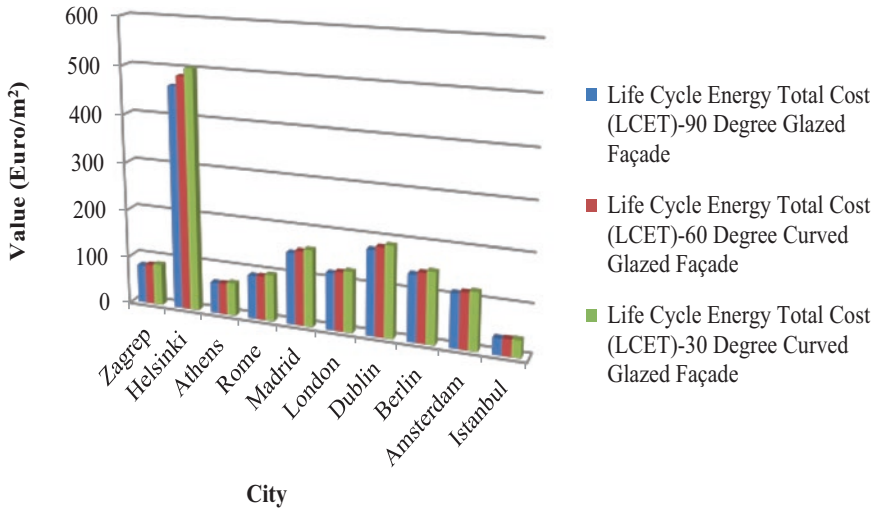


Fig. 6.5 Life cycle energy total cost (LCET) in glass facades with different angles for European cities

As described in Fig. 6.5, the highest values of life cycle energy total cost (LCET) are calculated as 464.5 euro/m² for 90° angled glazed facade, 485.5 euro/m² for 60° angle, and 502.3 euro/m² for 30° angle. The lowest life cycle total cost values are calculated as 33.6 euro/m² for a 90° angled glazed facade, 34.9 euro/m² for 60°, and 35.9 euro/m² for 30°. The highest life cycle total cost for 90°, 60°, and 30° angled glazed facades is calculated in Helsinki. The lowest is calculated in Istanbul.

Heating energy load: for the 90°, 60°, and 30° glazed facades, the highest was calculated in Helsinki and the lowest in Athens. Cooling energy load: for the 90°, 60°, and 30° glazed facades, the highest was calculated in Athens and the lowest in Helsinki. This is because the highest heat transfer coefficient value was determined for Helsinki and the lowest heat transfer coefficient value was determined for Athens.

The highest life cycle energy total cost (LCET) for 90°, 60°, and 30° angled glazed facades was calculated in Helsinki. The lowest is calculated in Istanbul. The most important reason for this is that electricity is used as an energy source in both heating and cooling periods in Helsinki. Electricity price is higher in euro per kWh. In Istanbul, the prices of natural gas are lower during the heating period and electricity prices during the cooling period. Fuel prices are given in Table 6.3.

As can be seen in Table 6.3, the unit price of natural gas used for the heating period in euros per kWh is Spain with the highest unit price of 0.0526 euro/kWh, while the lowest country is Turkey as 0.0178 euro/kWh. The unit price of electricity used for the cooling period in euros per kWh is 0.1873 euro/kWh, and Spain is the highest country, while the lowest country is Turkey at 0.0727 euro/kWh. However, Turkey is the country with the highest inflation and interest rates. The lowest country is Ireland.

Table 6.3 Unit price for natural gas and electricity and inflation and interest rates for European countries (based on the first half of 2018) <https://ec.europa.eu/eurostat/web/main/home>, (Eurostat 2018)

| Country | Natural gas price (Euro/kWh) | Electricity price (Euro/kWh) | Inflation rate (%) | Interest rate (%) |
|----------------------|------------------------------|------------------------------|--------------------|-------------------|
| Croatia | 0.0294 | 0.1020 | 1.60 | 2.70 |
| Finland ^a | – | 0.1074 | 1.22 | 0.66 |
| Greece | 0.0458 | 0.1132 | 0.80 | 4.19 |
| Italy | 0.0459 | 0.1285 | 1.20 | 2.61 |
| Spain | 0.0526 | 0.1873 | 1.70 | 1.42 |
| United Kingdom | 0.0425 | 0.1347 | 2.50 | 1.41 |
| Ireland | 0.0520 | 0.1846 | 0.70 | 0.95 |
| Germany | 0.0452 | 0.1379 | 1.90 | 0.40 |
| Netherlands | 0.0379 | 0.1187 | 1.60 | 0.58 |
| Turkey | 0.0178 | 0.0727 | 16.30 | 18.50 |

^aFinland does not use natural gas for heating

6.4 Conclusions

As the angle of inclination of the glass increases from 30° to 90° in the glass facades of the airport terminal buildings, the heat transfer coefficient of the glass decreases. In other words, the heat transfer coefficient of the glass facade at 90° is lower. It is higher at 30° inclinations. That is to say, as the angle of inclination increases, the heat transfer coefficient decreases. It is this feature that is desired. The important thing is to keep the heat transfer coefficient as low as possible.

In countries, such as Finland, geographically close to the North, the heating degree-day values, which are an important parameter for the heating period, are higher. On the other hand, the cooling degree-day values, which are an important parameter for the cooling period, are much lower. In Southern countries, such as Athens, Madrid, Rome, and Istanbul, close to the Mediterranean, the heating degree-day value is lower. On the other hand, the cooling degree-day values are higher.

The two most important parameters in heating energy and cooling energy load calculations are degree-day and heat transfer coefficient. Especially the degree-day value is more effective on these parameters. For this reason, the heating energy load has the highest value for Helsinki, which has the highest heating degree-day value.

In addition to the life cycle energy total cost (LCET) value, heating and cooling energy load, and energy prices, inflation and interest rates are other important parameters. Due to the fact that natural gas cannot be used during the heating period in countries such as Finland, and only electricity is used, this value was found to be the highest in Helsinki. In countries such as Turkey, where natural gas and electricity prices are relatively low, the total cost of life cycle energy (LCET) has been found to be lower.

References

- Al-Sibai, F., Hillemaier, B., Burghold, M., Kneer, R.: Untersuchung zur dämmwirkung von wärmedämm-materialien mit infrarot reflektierenden oberflächen. *Bauphysik*. **35**(4), 225–234 (2013)
- Arcı, M., Kan, M.: An investigation of flow and conjugate heat transfer in multiple pane windows with respect to gap width, emissivity and gas filling. *Renew. Energy*. **75**, 249–256 (2015)
- ASHRAE, Meteorological and Geographical Datas, (2006)
- ASHRAE, Chapter 3, Commercial and Public Buildings, (2019)
- ASHRAE, Chapter 15, Fenestration, (2009)
- Atalay, B.: Analysis of Aluminium Curtain Wall System Selection During Pre-Construction Phase. Istanbul Technical University, Institute of Science, Architecture Department, MS Thesis, Istanbul, Turkey, (2006)
- Çengel, Y.: A Practical Approach to Heat and Mass Transfer. Guven Kitabevi, Izmir (2011)
- Degree Days Calculated Accurately for Locations Worldwide
- Dombayci, O.A., Golcu, M., Pancar, Y.: Optimization of insulation thickness for external walls using different energy-sources. *Appl. Energy*. **83**(9), 921–928 (2006)
- Eurostat, Eurostat is the statistical office of the European Union, 2018 Datas
- Havalimani Mimarisi & Surdurulebilirlik, Ekoyapı dergisi, 07.24.2019. <https://www.ekoyapidergisi.org/6214-dosya-havalimani-mimarisi-surdurulebilirlik.html> (Date Accessed 10 Dec 2020)
- <https://ec.europa.eu/eurostat/web/main/home> (Date Accessed 10 Jan 2020)
- <https://www.degreedays.net/> (Date Accessed 10 Feb 2020)
- Jraida, K., Farchi, A., Mounir, B., Mounir, İ.: A study on the optimum insulation thickness of building walls respect to different zones in Morocco. *Int. J. Ambient Energy*. **38**(6), 550–555 (2017)
- Karabay, H., Arcı, M.: Multiple pane window applications in various climatic regions of Turkey. *Energ. Buildings*. **45**, 67–71 (2012)
- Kon, O., Caner, I.: Life Cycle Cost Analysis of the buildings in turkey related to energy consumption due to external wall insulation, *Environmentally-Benign Energy Solutions*. Cham: Springer International Publishing, 123–135. (2020)
- Samah, K., Alghoul, A.O., Gweshia, A.M.N.: The effect of electricity price on saving energy transmitted from external building walls. *Energy Res. J*. **7**(1), 1–9 (2016)
- Zeren, F. T. C.: Energy performance analysis of Adnan Menderes International Airport (ADM), Izmir Institute of Technology, MS Thesis, The Graduate School of Engineering and Sciences, Energy Engineering Department, Izmir, Turkey, (2010)

Chapter 7

An Overview of Aircraft Electric Power System for Sustainable Aviation



Halime Hizarci, Onur Demirel, Kemal Kalayci, and Ugur Arifoglu

Nomenclature

| | |
|-----------------|--|
| ABAC | Active bridge active clamp |
| ACARE | Advisory Council of Aviation Research |
| AEA | All-electric aircraft |
| ANPC | Active neutral point converter |
| ATRU | Auto-transformer rectifier unit |
| ATU | Auto-transformer unit |
| BDFM | Brushless doubly-fed machines |
| CO ₂ | Carbon dioxide |
| DAB | Dual active bridge |
| EMC | Electromagnetic compatibility |
| EMI | Electromagnetic interference |
| END | Environmental noise directive |
| EPA | Electric propulsion aircraft |
| EPS | Electric power system |
| FC | Fuel cells |
| GaN | Gallium nitride |
| GHG | Greenhouse gas |
| IATA | International Air Transport Association |
| IBCI | Interleaved boost with coupled inductors |
| IDG | Integrated drive generators |
| IEA | International Energy Agency |
| IGBT | Insulated-gate bipolar transistor |

H. Hizarci (✉) · O. Demirel · K. Kalayci · U. Arifoglu
Department of Electrical and Electronics Engineering, Sakarya University,
Serdivan, Sakarya, Turkey

Department of Electronics and Automation, Kırşehir Ahi Evran University, Kırşehir, Turkey
e-mail: hhizarci@sakarya.edu.tr

| | |
|-----------------|---|
| IM | Induction motor |
| MC | Matrix converter |
| MEA | More electric aircraft |
| MOSFET | Metal-oxide-semiconductor field-effect transistor |
| NASA | National Aeronautics and Space Administration |
| NO _x | Oxides of nitrogen |
| NPC | Neutral point clamped |
| NRA | NASA research announcement |
| PMSM | Permanent magnet synchronous machines |
| PWM | Pulse width modulation |
| RCTA | Radio Technical Commission for Aeronautics |
| RPDU | Remote power distribution units |
| SiC | Silicon carbide |
| SP | Specific power |
| SRM | Synchronous reluctance machines |
| SSPC | Solid-state power controllers |
| TMS | Thermal management systems |
| TNPC | T-type NPC |
| TRU | Transformer rectifier unit |
| VCSQC | Variable cross-section wet coil |
| VFG | Variable frequency generator |
| VSI | Voltage source inverter |
| WFSM | Wound field synchronous machine |

7.1 Introduction

Developments in the aviation industry in recent years have brought along a trend toward environmentally sustainable models and approaches. Considering that the environmental impacts of the fuels used in aircraft as well as being exhaustible, there is a need for a transition to a greener and more environmentally sensitive systems. Considering aviation industry in terms of fuel efficiency, emissions, and noise, a greener aviation is needed for sustainability.

Electrification is one of the approaches for reducing carbon emissions and sustainable green aviation. The most important motivation for the transition to electric aircraft is the environmental concerns caused by the greenhouse gas effects in recent years. As in many fields, several developments and innovations for more eco-friendly approaches are seen in the aviation industry, and they are appreciated for environmental sensitivity. It is seen that the emission growth of this sector will be given a different direction with the electric propulsion systems to be used in aviation. Electric propulsion systems, which open the door to new business models economically and reduce the fuel cost, will provide a quieter, safer, and environmentally cleaner transportation experience. In order to achieve the specified effects, high-energy-density battery technology, efficient system connection, electrical structure, and drive systems are needed.

Technological developments to be seen in electric aircraft in the future point the way of a greener aviation experience. Electric motors that are lighter, environmentally friendly, and easy-care can be used in place of conventional gas-powered engines. However, the factor limiting the electric aircraft technology is that the battery technology has not yet developed at the desired level. It is quite inefficient and poor in power density to provide the energy required for flight from batteries with the current technology.

This chapter gives an overview of the aircraft power systems and status of aircraft electrification from a technological point of view, considering environmental concerns. In the study, recent advancement in aircraft electric power systems is given; on the other hand, research and developments (R&D) projects for sustainable aviation are presented. In Sect. 7.1, environmental concerns about aviation sector are presented, and then, electric aircraft technology and issues for this technology are considered both in technical and environmental perspectives. Section 7.2 gives advance in technology electrical systems and aircraft propulsion systems. Power electronics converters and semiconductor technology are detailed in Sect. 7.3. Electric machine R&D concepts are presented in Sect. 7.4. Energy storage systems and thermal management issues are summarized in Sects. 7.5 and 7.6, respectively.

7.1.1 Environmental Effects of Aviation

Effects of aviation to the environment pave the way to make strict regulations on aircraft emissions. The National Aeronautics and Space Administration (NASA) and Advisory Council of Aviation Research (ACARE) have released requirements to meet environmental targets for a greener and sustainable aviation, and these targets are given in Table 7.1.

Table 7.1 Reduction goals of emissions and fuel burn according to the NASA and ACARE

| Goals | NASA (NASA 2015) | | | ACARE (Dareck et al. 2011) | |
|----------------------|---------------------|---------------------|---------------------|----------------------------|------------------------------|
| | NASA N + 1 (2015) | NASA N + 2 (2020) | NASA N + 3 (2025) | Vision 2020 ^a | Flightpath 2050 ^a |
| CO2 emission | – | – | – | –50% | –75% |
| Fuel burn | –33% ^b | –50% ^b | –60% ^b | – | – |
| Cruise NOx emissions | –55% ^b | –70% ^b | –80% ^b | –80% | –90% |
| LTO NOx emissions | –60% ^c | –75% ^c | –80% ^c | – | – |
| Noise | –32 dB ^d | –42 dB ^d | –71 dB ^d | –50% | –65% |

^aRelative to new aircraft capabilities of year 2000

^bRelative to new aircraft capabilities of year 2005

^cRelative to ICAO Aviation Environmental Protection (CAEP) 6

^dCumulative below stage 4

The NASA announces improvement targets on three advanced generation aircraft with N+ series for the civil aircraft industry. These are N + 1, N + 2, and N + 3, in which N represents current in-service airplanes. As seen in Table 7.1, the stringent requirements belong to N + 3. The ACARE has released guidelines and targets with Vision 2020 and then Flightpath 2050.

Environmental effects of aviation sector attract great interest when considered pollutant emissions and noise of aircraft. Harmful gases diffused around by avionics sector are carbon dioxide (CO₂), oxides of nitrogen (NO_x), water vapor (H₂O), contrail, and particles. Aviation represents approximately 2% of the total annual global CO₂ emissions from man-made activities according to the Carbon Dioxide Information Analysis Center (CDIAC 2016). When compared with its growth rate (about 4.5% p.a.), commercial aviation share seems stable with 2% over years according to the report of the International Air Transport Association (IATA 2019).

When greenhouse gas (GHG) emissions are evaluated on sectoral basis, the biggest share in total emissions is in the energy sector with 73.2% according to the report presented in 2016 (seen in Fig. 7.1) (Rtichie 2020). The transportation sector, which is one of the subsectors of energy, constitutes 16.2% of the total global emission. The percentages of the components that make up the transportation sector that are pipeline, rail, shipping, aviation, and road are given in Fig. 7.1. Aviation is seen as the subsector with the largest share in total emissions, after road transport.

Noise pollution is another environmental concern, and major noise sources are transportation (roads, railways, airports) and industry. Decibel (dB) is the unit of noise intensity measurement. Noise maps are developed for environmental noise assessment and may be built based on measurements (by sound level meter) or predictions (Murphy and King 2014). Day-evening-night-weighted sound pressure level (L_{den}) is a noise indicator to be applied in the assessment of environmental

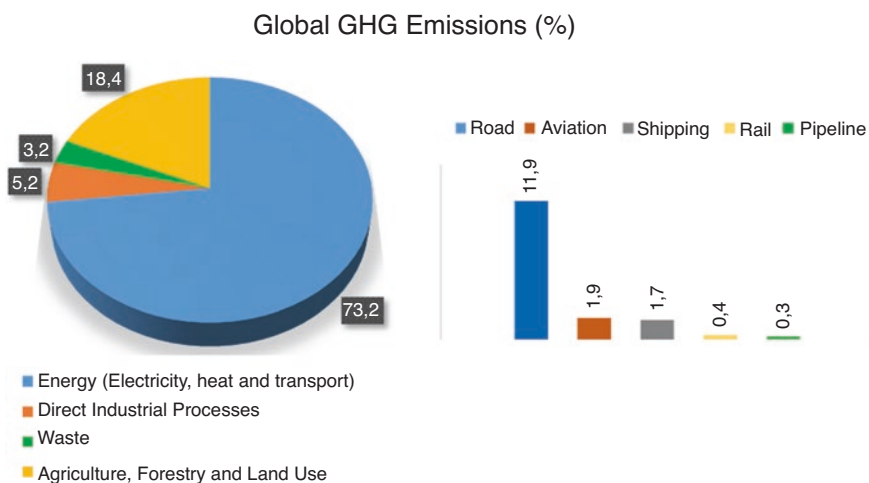


Fig. 7.1 Share of global GHG emissions based on sectors and subsectors

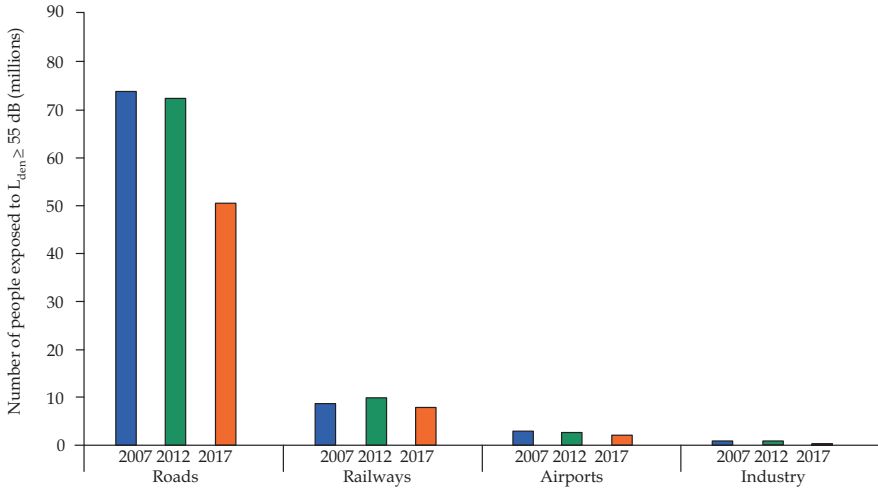


Fig. 7.2 Comparison of environmental noise sources (European Environment Agency (2020))

noise. High-noise level is defined as noise levels above 55 dB. Among all noise sources, aviation is responsible for 3.2% of the total population exposed to L_{den} above 55 dB from all sources comprised by the EU Environmental Noise Directive (END) in the year of 2017 (European Environment Agency (2020)). Environmental noise measurement results in a 5-year basis are shared by the EU END. The change of the noise sources over the years is given in Fig. 7.2. As seen in the figure, population affected by aircraft noise is much smaller than other transportation noise sources.

According to International Energy Agency (IEA), there is an 8% decrease in global CO_2 emissions in 2020 because of COVID-19, and this value has been seen as the 2010 emission level (Wheeler 2016). But it is also said that decline in emission will probably be short-dated, unless sustainable steps are taken for cleaner avionics. Some significant improvements have been made in aviation sector to reduce emissions in recent years such as aircraft technology, biofuels as an alternative to conventional jet fuel, and optimal operation (comprising weight-reduction regulation, filling empty seats, and air traffic control systems) (Nikoleris et al. 2011; Sgouridis et al. 2011). Efforts in aircraft technology have introduced the terms: more electric aircraft (MEA) and all-electric aircraft (AEA). The MEA technology is an approach to increase the efficiency of aircraft, but since conventional jet fuels are still used in this technology, emission reduction will not be sufficient level (IEA 2020) AEA technology needs to go a long way to be used in commercial aviation.

7.2 Electric Power System of Aircraft

Recently, with the advance in technology, electrical systems are replacing with the traditional hydraulic, pneumatic, and mechanical systems. This electrification approach has bought a new aircraft concept: “More electric aircraft.” Boeing 787 and A380 are important examples of the MEA application in aviation (Fig. 7.3).

The electrical power system (EPS) used in Boeing 787 is a hybrid voltage system and consists of different voltage types/levels. These are 235 volts alternating current (VAC), 115 VAC, 28 V direct current (VDC), and ± 270 VDC. The 115 VAC and 28 VDC voltage types are the traditional voltages of the EPS, and 235 VAC and ± 270 VDC voltage types are the new voltage types of the no-bleed electrical architecture. This architecture has six generators – two each per engine and auxiliary power unit (APU) – operating at 235 VAC for reduced generator feeder weight (Sinnett 2007).

Unlike the traditional EPS, the generators are directly connected to engine gear-boxes as seen in Fig. 7.4 in the more aircraft EPS. So, they operate at a variable frequency (360 to 800 Hz) proportional to the engine speed.

There are two electrical/electronics (E/E) bays, which are forward and aft bays as a feature of the EPS. In addition, an array of remote power distribution units (RPDU) that support aircraft electrical equipment is available. With this system, weight decreases by reducing the size of power feeders. RPDU substantially based on the solid-state power controllers (SSPC) are used instead of the traditional protection devices such as thermal circuit breakers and relays.

Figure 7.5 shows simplified electric power distribution systems for the traditional and the more electric aircraft examples. In B787, the traditional power

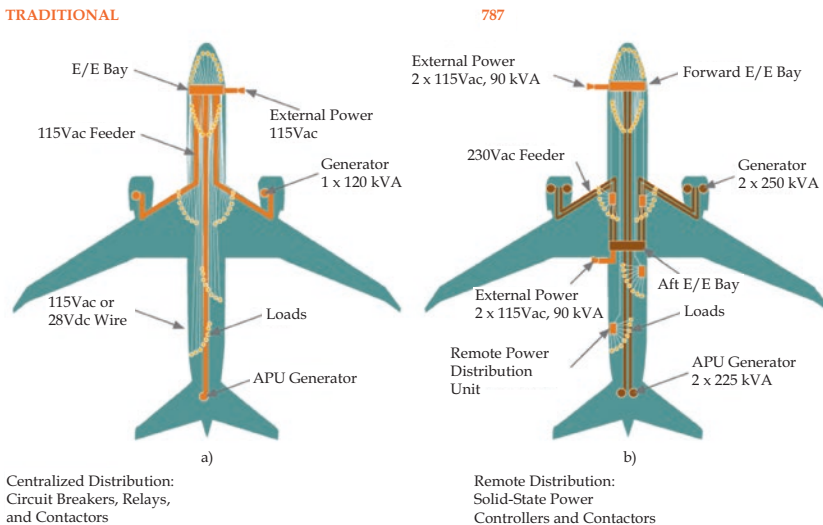


Fig. 7.3 Electrical power systems (a) traditional aircraft (b) Boeing 787

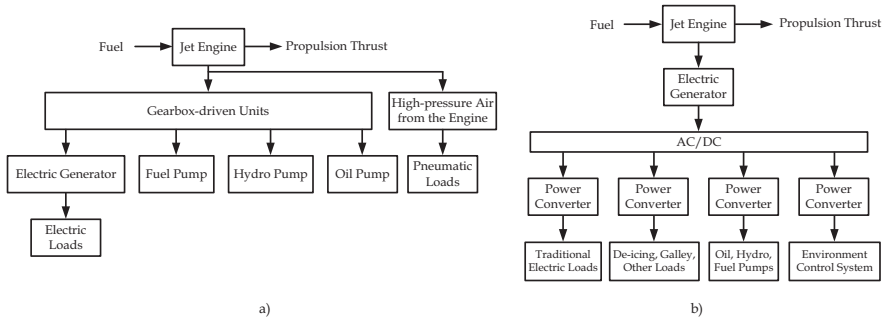


Fig. 7.4 EPS of conventional and the MEA aircraft

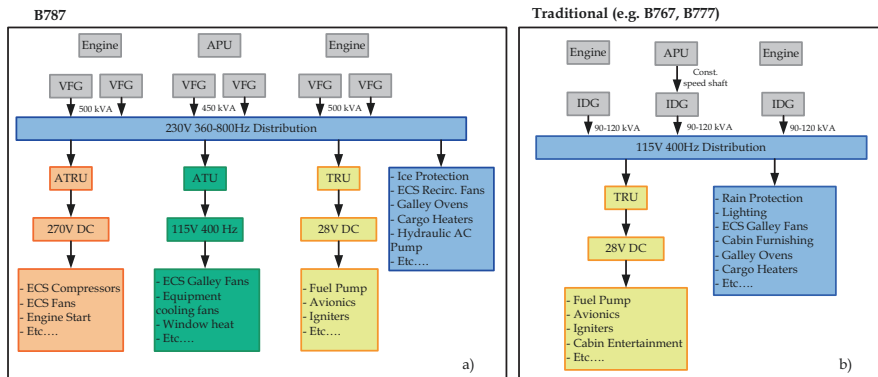


Fig. 7.5 Simplified EPS of Boeing 787 (more electric aircraft) and Boeing B767 and B777 (examples of the traditional aircraft) (Madonna et al. 2018)

generation system employing with integrated drive generators (IDG) has been replaced with the variable frequency generator (VFG).

In the MEA shown in Fig. 7.5 (a), the power ratings of the main generator and auxiliary power unit (APU) generator may reach up to 1MVA and 450kVA, respectively. In the EPS, the voltage rating of primary AC power bus is 230 V with a frequency range of 360–800 Hz, instead of 115 V with a frequency range of 400 Hz as the traditional systems. The transformation of power between primary and secondary buses is provided by the autotransformer rectifier unit (ATRU), autotransformer unit (ATU), and transformer rectifier unit (TRU). The ATRU and TRU are both used for AC/DC rectifier; however, in recent years, the ATRU has drawn more attention due to its reduced kVA rating when it is compared with the TRU.

As a result, the voltage levels used in the aircraft for the electrical system can be summarized as below:

For constant frequency distribution:

- AC-DC conversion: (115 V or 230 V) 400 Hz AC/28 V DC.

For variable frequency distribution:

- AC-AC conversion: (115 V or 230 V) 350 Hz–800 Hz AC/ (115 V or 230 V) 400 Hz AC.
- AC-DC conversion: (115 V or 230 V) 350 Hz–800 Hz AC/28 V DC.
- AC-DC conversion: (115 V or 230 V) 350 Hz–800 Hz AC/270 V DC.

In DC distribution:

- DC-DC conversion: 270 V DC/28 V DC.
- DC-AC conversion: AC voltage and frequency are depended on the loads.
- AC-DC conversion: (115 V or 230 V) 350 Hz–800 Hz AC/270 V DC.

7.2.1 *Electric Aircraft Propulsion Systems*

In recent years, with the technological developments, the subject of electric aircraft has become prominent, and an electric aircraft has been used as a propulsive energy source for greener and cleaner aviation. In the electric aircraft, an eco-friendlier air transportation is provided by using CO₂-emission-free electric motors in the propulsion system. With the increasing widespread use of electrical systems, the zero-emission environmental target of 2050 will be achieved.

Electric propulsion structures used in aircraft are basically examined in three groups as fully electric, hybrid, and turbo electric.

7.2.1.1 All-Electric Systems

In these systems, only batteries are used as the propulsion source as seen in Fig. 7.6. All-electric propulsion currently planned are small-sized aircraft and expected for short-haul transportation. The reasons for this are limitation of battery technology, size of the cooling systems (large sized aircraft requires more power and produce

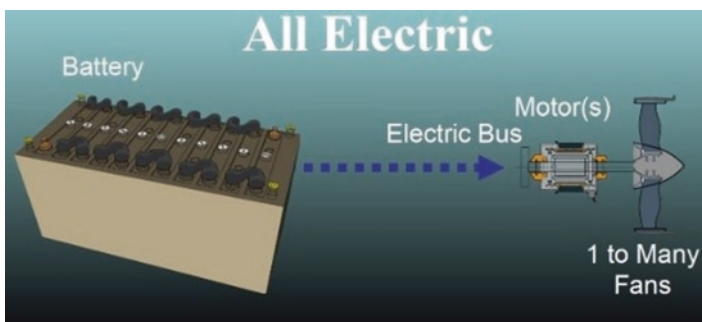


Fig. 7.6 All-electric concept for propulsion system (Bowman et al. 2018)

more heat in electronics devices), and economic constraints. A detailed research of all-electric aircraft has been currently evaluated or planned can be found in (Gnadt et al. 2019).

Some examples of conceptual all-electric aircraft designs are SCEPTOR X-57 of the NASA (Jansen et al. 2017) in general aviation category and VoltAir (Stückl et al. 2012) and Ce-Liner of Bauhaus Luftfahrt (Hornung et al. 2013) in commercial aircraft category. The other examples that had their flight are Pipistrel Velis Electro (Pipistrel Aircraft 2020), and Wisk Cora (Wisk Aero 2020) in general aviation category. Also, Volocopter VC200 (Volocopter GmbH 2020), Lilium Jet (Lilium 2020), Boeing Aurora (Aurora 2020), and City Airbus (Airbus 2020) are some examples of vertical take-off and landing (VTOL) category.

7.2.1.2 Hybrid Systems

The gas turbine engine, which is the driving power source in hybrid systems, is also responsible for charging battery systems. Battery systems ensure that the energy demand is met in certain phases of the flight. Hybrid systems, on the other hand, are examined in three subcategories as parallel, serial, and serial/parallel partial hybrid.

Parallel Hybrid In this concept of hybrid systems, both the turbine engine and the battery-powered engine are connected to the fan shaft. This configuration given in Fig. 7.7 allows one or both components to be used for propulsion.

Series Hybrid In series hybrid system, the only component in this system connected to the fan is the electric motor (Fig. 7.8). Here, the gas turbine is used to drive the engine over the electric generator and charge the batteries. The series hybrid system is suitable for use in distributed propulsion systems using small motors and fans.

Series/Parallel Partial Hybrid This system combines the characteristics of series and parallel systems, namely, one or more fans can be driven by gas turbines while

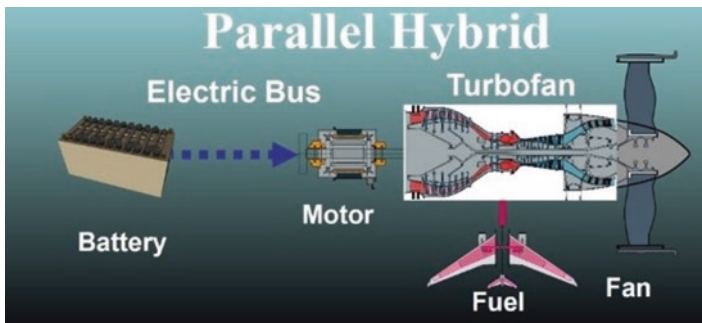


Fig. 7.7 Parallel hybrid concept for propulsion system (Bowman et al. 2018)

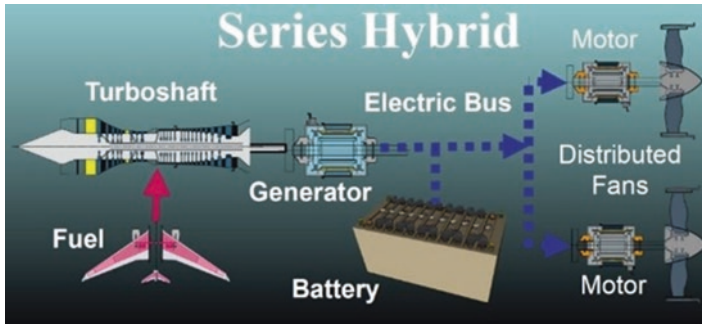


Fig. 7.8 Series hybrid concept for propulsion system (Bowman et al. 2018)

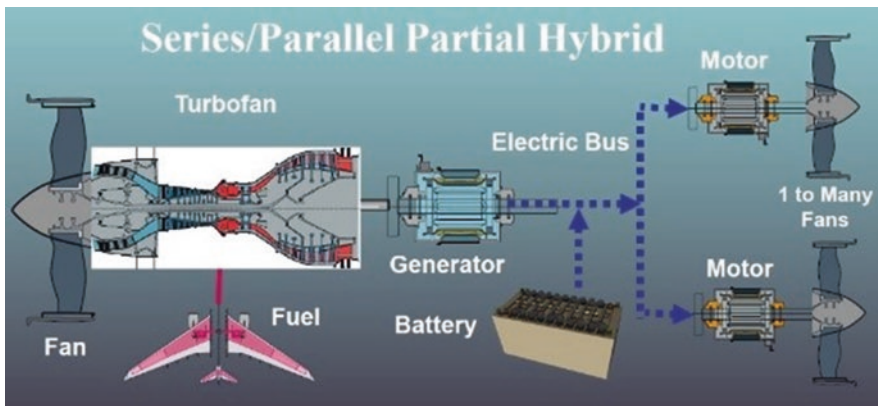


Fig. 7.9 Series/parallel hybrid concept for propulsion system (Bowman et al. 2018)

other fans can be driven by electric motors. In Fig. 7.9, the power sources of electric motors are battery, or the generator driven by the turbine.

Examples of parallel EPS concepts are Boeing Subsonic Ultra Green Aircraft Research (SUGAR) Volt (Jansen et al. 2017) (in large commercial category), United Technology Research Centre (UTRC)-Geared Turbofan design, Rolls-Royce North America (RRNA)-Electrically Variable Engine (EVE) (Jansen et al. 2017), Bauhaus Luftfahrt (BHL) conceptualized designs, and Turbo electRIC Aircraft Design Environment (TRADE). Also, Airbus/Rolls-Royce E-Thrust (in large commercial category) and Zunum Aero (in regional and large commercial category) are examples of series hybrid EPS (Schefer et al. 2020).

7.2.1.3 Turboelectric Systems

Turboelectric systems are battery-free systems, and their propulsion power is provided by gas turbines. Turboelectric systems are divided into full turboelectric (Fig. 7.10) and partial turboelectric (Fig. 7.11).

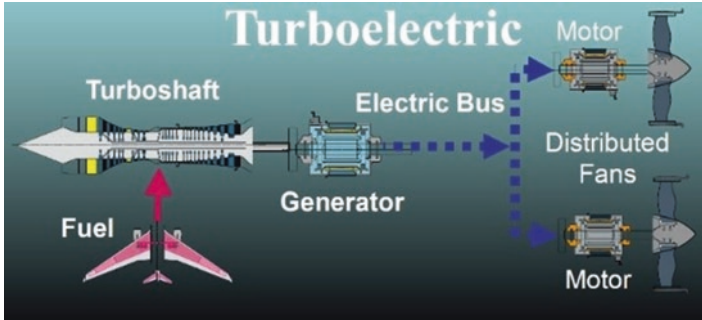


Fig. 7.10 Turboelectric concept for propulsion system (Bowman et al. 2018)

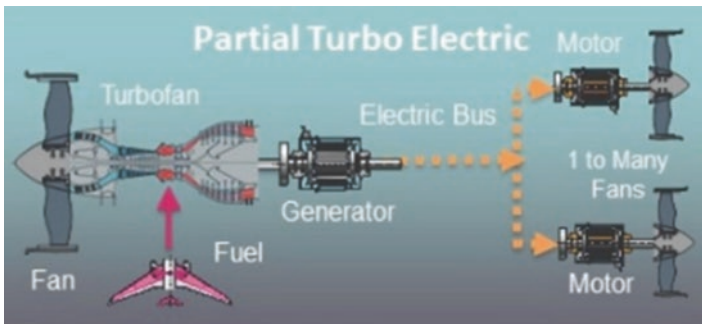


Fig. 7.11 Partial turboelectric concept for propulsion system (Bowman et al. 2018)

Full Turboelectric In this structure, turboshaft motors drive the electric generator and power the inverter and DC motors that drive the distributed fans.

Partial Turboelectric In this system, unlike the full turboelectric system, some of the driving powers are provided electrically, while the remaining parts are provided by the turbofans driven by the gas turbine.

The maintenance requirement of electric motors used in electric propulsion systems is much lower than combustion engines. As a result, the use of electric propulsion systems for aircraft is a major development step in the aviation field.

The NASA N3-X and ESAero ECO-150R are given as examples for the turboelectric configuration (Jansen et al. 2017). The partial turboelectric concept has been used in NASA’s single-aisle turboelectric aircraft with aft boundary (STARC-ABL) and Boeing SUGAR Freeze under large commercial category (Jansen et al. 2017). Since NASA’s STARC-ABL is a turboelectric concept, it does not have an energy storage system. The power needed for aircraft by tail-cone fan is supplied from underwing engines.

7.3 Power Electronics Converters

Nowadays, electric aircraft have become a popular research field, thanks to the advances and innovations in power electronics technology. Thus, hydraulic, pneumatic, and mechanics systems have started to give their place to electrical/electronic systems. In this section, power electronics circuit topologies used in aircrafts are examined. Firstly, information about voltage levels required for aviation power systems is given.

Multi-voltage level buses are used in the aircraft electric power system, and these buses are connected by power electronics converters. Moreover, power converters are also required for variable speed operation of electrical machines in the aircraft. NASA NRA goals to obtain efficiency greater than 98% and specific power 16–19 kW/kg for MW-scaled power converters in the upcoming 10 years. NASA-sponsored MW-sized converter design efforts are given in Table 7.2.

An aircraft electric network contains different AC and DC buses at varied voltage and frequency level. As a result of this, power electronics converters are needed for the conversion of power such as AC-AC, AC-DC, DC-DC, and DC-AC converters. In the propulsion concepts showed in Figs. 7.6, 7.7, 7.8, 7.9, 7.10, 7.11, the architecture of aircraft power systems includes several AC/DC loads and aircraft devices. In this section, a brief information has been given about power electronics converters.

7.3.1 DC-DC Converters

Secondary systems in the MEA and electric propulsion aircraft (EPA) are the applications of DC/DC converters in the aircraft architecture. Most used topologies are given below.

Dual Active Bridge (DAB) The DAB converter has a widespread usage area because of its advantages, such as the bidirectional power flow, high-power density,

Table 7.2 MW-sized converter development sponsored by the NASA

| Research project | Converter topology | Switch material | Performance |
|---|--|-----------------|--|
| Boeing (Jansen et al. 2017) | 1 MW three-level active neutral point converter (ANPC) | Si | SP (kW/kg): 26 η (%): 99.3 $V_{input (DC)}$: 1 kV output frequency: 0.2–3 kHz Cryogenic cooling |
| General Electric (Jansen et al. 2017) | 1 MW three-level active neutral point converter (ANPC) | Si/SiC | SP (kW/kg): 19 η (%): 99 $V_{input (DC)}$: 2.4 kV output frequency: 1–3 kHz Liquid cooling |
| University of Illinois (Jansen et al. 2017) | 0.2 MW seven-level flying capacitor | GaN | SP (kW/kg): 19 η (%): 99 $V_{input (DC)}$: 1 kV Liquid cooling |

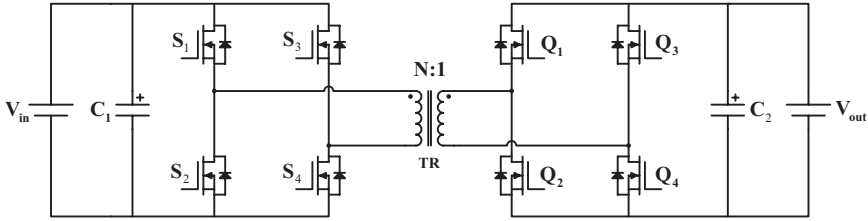


Fig. 7.12 Conventional DAB converter

and galvanic isolation. Since the topology given in Fig. 7.12 is isolated, it prevents failures, but the drawback of this property is the weight of converter because of the heavy transformer (De Doncker et al. 1988; Walter and De Doncker 2003; Naayagi et al. 2012; Tarisciotti et al. 2017).

Researchers have made improvements on the DAB converters, and many new topologies have been proposed for bidirectional DC-DC power conversion used for energy storage in aviation (Demirel et al. 2019).

Three-Phase DAB The three-phase DAB converter seen in Fig. 7.13 has a higher power capability and requires smaller passive filtering components than single-phase DAB converter (Blaabjerg 2018). Also, switching devices of this converter are under lower voltage stress compared to single-phase DAB. The converter can be used for the connection of high-voltage DC bus (270 VDC) to low-voltage DC bus (28 VDC) in the aviation systems.

Resonant A resonant converter basically has inductor and capacitor called as resonant tank as seen in Fig. 7.14. A resonant tank is used for tuning to resonate at a definite frequency. An advantage of resonant converter is achieving easily high efficiency and having wide soft-switching range by tuning switching frequency. Also, in some modified resonant converters, it is possible to utilize transformer magnetizing and leakage inductance as the resonant elements. So this reduces the cost and size of components (Safaei et al. 2011; Li and Wang 2016; Shakib and Mekhilef 2017; Chen and Mode 2018).

Active Bridge Active Clamp (ABAC) The ABAC converter is used to overcome the current ripple limitation by directly imposing the load current and proposed as an alternative to the DAB (Tarisciotti et al. 2017, 2019; Chen et al. 2017, 2019). The difference of ABAC given in Fig. 7.15 from DAB is that it provides a current-fed low-voltage stage with the help of external output inductors.

Interleaved Boost with Coupled Inductors (IBCI) As shown in Fig. 7.16, this converter replaces the H-bridge on the low-voltage side of DAB using two clamping circuits and a high-frequency transformer with two coupled inductors. Difference of IBCI topology from DAB, IBCI converter has active control on the load current that allows an accurate converter current overload limitation (Tarisciotti et al. 2017; Spiazzi and Buso 2015).

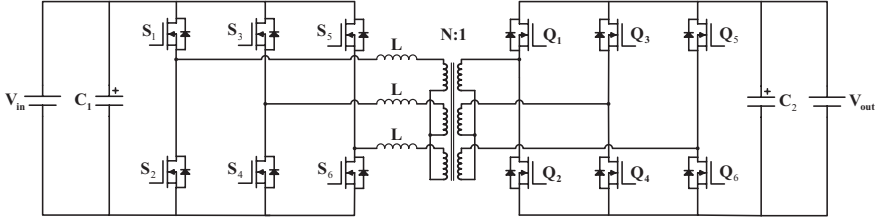


Fig. 7.13 Three-phase DAB converter

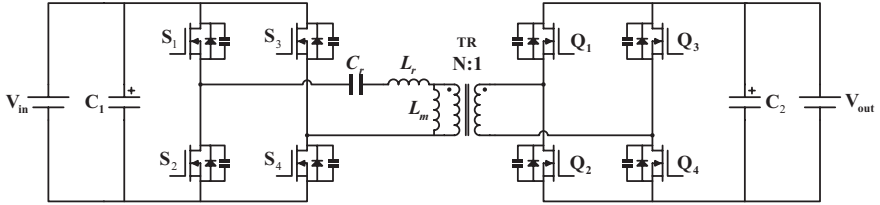


Fig. 7.14 Bidirectional LLC resonant converter topology

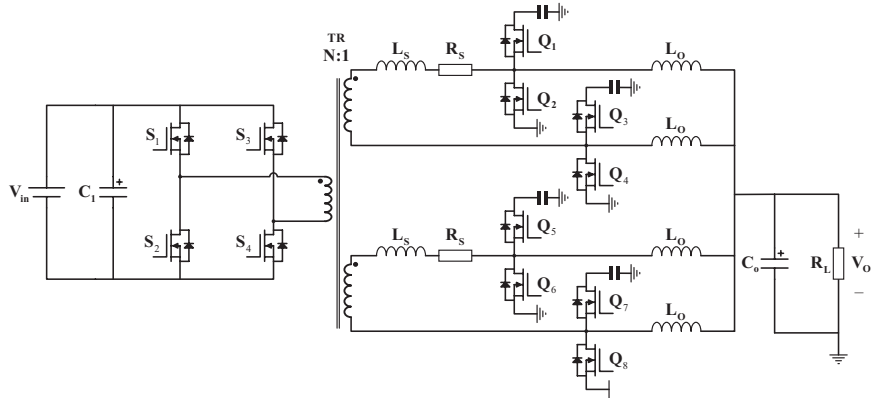


Fig. 7.15 ABAC converter topology (Chen et al. (2017))

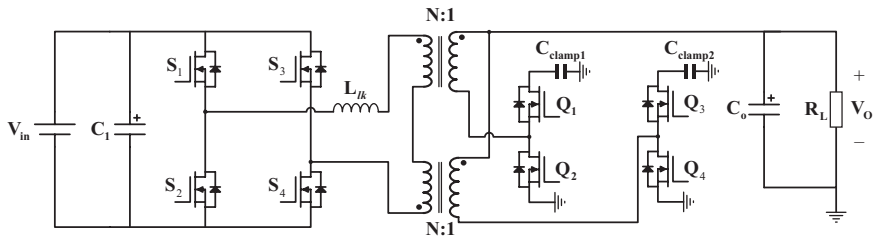


Fig. 7.16 Interleaved boost with coupled inductors (IBCI) topology (Tarisciotti et al. (2017))

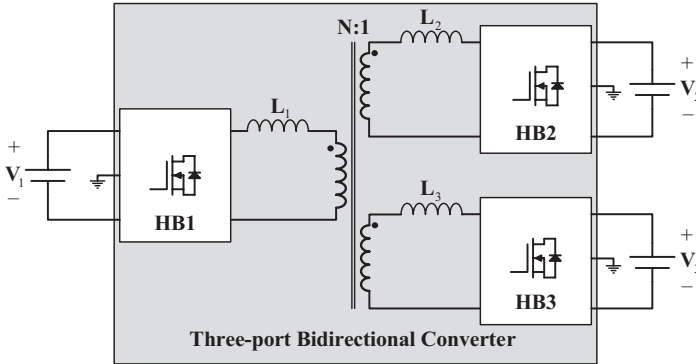


Fig. 7.17 Multiport DC-DC converter topology (Karanayil et al. 2017)

Multiport Multiport topologies are used for the combination of energy storage systems. These converters are realized using multi-winding transformers. The three-port bidirectional DC-DC converter topology is seen in Fig. 7.17, and the port number of this topology can be increased according to application (Buticchi et al. 2017; Karanayil et al. 2017).

7.3.2 DC-AC Converters

The DC-AC converter is defined as inverter. The DC-AC converters are used in secondary systems for MEA, while they are used in secondary and propulsion systems in the EPA. Generally, inverters are divided into two categories, and these are voltage source inverter and multilevel inverters.

Voltage Source Inverter (VSI) A two-level VSI (Fig. 7.18) is preferred in low-voltage/power applications. However, VSI generates a harmonic waveform, which affects the performance of the connected load. Examples of two-level VSI studies are available in (Yin et al. 2017; Nawawi et al. 2017; Lim et al. 2018).

Z-source In a traditional VSI, the two switches of the same-phase leg never be gated on at the same time, because of a short circuit to occur, and this would destroy the inverter. Also, the maximum value of output voltage obtainable can never exceed the DC bus voltage. To overcome these limitations, the Z-source inverter shown in Fig. 7.19 can be used. This topology uses an impedance network (called as Z network) instead of DC link. Hence, voltage can be bucked and boosted to any desired output voltage, which is greater than the available DC bus voltage in the Z-source inverter (Shen et al. 2006).

Neutral Point Clamped (NPC) The NPC topology is also known as I-type inverter. If the NPC is compared with two-level inverters, it has better efficiency and less harmonics distortion because of having more voltage levels, and the rated voltage of switching devices is much lower (Nawawi et al. 2017; Rodriguez et al. 2010).

Fig. 7.18 Voltage source inverter

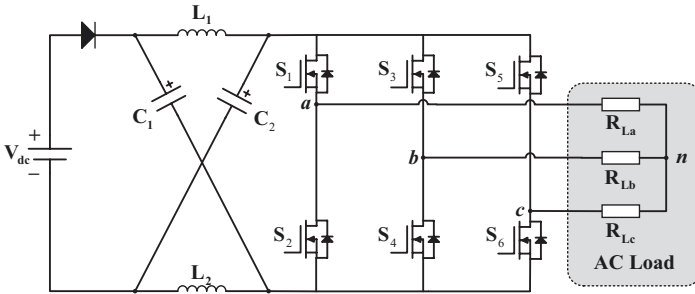
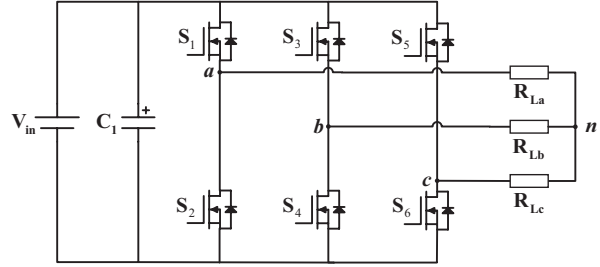


Fig. 7.19 Z-source inverter topology

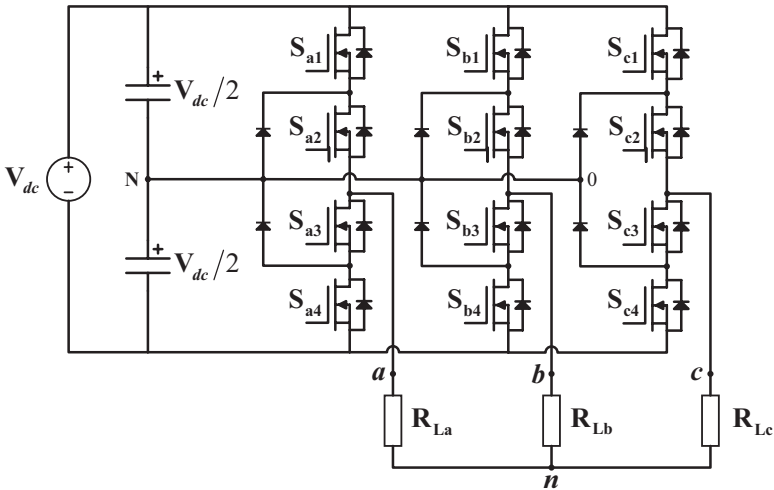


Fig. 7.20 Three-level NPC inverter topology

The main drawback of the NPC is its complex structure due to more switches and diodes. The three-level/phase NPC inverter is seen in Fig. 7.20, and the level of the inverter (lowest level of multilevel inverters) can be increased, such as five, seven, etc. However, this complicates the topology structure and decreases the efficiency of converters because of switching loss (Zhang et al. 2019a, b). For example, for an

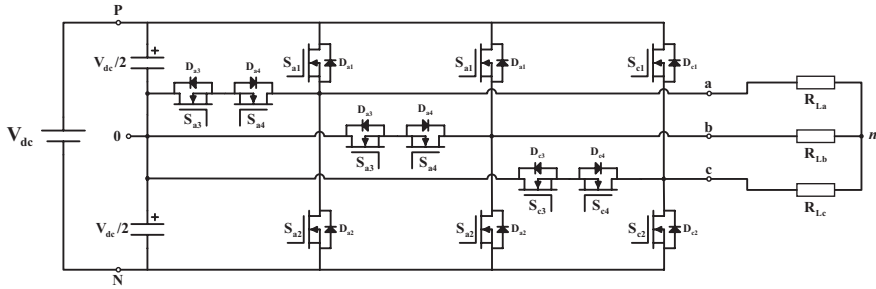


Fig. 7.21 T-type inverter topology

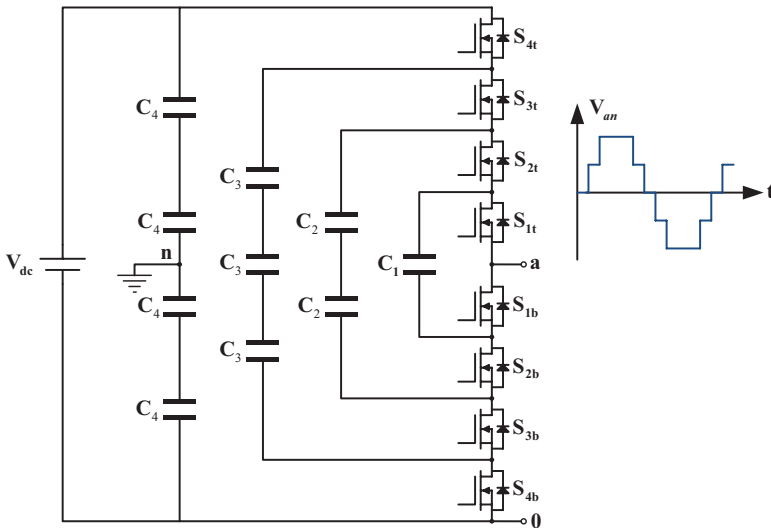


Fig. 7.22 Five-level flying capacitor inverter

n -level three-phase NPC converter, the number of semiconductor switches and diodes will be $6(n - 1)$ and $6(n - 2)$, respectively.

T-type NPC (TNPC) The difference of T-type from I-type is voltage stress on switching elements, and The TNPC is an advanced form of NPC converter topology (Nawawi et al. 2017; Schweizer and Kolar 2013). In addition, The TNPC has a lower number of switching elements, and it is more efficient compared to the NPC converter. The TNPC is a reduced NPC converter, which eliminates the clamping diodes from the power circuit as seen in Fig. 7.21.

Flying Capacitor In this topology, the main idea is using capacitors to transfer the voltage to output. Switching states of flying capacitor topology resemble to a NPC inverter, and in the topology, there is no need of clamping diodes. Also, the maximum voltage value achieved in the topology cannot be more than half of the input DC voltage. The flying capacitor topology is one of the members of multilevel inverter topologies, and a five-level flying capacitor inverter is seen in Fig. 7.22.

The improvement on multilevel flying capacitor topology is continued as in (Modeer et al. 2020), where a nine-level interleaved flying capacitor is designed for aviation applications with 98.6% peak efficiency and 15 kW/kg peak power density.

Cascaded H-bridge This topology (Fig. 7.23) uses capacitors and switches (combination of switches called as H-bridge) and needs a fewer number of components for each level. The topology is made of a series power conversion cells; thus, power can be easily adjusted. An advantage of this inverter is the need of less components compared with NPC and flying capacitor of inverters (Prasad et al. 2013).

7.3.3 AC-AC Converters

Secondary systems in the MEA is the application area of these converters, and the types of AC-AC converters are cycloconverter and matrix converter.

Cycloconverter This topology used in the single-stage conversion of AC-AC as given in Fig. 7.24 and is also known as the direct AC-AC converter or frequency changer. Cycloconverter can convert an AC supply of fixed input frequency directly to an AC output of another frequency (Liu et al. 2020). Another type of AC-AC conversion is the circuits known as two-stage converters and contains a rectifier (AC-DC) and inverter (DC-AC). Such AC-AC converters are called indirect converters.

Matrix Converter (MC) This type of converter used for AC-AC power conversion is mainly based on controlled semiconductor switches and the least requirement of passive components. As it is an array of bidirectional switches arranged like matrix, it takes the name from its structure (Wheeler et al. 2002). As seen in Fig. 7.25, there is no DC-link circuit in MC, and it does not require large energy storage elements. To obtain the desired output voltage, it is needed to modulate the gating of the devices.

7.3.4 AC-DC Converters

AC-DC converters are used for the TRU/ATRU of secondary systems in the MEA. Also, they are used in the TRU of secondary systems and propulsion systems in turbo and hybrid electric aircraft.

Vienna Rectifier This rectifier topology is used in high-power, three-phase power applications, and it is popular due to its operation in continuous conduction mode (Liu et al. 2018; Borovic et al. 2016). Also, it has reduced voltage stress on the power devices, having intrinsically three-level switching as seen in Fig. 7.26 (Kolar et al. 1996).

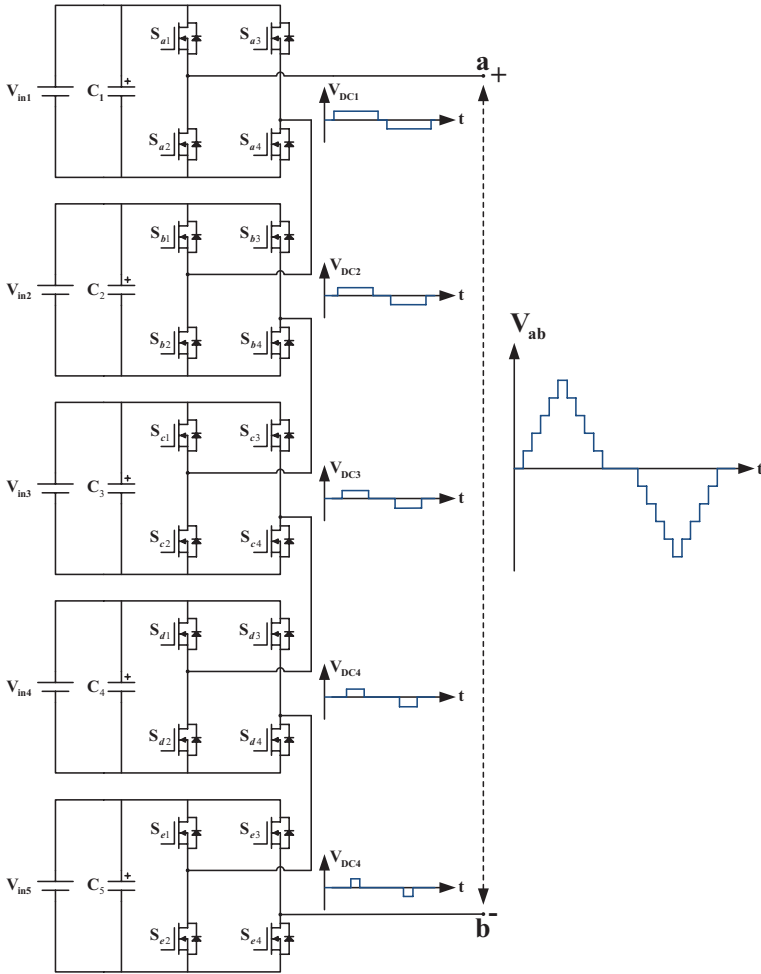


Fig. 7.23 Cascaded H-bridge multilevel (five-level) inverter

Neutral Point Clamped (NPC) and T-Type Rectifiers These rectifiers are the inverse of inverter versions as seen in Fig. 7.27. The NPC and TNPC rectifiers are examined in (Lim et al. 2018; Ventosa-Cutillas et al. 2019), respectively. The three-level/phase T-type rectifier has significant advantages, such as high-power density, low total harmonic distortion, and high efficiency, than the NPC rectifier.

Two-Level Rectifiers The rectifier topology is the same as the inverter in two-level topologies as in the T-type. The schematic of two-level rectifier is given in Fig. 7.28 (Lim et al. 2018). Two-level topologies are a popular choice from the industry because of its simplicity. However, the three-level ones, thanks to the lower voltage stress on switches, provide higher efficiency than two-level topologies.

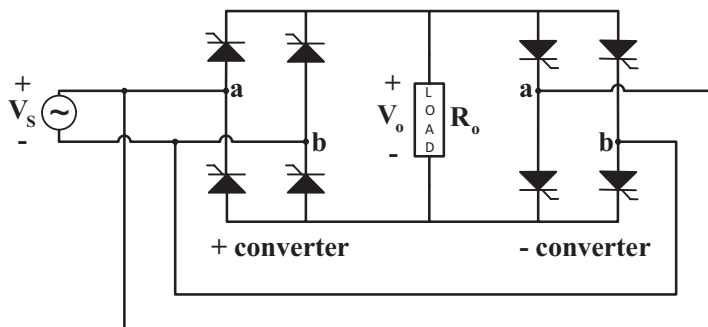


Fig. 7.24 Single-phase cycloconverter topology

Fig. 7.25 Matrix converter topology

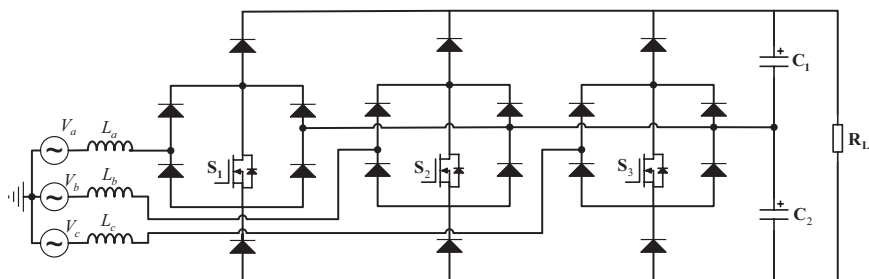
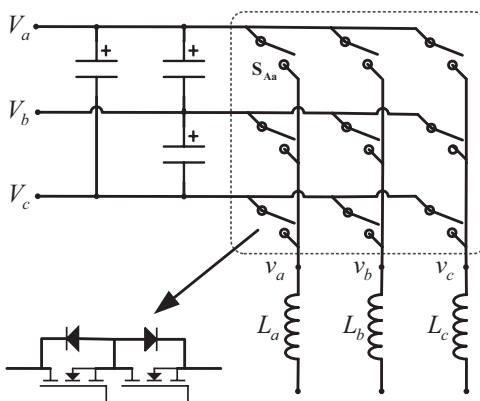


Fig. 7.26 VIENNA rectifier topology

7.3.5 Semiconductor Technology

Semiconductors used in converter topologies are silicon (Si), silicon carbide (SiC), and gallium nitride (GaN). When the impact on the topology efficiency is considered, the proper choice of semiconductor is an important issue in power converters.

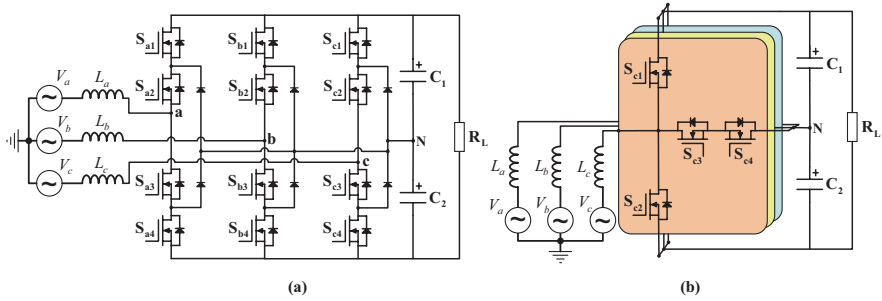


Fig. 7.27 a) Three-level/phase NPC rectifier topology, b) three-level/phase T-type rectifier

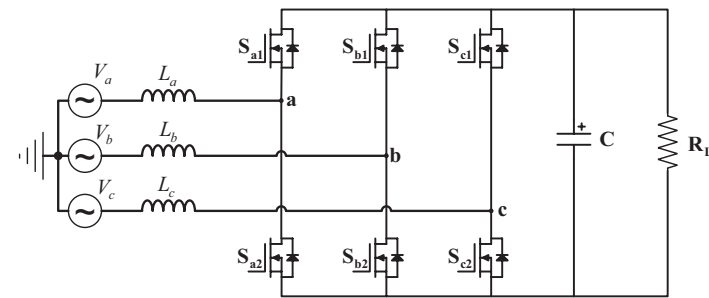


Fig. 7.28 Two-level PWM rectifier

- **Silicon (Si):** Si semiconductor components are the most used and mature ones in semiconductor types. Si-based technology has been preferred in various fields of application and covers a wide power and voltage range (Schefer et al. 2020). The operating temperature of Si components is less than 175 °C, and it has a limited switching speed.
- **Silicon Carbide (SiC):** SiC semiconductors have a higher bandgap and better thermal conductivity compared silicon carbide (SiC) to Si. In addition, it is reported that SiC power devices can operate at high ambient temperatures up to 500 °C. These characteristics make SiC-based devices operate in a harsh environment such as aviation and can also handle the same power level as Si devices at half size and weight of Si.
- **Gallium Nitride (GaN):** GaN semiconductors are a new technology and currently commercially available for relatively low voltage (600/650 V) that fit for a great number of application fields. The advantages of GaN are fast switching speed and excellent reverse-recovery performance that are especially important for low-loss, high-efficiency performance. A comparison of semiconductor technologies described above is given in Fig. 7.29.

Developments of new semiconductor technologies allow power electronics circuits to operate at high frequencies, and high performance can be achieved in

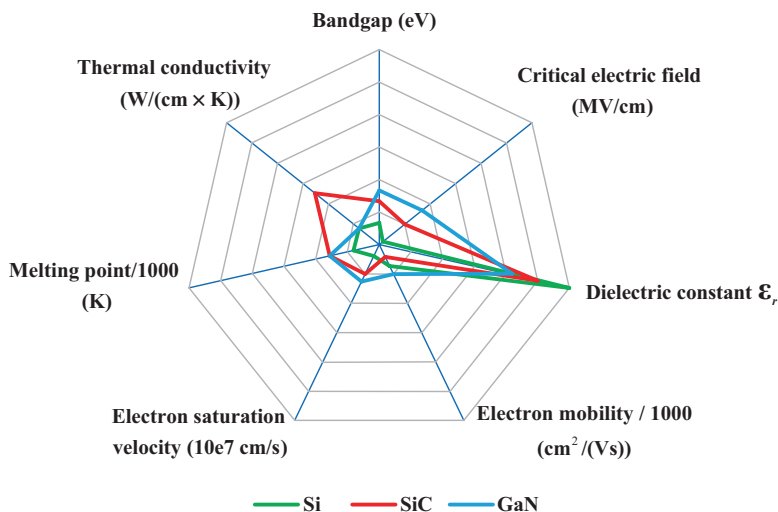


Fig. 7.29 Parameter comparison of Si, SiC, and GaN

electrification of aircraft. Switching at high frequency reduces the size of passive components. However, high-switching speed increases electromagnetic interference (EMI) problems. Attention should also be paid to the issue of electromagnetic compatibility (EMC) so that many electrical/electronic devices can operate safely and properly. To attenuate the interference, noise limits determined by the relevant standard should be ensured by the realization of EMI filter design.

Power electronics systems with high-power density can contain devices with wideband range (WBG). However, high-frequency switching brings along an EMI problem (Zhang and Wang 2020). In a study where semiconductor technologies were compared in terms of an EMI effect, it was observed that Si IGBT switches at the same switching frequency caused less EMI noise than SiC MOSFETs (Trentin et al. 2015). By filtering against EMI noise, interferences can be reduced, and the system can be operated reliably. However, as seen in Fig. 7.30, the EMI filter size is appeared as an important design criterion affecting the power density.

DC and AC output sides of inverter need to meet RTCA/DO160 EMC standard to maintain reliable operating and not emit interference. The EMI filter increases the volume of the power electronics systems and the weight of motor drive circuit in aircraft.

Standards and regulations have been published by authorized committees to ensure the safety and reliability of all electronic and other equipment used in aviation. Commissions and organizations operating in the aviation industry for this purpose are the Radio Technical Commission for Aeronautics (RCTA), European Organization for Civil Aviation Equipment (EUROCAE), and SAE International. The RCTA DO-160G provides information on standard procedures and environmental test criteria for testing the aircraft-carried equipment in the full spectrum of

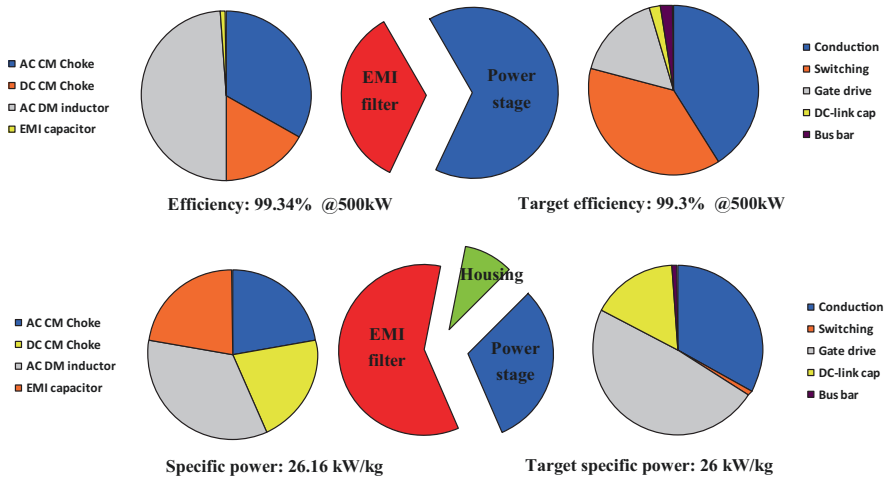


Fig. 7.30 Volume evaluation of EMI filter (NASA Glenn Research Center 2019)

light general aviation aircraft and helicopters to supersonic transport categories of jumbo jets and aircraft (RCTA 2014). For instance, briefs of DO160 standard are followed for the design of EMI filter.

7.4 Electric Machines

Design of an electrical machine for aircraft necessitates several criteria, such as high efficiency, high reliability, low weight, low volume, and low cost (Sahoo et al. 2020). In addition to these criteria, high specific power is required for the machine design. The NASA Research Announcement (NRA) has set goals for megawatt-level machine technologies with a power density greater than 13.2 kW/kg and efficiency greater than 96% in the next 10 years for the non-cryogenic section. MW-level devices are selected to support partially turboelectric systems (up to single-aisle aircraft) and hybrid electric systems or fully turboelectric systems (for small aircraft) (Jansen et al. 2017).

Several of electric machine concepts have been examined in (Zhang et al. 2018), and these are induction motor (IM), synchronous reluctance machines (SRM), permanent magnet synchronous machines (PMSM), wound field synchronous machine (WFSM), and brushless doubly-fed machines (BDFM). Every machine type has advantages and drawbacks, but the PMSM has more advantages in providing requirement of aviation applications. A comparison of the performance of machine prototypes as efficiency (η), specific power (SP), and power size is given in Table 7.3.

Table 7.3 Machine prototype projects for electric aircraft

| Research project | Machine type | Performance |
|---|--|---|
| NASA Glenn Research Center (Jansen et al. 2018) | Partially superconducting WFSM | η (%): 98 SP (kW/kg): 16 1.4 MW |
| Boeing SUGAR Volt (Bradley et al. 2015) | SRM | η (%): 93 SP (kW/kg): 3–5 |
| Siemens/Rolls-Royce (Anton 2019) | Direct drive permanent magnet (SP260D) | η (%): 95 SP (kW/kg): 5.9 0.26 MW |
| Siemens/Rolls-Royce E-Fan X (Anton 2019) | Permanent magnet (SP2000D) | SP (kW/kg): 7.7 2 MW |
| University of Illinois (Yoon et al. 2016) | Air-core PMSM | η (%): 95 SP (kW/kg): 13 1 MW |
| Ohio State University (Jansen et al. 2017) | IM variable cross-section wet coil (VCSQC) | η (%) > 96 SP (kW/kg): 13 2.7 MW |

7.5 Energy Storage

Impacts of wastes and emissions to the environment are characterized as “footprint” of a product’s life cycle. So, usage of storage systems instead of jet fuel is a greener option for the environment. When the mass of the plane is reduced by 1 kg, the annual emission of 1700 tons of fuel and 5400 tons of CO₂ can be reduced in air traffic all over the world (Roboam et al. 2012).

Electric aircraft offers an eco-friendly aviation experience by eliminating direct and indirect carbon emissions. The biggest obstacle that limits the development of electric aircraft technology is the lack of high-performance storage units.

Firstly, for better understanding of storage systems, some parameters used in the evaluation of storage systems should be known. These are specific energy (Wh/kg), specific power (kW/kg), and volumetric energy density (Wh/L). There are four technologies for storage systems that are critical in the design of electric aircraft: battery, fuel cell, super capacitor, and flywheel.

7.5.1 Batteries

Battery technologies used in aviation are lead-acid in general aviation/light aircraft and nickel-cadmium batteries in larger aircraft and helicopters. Lithium-ion and its derivatives are used in battery technology in more electric aircraft and all-electric aircraft, which are the products of developing technology. Lithium-ion batteries

have been used for the Boeing 787 Dreamliner, the more electric aircraft example, and the Airbus E-Fan, the all-electric aircraft. Considering their environmental and economic contributions, providing smaller storage with high-energy-density batteries is a need for aircraft (Tariq et al. 2017). Battery specific energy is the decisive factor in the use of battery technologies.

Today, although storage systems can provide enough power for very short-haul flights, studies are continuing to provide the required battery density for longer-haul flights. Technology with lighter and higher power density needs to be developed for providing the necessary capacity for long flights. In studies conducted so far, a prototype of a 470 Wh/kg capacity lithium-sulfur cell has been developed, and it is aimed to reach 600 Wh/kg by 2025 due to the fact that it is a new battery technology (Crittenden 2020). Considering that the field of battery technology is an immature field, it seems unlikely that all-electric aircraft will become widespread soon. However, further studies predict that the specific energy density of the batteries will increase. The developments in battery technology progress are slower than other fields, and the reasons of slow progress are the prone structures to fault and fire of the batteries. Therefore, improved batteries are required to pass the stringent approval tests, and these security tests should be done properly.

Batteries used as an energy storage system provide energy continuity by responding rapidly to changing energy demand. An environment-friendly approach is applied by supplying the energy needs of aircraft directly through batteries that do not cause carbon emissions. Although it is thought that battery systems do not cause carbon emissions, it is clear that batteries are indirect emission sources due to the emission effect of the energy sources they are charged (National Academies of Sciences, Engineering and Medicine 2016).

When the battery technologies are examined, there are two types of batteries: rechargeable and non-rechargeable batteries. Rechargeable batteries are called as secondary batteries, and they can be used safely during their cycle life. Non-rechargeable batteries are disposable batteries that are called primary batteries.

Battery technologies can be divided to three groups according to their active materials. These are lead-based, nickel-based, and lithium-based batteries.

- Lead-Based Batteries.

Lead-acid (Pb-acid) batteries are the oldest secondary battery technology (invented in 1859) and used in various aerospace applications as it is a mature battery technology. These low-cost batteries have begun to give way to new battery technologies due to their low energy density and limited charging cycle. The other disadvantage of lead-acid batteries is that they contain toxic components in their chemical structure, and the components are harmful to the environment (Freeman et al. 2014).

- Nickel-Based Batteries.

Nickel-based battery is a mature battery technology. Although it has a long service life, low maintenance, high-temperature resistance (allow to operate in wide-range temperatures), and energy density, it is a big problem that it contains poisonous metals. Most common nickel-based batteries are nickel-cadmium (Ni-Cd),

nickel-metal-hydride (Ni-MH), nickel-iron (Ni-Fe), nickel-zinc (Ni-Zn), and nickel-hydrogen (Ni-H). Ni-Cd batteries, which have proven themselves with their high durability, are preferred especially because of their high safety in aviation.

- Lithium-Ion-Based Batteries.

The use of lithium-ion (Li-ion) batteries has become widespread, thanks to their features such as longer life cycle, high efficiency, high power, and energy density compared to other battery types. However, protection circuitry is required in Li-ion batteries due to safety concerns. The importance of battery protection system has been understood with a bad experience of an incident in the past (Japan Transport Safety Board 2014). Even if it is an expensive battery compared to other battery types, high-energy density, high cycle count, and low maintenance are the features that prevent the cost (Panasonic 2012). There are various types of Li-ion batteries; these are lithium iron phosphate (LiFePO_4 , LFP), lithium nickel manganese cobalt oxide (LiNiMnCoO_2 or NMC), lithium manganese oxide (LiMn_2O_4 , Li_2MnO_3 , or LMO), lithium cobalt oxide (LiCoO_2 or LCO), lithium nickel cobalt aluminum oxide (LiNiCoAlO_2 or NCA), and lithium titanate (Li_2TiO_3 or LTO) (Buchmann 2016). NMC and LFP are especially used for electric vehicles due to their good specific densities.

- Future Battery Technologies.

Battery companies have great effort to find more powerful, durable, cheaper, and lighter battery technology. New battery technologies that could be used in the future are metal-air and lithium-sulfur batteries. The most common types of metal-air are zinc-air (Zn-air) and lithium-air (Li-air). Zn-air batteries are safe and eco-friendly and have higher energy density as compared with the other batteries. As the raw materials of Zn-air are abundant on earth, the production costs of Zn-air batteries are currently the lowest among in all secondary batteries (Arotech 2020). Among the metal-air batteries, Zn-air is relatively mature, and it has high theoretical specific energy density of 1087 Wh/kg. In a recent R&D study, 400 Wh/kg specific energy density for Zn-air has been realized (Arotech 2020).

Li-air is also known as li-oxygen battery, and it is seen as a potential alternative to lithium-ion. As cathode active material of battery is accessible from the environment (like air breathing of battery), not from the battery inside, Li-air has the highest energy density among the metal-air batteries (SolidEnergy 2017). The theoretical specific energy of Li-air is 3458 Wh/kg (Li and Dai 2014), and this makes Li-air very useful for aerospace applications. But the drawback of Li-air is loss of about 25% of its capacity even after 50 discharge cycles.

Recently, lithium-sulfur (Li-S) batteries have drawn attention as a new battery technology that offers higher energy density compared to conventional lithium-ion batteries. An example of Li-S battery is unmanned aircraft Zephyr of Airbus (Airbus 2018). Sulfur is abundant in the earth's crust, and this makes sulfur attractive for as a new battery technology. Also, thanks to its nontoxic nature, it is eco-friendly. With the use of nonconductive sulfur material, safety and energy density are increased compared to lithium-ion batteries. Li-S is theoretically predicted to have a specific

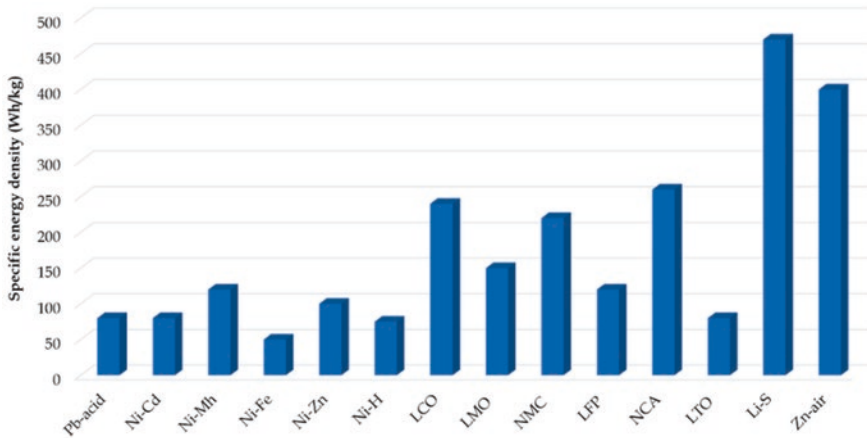


Fig. 7.31 Specific energy densities of different battery technologies (Crittenden 2020; Panasonic 2012; Li and Dai 2014)

energy of more than 2600 Wh/kg, and this value corresponds to approximately five times the specific energy value of Li-ion. To obtain this, specific energy is not yet possible because of low electrical conductivity and extreme volumetric expansion in discharge. Another drawback is the limited life cycle of Li-S, but advancement in battery technology is expected to overcome low life cycle. Figure 7.31 summarizes the specific energy of various battery technologies.

7.5.2 Fuel Cells

Fuel cells (FC) have currently been used for space applications, and they are regarded as advanced alternative power sources for propulsion systems in the aircraft. Basically, the FC system stores the chemical energy in the form of liquid or gaseous and then converts it to electrical energy through chemical reaction. FC can be powered from hydrocarbon or hydrogen (H_2). The first option produces CO_2 while not producing NO_x and any other particulate emissions. As a second option H_2 , it is emission-free, but it is still a source of the contrails. The FC systems have higher energy density compared to Li-ion batteries because the weight of FC is about four times lower. In a study, hydrogen FCs that could offer a specific energy up to 800–10,000 Wh/kg is reported (Chen et al. 2009). Energy produced from FC is more efficient and greener than the internal combustion engine. As a new technology for aviation sector, FCs are immature about weight and volume. Also, storage of gas or liquid form of H_2 is required high safety conditions.

7.5.3 *Supercapacitors*

Supercapacitors, also known as ultracapacitor, have high specific power and long cycle life. Besides, it can operate under wide temperature range. In A380 aircraft, supercapacitor is used for backup power of emergency exits and to power electrochemical actuators (Sahoo et al. 2020). According to the research of the NASA, specific energy level of supercapacitors will reach 100–150 Wh/kg in the next 15 years.

7.5.4 *Flywheel*

Flywheels are one of the oldest energy storage systems and store the energy mechanically. Specific energy of flywheels changes in the range of 100–130 Wh/kg. Flywheels store energy based on rotating mass theory, and they are in the group of mechanical storage. When compared with battery technologies, flywheels have higher discharge rate and also are low toxic and less sensitive to temperature (Chen et al. 2009). NASA GRC has flywheel technology development program for flywheel energy store in aerospace applications (McLallin et al. 2001). Again, an example of flywheel energy storage system built by Boeing is given in (Strasik et al. 2007).

7.6 Thermal Management

Thermal management systems (TMS) are essential for heat removal in the propulsion systems' components (such as converter, battery, motor/generator) to maintain their proper operation. The TMS is a very important issue for aircraft, and it is one of the contributors on weight increase of aircraft. A study on TMS design for the electric propulsion system has shown that the weight of TMS can be 5% of the total propulsion system weight (Sahoo et al. 2020).

Heat is one of the fault reasons on electrical/electronic devices used in aircrafts and decreases the reliability of device by reducing its operation lifetime. By controlling the thermal stress occurring in the devices, the device is protected against the faults caused by overheating. Thus, operation performance can be improved by allowing the device to operate within an acceptable thermal range.

The thermal management of power electronics systems is a challenging issue, and a cooling system is needed for the integrated power modules used in converters. Technologies that improve the thermal performance of the systems are required to be light in weight. Supercooling of electronics equipment and the use of superconductive materials are some of the solutions to reduce electrical resistance in aircraft

for thermal management. Removal of heat generated in these systems is carried out through conduction, natural convection, forced convection, magnetocaloric effect, and thermoelectric effect.

7.6.1 Thermal Management of Power Electronics Circuits

Thermal management is a limiting factor in the design of high-power-density electric propulsion systems such as aircrafts. Considering the working conditions of aircraft, power electronics converters are desired to operate in a reliable way, by complying with harsh ambient conditions ranging from $-55\text{ }^{\circ}\text{C}$ to $80\text{ }^{\circ}\text{C}$ (Dorn-gomba et al. 2020). Increase of heat reduces component reliability, shortening their lifetime. Thermal management in power electronics circuits is a decisive criterion in terms of heat dissipation, increasing the power density by using optimum cooling techniques, limiting failures, and increasing operating performance and system reliability. In addition to its effect on system performance, it is also effective in the decrease of device and system cost by reducing the circuit size. A detailed research of the cooling methods used for high-efficiency system designs is presented in Table 7.4.

Table 7.4 Classification of cooling technologies (Laloya et al. 2016)

| Coolant agent | Transfer mechanism | | | | |
|---------------|------------------------------------|--------------------|-----------------------------|-----------------------|---|
| | Conduction | Natural convection | Forced convection | Magnetocaloric effect | Peltier effect, Tunnel and Thermionic effects |
| Solid | - Conduction plates and heat sinks | | | - Magnetic cooling | - Thermoelectric cooling |
| | - Thermal interface materials | | | | - Thermotunnelling and thermionic cooling |
| | - Advanced conduction plates | | | | |
| Gas (air) | | - Air cooling | - Standard fans | | |
| | | | - Piezoelectric devices | | |
| | | | - Synthetic jet impingement | | |

(continued)

Table 7.4 (continued)

| Coolant agent | Transfer mechanism | | | | |
|---------------|--------------------|--------------------|-------------------------|-----------------------|---|
| | Conduction | Natural convection | Forced convection | Magnetocaloric effect | Peltier effect, Tunnel and Thermionic effects |
| | | | - Electrohydrodynamics | | |
| | | | - Thermoacoustic | | |
| Liquid | | - Immersion | - Cold plates | | |
| | | | - MicroChannel | | |
| | | | - Electro wetting | | |
| | | | - Immersion | | |
| | | | - Jet impingement | | |
| Two-phases | | - Immersion | - Cold plates | | |
| | | | - MicroChannel | | |
| | | | - Electrowetting | | |
| | | | - Immersion | | |
| | | | - Jet impingement | | |
| | | | - Heat pipes | | |
| | | | - Spray | | |
| | | | - Phase change material | | |

7.6.2 Thermal Management of Batteries

With the thermal management of the battery systems, element reliability is ensured against failures by extending the lifetime of the batteries, and thus an efficient storage system is obtained. Thermal management is crucial for economical and safe operation of the batteries. Low temperatures reduce the battery performance, while high temperatures reduce the lifetime. For this purpose, many studies have been done on thermal management. As for the cooling method, air cooling, liquid cooling, phase change material cooling, and heat pump are commonly used.

7.7 Conclusion

Increasing environmental concerns have highlighted the need for sustainable innovations in the aviation industry. For this industry, environmental targets have been determined with the related regulations, considering environmental awareness. It is very important to take effective technological and environmental steps to achieve these targets. There is a great effort on environmentally and technologically efficient aircraft design studies for sustainable aviation. Recently, the mechanical,

hydraulic, and pneumatic systems used in conventional aircraft have been replaced by electrical systems, resulting in the emergence of the more electric aircraft and all-electric aircraft concepts. In addition to providing lighter designs in weight, the electric aircraft is an environmentally cleaner option. In this study, the technological approaches developed for electric aircraft have been examined. An overview of current developments in subjects such as power systems used in electric aircraft, electric propulsion system concepts, power electronics converters, semiconductor technologies, and energy storage systems is presented.

References

- Airbus. Zephyr- Pioneering the Stratosphere. <https://www.airbus.com/defence/uav/zephyr.html> (2018). Accessed 07 Dec 2020
- Airbus. City Airbus. <https://www.airbus.com/innovation/zero-emission/urban-air-mobility/cityairbus.html> (2020). Accessed 05 Dec 2020
- Anton, F., eAircraft : Hybrid-elektrische Antriebe für Luftfahrzeuge. https://www.bbaa.de/fileadmin/user_upload/02-preis/02-02-preistraeger/newsletter-2019/02-2019-09/02_Siemens_Anton.pdf (2019). Accessed 01 Sept 2020
- Arotech. Zinc-Air batteries. <https://www.arotech.com> (2020). Accessed 15 Sept 2020
- Aurora. Boeing Aurora. <https://www.aurora.aero> (2020). Accessed 05 Dec 2020
- Blaabjerg, F. (ed.): Control of Power Electronic Converters and Systems. Academic Press, London (2018)
- Borovic, U., Zhao, S., Silva, M. et al.: Comparison of three-phase active rectifier solutions for avionic applications: Impact of the avionic standard DO-160 F and failure modes. Paper presented in 2016 IEEE Energy Conversion Congress and Exposition (ECCE), Milwaukee, 18–22 Sept 2016
- Bowman, C.L., Marien, T.V., Felder, J.L.: Turbo- and Hybrid-Electrified Aircraft Propulsion for Commercial Transport. Paper presented in 2018 AIAA/IEEE Electric Aircraft Technologies Symposium, Cincinnati, 9–11 July 2018
- Bradley, M.K., Allen, T.J., Droney, C.K.: Subsonic Ultra Green Aircraft Research Phase II – Volume I – Truss Braced Wing Design Exploration. <https://ntrs.nasa.gov/citations/20150017036> (2015). Accessed 01 Sept 2020
- Buchmann, I.: Safety of lithium-ion batteries. Cadex Electronics <https://www.cadex.com/en/batteries/safety-of-lithium-ion-batteries> (2016). Accessed 09 Dec 2020
- Buticchi, G., Costa, L., Liserre, M.: DC/DC conversion solutions to enable smart-grid behavior in the aircraft electrical power distribution system. Paper presented at the 43rd Annual Conference of the IEEE Industrial Electronics Society, Beijing, 29 Oct- 1 Nov 2017
- CDIAC. Global Carbon Budget 2016. <https://cdiac.ess-dive.lbl.gov/GCP/carbonbudget/2016> (2016). Accessed 10 Sept 2020
- Chen, H., Mode, A.W.: Research on 270V / 28V aviation bidirectional DC / DC converter. Paper presented in CSAA/IET International Conference on Aircraft Utility Systems (AUS 2018), Guiyang, 19–22 June 2018
- Chen, H., Cong, T.N., Yang, W., et al.: Progress in electrical energy storage system: a critical review. Prog. Nat. Sci. **19**(3), 291–312 (2009)
- Chen, L., Tarisciotti, L., Costabeber, A. et al.: Advanced modulation for the Active-Bridge-Active-Clamp (ABAC) converter. Paper presented in 2017 IEEE Southern Power Electronics Conference (SPEC), Puerto Varas, 4–7 Dec 2017
- Chen, L., Tarisciotti, L., Costabeber, A., et al.: Phase-shift modulation for a current-fed isolated DC–DC converter in more electric aircrafts. IEEE Trans. Power Electron. **34**(9), 8528–8543 (2019)

- Crittenden, M.: Ultralight batteries for electric airplanes. *IEEE Spectr.* **57**(9), 44–49 (2020)
- Dareck, M., Edelstenn, C., Ender, T.: Flightpath 2050 Europe's Vision for Aviation. <https://ec.europa.eu/transport/sites/transport/files/modes/air/doc/flightpath2050.pdf> (2011). Accessed 05 Sept 2020
- De Doncker, R.W., Divan, D.M., Kheraluwala, M.H.: A three-phase soft-switched high power density DC/DC converter for high power applications. Paper presented in Conference Record of the 1988 IEEE Industry Applications Society Annual Meeting, Pittsburgh, 2–7 Oct 1988
- Demirel, O., Arifoglu, U., Kalayci, K.: Novel three-level T-type isolated bidirectional DC–DC converter. *IET Power Electron.* **12**(1), 61–71 (2019)
- Dorn-gomba, L., Ramoul, J., Reimers, J., et al.: Power electronic converters in electric aircraft : current status , challenges, and emerging technologies. *IEEE Trans. Transp.* **6**(4), 1648–1664 (2020)
- European Environment Agency. Environmental noise in Europe – 2020. <https://www.eea.europa.eu/publications/environmental-noise-in-europe> (2020). Accessed 07 Dec 2020
- Freeman, J., Osterkamp, P., Green, M., et al.: Challenges and opportunities for electric aircraft thermal management. *Aircr. Eng. Aerosp. Technol.* **86**(6), 519–524 (2014)
- Gnadt, A.R., Speth, R.L., Sabnis, J.S., et al.: Technical and environmental assessment of all-electric 180-passenger commercial aircraft. *Prog. Aerosp. Sci.* **105**, 1–30 (2019)
- Hornung, M., Isikveren, A.T., Cole, M. et al: Ce-Liner – Case Study for eMobility in Air Transportation. Paper presented in 2013 Aviation Technology, Integration, and Operations Conference, Los Angeles, 12–14 Aug 2013
- IATA. Aircraft Technology Roadmap to 2050. <https://www.iata.org/contentassets/8d19e716636a47c184e7221c77563c93/technology20roadmap20to20205020no20foreword.pdf> (2019). Accessed 05 Sept 2020
- IEA. Global energy and CO2 emissions in 2020. <https://www.iea.org/reports/global-energy-review-2020> (2020). Accessed 08 Oct 2020
- Jansen, R., Bowman, C., Jankovsky, A. et al.: Overview of NASA Electrified Aircraft Propulsion (EAP) Research for Large Subsonic Transports. Paper presented at the 53rd AIAA/SAE/ASSEE Joint Propulsion Conference, Atlanta, 10–12 July 2017
- Jansen, R., De Jesus-Arce, Y., Kascak, P. et al.: High Efficiency Megawatt Motor Conceptual Design. Paper presented in 2018 Joint Propulsion Conference, Ohio, 9–11 July 2018
- Japan Transport Safety Board, AI2014-4: Aircraft serious incident investigation report (2014)
- Karanayil, B., Ciobotaru, M., Agelidis, V.G.: Power flow Management of Isolated Multiport Converter for more electric aircraft. *IEEE Trans. Power Electron.* **32**(7), 5850–5861 (2017)
- Kolar, J.W., Ertl, H., Zach, F.C.: Design and experimental investigation of a three-phase high power density high efficiency unity power factor PWM (VIENNA) rectifier employing a novel integrated power semiconductor module. Paper presented in Proceedings of Applied Power Electronics Conference. APEC '96, San Jose, 3–7 Mar 1996
- Laloya, E., Lucía, Ó., Sarnago, H., et al.: Heat Management in Power Converters: from state of the art to future ultrahigh efficiency systems. *IEEE Trans. Power Electron.* **31**(11), 7896–7908 (2016)
- Li, Y., Dai, H.: Recent advances in zinc–air batteries. *Chem. Soc. Rev.* **43**(15), 5257–5275 (2014)
- Li, Z., Wang, H.: Comparative analysis of high step-down ratio isolated DC/DC topologies in PEV applications. Paper presented in 2016 IEEE Applied Power Electronics Conference and Exposition (APEC), Lon Beach, 20–24 Mar 2016
- Lilium, GmbH Lilium Jet. <https://lilium.com>. (2020) Accessed 05 Dec 2020
- Lim, Z., Liu, Y., Zhang, L. et al Design of 100 kVA SiC Power Converter for Aircraft Electric Starter Generator. Paper presented at the 4th Southern Power Electronics Conference (SPEC), Singapore, 10–13 Dec 2018
- Liu, B., Ren, R., Jones, E.A., et al.: A modulation compensation scheme to reduce input current distortion in GaN-based high switching frequency three-phase three-level Vienna-type rectifiers. *IEEE Trans. Power Electron.* **33**(1), 283–298 (2018)
- Liu, Y., He, J., Ge, B., et al.: A simple space vector modulation of high-frequency AC linked three-phase-to-single-phase/DC converter. *IEEE Access.* **8**, 59278–59289 (2020)

- Madonna, V., Giangrande, P., Galea, M.: Electrical power generation in aircraft: review, challenges, and opportunities. *IEEE Trans. Transp. Electrification*. **4**(3), 646–659 (2018)
- McLallin, K.L., Jansen, R.H., Fausz, J. et al: Aerospace Flywheel Technology Development for IPACS Applications. Paper presented in 36th Intersociety Energy Conversion Engineering Conference, Savannah, 29 Jul–01 Aug 2001
- Modeer, T., Pallo, N., Foulkes, T., et al.: Design of a GaN-based interleaved nine-level flying capacitor multilevel inverter for electric aircraft applications. *IEEE Trans. Power Electron.* **35**(11), 12153–12165 (2020)
- Murphy, E., King, E.A.: *Environmental Noise Pollution: Noise Mapping, Public Health, and Policy*. Elsevier, Burlington (2014)
- Naayagi, R.T., Forsyth, A.J., Shuttleworth, R.: High-power bidirectional DC–DC converter for aerospace applications. *IEEE Trans. Power Electron.* **27**(11), 4366–4379 (2012)
- NASA. NASA Aeronautics: Strategic Implementation Plan-2017 Update. <https://www.nasa.gov/sites/default/files/atoms/files/sip-2017-03-23-17-high.pdf> (2015). Accessed 05 Sept 2020
- NASA Glenn Research Center. Boeing Cryogenically Cooled Inverter. <https://www1.grc.nasa.gov/aeronautics/eap/larger-aircraft/converters/cryogenically-cooled-inverter> (2019). Accessed 10 Sept 2020
- National Academies of Sciences, Engineering, and Medicine: *Commercial Aircraft Propulsion and Energy Systems Research: Reducing Global Carbon Emissions*. The National Academies Press, Washington, DC (2016)
- Nawawi, A., Tong, C.F., Yin, S., et al.: Design and demonstration of high power density inverter for aircraft applications. *IEEE Trans. Ind. Appl.* **53**(2), 1168–1176 (2017)
- Nikoleris, T., Gupta, G., Kistler, M.: Detailed estimation of fuel consumption and emissions during aircraft taxi operations at Dallas/Fort Worth international airport. *Transp. Res. Part D Transp. Environ.* **16**(4), 302–308 (2011)
- Panasonic. Panasonic Lithium Ion NCR18650B. <https://industrial.panasonic.com/ww/products/batteries/secondary-batteries/lithium-ion> (2012). Accessed 15 Sept 2020
- Pipistrel Aircraft. Pipistrel Velis Electro. <https://www.pipistrel-aircraft.com/aircraft/electric-flight/velis-electro-easa-tc> (2020). Accessed 06 Dec 2020
- Prasad, K.N.V., Kumar, G.R., Kiran, T.V. et al: Comparison of different topologies of cascaded H-Bridge multilevel inverter. Paper presented in 2013 International Conference on Computer Communication and Informatics, Coimbatore, 4–6 Jan 2013
- RCTA. User Guide Supplement to DO-160G. <https://do160.org/rcta-do-160g> (2014). Accessed 21 Sept 2020
- Roboam, X., Sareni, B., Andrade, A.: More Electricity in the air: toward optimized electrical networks embedded in more-electrical aircraft. *IEEE Ind. Electron. Mag.* **6**(4), 6–17 (2012)
- Rodriguez, J., Bernet, S., Steimer, P.K., et al.: A survey on neutral-point-clamped inverters. *IEEE Trans. Ind. Electron.* **57**(7), 2219–2230 (2010)
- Rtichie, H.: Sector by sector: where do global greenhouse gas emissions come from?. <https://our-worldindata.org/ghg-emissions-by-sector> (2020). Accessed 08 Dec 2020
- Safaei, A., Bakhshai, A., Jain, P.: A resonant bidirectional dc-dc converter for aerospace applications. Paper presented in 2011 IEEE Energy Conversion Congress and Exposition, Phoenix, 17–22 Sept 2011
- Sahoo, S., Zhao, Z., Kyprianidis, K.: A review of concepts, benefits, and challenges for future electrical propulsion-based aircraft. *Aerospace*. **7**(4), 44 (2020)
- Schefer, H., Fauth, L., Kopp, T.H.: Discussion on electric power supply systems for all Electric Aircraft. *IEEE Access*. **8**, 84188–84216 (2020)
- Schweizer, M., Kolar, J.W.: Design and implementation of a highly efficient three-level T-type converter for low-voltage applications. *IEEE Trans. Power Electron.* **28**(2), 899–907 (2013)
- Sgouridis, S., Bonnefoy, P.A., Hansman, R.J.: Air transportation in a carbon constrained world: long-term dynamics of policies and strategies for mitigating the carbon footprint of commercial aviation. *Transp. Res. Part A Policy Pract.* **45**(10), 1077–1091 (2011)
- Shakib, S.M.S.I., Mekhilef, S.: A frequency adaptive phase shift modulation control based LLC series resonant converter for wide input voltage applications. *IEEE Trans. Power Electron.* **32**(11), 8360–8370 (2017)

- Shen, M., Wang, J., Joseph, A., et al.: Constant boost control of the Z-source inverter to minimize current ripple and voltage stress. *IEEE Trans. Ind. Appl.* **42**(3), 770–778 (2006)
- Sinnett, M.: Saving fuel and enhancing operational efficiencies. *Aero Q.* **4**, 6–11 (2007)
- Solid Energy. Hermes™ High Energy Rechargeable Metal Cells for Space. <http://sustainableaviation.org/sas2017/session/hermes-high-energy-rechargeable-metal-cells-space/index.html> (2017). Accessed 10 Oct 2020
- Spiazzi, G., Buso, S.: Analysis of the interleaved isolated boost converter with coupled inductors. *IEEE Trans. Ind. Electron.* **62**(7), 4481–4491 (2015)
- Strasik, M., Johnson, P.E., Day, A.C., et al.: Design, fabrication, and test of a 5-kWh/100-kW fly-wheel energy storage utilizing a high-temperature superconducting bearing. *IEEE Trans. Appl. Supercond.* **17**(2), 2133–2137 (2007)
- Stückl, S., van Toor, J., Lobentanzer, H.: Voltair- The All Electric Propulsion Concept Platform—A Vision for Atmospheric Friendly Flight. Paper presented in 28th International Congress of the Aeronautical Sciences, Brisbane, 23–28 Sept 2012
- Tariq, M., Maswood, A.I., Gajanayake, C.J., et al.: Aircraft batteries: current trend towards more electric aircraft. *IET Electr. Syst. Transp.* **7**(2), 93–103 (2017)
- Tarisciotti, L., Costabeber, A., Linglin, C. et al.: Evaluation of isolated DC/DC converter topologies for future HVDC aerospace microgrids. Paper presented in 2017 IEEE Energy Conversion Congress and Exposition (ECCE), Cincinnati, 1–5 Oct 2017
- Tarisciotti, L., Costabeber, A., Chen, L., et al.: Current-fed isolated DC/DC converter for future aerospace microgrids. *IEEE Trans. Ind. Appl.* **55**(3), 2823–2832 (2019)
- Trentin, A., de Lillo, L., Empringham, L., et al.: Experimental comparison of a direct matrix converter using Si IGBT and SiC MOSFETs. *IEEE J. Emerg. Sel. Top. Power Electron.* **3**(2), 542–554 (2015)
- Ventosa-Cutillas, A., Montero-Robina, P., Umbría, F., et al.: Integrated control and modulation for three-level NPC rectifiers. *Energies.* **12**(9), 1–15 (2019)
- Volocopter GmbH. Volocopter VC200. <https://www.volocopter.com/en> (2020). Accessed 05 Dec 2020
- Walter, J., De Doncker, R.W.: High-power galvanically isolated DC/DC converter topology for future automobiles. Paper presented at the 34th IEEE Annual Conference on Power Electronics Specialist, 2003. PESC '03, Acapulco, 15–19 June 2003
- Wheeler, P.: Technology for the more and all electric aircraft of the future. In: Paper presented at 2016 IEEE International Conference on Automatica (ICA-ACCA), Curico, 19–21 Oct 2016
- Wheeler, P.W., Rodríguez, J., Clare, J.C., et al.: Matrix converters: a technology review. *IEEE Trans. Ind. Electron.* **49**(2), 276–288 (2002)
- Wisk Aero. Wisk Cora. <https://wisk.aero/cora> (2020). Accessed 05 Dec 2020
- Yin, S., Tseng, K.J., Simanjorang, R., et al.: A 50-kW high-frequency and high-efficiency SiC voltage source inverter for more electric aircraft. *IEEE Trans. Ind. Electron.* **64**(11), 9124–9134 (2017)
- Yoon, A., Yi, X., Martin, J. et al: A high-speed, high-frequency, air-core PM machine for aircraft application. Paper presented in 2016 IEEE Power and Energy Conference at Illinois (PECI), Urbana, 19–20 Feb 2016
- Zhang, B., Wang, S.: A survey of EMI research in power electronics systems with wide-bandgap semiconductor devices. *IEEE J. Emerg. Sel. Top. Power Electron.* **8**(1), 626–643 (2020)
- Zhang, Z., Bowman, C.L., O’Connell, T.C., et al.: Large electric machines for aircraft electric propulsion. *IET Electr. Power Appl.* **12**(6), 767–779 (2018)
- Zhang, D., He, J., Pan, D.: A megawatt-scale medium-voltage high-efficiency high power density ‘SiC+Si’ hybrid three-level ANPC inverter for aircraft hybrid-electric propulsion systems. *IEEE Trans. Ind. Appl.* **55**(6), 5971–5980 (2019a)
- Zhang, D., He, J., Pan, D. et al: High power density medium-voltage megawatt-scale power converter for aviation hybrid-electric propulsion applications. Paper presented in 2019 IEEE Energy Convers. Congr. Expo. ECCE 2019, Baltimore, 29 Sept–3 Oct 2019b

Chapter 8

Life Cycle Cost Methodology for Replacement Decisions of Aging Aircraft



Zeliha Akça

Nomenclature

| | |
|-----------------|------------------------------------|
| LCC | Life cycle cost |
| CASK | Cost per available seat kilometers |
| CO ₂ | Carbon dioxide |

8.1 Introduction and Literature Review

An aircraft is a long-life asset that requires a high amount of investment, including acquiring and operating. Therefore, fleet composition and operating conditions of the fleet can have a major economic impact on airlines. In this direction, aircraft replacement decisions are strategic level and critical decisions. In addition to the direct impact on financials, fleet is the main determinant of overall operating efficiency, customer satisfaction and competitiveness, and therefore overall sustainability of the airline. The replacement analysis for old aircraft also contributes to the improvement of the sustainability of the airline industry due to the CO₂ emission and noise levels of old aircraft compared to new generation aircraft. This chapter proposes a systematic methodology to evaluate and decide a replacement plan for aging aircraft for an airline's fleet.

The author in (Jiang 2015) reports that the average retirement age for an aircraft is estimated to be between 25 years and 38 years: 25 years for wide-body passenger aircraft, 28 years for single-aisle passenger aircraft, 31 years for wide-body freighters, and 38 years for smaller freighters. The reference (Jiang 2013) states that unlike the retirement age of an aircraft, the economic life of an aircraft may vary from operator to operator, depending on the specifics of the aircraft and the operator's strategies. Based on (Airbus 2019), the number of aircraft will grow more than

Z. Akça (✉)
Turkish Aerospace, Ankara, Turkey

double in the next 20 years, and about 60% of the current aircraft fleet will be replaced with a new aircraft.

Life cycle cost (LCC) analysis is a systematic methodology that simulates and estimates all costs and benefits over the lifespan of an asset or a project and calculates the estimated total cost of having the asset or executing the project. The LCC methodology can be used to obtain the economical assessment of alternative strategies/options/decisions across the lifespan. In general, in literature, this methodology is proposed for the product design and manufacturing phases. However, LCC analysis can be easily generalized for investment projects by considering the time span from the initialization of the project to the finalization of the project. In this chapter, we propose to use LCC analysis to evaluate the aircraft replacement projects for aging aircraft. The methodology that utilizes a scenario analysis is a simple approach for a decision-making process that includes complex cost functions and various stochastic operational parameters.

In (Akça 2018), the author reviews the capabilities of LCC analysis and the related literature on this topic. The study points out the lack of literature on the application of LCC to aircraft replacement project and proposes the approach for evaluation of replacing aging aircraft with younger and/or next-generation aircraft within the scope of industry sustainability trends and their impact to airline replacement strategies.

Some of the earlier literature that are explaining the LCC concept, terminology, principles, main steps, and applications are (Barringer 2003; Barringer 2004; Barringer and Weber 1996; Davis Langdon Management Consulting 2007; Fabrycky and Blanchard 1991; Kawauchi and Rausand 1999; Moore 1964).

Even though the steps of an LCC analysis vary from one case study to another, the authors in (Kawauchi and Rausand 1999) generalize the main steps of a LCC analysis into six activities: problem definition, definition of the cost elements, system modeling, data collection, cost profile development, and evaluation. These activities are advised to be repeated iteratively to improve the overall process.

Determining cost elements and estimating cost functions are very crucial steps in the LCC process in order to have good estimates of economic values of alternative scenarios. To economically evaluate aircraft replacement decisions, all costs in the planning horizon are needed to be simulated and estimated. In (Fabrycky and Blanchard 1991), authors divide these costs into two main categories: acquisition costs and operating and sustaining costs. The sustaining and operating costs can be two to 20 times larger than acquisition costs (Barringer 2003). Therefore, besides initial acquisition costs, it is essential to include all costs associated with the operation of the assets into evaluation to obtain a better economical assessment of aircraft replacement plans.

The first applications of the LCC methodology appeared in military cases (Kawauchi and Rausand 1999). Then, after the 1980s, studies for other industries followed. LCC analysis in literature is mainly applied to product design projects from the perspective of a manufacturer. One close study of aircraft replacement is the replacement of military aircraft F-4 and A-7 with F/A 18 Hornet that is described in (Clarke 1990; McClellan and Dighton 1983). In (Khan and Houston 1999),

authors use the methodology to evaluate two new designs for Bombardier aircraft. Another application related to airline industry is the study (Dawei and Xuefeng 2012) that describes LCC analysis to evaluate aircraft assembly line for cost controlling.

There are not many literatures on the application of LCC analysis directly to aircraft replacement decisions in airline industry from the perspective of an airline. The earlier version of this research is the presentation (Akça 2012) that describes an LCC application for economic evaluation of an aircraft replacement project and briefly includes the case study. In addition, the only other study that we are aware of is (Bastos 2016). In (Bastos 2016), the author does economic evaluation of a replacement of a narrow body aircraft with its new-generation version by using life cycle cost and real options approaches. Looking from a perspective of an airline, the study considers the cost of CO₂ emissions as well as the acquisition and operating costs over the life of the project. The study advises the replacement of the classical model with the more efficient new-generation one in the first year.

There are some LCC projects from a manufacturer's perspective that also partially consider airline perspective. In (Marx et al. 1995), the authors describe a cost model that compares the design and manufacturing alternatives for major components of the wing of an aircraft and discusses the economic impact of the variation on the manufacturer and the airline as well. In (Hölzel et al. 2014), the authors propose a LCC model to evaluate aircraft technologies and operation concepts on future aircraft models from an airline's perspective.

In (Aircraft Commerce 2005), they analyze the economies of replacement of Boeing 757 with a different type and capacity aircraft. Even though the analysis does not consider the life cycle cost of the alternatives, trip cost and cost per seat are calculated based on the operating costs and determined operating environment.

In this chapter, we develop and implement a LCC methodology for the replacement of aging aircraft. The model simulates all the acquisition and sustaining costs that incur during the operation of the aircraft, including depreciation and passenger spill costs. This book chapter demonstrates a simple and flexible methodology that can serve as a decision support tool for an airline's aircraft investment project. The methodology is demonstrated in a case study by describing alternative replacement scenarios with different type of aircraft and acquisition strategies. In addition, a sensitivity analysis for critical parameters and a strategic comparison based on competitive fitness factors are performed. The results reveal the impact of a technological change in the industry to acquisition strategies. The new-generation aircraft can change the cost and operational efficiency that may affect the replacement schedule and acquisition plan.

The structure of this chapter is as follows. Section 8.2 presents the problem definition. Section 8.3 gives the details of the LCC model. Section 8.4 describes the details of the case study as well as the replacement scenarios. The application details of the steps of the LCC methodology are also described in this section. Section 8.5 presents the economic evaluation results and general assessments. Section 8.6 concludes the paper with the final remarks.

8.2 Problem Definition

In this chapter, we look into the replacement problem of aging aircraft in an airline's fleet. The aims of the problem are to answer the following questions:

- When should the aging aircraft be replaced?
- With which type of aircraft should they be replaced?
- What should be the acquisition strategy in the replacement?
- Should be a new-generation aircraft ordered?

Some external and internal factors affect the replacement decisions of an airline. The dynamics of current fleet market, competitor strategies, customer expectations, current market characteristics, and airline's strategies and financials are examples of such factors. Based on these, airline experts can construct applicable replacement scenarios that are specific to the airline's case study. We propose to utilize the LCC methodology to economically evaluate constructed replacement scenarios.

8.3 LLC Methodology

Life cycle is the time span of the replacement project, and LCC is the total cost of the project over its life span that starts at the initialization of the project and ends at the finalization of the project. Life cycle costing or LCC methodology is a technique that enables comparative cost assessments to be made over a specified period of time, taking into account all relevant economic factors both in terms of initial capital costs and future operational and asset replacement cost (definition in (Davis Langdon Management Consulting 2007)). Since it is a noncomplex and flexible tool, we propose a LCC methodology to decide the replacement policy of a set of aging aircraft. In addition, even though there are applications in other sectors especially from the point of a manufacturer and for the product's design phase, the application of LCC for aircraft replacement projects from the point of an airline is scarce.

8.3.1 Main Steps of the Methodology

We implement the LCC methodology in six main steps:

- Design alternative replacement scenarios over the life span of the project.
- Define all related acquisition and sustaining cost elements for all alternatives over the time span.
- Collect data and forecast cost functions over the life span of the project for each scenario.
- Estimate net present value of the total life cycle cost of each alternative.

Do sensitivity analysis of critical costs and parameters, and study possible risks that may alter the replacement decisions.

Do fitness analysis and elect the economically viable and fit scenario.

8.3.2 Airline Operating Costs

Based on the specifications of the case study and airline external and internal factors, alternative scenarios are constructed. These will be explained in the next section. As the second step of the LCC methodology, to properly evaluate aircraft replacement alternatives, all related costs are needed to be identified and simulated in the planning horizon. Cost elements are divided into two groups:

Costs of acquiring or obtaining the aircraft or cost of ownership.

Costs of sustaining the aircraft in the fleet.

Ownership costs for an aircraft are functions that depend on the ownership strategy. In general practice, there are three acquisition/ownership strategies:

Purchasing the aircraft/financial lease: One option for obtaining an asset is to purchase the asset. However, since the purchase cost is very high especially for new aircraft, in general, airlines use the financial lease method. In this chapter, we use financial lease to purchase an aircraft. In financial lease option, monthly rental (financing) cost is paid for 10–15 years (for new aircraft, in general), depending on the period agreed with the financier. After the payment period ends, the airline becomes the owner of the asset, depending on the agreement. In this method, since the airline will get the ownership, the airline will have the residual value risk of the aircraft.

Operational lease: It is an option to obtain an asset from a lessor (the legal owner of the asset) by paying monthly rental fees. In this option, a short term, such as 4–8 years, or a longer term, such as 12–14 years, can be used as operational lease periods. In this option, lessor has the residual value risk. Depending on the agreement and the lease period, after the lease period, especially for longer periods, lessor may offer a purchase option to the lessee. In this chapter, when we use operational lease, we assume that the lessor remains the legal owner of the aircraft and the airline will return the asset to the lessor at the end of the agreed lease period.

Wet lease: Similar to operational lease, the aircraft is rented from a lessor by renting monthly rental fees. However, in wet lease option, the cockpit crew (depending on the agreement also the cabin crew) that will fly that specific rental aircraft comes with the aircraft to operate it. Therefore, rental fee includes the cost of the crew who is actually employed by the lessor company. In general, wet lease periods are relatively short such as 1–2 years. At the end of the term, aircraft and its crew are returned to the lessor company. Since the crew hours are included in the rental fees, the rents are higher than the operational lease cases. In addition,

operating cost of a wet-leased aircraft is calculated differently than the financial or operational leased aircraft, since some of the operating costs are already included in the monthly rental fee.

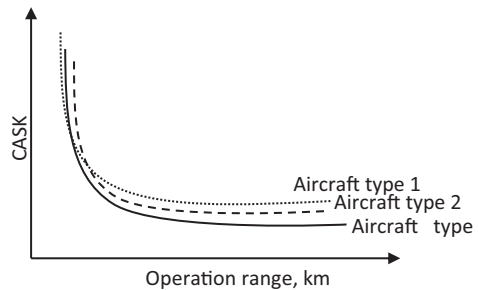
Ownership cost for an aircraft is a function that depends on the ownership strategy, aircraft type, lease period, and age of the aircraft. Insurance cost can also be included into the ownership cost. In addition, if the airline is the legal owner of the aircraft, a salvage value (a revenue item) occurs when removing the aircraft from the fleet.

The major components of aircraft sustaining costs, in other terms operating costs (excluding ownership costs), are maintenance, fuel, crew, navigation, landing, handling, airport, catering and indirect costs, etc. In this research, it is assumed that all aircraft are operated and none of them is kept unused, and therefore sustaining costs are equal to the operating cost. These costs are functions of an airline's operational parameters (such as block hour, utilization, network structure, load factor, etc.), type of the aircraft, age of the aircraft, and specific unit costs.

The summation of ownership and sustaining costs is the total operating cost. Based on the airline data analyzed in (Lee et al. 2001), ownership costs, including insurance, depreciation, and amortization, are about 25% of the total direct operating costs. This rate may change depending on the airline's characteristics.

Estimation of cost components is very important for replacement problems. Since aircraft have high operating costs, total unit costs may change dramatically depending on the type of the aircraft and operational environment (such as the route served, number of passengers or cargo load, utilization, speed and block hour, etc.). Figure 8.1 presents the hypothetical unit cost (cost per available seat kilometers (CASK)) functions based on the operation range (hypothetically derived from processing the airline data). Depending on the range of a route, an aircraft may result in significantly alternating unit operating cost. For each cost component, cost functions are determined and estimated based on the airline data. Details are explained in the next section.

Fig. 8.1 Hypothetical unit cost functions (based on sample data) depending on the range and aircraft type



8.4 Case Study: Aircraft Replacement Project

8.4.1 General Information

In this section, we describe the implementation details of the LCC methodology for an aircraft replacement project. There is a fleet of wide-body Airbus 340–300 aircraft (N aircraft). All have the same two-class seating configuration. There are 34 business class and 236 economy class seats in each. Some of the aircraft are 14 years old and some are 19 years old. This makes two subtypes, T1 (aircraft that are 14 years old) and T2 (aircraft that are 19 years old). These aircraft are operated on certain long-haul routes that have 9–12 h of one-way block hour. With the east and west balance of routes, one frequency (in a day) of these routes can be operated by an aircraft in Airbus 340 fleet. Each aircraft rotates from one route to another in a circular order; therefore, each aircraft in the fleet operates the same set of routes with same number of total frequencies and block hours per year. All aircraft have the identical operation conditions (utilization, block hour, maintenance time, etc.) and number of landings per year. The planning horizon is 20 years. Airbus 340 is a four-engine old-generation aircraft, and the manufacturer stopped the production line of the type.

8.4.2 Replacement Scenarios

There can be many possible replacement scenarios including alternating new aircraft types and different replacement periods. However, in real life, depending on the characteristics and the strategies of the airline and current aircraft market, there are not many viable options, and it is reasonable that the airline analysts and decision makers build the limited number of alternative scenarios to be evaluated. Four different scenarios are built for the replacement of old aircraft. A general description of the four scenarios is given in Fig. 8.2. Details are as follows.

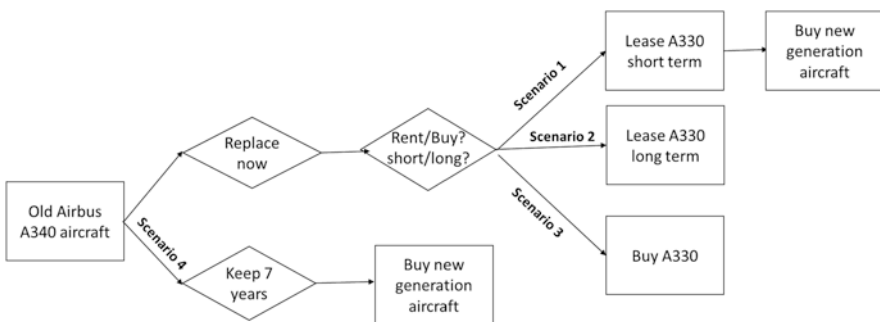


Fig. 8.2 General description of scenarios

Even though there are two subtypes, T1 and T2, since all aircraft are old and cost inefficient (mainly due to four engines), all are decided to be replaced together. The closest wide-body aircraft within the market, Airbus 330–200 (this type of A330 is selected due to the required range), or a new-generation wide-body aircraft Boeing 787 with similar capacity is considered as replacement options. At the beginning of the project, the new-generation aircraft is not available in the market. They are still in the design or test phase and will be expected to start operation after 7 years. The four scenarios are built based on the two main questions. The first main question is that whether we replace them now or wait for 7 years until the new-generation aircraft is available. The second question is that if we replace them now, which acquisition strategy is the best.

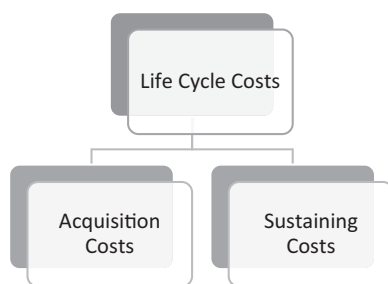
In the first three scenarios, we replace all N aircraft at the beginning of the horizon. In Scenario 1, we get N Airbus 330 for 7 years using a short-term operating lease and afterward purchase (using financial lease) N new-generation aircraft. In Scenario 2, we get N Airbus 330 for 20 years using a long-term operating lease. In Scenario 3, we purchase (using financial lease) N Airbus 330. In Scenario 4, we keep using current aircraft for 7 years and then purchase (using a financial lease) N new-generation aircraft.

8.4.3 Cost Items

In order to properly evaluate aircraft replacement alternatives, all related costs are needed to be identified and simulated in the planning horizon. We categorize the life cycle costs into two groups: acquisition costs and sustaining costs (Fig. 8.3.).

In this study, acquisition costs are the costs related to ownership of the aircraft. Those include operating lease and financial lease payments such as aircraft-related insurance costs. In addition, salvage value and the tax benefit due to depreciation costs are in this category. Salvage value is the resale value of an owned aircraft, and tax benefit is the reduction amount in the tax liability due to the noncash (implicit) depreciation cost of owned assets. Depreciation cost reduces the total taxable profit and therefore reduces the tax liability with the applicable tax rate. Purchased (financially leased) assets have a periodic depreciation cost and salvage value when they

Fig. 8.3 LCC categories



are sold (if sold after the ownership passed on the airline). Salvage value and tax benefit due to depreciation are negative cost items (revenue items). Since whether we get a salvage value or a depreciation tax benefit from an aircraft depends on the acquisition strategy and different acquisition strategies are evaluated in the scenarios, it is important to add these items to the life cycle cost value of a scenario.

Sustaining costs are the direct and indirect costs (excluding the ownership costs) that the airline bears in order to operate these aircraft on these routes. Sustaining costs that are considered here are operating costs, such as maintenance, fuel, airport, air navigation, crew, landing, handling, sales and marketing, passenger services and catering, and indirect costs, such as the general administration cost.

In addition, we calculate the spill cost that is the loss of revenue due to the passengers that are rejected because of the insufficient capacity of the aircraft. In this research, different aircraft with different seating configuration are evaluated. Therefore, spill cost must be included to measure the cost of the airline to use different capacity aircraft. The list of cost items used are as follows:

Acquisition costs:

Periodic (operational or financial) lease payments (if any).

Insurance cost.

Salvage value (negative cost).

Tax benefit due to depreciation (negative cost).

Sustaining costs:

Maintenance cost.

Fuel cost.

Other direct costs such as airport cost, air navigation cost, crew cost, landing cost, handling costs, sales and marketing costs, passenger services, and catering.

Indirect costs such as general administration cost.

Spill cost.

8.4.4 Cost Functions

One of the most difficult part of the LCC methodology is to estimate the costs over the planning horizon. In this case study, we use mostly the historical data and some directions from the literature to estimate the cost functions.

Lease costs, salvage value, and tax benefit depend on the aircraft type, lease type, lease period, age of the aircraft, and block hour dedicated for this project, i.e., total amount of block hour used to operate these four routes. In addition, tax rate is used to calculate the tax benefit.

Similarly, sustaining costs depend on the aircraft type, age of the aircraft, and block hour. In addition, unit fuel cost is used for fuel cost, average load factor is utilized to estimate passenger-specific costs, and destination specific historical costs are used to estimate navigation, airport, and landing costs. Indirect costs are allocated based on the block hour of the routes.

One of the most important motivation behind the replacement projects is that the aircraft becomes cost inefficient, as it gets older. Maintenance and fuel costs increase with the age of the aircraft. Furthermore, new aircraft is more cost efficient compared to the previous models. In (Air Transport Action Group 2010), a graph that is showing the fuel efficiency gained with the aircraft models introduced from 1960 to 2010 is presented. Aircraft models today are about 82% more fuel efficient compared to models introduced in the 1960s due to design enhancements (Air Transport Action Group 2010). Similarly, aircraft engines are about 50% more efficient compared to models in the 1960s (Air Transport Action Group 2010). In (TBE International 2014), the reduction in base maintenance costs obtained with the new-generation aircraft is investigated and confirmed.

We have the average maintenance and fuel costs (per block hour for each type of currently available aircraft) based on airline data and based on supplier data (for the new-generation aircraft). However, we also need to estimate these costs over the planning horizon changing based on the age of the aircraft. Even with the historical data, it is very difficult to estimate the cost functions of maintenance and fuel with respect to the age of the aircraft, since there are many other operational metrics and strategies (such as load factor, utilization of the aircraft, flight and maintenance schedules, etc.) that may impact the cost efficiency. There are only a few research in literature investigating the maintenance cost change based on the aircraft age. (Dixon 2006; International Air Transport Association 2018) are one of these literatures. Airframe and engine maintenance and a different type of maintenance checks based on age are investigated in these.

In this case study, we consider the maintenance check periods and apply slightly conservative estimation for fuel and maintenance costs based on age. For fuel consumption, we assume 0.1% to 0.2% consumption change, as the age gets older for the first 12 years; after that, we assume constant 0.2% fuel consumption increase per year. Similarly, for maintenance cost, we assume 2% to 6% increase rates that can change depending on the year of the heavy maintenance for the first 12 years. Afterward, we assume 6% maintenance cost increase per year. We assume slight rate decreases for both fuel and maintenance for couple years after year eight, that is, the year of the heavy maintenance check. Figure 8.4 shows the estimation of the fuel consumption and maintenance cost increase relative to the first year.

Spill cost is calculated for both business class and economy class separately based on the average demand and average revenue per passenger for each

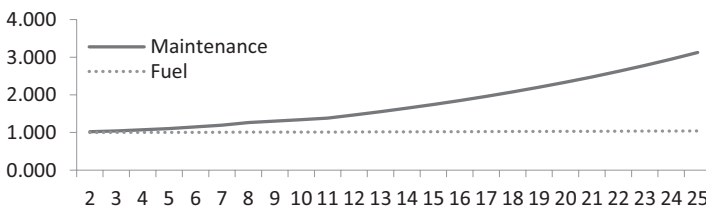


Fig. 8.4 Fuel consumption and maintenance cost relative to the first year

destination. Based on the historical data of the routes, with the assumption of normal demand, mean and standard deviation of the demand are estimated. Some demand growth for the mean demand is assumed over the 20-year planning horizon per year. Demand samples of size 500 are generated for each day in a year. Based on the samples, average spilled passenger numbers are calculated. Spill cost is obtained by multiplication of spilled passengers with an average passenger revenue.

8.4.5 Basic Assumptions

In real life, all aircraft in a fleet are economically dependent. For simplicity, within the scope of LCC analysis and the scenario analysis, we assume that the assets that we consider in the project are economically independent from other aircraft in the airline fleet. However, to consider some limited dependency indirectly, while constructing the scenarios, only the aircraft that are compatible with the current airline fleet are considered as replacement. In addition, in this project, Airbus A340 fleet and the routes that are operated by those are assumed independent from other airline operations.

In addition, we assume that all cost parameters are deterministic and the 20-year planning horizon does not include any disruptions other than small demand fluctuations.

All of the acquisition and sustaining costs are in US dollars, and costs over the planning horizon are discounted with the discount rate of 5% to obtain the net present value of each scenario.

8.5 LCC Results

8.5.1 General Results

The net present value of the LCC for 20 years of each scenario is calculated. Due to the confidentiality of the real costs, we do not list cost values in the previous section, and here we present normalized comparative results. We normalize the LCC results of the scenarios based on the minimum value. Figure 8.5 presents the normalized net present value of the total cost for each scenario. Scenario 1 has the lowest cost while Scenario 2 has 6%, Scenario 3 has 2%, and Scenario 4 has 3% higher cost than Scenario 1, respectively. Comparison of the scenarios provides the following conclusions:

Based on cost, Scenario 1 (replacing the old aircraft at the beginning of the project with Airbus 330 using a short-term lease and then replacing them with the new-generation aircraft) is superior (about 2–6%) to other scenarios.

Fig. 8.5 Total LCC of each scenario (normalized net present values)

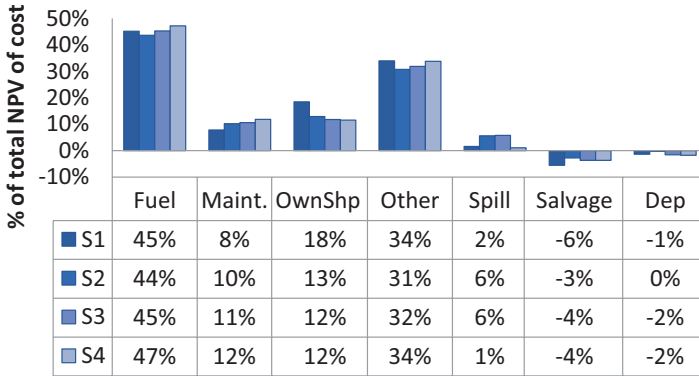
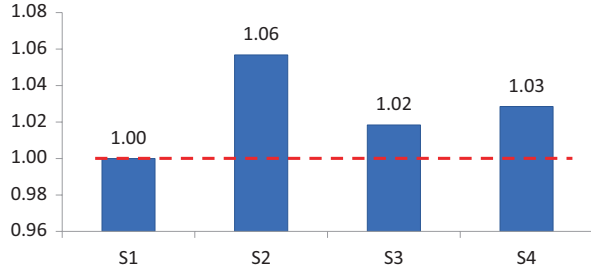


Fig. 8.6 % distribution of cost components

Comparison of Scenarios 2 and 3 shows that in the long term, financial lease is better than the operating lease in terms of cost.

The new-generation aircraft provides a significant cost advantage.

Comparison of Scenario 1 and 4 shows that the sustaining cost of the old aircraft is very high. Even the cost advantage due to zero ownership cost for 7 years is not enough to compensate the sustaining cost of the old aircraft.

Figure 8.6 presents the percentage distribution of cost components in each scenario. Due to the nature of the scenarios, there are some clear outcomes. Percentages of fuel and maintenance costs are largest, and the ownership cost is smallest in Scenario 4 due to the usage of old owned aircraft for 7 years. The ownership percentage is highest in the first scenario since the new-generation aircraft is more expensive than the classical models as well as the short terms lease that is used for 7 years. In addition, spill cost is highest in Scenarios 2 and 3, since the total capacity is smallest in these scenarios.

Figure 8.7 compares the cost items in each scenario. Each cost item is normalized separately and is normalized based on the minimum value of that cost item in all scenarios. Results are in align with the results of Fig. 8.6 Scenario 4 has the largest fuel and maintenance costs and the smallest ownership cost. Scenario 1 has the lowest fuel and maintenance costs however the largest ownership cost. Scenarios 2

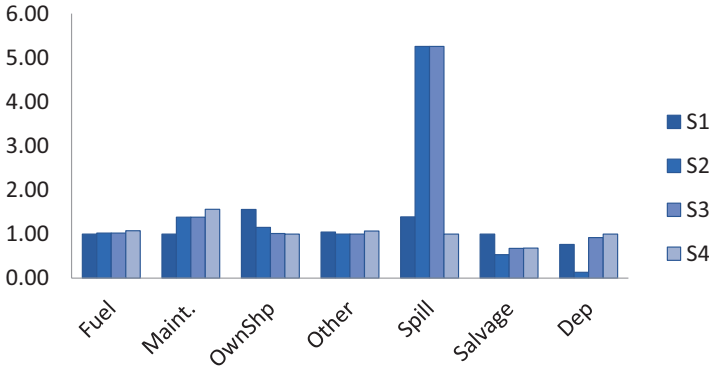


Fig. 8.7 Comparison of cost items (each one is normalized to minimum)

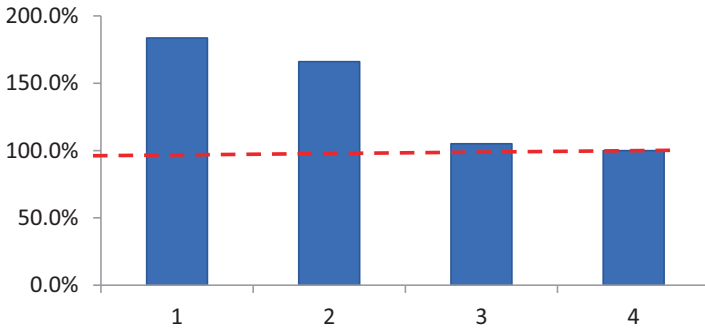


Fig. 8.8 Comparison of acquisition costs (normalized to minimum)

and 3 have about five times spill cost of other scenarios due to the capacity of the aircraft. Scenario 1 has the largest salvage value since we sell the old aircraft immediately and get a higher salvage value in today’s dollars. Tax benefit due to depreciation is smallest in Scenario 2 since operating lease option does not have any depreciation since the airline has not the ownership of the aircraft in operating lease.

Figure 8.8 presents comparison of acquisition costs (including ownership cost, salvage value, and depreciation) of scenarios. Scenario 4 has the smallest acquisition cost even though with the new-generation aircraft since owned aircraft are used for 7 years and the new-generation aircraft are used for 13 years. Scenario 1 has about 1.8 times acquisition cost of Scenario 4. Scenario 3 has the second smallest acquisition cost due to the ownership strategy in the scenario. In the long run, purchasing an aircraft has lower acquisition cost than the operating lease. In addition, a classical aircraft model is cheaper than the new-generation aircraft.

In this research, we assume that the fuel consumption and maintenance costs naturally increase with the age of the aircraft, and we estimate these costs as a function of age. In this section, we investigate the answer to the question of what if we ignore the age effect in the fuel and maintenance cost functions. Figure 8.9 presents

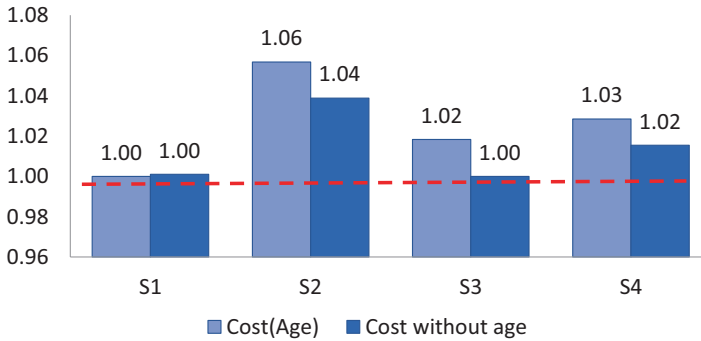


Fig. 8.9 Addition of age effect to total costs in the scenarios

the LCCs of the scenarios with constant fuel and maintenance costs over the years and compare the results with the LCCs considering the age impact. Without the age impact, even though the cost of Scenario 1 is very close to 3, Scenario 3 has the lowest cost. The impact of the new-generation aircraft is not large if the aircraft does not get fuel and maintenance inefficient with the age. In addition, the costs of Scenarios 2 and 4 are closer to Scenario 3 with the lowest cost. The results of this case study reveal the importance of estimation of cost functions and the impact of this step to the overall outcome.

8.5.2 Sensitivity Analysis

Some of the parameters might be critical and have a major impact on the results. In order to investigate critical parameters and update estimations, we can measure the sensitivity of the results to parameters. The nature of the LCC methodology enables a sensitivity analysis that would provide a complete evaluation of the scenarios.

Some of the parameters that needs more attention can be the unit fuel price, unit maintenance cost, aircraft utilization, lease prices, and average passenger revenue. We did a sensitivity analysis for these parameters. The best scenario is Scenario 1 and this result does not seem to be sensitive to these parameters. As an example, here we present the sensitivity analysis results for fuel prices. We assume that the unit fuel price is constant in the planning horizon. Results presented in Section 8.5.1 are based on this assumption. Here, we compare the constant fuel price results with the cases where the fuel price increases or decreases with a constant rate in every year. Figure 8.10 presents the results of scenarios with yearly changing fuel prices. Overall, Scenario 1 is the best scenario with the lowest cost. Results are not sensitive to the yearly increasing or decreasing fuel prices. Figure 8.11 presents the comparison of scenarios with different unit fuel prices. Even with different unit fuel prices, Scenario 1 is the best scenario. Results of Scenario 4 are very sensitive to the fuel price due to the usage of old aircraft for 7 years before the new-generation

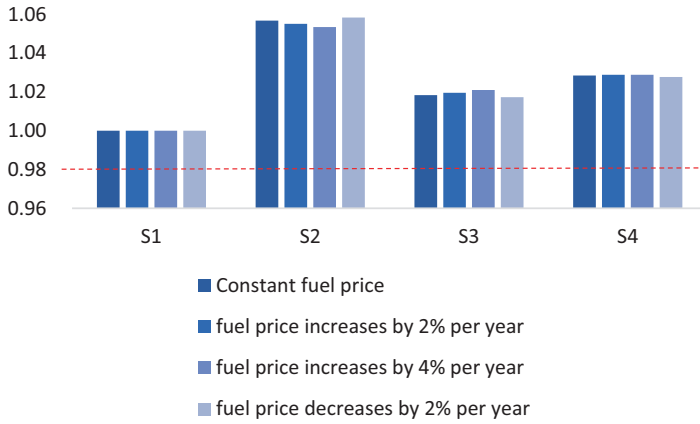


Fig. 8.10 Comparison of scenarios with different fuel price increase rates

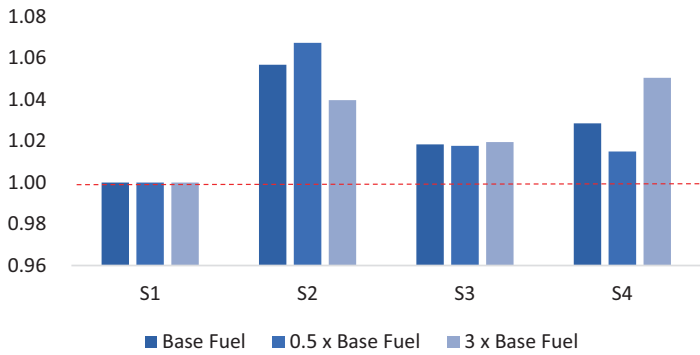


Fig. 8.11 Comparison of scenarios with different base fuel price rates

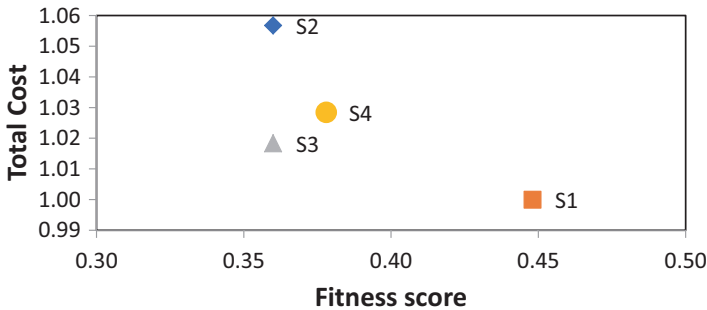
aircraft. If the fuel price is very low, then the cost of using the owned old aircraft does not hurt too much.

8.5.3 Cost Vs. Fitness

In real life, when we select the best solution, there might be other objectives to consider in addition to the total cost of the project. In this section, we evaluate the scenarios and measure their fitness to other objectives. Five criteria are considered for the fitness: unscheduled maintenance and reliability, demand capture, compatibility with current fleet, future aircraft market and airline’s fleet strategy, and customer satisfaction. Table 8.1. presents the fitness score of each scenario for each criterion. The general motivations underlying the scores given in Table 8.1. are as follows.

Table 8.1 Evaluation of fitness based on selected factors

| Factors | S1 | S2 | S3 | S4 |
|---|-------|------|------|-------|
| <i>Unscheduled maintenance and reliability</i> | 0.8 | 1 | 1 | 0.6 |
| <i>Demand capture</i> | 0.8 | 0.5 | 0.5 | 1 |
| <i>Compatibility to current fleet</i> | 0.7 | 1 | 1 | 0.7 |
| <i>Future market and fleet strategy</i> | 1 | 0.9 | 0.9 | 1 |
| <i>Customer satisfaction</i> | 1 | 0.8 | 0.8 | 0.9 |
| <i>Overall score (multiplication of all scores)</i> | 0.448 | 0.36 | 0.36 | 0.378 |

**Fig. 8.12** Assessing cost vs. fitness for scenarios

The new-generation aircraft has a lower score for the unscheduled maintenance and reliability (since it will be new to the market).

The old aircraft has a lower score for the unscheduled maintenance and reliability (due to age).

The new-generation aircraft has lower score for the compatibility with the current fleet.

Demand capture scores are based on the capacity of each aircraft type and spill costs. In the future, sector and airline tend to have more new-generation aircraft.

Customer satisfaction rates for new-generation aircraft are higher.

We evaluate the overall fitness function by multiplying scores for each criterion. Scenario 1 has the highest fitness score of 0.448. Figure 8.12 presents the total cost and fitness of each scenario. Scenario 1 is the best replacement solution in terms of cost as well as fitness to other airline objectives. In order to evaluate projects, a decision maker may need to consider all important objectives. In some cases, when the cost or total economic value of the projects is very close to each other, a decision maker may select a project that has higher fitness value and slightly lower economic value.

8.6 Conclusion

In this chapter, a LCC methodology is proposed in order to decide aircraft fleet replacement schedule and acquisition strategy for the aging aircraft from the perspective of an airline. Fleet composition and specifics of the aircraft in the fleet have major impact on operating efficiency of the airline. Furthermore, new aircraft models are more fuel-efficient (and less noisy) compared to the previous models. Therefore, a methodology to evaluate aircraft replacement projects contributes to the sustainability of the industry and the airline. This topic, application of LCC for an airline decision maker, is scarce in the literature. To demonstrate the methodology, a case study is conducted by constructing four real scenarios that define replacement strategies with different type of aircraft and acquisition strategies. LCC methodology calculates total cost of each scenario to economically evaluate and compare aircraft types, and assess operation dynamics and replacement strategies. The analysis also considers depreciation and passenger spill costs, which is also different from previous literature. In addition, the chapter includes a sensitivity analysis for critical parameters and a strategic comparison of scenarios based on alternative objectives. For the case study described, four replacement scenarios are determined based on the characteristics of the airline and the aircraft to be replaced. In the three of the scenarios, the old aircraft are replaced immediately, while in one scenario, the old aircraft will be used until a new-generation aircraft is available for the replacement. Two of the four scenarios include a new-generation aircraft that would bring significant fuel and maintenance cost advantage compared to the classical models.

In order to calculate the total LCC of the scenarios, all acquisition and sustaining costs that would incur during the life span of the project are estimated. The analysis considers periodic aircraft lease payments, insurance cost, salvage value when aircraft is sold, tax benefit due to depreciation values, maintenance cost, fuel cost, and other direct costs (such as airport cost, air navigation cost, crew cost, landing cost, handling costs, sales and marketing costs, passenger services, and catering) and indirect costs (such as general administration cost and passenger spill cost). In addition, aging impact for the fuel consumption and maintenance cost functions is estimated and included in the analysis. Purchasing through financial lease, short-term operating leasing, and long-term operating leasing are the three acquisition strategies that are used in scenarios.

The chapter presents various results of economic assessment of the scenarios based on the calculated LCC results. Results advise the replacement of old aircraft immediately at the beginning of the horizon. Due to the significant maintenance and fuel cost advantage of the new-generation aircraft, the results prove that the best replacement strategy is to replace the old aircraft with the new-generation aircraft. Until the new-generation aircraft is available in the market, a compatible classic aircraft acquired with a short-term operating lease is used. In addition, the results show that in the long run, financial lease option is better than the operational lease option. In addition, case study results reveal the importance of including age impact

on the fuel and maintenance cost, which may change the economic assessment of the decision maker.

One major limitation of the proposed LCC methodology is its failure to consider uncertainty. All parameters and cost functions are assumed deterministic. In reality, there are great level of uncertainty in the passenger and aircraft markets, affecting the major operating costs, aircraft lease, and salvage values. However, aircraft are long-term high-value assets; decision maker needs to take high investment risks. Therefore, in general, airlines use different acquisition strategies, including purchasing, short-term leasing, and long-term leasing, to obtain some flexibility to manage investment risks. In addition, using options in the purchase agreements is a way to get some investment flexibility. Here, even the methodology is deterministic; it is easy to evaluate the impact of some parameters using the sensitivity analysis based on some variations of critical parameters. The best scenario selected is shown to be insensitive to possible operating uncertainties. When the project value and risk are large, more comprehensive methods that would also consider stochastic nature of the environment are needed for the decision maker. For such cases, sensitivity analysis may be insufficient to cover all uncertainties. Development of such methodology for aircraft replacement project is left for future work.

Acknowledgments I gratefully thank Prof. Dr. Ahmet Bolat and Cengiz Polat for their expert opinions and contributions to the design of the study and computational experiments.

References

- Air Transport Action Group. Beginner's guide to aviation efficiency. <https://www.atag.org/our-publications/latest-publications.html> (2010). Accessed 19 Apr 2020
- Airbus. Global market forecast 2019–2038 Booklet. In: Airbus Global Market Forecast. <https://www.airbus.com/aircraft/market/global-market-forecast.html> (2019). Accessed 19 Apr 2020
- Aircraft Commerce. Analysing the options for 757 replacement. Aircraft Commerce (42). <http://docplayer.net/20886604-Analysing-the-options-for-757-replacement-the-757-has-been-in-operation.html> (2005). Accessed 19 Apr 2020
- Akça, Z.: Fleet replacement model and aircraft LCC to determine acquisition strategies. In: Abstracts of AGIFORS scheduling and strategic planning study group meeting, AGIFORS, Barcelona, 3–4 May 2012
- Akça, Z.: Reflection of sustainability issues in airline strategies and overview of life cycle cost analysis. *Int. J. Sustain. Aviation*. **4**(2), 133–146 (2018)
- Barringer, H.P.: A life cycle cost summary. In: International conference of maintenance societies, ICOM-2003, Perth, 20–23 May 2003
- Barringer, H.P.: Life cycle cost analysis—who does what? In: Maintenance conference and exhibition, National Petrochemical and Refiners Association, San Antonio, 25–28 May 2004
- Barringer, H.P., Weber, D.P.: Life cycle cost tutorial. In: Fifth international conference on process plant reliability, Houston, 2–4 October 1996
- Bastos, M.D.: Economical Evaluation of Aircraft Replacement the A320 Case Study. Master thesis, Técnico Lisboa (2016)
- Clarke, J.D.: Life Cycle Cost: An Examination of Its Application in the United States, and Potential for Use in the Australian Defense Forces. M.S. Thesis, Naval Post Graduate School (1990)

- Davis Langdon Management Consulting. Life cycle costing (LCC) as a contribution to sustainable construction: a common methodology literature review. <http://ec.europa.eu/DocsRoom/documents/5059/attachments/1/translations/en/renditions/native> (2007). Accessed 19 Apr 2020
- Dawei, L., Xuefeng, Z.: Research on the application of life cycle cost management in the civil aircraft assembly line project. *Phys. Procedia*. **25**, 443–451 (2012)
- Dixon, M.: The maintenance cost of aging aircraft insights from commercial aviation. In: RAND Corporation monograph series. RAND Corporation. https://www.rand.org/content/dam/rand/pubs/monographs/2006/RAND_MG486.pdf (2006). Accessed 19 Apr 2020
- Fabrycky, W., Blanchard, B.: *Life-Cycle Cost and Economic Analysis*. Prentice Hall, Englewood Cliffs (1991)
- Hölzel, N.B., Schilling, T., Gollnick, V.: An aircraft life cycle approach for the cost-benefit analysis of prognostics and condition-based maintenance based on discrete-event simulation. In: Annual conference on the prognostics and health management society, Fort Worth, 29 September – 2 October 2004, (2014)
- International Air Transport Association. Maintenance costs for aging aircraft. <https://www.iata.org/contentassets/bf8ca67c8bcd4358b3d004b0d6d0916f/mcaa-Isted-2018.pdf> (2018). Accessed 19 Apr 2020
- Jiang, H.: Key Findings on Airplane Economic Life. Boeing Commercial Airplane Company. http://www.boeing.com/assets/pdf/commercial/aircraft_economic_life_whitepaper.pdf (2013). Accessed 19 Apr 2020
- Jiang, H. Trends in Fleet and Aircraft Retirement. Boeing Commercial Airplane Company. <https://www.aviationsuppliers.org/ASA/files/ccLibraryFiles/Filename/000000001327/GS%20Tues%20-%20Jiang.pdf> (2015). Accessed 19 Apr 2020
- Kawauchi, Y., Rausand, M.: Life cycle cost (LCC) analysis in oil and chemical process industries. https://www.researchgate.net/publication/228594034_Life_Cycle_Cost_LCC_Analysis_in_Oil_and_Chemical_Process_Industries (1999). Accessed 19 Apr 2020
- Khan, K.A., Houston, G.D.: Design optimization using life cycle cost analysis for low operating costs. Defense Technical Information Center Compilation Part Notice, ADPO10423 (1999)
- Lee, J.J., Lukachko, S.P., Waitz, I.A.: Historical and future trends in aircraft performance, cost and emissions. *Annu. Rev. Energy Environ.* **26**, 167–200 (2001)
- Marx, W.J., Mavris, D.N., Schrage, D.P.: A Hierarchical Aircraft Life Cycle Cost Analysis Model. American Institute of Aeronautics and Astronautics. https://www.researchgate.net/publication/2434807_A_Hierarchical_Aircraft_Life_Cycle_Cost_Analysis_Model (1995). Accessed 19 Apr 2020
- McClellan, H., Dighton, R.S.: The F/A 18 hornet-low life cycle cost by design. In: Proceedings of annual reliability and maintainability symposium 1983:403–410.
- Moore, C.L.: The present value method and replacement decision. *Account. Rev.* **39**, 94–102 (1964)
- TBE International. Impact of technology changes on maintenance costs, (2014)

Chapter 9

Numerical and Experimental Investigation of Aerodynamic Characteristics of an Unmanned Aerial Vehicle in a Low Subsonic Wind Tunnel



Furkan Dilbaz, Adnan Burak Incedal, Talha Batuhan Korkut, Yasemin Nur Aydın, Seda Kırmacı Arabacı, and Aytaç Gören

Nomenclature

| | |
|---------------------------|---|
| ρ | Fluid density |
| P | Pressure |
| μ | Coefficient of dynamic viscous |
| u_i | Fluctuating velocity |
| G_ω, G_k | The formation of kinetic energy of turbulent and specific dissipation |
| Γ_k, Γ_ω | Diffusivity |
| S_k, S_ω | Source terms |
| Y_k, Y_ω | Dissipation |
| u_T | The friction velocity |
| τ_w | The wall shear stress |
| C_f | The skin friction coefficient |
| u_i | Fluctuating velocity |
| ν | The kinematic viscosity |
| V | The flight speed |
| c_{root} | The length of root chord |
| λ | Taper ratio |
| c_{tip} | The length of tip chord |
| C_L | Aerodynamic lift coefficient |
| C_D | Aerodynamic drag coefficient |

F. Dilbaz · A. B. Incedal · Y. N. Aydın · S. K. Arabacı
Department of Mechanical Engineering, Celal Bayar University, Manisa, Turkey
e-mail: seda.kirmaci@cbu.edu.tr

T. B. Korkut · A. Gören (✉)
Department of Mechanical Engineering, Dokuz Eylül University, Izmir, Turkey
e-mail: aytac.goren@deu.edu.tr

9.1 Introduction

9.1.1 Literature Investigations

Unmanned aerial vehicles (UAV) are widely preferred today in the field of military and civil aviation due to parameters, such as ease of use, cost, life safety, and operational advantages (Ehrhard 2010). With the start of working on the UAV in the World War I and the increased interest in cruise missiles in the World War II, the interest in the UAV culture had increased rapidly (Keane and Carr 2013). In favor of the UAV, during the war, the crew was not damaged, and the opportunity of observation and data flow, as well as the opportunity to attack with the ammunition it could carry within its load-carrying capacity, was provided. In order to meet the military and civilian demands of the UAVs, which have been actively developing since the World War I, different designs are modeled according to the environmental conditions. While continuing the development of UAVs plays an active role in the war, UAVs are at the entrance of the Turkey market in the 2000s (Kahvecioglu and Oktal 2016). Following Bayraktar UAV, which was the first Turkish design and production of the Mini UAV system in 2006, the Turkish UAV market has grown with designs, such as Anka, Keklik, Gözcü, Turna, and Malazgirt (Kahvecioglu and Oktal 2016).

Unmanned aerial vehicles in both the world and Turkey aviation industry sector continue to work unabated. As time is processed, improvements are made in many parameters, such as aerodynamics, strength, lightweight, and fuel savings on the UAV. It is very important to examine the aerodynamic effects on aircraft such as UAVs, in order to reveal the change due to the air effect during the movement of the aircraft. In addition to military use, aerodynamic studies of single-rotor or multi-rotor drone UAVs, which are accepted as small aircraft in the literature in commercial use, are also continuing (Ventura Diaz and Yoon 2018). Vuruskan et al. defined the TURAC transition-flight mathematical model of the unmanned aerial vehicle (UAV) and examined the aerodynamic effects on CFD to define transition-flight regimes and aerodynamic coefficients (Vuruskan et al. 2014). Kapseong Ro and Kaushik Raghu analyzed the aerodynamic study of the free-wing tilt-body concept using the mathematical panel method and compared it with the experimental wind tunnel results (Ro et al. 2007). Wisnoe et al. examined the effect of different Mach numbers on aerodynamic lift coefficient (C_L), drag coefficient (C_D), and pitching moment coefficient (C_M) values on the blended wing body (BWB) aircraft designed at MARA University of Technology (UiTM; Wisnoe et al. 2009). Funes-Sebastián and Ruiz-Calavera examined the effect of wind tunnel test walls on the Eikon model, a high-transonic UAV prototype, and compared the experimental data with CFD numerical results (Funes-Sebastian and Ruiz-Calavera 2014). Pattinson et al. produced 5 degrees of freedom hardware equipment suitable for the wind tunnel so that the maneuvering movements of aircraft models could be analyzed experimentally (Pattinson et al. 2013). In addition to these studies, aerodynamic studies were carried out on models such as medium-altitude long-endurance (MALE) unmanned aerial vehicle (UAV) (Panagiotou et al. 2014, 2016), quad tilt-wing VTOL (Vertical Take-Off and Landing) UAV (Muraoka et al. 2009), quadrotor UAV (Dong et al. 2013), and a twin-engine tail-sitter unmanned air vehicle (UAV) (Stone 2002).

In order for the experiment to reflect the real conditions in the wind tunnel, the geometry to be examined must be proportionally reduced. While reducing the geometry, blockage rates are calculated based on the dimensions of the experimental setup. So as to examine the effect of blockage rate on aerodynamic terms such as the pressure distribution and the drag coefficient, studies were first conducted on simple geometries. To observe the aerodynamic effects of more complex models, computational fluid dynamics (CFD) package programs have become widespread in order to obtain a faster and more economical solution. Some articles on calculating the blockage can be listed as follows:

West and Apelt experimentally demonstrated the effect of different blockage rates in the range of 2–16% on pressure distribution, the drag coefficient, and Strouhal number on a circular cylinder (West and Apelt 1982). Perzon discussed the effect of two different geometric parameters on the blockage ratios and emphasized that the effect of the windscreen angle on blockage ratios was critical, while the effect of the front radius was not sensitive. Subsequently, the effect of blockage rates on a full-scale car was analyzed on CFD analysis and a slotted wall wind tunnel was modeled (Perzon 2001). Lian analyzed the effect of sidewall and blockage rate on flapping wing with different domain sizes numerically and interpreted aerodynamic forces and reduced pitching frequencies due to different blockage rates (Lian 2010). Ross and Altman discussed the aerodynamic effects of rotating disordered flow of rotating vertical axis wind turbines on the wake and solid blockage rate in the wind tunnel test environment (Ross and Altman 2011). Chen and Liou investigated the factors that are affecting the blockage ratio in their studies. According to the results obtained from the experimental setups with and without rotors, they determined that the rotor-type speed ratio, the blade pitch angle, and the tunnel blockage ratio had a direct effect on the blockage rate (Chen and Liou 2011). Altinisik et al. examined and compared aerodynamic effects on passenger cars numerically and experimentally. After verifying their experimental studies on wind tunnel with computational fluid dynamics (CFD), they examined the effects of different blockage ratios through CFD studies (Altinisik et al. 2015). Mokhtar and Hasan examined the wall interference effect that occurs with the different blockage rates on the same geometry on the computational fluid dynamics (CFD) package program (Mokhtar and Hasan 2016). Latif et al. examined the aerodynamic analysis of the tail sweep 45° effects of the UAV baseline 5 model, which was 71.5% reduced, by calculating solid blockage, wake blockage, and streamline curvature blockage corrections (Abd Latif et al. 2017).

9.1.2 *Mathematical Formulations*

9.1.2.1 **Governing Equations**

Continuity Equation and Navier-Stokes Equations

For UAV analyses, the flow is accepted to be incompressible through the speed of 40 m/s.

For this reason, the Navier-Stokes equations are solved at the same time with the k-omega SST and the continuity equation. The motion of incompressible Newtonian

fluid forms the continuity equation and momentum conservation equation (Wilcox 1998).

$$\frac{\partial \rho}{\partial t} + \frac{\partial(\rho u_i)}{\partial x_i} = 0 \quad (9.1)$$

$$\frac{\partial(\rho u_i)}{\partial t} + \frac{\partial(\rho u_i u_j)}{\partial x_j} = -\frac{\partial P}{\partial x_j} + \frac{\partial}{\partial x_j} \left(\mu \frac{\partial u_i}{\partial x_j} - \overline{\rho u_i u_j} \right) + S_j \quad (9.2)$$

u_i and u_j ($i, j = 1, 2, 3$) are components of the time-averaged velocity; ρ is the fluid density, P is the pressure of time-averaged, $\overline{\rho u_i u_j}$ is the Reynolds stress, μ is the coefficient of dynamic viscous; S_j is the translation of the source used in the momentum equation.

The Reynolds-averaged Navier-Stokes equations are the most recently used turbulence modeling in CFD. In that approach, the Navier-Stokes equations are decomposed into ensemble-averaged or time-averaged and floating components. The total velocity u_i , $\overline{u_i}$ mean velocity, u_i' is fluctuating velocity as given in the below equation.

$$u_i = \overline{u_i} + u_i' \quad (9.3)$$

Turbulence Model Equations

Turbulence model selection depends on the grid type, i.e., for the structured grid as the present simulation, the SST model has been used. Standard the two-equation models exude the separation and predict foreboded flow even pressure gradient flows. However, the SST model is one of the specific two-equation models for separation estimation and also makes advantageous calculations of even more flowing wall-flow which highly separated regions. This model is correct than k-epsilon particularly near-wall layer, for flow with acceptable reverse pressure gradients (Menter et al. 2003; Menter 1992).

The following equations (which are in the form of Cartesian tensor) are called as the Reynolds-averaged Navier-Stokes (RANS) equations.

$$\frac{\partial(\rho u_i)}{\partial t} + \frac{\partial(\rho u_i u_j)}{\partial x_j} = \frac{\partial \rho}{\partial x_i} + \frac{\partial}{\partial x_j} \left[\mu \left(\frac{\partial u_i}{\partial x_j} + \frac{\partial u_j}{\partial x_i} - \frac{2}{3} \delta_{ij} \frac{\partial u_k}{\partial x_k} \right) \right] + \frac{\partial}{\partial x_i} \left(-\overline{\rho u_i u_j} \right) \quad (9.4)$$

The Boussinesq hypothesis is adapted with the Reynolds stress and mean velocity;

$$-\overline{\rho u_i u_j} = \mu_t \left(\frac{\partial u_i}{\partial x_j} + \frac{\partial u_j}{\partial x_i} \right) - \frac{2}{3} \left(\rho k + \mu_t \frac{\partial u_k}{\partial x_k} \right) \delta_{ij} \quad (9.5)$$

The SST $k-\omega$ is the combination of Wilcox $k-\omega$ model and the standard $k-\epsilon$ model. The shear-stress transport (SST) was developed by Menter (1994).

The shear-stress transport (SST) $k-\omega$ model nearly integrated the certain formulation of the $k-\omega$ model in the near-wall zone with the free-stream determination of the $k-\omega$ model in the far domain. The standard $K-\omega$ model captures the effects on the outer layer as well as the lower viscous layer effects on the inner layer.

Coupling of transition model with SST $k-\omega$ by modification of k equations is given as follows,

$$\frac{\partial}{\partial t}(\rho k) + \frac{\partial}{\partial x_i}(\rho k u_i) = \frac{\partial}{\partial x_j} \left(\Gamma_k \frac{\partial k}{\partial x_j} \right) + G_k - Y_k + S_k \quad (9.6)$$

$$\frac{\partial}{\partial t}(\rho \omega) + \frac{\partial}{\partial x_j}(\rho \omega u_j) = \frac{\partial}{\partial x_j} \left(\Gamma_\omega \frac{\partial \omega}{\partial x_j} \right) + G_\omega - Y_\omega + D_\omega + S_\omega \quad (9.7)$$

G_ω and G_k are the formations of the kinetic energy of turbulent and specific dissipation. Γ_k and Γ_ω are diffusivity, Y_k and Y_ω are dissipation, and S_k and S_ω are source terms. For standart $k-\epsilon$ and $k-\epsilon$ model, D_ω is extra-diffusion term, which is the function of blending.

$$D_\omega = 2(1 - F_1) \rho \sigma_\omega \omega + \frac{1}{\omega} \frac{\partial k}{\partial x_j} \frac{\partial \omega}{\partial x_j} \quad (9.8)$$

9.2 Material and Method

9.2.1 UAV Design Similar Model with Anka UAV

The Anka-like UAV models, which are inspired by the Turkish Anka unmanned aerial vehicle (UAV) geometry, are analyzed in the CFD program and compared with the experimental data. The TAI Anka is an unmanned aerial vehicle developed by Turkish Aerospace Industries (TAI) for the Turkish Armed Forces. In this study, the UAV model is designed and imported into a 3D package CAD program, and surfaces are generated. The designed model is shown in Fig. 9.1.

The geometry of the main wing has a span of 9 m and a NACA4415 airfoil at the wingtip, NACA 2412 airfoil at tail fuselage length is 8.13 m, and the wing MAC, aspect ratio, taper ratio, wing area, projected area, the volume of UAV, respectively, are 0.91, 9.83, 0.4698, 7.97 m², 2.24 m², and 5.63 m³.

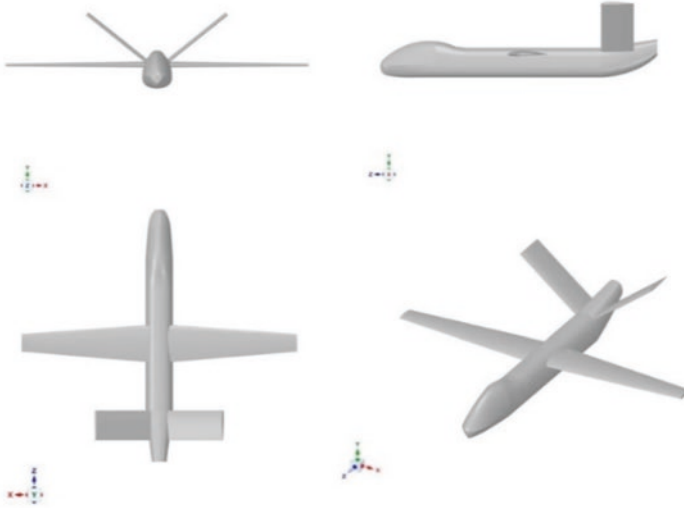


Fig. 9.1 Anka-like UAV model

9.2.2 Numerical Setup on ANSYS: Computational Fluid Dynamics (CFD) Package Program

9.2.2.1 Brief Description of Analysis

Firstly, different lengths of wingspan are compared, the effects of wing lengths on the drag coefficient are investigated, and depending on the wingspan, the stability of drag coefficient is examined. Since it will be

compared with wind tunnel tests, the most efficient length will be determined to fit into the tunnel. This length will be chosen where the pressure acting on the wall is the minimum and the length most suitable for the tunnel in terms of size. The wing's length reduction study is carried out to obtain a drag coefficient stability of the wings for the designs with 17-meter wing lengths in the wind tunnel test room. Firstly, the drag coefficient changes of the existing models according to the wing lengths are examined. The variations of C_D with these measurements are determined on the results obtained with 0, 5, 7, 8, 9, 11, 13, and 17 m. The pressure and drag coefficients of the model in the tunnel test chamber are compared according to the optimum wing lengths. Determined into the existing control domain, the models are placed in smaller sizes. For blockage approach, analyses are made in 6 different sizes for the Anka-like UAV. Before the experimental study, CFD analysis was performed on the UAV test model to specify the correct scale for the unmanned aerial vehicle. While determining the test scale, the following factors were taken into consideration. Pressure-position graphs were obtained by increasing wing lengths by 20 cm at 40 m/s. These wing structures, which are created by increasing 20 cm, have the ratio of the body to 1/39, 1/40, 1/42, 1/52, 1/59, 1/69 scale, respectively

The resulting drag coefficients, lift coefficients, and aerodynamic efficiencies are then averaged to obtain the drag at a given angle of attack as 0, 4, 8, 12, and 16 degrees in CFD. For the angle of attack $+4^\circ$ drag coefficient of the Anka-like UAV which length is 8 m, wingspan is 17.3 m was found to be 0.06 in 3.45×10^6 Reynolds number in CFD (Kırmacı Arabacı and Dilbaz 2019). The lift and drag measurements are corrected to account for the effects of wake blockage, solid blockage, and streamline curvature.

9.2.2.2 Grid Independence Check

One of the most important issues in computational fluid dynamics is the mesh. Depending on the number and quality of the mesh, the results can be different. Grid independence study is carried out varying of the mesh size. The Navier-Stokes equations are solved, assuming incompressible flow and Steady-state. The mesh independence study is performed at a speed of 40 m/s using the K- ω SST turbulence model. Small boxes are created around the UAV in the domain. The Anka-like UAV mesh is actualized in the range of 2 million–24 million. Figure 9.2 shows the size of the mesh elements of the cell grid. Results show that 21 million mesh can be chosen as the converged for this study. The grid was quite sufficient to capture the results.

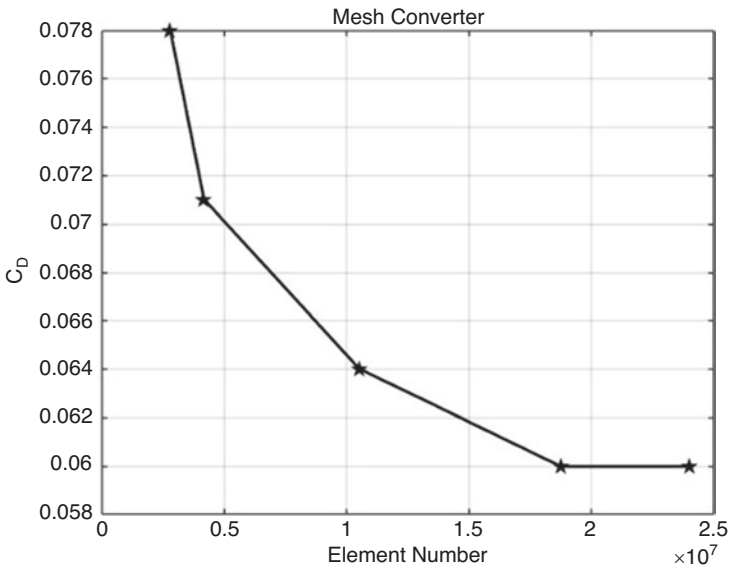


Fig. 9.2 Grid independence results

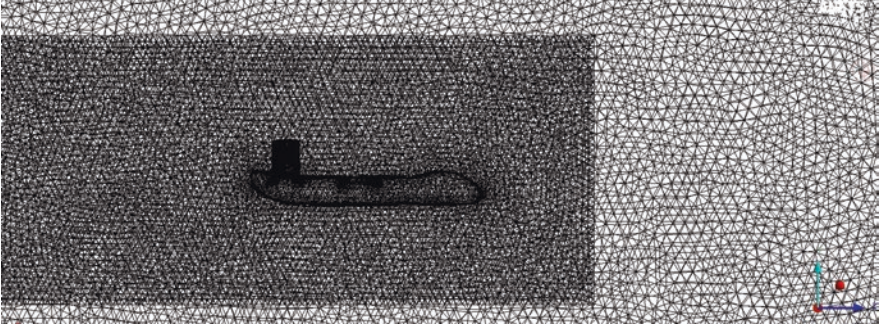


Fig. 9.3 Meshing of the Anka-like UAV

9.2.2.3 Boundary Conditions

The test model was imported into the ANSYS-FLUENT environment for meshing. In Fig. 9.3, control volumes are formed around the models.

The computational domain is selected after a comprehensive evaluation. In this study, the fuselage axis of each model is considered as the axis of symmetry, the control volume is placed 3 aircraft lengths away from the air intake surface and 6 aircraft lengths away from the air outlet surface, and 2.5 aircraft wings were left on the right side for 1/1 scale. For other scales, the control domain is selected as the room sizes of the wind tunnel.

The body of influence region to the models has high grid density, and taken by surround a layer of very fine mesh. In the outlet zone, the density of the mesh is progressively increased, so it is coarse as it goes outer far from the surface of models. The wall functions have confidence in the comprehensive law of the wall, which actually states the velocity dispersion near to a wall is similar for nearly all turbulent flows. One of the most significant parameters when appreciating the applicability of the wall functions is called dimensionless wall distance (y^+), demonstrated by Schlichting and Gersten (2016). Turbulent flows are remarkably affected by the asset of walls, where viscosity influenced regions have large gradients in the solution variables, but exactly calculating regions near the wall is very significant for accomplished estimation of wall-related flows (Gerasimoc 2006; Menter 1993).

For this case, the boundary layer thickness should be resolved in CFD problems. The first boundary layer thickness determined as inflation in the analysis calculated with the equation is as follows. The boundary layer thickness of the analysis to be solved with the Reynolds-averaged Navier-Stokes simulation (RANS) model in a computational fluid dynamics solver must first be calculated.

$$y^+ = \frac{yu_T}{\nu}; u_T = \sqrt{\frac{\tau_w}{\rho}}, \tau_w = 0.5C_f\rho U_\infty^2; C_f = 0.0576\text{Re}_d^{-\frac{1}{5}} \quad (9.9)$$

As a result of the equations, the Reynolds number is calculated primarily to find the boundary layer thickness. u_T is the friction velocity, τ_w is the wall shear stress, C_f is the skin friction coefficient, y is the absolute distance (it is from the Wall), and ν is the kinematic viscosity.

Before starting to calculate, a y value is determined, and accordingly, the height of the first element is calculated by friction velocity and kinematic viscosity (Bredberg 2000). In this study, the first boundary layer thickness y was found by taking $y^+ = 1$. It is observed that the $k-\omega$ SST (shear-stress transport) model performs better in regions with flow separation compared to the other turbulence models. The $k-\omega$ SST turbulence model was used in analyses to model the flow in areas where there may be flow separation with the lowest possible error (Menter 1993). 21×10^6 tetrahedral elements were used for the Anka-like meshing, and the C_L and C_D coefficients are calculated in a $y^+ \approx 1$ for 1/1 scale. With respect to the heights of the first element, the inflation layers are conceived on models, and 3D control volumes are created on every side boundary region. It is important to attention of y^+ in order to capture the flow separation.

The first element heights of inflation layers are calculated, and, according to the y^+ value which is equal to 1, the first element heights are created. The cell properties for the 1/1-scale Anka-like UAV model are as follows: 9 m length, first layer height is 9.347×10^{-6} , inflation layer is 6, maximum skewness is 0.83, minimum orthogonal quality is 9.0856×10^{-2} , and element number is 21245756.

The Reynolds number is found using the mean aerodynamic chord (MAC); MAC is denoted by \bar{c} , V is the flight speed, c_{root} is the length of root chord, λ is the taper ratio, and c_{tip} is the length tip chord. All of the conditions are in-flight conditions.

$$Re = \frac{\rho V \bar{c}}{\mu} \quad (9.10)$$

$$\bar{c} = \frac{2}{3} * c_{root} * \left(\frac{1 + \lambda + \lambda^2}{1 + \lambda} \right) \quad (9.11)$$

$$\lambda = \frac{c_{tip}}{c_{root}} \quad (9.12)$$

The boundary conditions of UAVs are defined as a wall and no-slip conditions. Air velocity is accepted as 40 m/s for 1/1 scale in the inlet, the outlet is defined as the pressure outlet, and 0 Pa is taken. The 1/40 scale, the UAVs, and sides are taken wall and defined no-slip conditions like the wind tunnel. The turbulence intensity is set at 1.29%, and the turbulence viscosity ratio is 5 in CFD. The flow is incompressible; a pressure-based solver is used. It is chosen for the low-altitude flight regime as subsonic.

The parameters, which are the outlet pressure, inlet viscosity, and density of air, are received at sea-level conditions for analysis. The density and temperature are,

respectively, 1.225 kg/m^3 and $15.5 \text{ }^\circ\text{C}$, while the dynamic viscosity is $1.789 \times 10^{-5} \text{ kg/ms}$.

The sides of the control volume are defined as a wall. The reason for this is wind tunnel tests, and analyses should be under the same boundary conditions. The experiments are performed in the Manisa Celal Bayar University open-return sub-sonic wind tunnel.

9.2.2.4 Dynamic Similarity

To ensure geometric similarity, the sizes of the model should be proportional to that of the prototype. The Reynolds number must be checked for dynamic similarity. The Reynolds number of the test model and its prototype have to be calculated equally. The Reynolds number independence was obtained in all of the experimental work.

The maximum wind speed in the test section is 40 m/s , and the length of the wind tunnel is 1 m . In Eq. 9.13, the dynamic similarity studies have been performed, and then the scaling factor has been obtained. It was decided to continue the studies on a $1/40$ -scale model.

$$\text{Re}_{1/40} = \frac{40 \times \bar{C}_{1/40}}{\nu} = R_{1/1} = \frac{U_\infty \times \bar{C}_{1/1}}{\nu} \quad (9.13)$$

Before the numerical and experimental studies, critical flow regions should be determined on the relevant test model, and the differences in these regions as a result of the analysis should be interpreted on the accuracy of the relevant numerical test methods. Specified critical flow regions on the Anka-like UAV model is shown in Fig. 9.4. On the Anka-like UAV model, there are three specified regions to the comparing numerical results. These regions are determined in line with the regions where flow separations are intense. The pressure distributions, drag force and lift force obtained as a result of the computational fluid dynamics (CFD) analysis of the test models obtained as a result of dynamic similarity are shown in Table 9.1 and Fig. 9.5. According to the results, a 1.33% difference was obtained between 1 -scale and 40 -scale test models. When the pressure distributions over the critical regions are examined, a 1.75% difference occurs.

9.2.2.5 Pressure Distribution Between the Anka-Like UAV Model

Before the experimental study, CFD analysis was performed on the UAV test model to specify the correct scale for the unmanned aerial vehicle. While determining the test scale, the following factors were taken into consideration (Korkut and Goren 2020; Cook 1978; Pettersson and Rizzi 2008):

1. Test models must be able to be positioned in the wind tunnel test section.

Fig. 9.4 Specified critical flow regions on the Anka-like UAV model

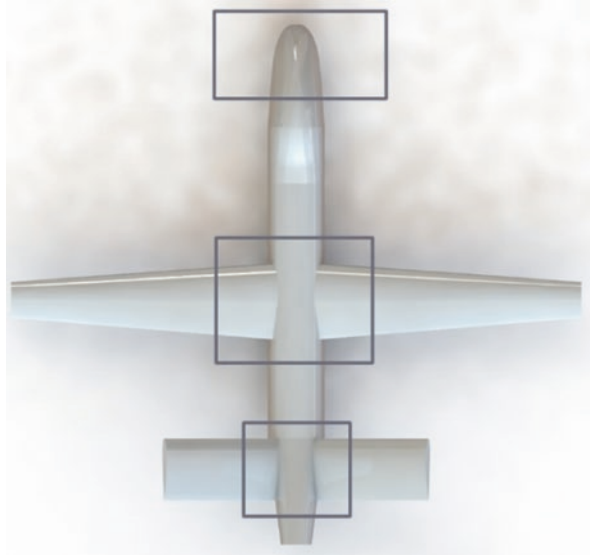


Table 9.1 Dynamic similarity studies of the Anka-like UAV model

| Model | Scale | V [m/s] | F_D | F_L | C_D | C_L |
|-----------|-------|---------|-------|-------|-------|-------|
| Anka-like | 1/1 | 1 | 0.34 | 1.2 | 0.069 | 0.245 |
| | 1/40 | 40 | 0.33 | 1.1 | 0.069 | 0.232 |

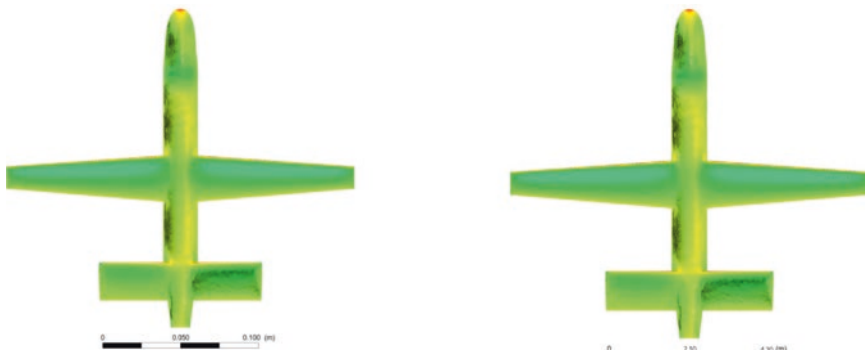


Fig. 9.5 The dynamic similarity comparison of 1/1 and 1/40 models

2. The test model has to be scaling with the blockage ratio of the wind tunnel.
3. The airflow beyond the borders of the scaled test model should return to the normal behavior as it approaches the test section walls of the wind tunnel.

The x-axis of the graphics in Fig. 9.6 expresses the symmetrical width of the wind tunnel test chamber. On the x-axis presented in the graph, the value 0 represents the test model and the test chamber center position, and the value 0.15

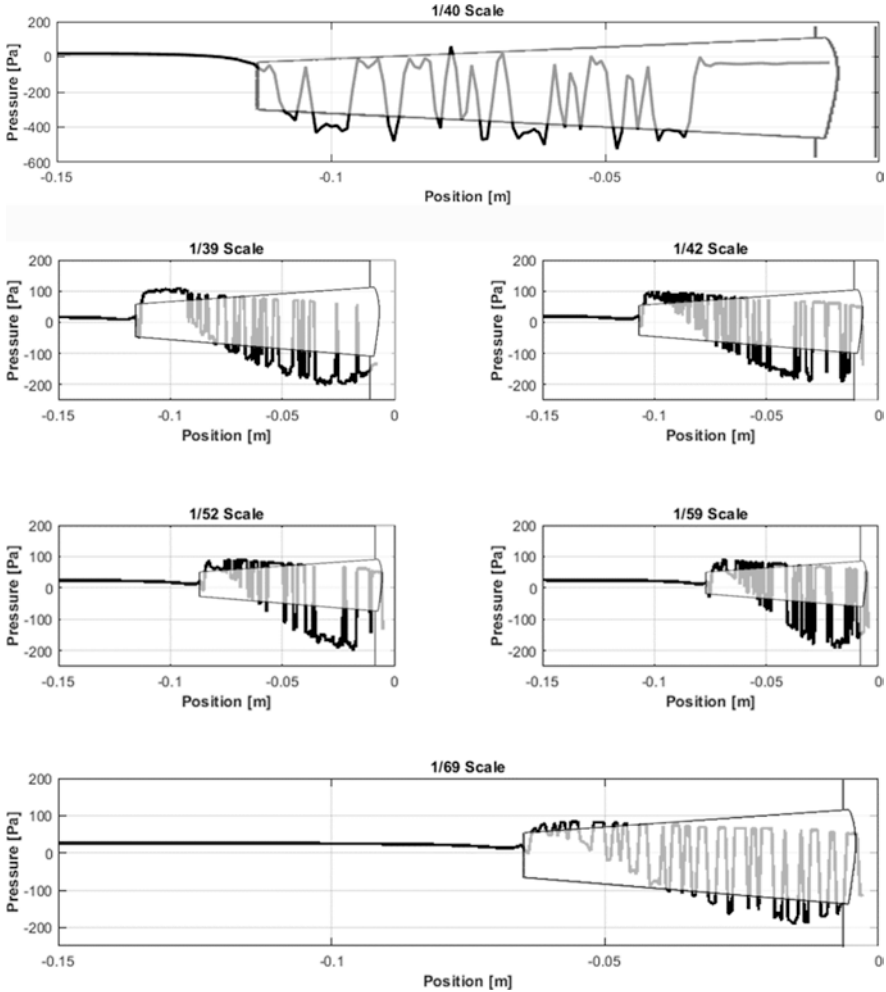


Fig. 9.6 Pressure distribution between the Anka-like UAV and wall of the wind tunnel

represents the test chamber wall. All scaled test models meet the condition specified in Clause 3. As a result of the wind tunnel testing capabilities and dynamic similarity condition, it was decided to examine the most appropriate scale 1/40 in experimental studies.

As shown in Fig. 9.6, pressure distributions on the line, which is located on the wing, were obtained to specify the correct scale. The pressure difference is converged 3.5 cm away from the sidewalls of the wind tunnel on the 1/40-scale model of the UAV. Therefore, the appropriate scale has been chosen and ensured as a 1/40 scale. In this study, the blocking rate is 1.56% and in agreement with the literature (Boutillier and Yarusevych 2012).

9.2.3 Experimental Setup

The wind tunnel is an open-loop-type wind tunnel environment with general dimensions of 1500 mm × 2000 mm × 6500 mm as shown in Fig. 9.7. It is operated by a blower system supported by a 15kW motor with a 600 mm axial fan, which works at a maximum rev of 3000 rpm, as shown in Fig. 9.8. The maximum wind speed of the wind tunnel is created by 70 m/s (Arabacı and Pakdemirli 2016). The contraction ratio of the wind tunnel is 11.1.

Futek LSB200 Load Cell sensors are used for force measurement in the wind tunnel. The strain gauge is created by placing a thin resistor strip on an elastic material with a specific geometric design. It allows the measurement of the axial force on the elastic material with the effect of the load.

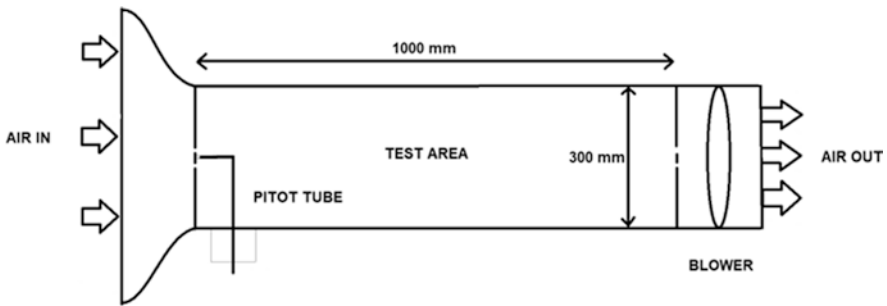


Fig. 9.7 Two-dimensional representation of the wind tunnel



Fig. 9.8 Manisa Celal Bayar University wind tunnel

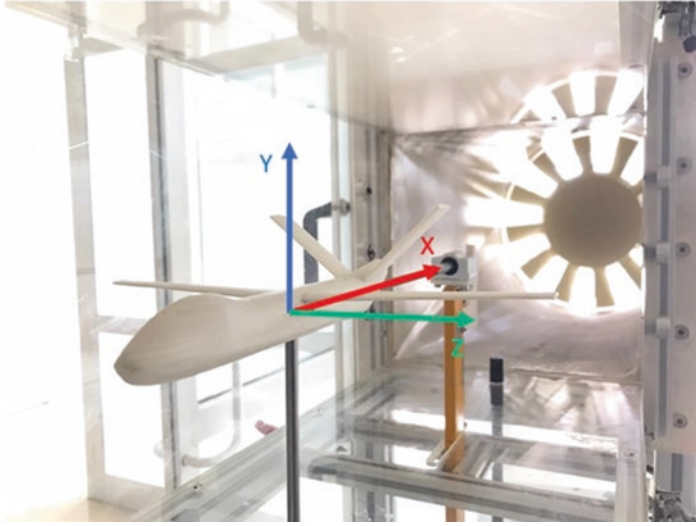


Fig. 9.9 Display of the supports of the test model produced with 3D printer in the experimental environment. (Turbotek n.d.)

In this study, the effects of the current with the force measurement mechanisms are designed for the x- and y-axis as shown in Fig. 9.9. Y-axis force measurement mechanism is created on the center of gravity of the test object to eliminate the mass forces. High-precision linear bearings and high-precision shafts are used in both axes to be measured, in order to eliminate the effects of the **undesirable** forces.

The connection between the test object and the force measurement mechanisms in the test room is provided with an 8 mm diameter shaft. Linear bearings are used in both axes to prevent misalignments. The data obtained from the sensors are recorded. The measurements are taken from the x- and y-axes during the experiments. After measurements are transferred to the LabView program, the data were processed and recorded. During the experiments, it is paid attention that there is not a strong wind, temperature changes, and pressure changes (rain, etc.) in the environment. Outdoor parameters are continuously observed and recorded.

The 1/40-scaled models used in the experiments are created by using 3D printers and PLA material with a 100% occupancy rate. Holes are drilled for shafts in the x- and y-axes, aligning from the center of

gravity. It has been sanded with fine sandpaper to remove the roughness of the surface gradually. After sanding, the models are spray-painted and varnished with spray varnish. In order to have the axial misalignment and angle of attack 0° , a spirit level is used after the assembly of the Anka-like model.

9.3 Results and Discussion

9.3.1 Variation of Drag Coefficient According to Wingspan

In order to reveal the aircraft design suitable for the experimental test room, the drag coefficient graph based on the symmetry wingspan is presented in Fig. 9.10. The symmetry wingspan limits are kept between 17 m and 0 m. The symmetry wingspan range, which has stabilized the drag coefficient value, is considered to be suitable for the experimental environment. As shown in Fig. 9.10, it is observed that the drag coefficient is stable between 4.5 m and 5.5 m, and therefore, it is decided that the length suitable for the experimental environment should be 4.5 m for a single wing.

9.3.2 Aerodynamic Performance of the Anka-Like Model for Different Reynolds Numbers at Angle of Attack= 0°

As shown in Fig. 9.11, the ratio of C_L to C_D , which is an indication of aerodynamic efficiency, for an angle of attack value of 0° and for the range of the Reynolds number was investigated in this study. Increasing the Reynolds number reduces the drag, resulting in an increased aerodynamic performance of the Anka-like unmanned aerial vehicle. The experimental studies of the aerial vehicle aerodynamics with

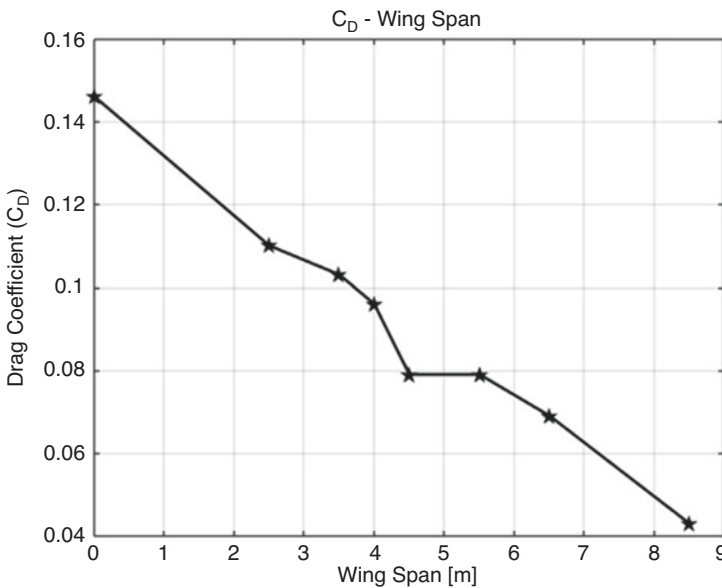


Fig. 9.10 Drag coefficient values depending on wingspan

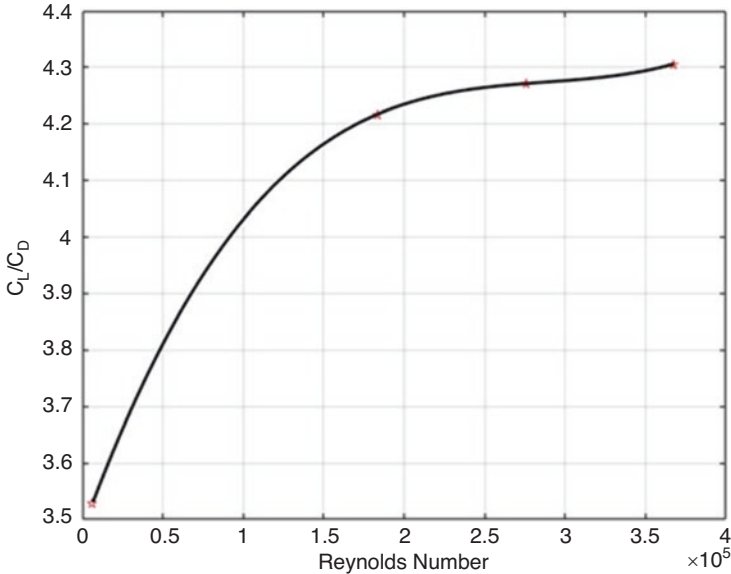


Fig. 9.11 Effects of the Reynolds number on C_L to C_D ratio for $\alpha = 0^\circ$

1/1-scale prototypes are quite expensive and difficult. Therefore, the scaled test models are used in experimental studies. Before the preparation of the test model, there are some similarity rules for consideration. The ratios of the velocity vector on prototypes and models should be fixed for providing dynamic similarity.

Besides that, the dynamic similarity depends also on the blocking effect. The blockage ratio is defined as the ratio between the front sectional area of the test section and the test model. The blockage ratio is recommended to be below the 10% limit for the blocking effect to be neglected in the wind tunnel tests (Skalak et al. 1989; Ku 1997; Jones 1969).

9.3.3 Comparison of Experimental and Numerical Aerodynamic Coefficients

As shown in Table 9.2, experimental and numerical aerodynamic coefficients were compared in the 1/40-scale Anka-like model. As a result of this comparison, a 5.47% error value was observed between the experimental and numerical drag coefficient values, while a maximum error of 11% error was observed between the lift coefficient values. In this way, the experimental environment and the numerically modeled CFD environment have been verified.

Table 9.2 Comparison with experimental and numerical aerodynamic coefficient results

| | | |
|--|-------|-------------|
| Experimental drag coefficient (C_D) values | 0.073 | 5.47% error |
| Numerical drag coefficient (C_D) values | 0.069 | |
| Experimental lift coefficient (C_L) values | 0.209 | 11% error |
| Numerical lift coefficient (C_L) values | 0.232 | |

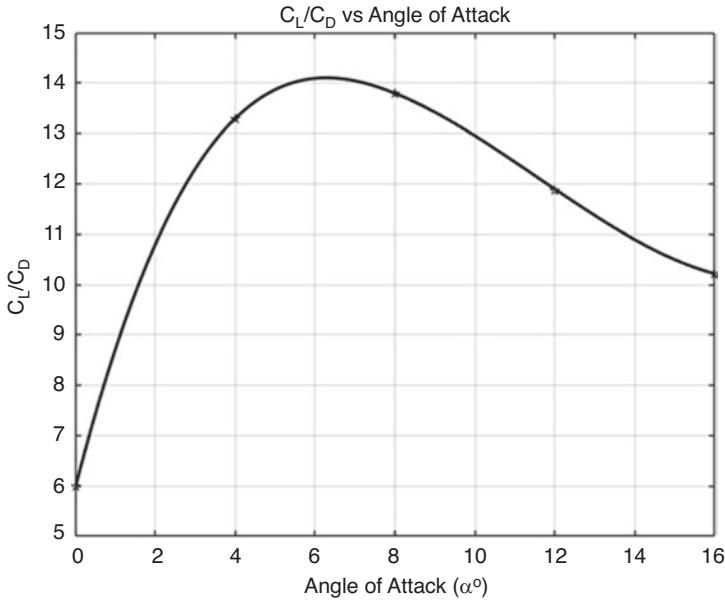


Fig. 9.12 Graphic of C_L/C_D : angle of attack (α°)

9.3.4 Change in Aerodynamic Efficiency Due to Angle of Attack

Figure 9.12 shows the variation of aerodynamic efficiency according to the angle of attack. Aerodynamic efficiency is an important design parameter in unmanned aircraft designs, and low drag is desired despite high lift. High aerodynamic efficiency means higher load-carrying capacity and lower thrust power. (The low drag of the aircraft against high lift means that it has a high load-carrying capacity and a lower thrust power.) This provides a better fuel economy, climbing performance, and glide rate in the aircraft. It is seen that the ratio of the lift coefficient to drag coefficient (C_L/C_D) increases up to a certain angle of attack and decreases after this angle value.

The main reason for this is that, up to a certain angle of attack, the increase in the lift coefficient is higher than the drag coefficient. But after this critical angle value, aerodynamic efficiency begins to decrease. The most obvious reason for this situation is that flow separation starts over the wing and increases the drag. The highest C_L/C_D value was reached at 6° , and this value is 14.

9.3.5 Drag Coefficient (C_D) Variation Depending on the Angle of Attack

The variation of drag coefficient (C_D) according to the angle of attack is shown in Fig. 9.13. As the angle of attack increases, there is a continuous increase in the drag coefficient. As the stall angle is approached, the drag increases at a higher rate due to flow separation. At this critical angle of attack value, the highest drag coefficient is 0.182. The lowest drag coefficient was seen when the angle of attack was 0° and its value was 0.059.

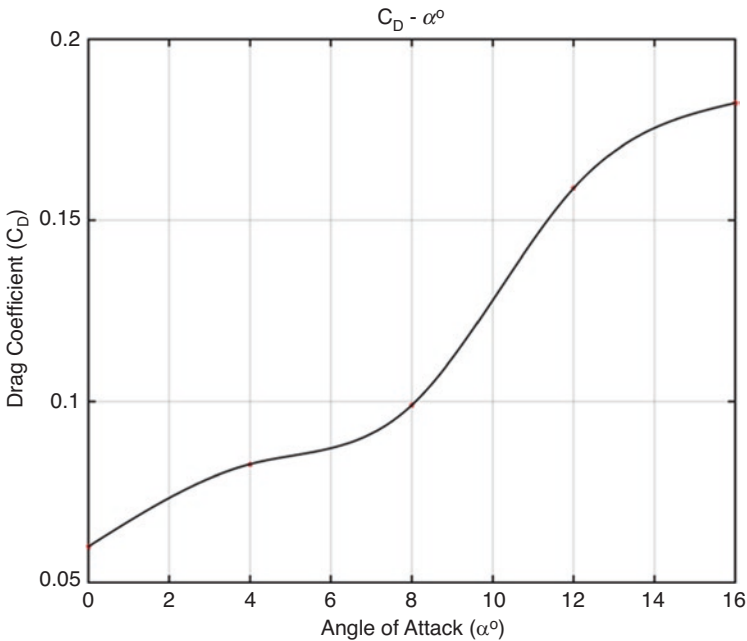


Fig. 9.13 Graph of C_D : angle of attack (α°)

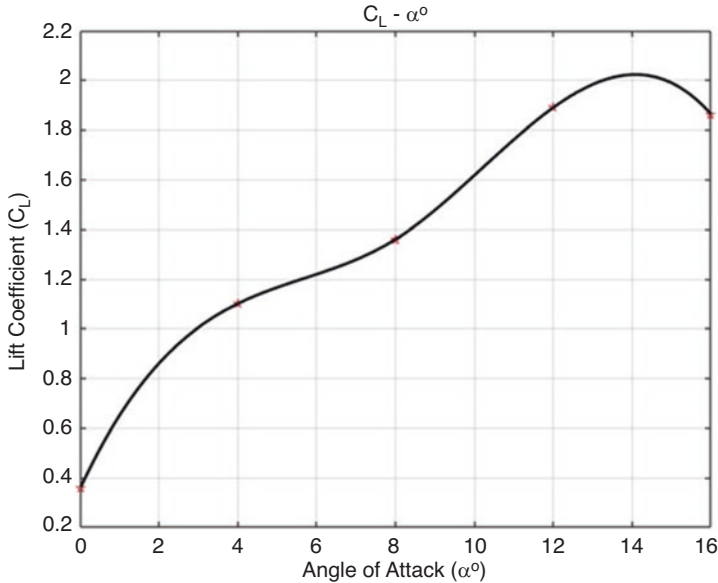


Fig. 9.14 Graph of C_L : angle of attack (α°)

9.3.6 Lift Coefficient (C_L) Variation Depending on Angle of Attack

The variation of the lift coefficient (C_L) according to the angle of attack is shown in Fig. 9.14. Increasing the angle of attack also increases the lift coefficient. However, when the angle of attack is 15° , the lift coefficient decreases. At this angle, flow separation occurs on the wing. This causes a loss of lift in the wing. This critical angle of attack is called the stall angle. As it can be understood from the graph of the change of aerodynamic efficiency, according to the attack angle, when the angle of attack is 12° , the lift coefficient reaches its highest value, and this value is 1.89. On the other hand, the angle of attack has the lowest lift coefficient at 0° , and its value is 0.36.

9.3.7 Pressure Distribution and Vortex Core Region Results

Pressure distribution and vortex core regions are shown in Fig. 9.15. It was observed that the pressure change increases around the stagnation points on the wings and body. Pressure changes have calculated as 1 kPa around the wings and body. Sudden pressure change causes the vortex around the solid body. In continuum mechanics, vortex is a pseudovector field that describes the local spinning motion of a

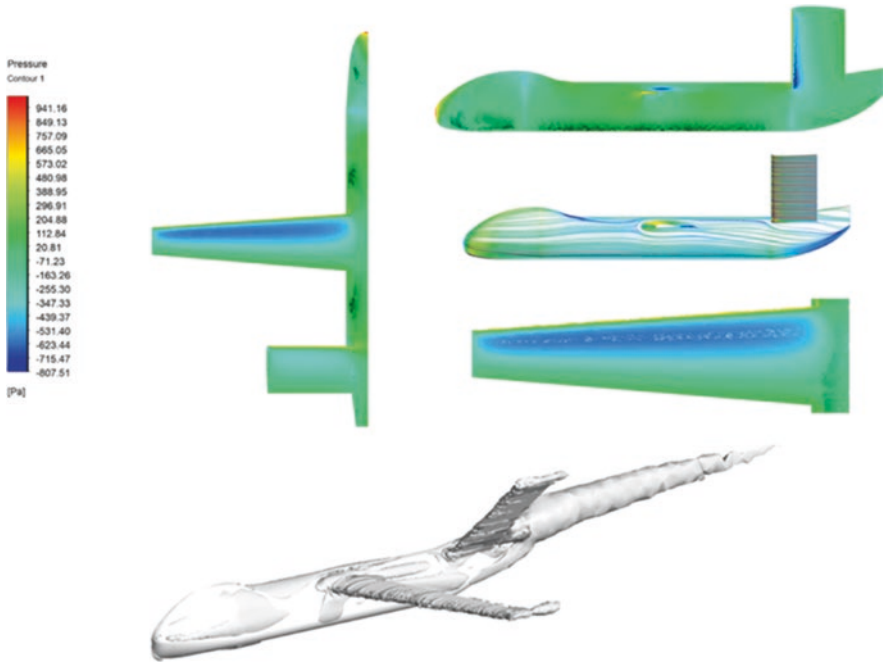


Fig. 9.15 Pressure contours and vortex core regions on the Anka-like UAV model

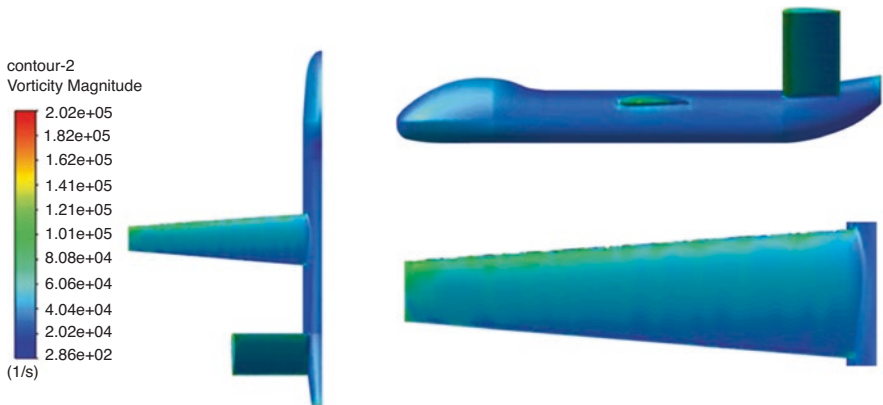


Fig. 9.16 Vorticity magnitude changes on the Anka-like UAV model

continuum near some point, as would be seen by an observer located at that point and traveling along with the flow. It is an important quantity in the dynamical theory of fluids and provides a convenient framework for understanding a variety of complex flow phenomena, such as the formation and motion of vortex rings (Lecture Notes 2015; Moffatt 2015; Guyon et al. 2002). As shown in Fig. 9.16, the vorticity magnitude increased at the flow separation points and returned to the normal behavior on the body.

9.4 Conclusion

In this study, the aerodynamic effects of the similar model with the Anka model were examined in both experimental and numerical environments. On the model similar to Anka, aerodynamic coefficients due to different angles of attack, wingspan selection, dynamic similarities, aerodynamic effects according to different Reynolds numbers, experimental verification of the results, and the pressure distribution of models in different scales were examined. Several conclusions were drawn from this study as follows:

1. The drag coefficient value depending on the wingspan was examined, and the wingspan suitable for the experimental wind tunnel room was taken as 4.5 m from the range where the drag coefficient value was stable.
2. In order to select the scaled geometry suitable for the experimental environment, CFD analysis was performed in six different scales, and it was observed that the 1/40 scale with a blocking rate of 1.56% was suitable for the experimental environment.
3. In order to determine the aerodynamic performance of the designed model, aerodynamic coefficients depending on the angle of attack were determined. After increasing the lift coefficient up to the critical angle of attack, a decrease was observed. In the drag coefficient, the coefficient increased as the angle of attack increased.
4. Depending on the Reynolds number, an increase in C_L/C_D values was observed, but, as the Reynolds number was increased, the rate of increase was decreased.
5. It was found that the experimental results are in good agreement with the numerical solution in the C_D and C_L values of the 1/40-scale model.

References

- Abd Latif, M.Z.A., Ahmad, M.A., Nasir, R.M., Wisnoe, W., Saad, M.R.: An analysis on 45 sweep tail angle for blended wing body aircraft to the aerodynamics coefficients by wind tunnel experiment. In: IOP Conference Series: Materials Science and Engineering, vol. 270, no. 1, p. 012001. IOP Publishing (2017, December)
- Altınışık, A., Kutukceken, E., Umut, H.: Experimental and numerical aerodynamic analysis of a passenger car: influence of the blockage ratio on drag coefficient. *J. Fluids Eng.* **137**(8) (2015)
- Arabacı S., Pakdemirli M.: Improvement of aerodynamic design of vehicles with inspiration from creatures, PhD Thesis, Department of Mechanical Engineering, Manisa Celal Bayar University (2016)
- Boutillier, M.S., Yarusevych, S.: Effects of end plates and blockage on low-Reynolds-number flows over airfoils. *AIAA J.* **50**(7), 1547–1559 (2012)
- Bredberg, J.: On the wall boundary condition for turbulence models. Chalmers University of Technology, Department of Thermo and Fluid Dynamics. Internal Report 00/4. Goteborg, pp. 8–16 (2000)
- Chen, T.Y., Liou, L.R.: Blockage corrections in wind tunnel tests of small horizontal-axis wind turbines. *Exp. Therm. Fluid Sci.* **35**(3), 565–569 (2011)

- Cook, N.J.: Determination of the model scale factor in wind-tunnel simulations of the adiabatic atmospheric boundary layer. *J. Wind Eng. Ind. Aerodyn.* **2**(4), 311–321 (1978)
- Dong, W., Gu, G.Y., Zhu, X., Ding, H.: Modeling and control of a quadrotor uav with aerodynamic concepts. In: *Proceedings of World Academy of Science, Engineering and Technology*, vol. 77, p. 437. World Academy of Science, Engineering and Technology (WASET) (2013)
- Ehrhard, T.P.: *Air Force UAV's: The Secret History*. Mitchell Institute for Airpower Studies Arlington VA. (Ehrhard, 2010) (2010)
- Funes-Sebastian, D.E., Ruiz-Calavera, L.P.: Numerical simulations of wind tunnel effects on intake flow of a UAV configuration. In: *52nd Aerospace Sciences Meeting*, p. 0372 (2014)
- Gerasimoc, A.: *Modelling Turbulence Flows with Fluent*. Europe ANSYS Inc. (2006)
- Guyon, E., Hulin, J.P., Petit, L., Mitescu, C.D., Jankowski, D.F.: Physical hydrodynamics. *Appl. Mech. Rev.* **55**(5), B96–B97 (2002)
- Jones, R.T.: Blood flow. *Annu. Rev. Fluid Mech.* **1**(1), 223–244 (1969)
- Kahvecioglu, S., Oktal, H.: Historical development of UAV technologies in the world: the case of Turkey. In: *Sustainable Aviation*, pp. 323–331. Springer, Cham (2016)
- Keane, J.F., Carr, S.S.: A brief history of early unmanned aircraft. *Johns Hopkins APL Tech. Digest.* **32**(3), 558–571 (2013)
- Kırmacı, A.S., Dilbaz, F.: Aerodynamic analysis of Anka UAV and Heron UAV. In: *2nd International Conference on Energy Research*, 11–13 April, Marmaris, Turkey (2019)
- Korkut, T.B., Goren, A.: Aerodynamic effect of wing mirror usage on the Solaris 7 solar car and demobil 09 electric vehicle. *Int. J. Automot. Mech. Eng.* **17**(2), 7868–7881 (2020)
- Ku, D.N.: Blood flow in arteries. *Annu. Rev. Fluid Mech.* **29**(1), 399–434 (1997)
- Lecture Notes from University of Washington, at the Wayback Machine, Archived 16 Oct 2015 (2015)
- Lian, Y.: Blockage effects on the aerodynamics of a pitching wing. *AIAA J.* **48**(12), 2731–2738 (2010)
- Menter, F.R.: Improved Two-equation k-omega Turbulence Models for Aerodynamic Flows. Nasa Sti/Recon Technical Report N, 93, 22809 (1992)
- Menter, F.: Zonal two equation kw turbulence models for aerodynamic flows. In: *23rd Fluid Dynamics, Plasmadynamics, and Lasers Conference*, p. 2906 (1993, July)
- Menter, F.R.: Two-equation eddy-viscosity turbulence models for engineering applications. *AIAA J.* **32**(8), 1598–1605 (1994)
- Menter, F.R., Kuntz, M., Langtry, R.: Ten years of industrial experience with the SST turbulence model. *Turbulence Heat Mass Transf.* **4**(1), 625–632 (2003)
- Moffatt, H.K.: Fluid dynamics. In: *The Princeton Companion to Applied Mathematics*, pp. 467–476. Princeton University Press (2015)
- Mokhtar, W., Hasan, M.: *A CFD Study of Wind Tunnel Wall Interference*. American Society for Engineering Education (2016, March)
- Muraoka, K., Okada, N., Kubo, D.: Quad tilt wing VTOL UAV: aerodynamic characteristics and prototype flight. In: *AIAA Infotech@ Aerospace Conference and AIAA Unmanned. Unlimited Conference*, p. 1834 (2009)
- Panagiotou, P., Kaparos, P., Yakinthos, K.: Winglet design and optimization for a MALE UAV Using CFD. *Aerosp. Sci. Technol.* **39**, 190–205 (2014)
- Panagiotou, P., Kaparos, P., Salpingidou, C., Yakinthos, K.: Aerodynamic Design of a MALE UAV. *Aerosp. Sci. Technol.* **50**, 127–138 (2016)
- Pattinson, J., Lowenberg, M.H., Goman, M.G.: Multi-degree-of-freedom wind-tunnel maneuver rig for dynamic simulation and aerodynamic model identification. *J. Aircr.* **50**(2), 551–566 (2013)
- Perzon, S.: *On Blockage Effects in Wind Tunnels—A CFD Study* (No. 2001-01-0705). SAE Technical Paper (2001)
- Pettersson, K., Rizzi, A.: Aerodynamic scaling to free flight conditions: past and present. *Prog. Aerosp. Sci.* **44**(4), 295–313 (2008)
- Ro, K., Raghu, K., Barlow, J.B.: Aerodynamic characteristics of a free-wing tilt-body unmanned aerial vehicle. *J. Aircr.* **44**(5), 1619–1629 (2007)

- Ross, I., Altman, A.: Wind tunnel blockage corrections: review and application to savonius vertical-axis wind turbines. *J. Wind Eng. Ind. Aerodyn.* **99**(5), 523–538 (2011)
- Schlichting, H., Gersten, K.: *Boundary Layer Theory*, 9th edn, p. 572. Springer, Berlin/Heidelberg (2016)
- Skalak, R., Ozkaya, N., Skalak, T.C.: Biofluid mechanics. *Annu. Rev. Fluid Mech.* **21**(1), 167–200 (1989)
- Stone, R.H.: Aerodynamic modelling of a wing-in- slipstream tail-sitter UAV. In: 2002 Biennial International Powered Lift Conference and Exhibit, p. 5951 (2002)
- Turbotek.: <https://www.turbotek.com.tr/egitim-amacli-ruzgar-tuneli-v2,2,16283#.X7h9m8gzaUk>. Accessed 10 Nov 2020 (n.d.)
- Ventura Diaz, P., Yoon, S.: High-fidelity computational aerodynamics of multi-rotor unmanned aerial vehicles. In: 2018 AIAA Aerospace Sciences Meeting, pp. 1–22 (2018)
- Vuruskan, A., Yuksek, B., Ozdemir, U., Yukselen, A., Inalhan, G.: Dynamic modeling of a fixed-wing VTOL UAV. In: 2014 International Conference on Unmanned Aircraft Systems (ICUAS), pp. 483–491. IEEE (2014)
- West, G.S., Apelt, C.J.: The effects of tunnel blockage and aspect ratio on the mean flow past a circular cylinder with Reynolds numbers between 10^4 And 10^5 . *J. Fluid Mech.* **114**, 361–377 (1982)
- Wilcox, D.C.: *Turbulence Modeling for CFD*, vol. 2, pp. 103–217. DCW Industries, La Canada (1998)
- Wisnoe, W., Nasir, R.E.M., Kuntjoro, W., Mamat, A.M.I.: Wind tunnel experiments and CFD analysis of Blended Wing Body (BWB) Unmanned Aerial Vehicle (UAV) at Mach 0.1 and Mach 0.3. In: International Conference on Aerospace Sciences and Aviation Technology, vol. 13, no. Aerospace Sciences & Aviation Technology, ASAT-13, May 26–28, 2009, pp. 1–15. The Military Technical College (2009, May)

Chapter 10

Sustainability Practices in Airport



Hakan Rodoplu and Serap Gürsel

10.1 Introduction

Today, aviation is one of the fastest-growing global industries in the world due to its characteristics that connect markets and geographies in the shortest way and facilitate international trade in every sense. The demand for air travel is increasing in parallel with the development of the aviation industry as a whole and increasing prosperity. In the future, the ability of cities and countries to derive the greatest possible benefit from the global economic functioning will be largely determined by their position in the aviation industry (Grubestic and Matisziw 2012; Upham et al. 2003).

Although the economic and social benefits provided by the aviation sector are important, considering the technologies and operating systems of the sector and taking into account the environmental and social costs that increase year by year, the unsustainability of the current situation is a plain fact. Due to the international nature of the aviation industry, the negative effects of aviation turn into a problem for all humanity in the form of global air and environmental pollution and climate change (Schäfer and Waitz 2014). A significant increase in airline passenger traffic means higher fuel consumption and higher greenhouse gas emission levels. On the other hand, the energy consumption of the airline industry has increased by more than 6% in the last decade, while global energy production has increased by less than 6% in the same period, raising concerns about sustainability (Cui and Li 2015). Global environmental events that lead to the emergence of sustainability policies will also have a high impact on the sustainability of aviation. In other words, sustainability affects the aviation industry negatively, and the aviation industry affects sustainability negatively.

H. Rodoplu · S. Gürsel (✉)

Aviation Management Department, Kocaeli University, Kocaeli, Turkey

Aviation is a challenging sector for sustainability as one of the areas where the conflicting practices of environmental and economic policies are most clearly observed. In cases where decision-making units focus more on economic results, it is too late to compensate for the environmental negativities that the process will cause. To cope with the increase in demand, aviation operations require a sustainable approach. It is not an easy task to take care of environmental impacts while maintaining economic benefits in the process of establishing a management process that takes into account the concept of sustainability in aviation (Walker and Cook 2009). In this context, the solution to this dilemma that the sector has at the point of ensuring the sustainability of the aviation industry is a challenging topic.

Based on the close relationship between sustainability and aviation, sustainability practices gain importance, especially at airports, both due to international regulations and in line with the requests of investors and stakeholders in the sector. While national and international regulations in the sector attach importance to sustainability, they often do not include which practices should be used due to commercial concerns. Therefore, airport operators and other airport users have different applications for sustainability around the world. Systems and technologies used for sustainability have high investment costs and a late return on investment. At this point, the results of sustainability practices used by other countries and airports also gain great importance.

In the study, primarily the concept of sustainability was discussed. New issues added to the content of the sustainability concept in aviation were explained. Following the effects of sustainability in aviation and the effects of sustainability on aviation, the sustainability strategies and projects, which were accepted at the center and put into practice, were introduced in order to benefit all stakeholders in the sector. In order to increase the importance given to sustainability, it is aimed to encourage the implementation of sustainability practices, even if there are no national and/or international regulations.

10.2 Aviation Industry

The aviation industry is one of the most influential and important industries in today's globalized and relatively prosperous world. However, the excessive increase in demand for air transport has brought along unsustainable problems. The global aviation industry alone is responsible for approximately 2% of the world's carbon emissions. If we accept the aviation industry as a country, it will be among the top ten carbon emission officers in the world. Airport-based activities are also considered responsible for 2–3% of the percentage of aviation. The aviation industry is estimated to grow between 3.5% and 7% annually globally. It is estimated that this increase will lead to a large increase in carbon emission. There is concern about the negative impact of this situation on the environment (Learmonth 2020).

First of all, the environmental consequences caused by aviation are important today. Although the carbon emission rate of aviation on a global scale is not a big

concern, as it follows a course that is equivalent to the carbon emission rates of industrialized countries, the noise phenomenon caused by aircraft and airport operations is accepted as a much more serious environmental problem especially for the local people, because the perception of noise is subjective and noise commonly triggers sleep disturbance and other related physiological and psychological problems (Morrell et al. 1997). Other environmental problems associated with airports include soil pollution, pollution of ground and surface waters from jet fuel, waste generation from de-icing, (Turnbull and Bevan 1995) occupation of agricultural land, and air pollution caused from airport-city link roads that can be counted negativities (Peace et al. 2006).

Global concerns about the effects of climate change and its impact on infrastructure are becoming more common. From sea level rise to changes in temperature, weather, wind, and storm patterns, the impacts of climate change are predicted to pose a serious risk to airport operations. It is estimated that bad weather causes about 70% of annual flight delays, and future weather changes could exacerbate these challenges. Other economic challenges include volatile electricity prices and a fluctuating jet fuel market. Increasing consumer and investor awareness of the social and environmental impacts of the aviation industry's activities increases this pressure to move toward a low-carbon economy. Globally, this has led to an increase in net-zero carbon emissions or commitments to emission reduction plans (Learmonth 2020).

10.3 Sustainability

In the postindustrial revolution period, economic policy practices based on growth created an increasing need for energy and raw materials. Due to the limited resources, the growth-focused system has come to the point of collapse. On the other hand, the damage to the environment in parallel with the incredible increase in production and consumption in the process endangers the continuation of human life. The intensive production activity, aimed at meeting the demand arising as a result of the efforts to increase consumption unlimitedly in parallel with the population growth, has brought about the excessive consumption of relatively cheap natural resources. As a natural consequence of this process, the level of waste and pollution on a global scale has reached unmanageable levels, and the destruction of the ecosystem has brought irreversible problems.

These long-term and extremely destructive efforts on the basis of economic growth ultimately did not increase social welfare as expected, apart from the welfare of a limited group. In other words, the economic operation, which has been implemented for more than two centuries and aimed at maximizing profit by increasing production and consumption, has left societies to face with problems such as increasing impoverishment, environmental destruction, climate change, physical, and human capital bottlenecks.

The fact that the sustainability of economic models based on growth has reached the limit for many different reasons brought the concept of “sustainability” to the agenda in the early 1980s. The concept of sustainability was used for the first time by the International Union for Conservation of Nature (IUCN) for the conservation of natural resources. However, it was the World Environment and Development Commission established within the United Nations that effectively brought the concept of “sustainability” to the world agenda.

Former Norwegian Prime Minister Gro Harlem Brundtland, whose name was given to the report, played an active role as the President of the World Commission on Environment and Development. The definition of sustainability is widely accepted by the scientific community and is in the Brundtland Commission Report (1987) prepared for the World Commission on Environment and Development. The report expresses “sustainability and sustainable development” as follows (WCED 1987):

Sustainable development is the provision of development in order to meet daily needs without jeopardizing the ability of nature and future generations to respond to their needs.

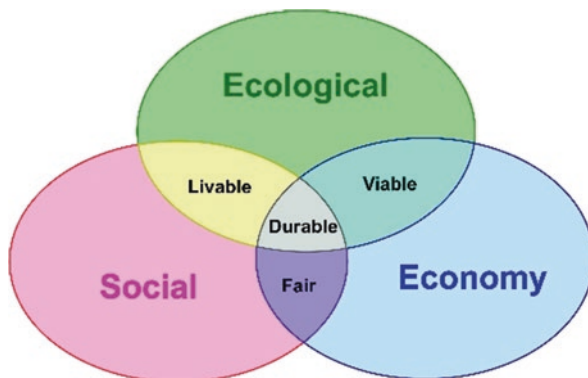
In other words, what is meant by sustainable development is to observe the rights and benefits of present and future generations, by taking into account the limitations of environmental phenomena and natural resources at the point of sustaining economic development (Keles and Hamamcı 2005).

One of the main recommendations of the Brundtland Commission Report, titled *Our Common Future*, is a regional or/and global organization in order to find solutions to the economic, ecological, and social crises experienced as a whole. In this context, the UN Conference on Environment and Development held in Rio in 1992 aimed to determine sustainable and environmentally friendly economic development strategies and measures to prevent nature and environmental damage in the world (World Environment and Development Commission 1992).

The Rio Conference concluding declaration included 27 principles that will guide the future in environmental and economic development issues. The highlights of these principles are as follows: the right of living creatures to a healthy life, the right to access welfare, environmental economic development, cooperation, information exchange, legislation, accountability, participation, prudence, and environmental impact assessment. At the same time, it was decided to harmonize all policies and related regulations with a holistic approach in the fields of economy, environment, and society.

The concept of sustainability is a holistic approach covering the environment, economy, and social dimensions. Its essence is to leave a liveable world to future generations in every aspect. In this context, the target is a clean natural environment that is not destroyed and can renew itself, social conditions based on equality and prosperity, and an economic system that takes care of society and the environment. In addition to these, the sustainability approach is also a set of social efforts that includes law, urban planning, transportation, supply chain management, local and individual lifestyle, and ethical consumerism.

Fig. 10.1 Aspects of sustainability. (Schäfer and Waitz 2014)



The concept of sustainability in essence suggests that general thinking structures should change without reducing the quality of life of individuals. In this context, it is expected that individuals and countries will review their consumption patterns under the headings of environment, society, and economy and realize a universal solidarity. Sustainability actually consists of three closely interdependent and intertwined components (Fig. 10.1).

Sustainability is primarily the determinant of environmental policies, but its impact area is not limited to the environment. Sustainability has also been integrated with economic and social development approaches. Economically, sustainability has aims such as giving up the present-day life style that is a threat to the quality of life and ensuring energy efficiency in production and consumption processes. Environmental sustainability includes targets such as preserving the natural capital stock, storing and recycling the pollution, and waste generated as a result of production and consumption processes. Social sustainability basically focuses on goals such as poverty alleviation and cultural diversity. In other words, in order to ensure a sustainable economic development, countries should take into account environmental factors such as air, water, and soil pollution while growing economically, and on the other hand, they should consider social factors such as health, education, accommodation, equality, and security.

Sustainability has become an important component of the agenda of most organizations in the business world, as it is in many areas today. It has been revealed in many studies that performing a performance within the framework of sustainability norms is a necessity both as a requirement of today's competition and in terms of the economic worthiness of the organization (Epstein and Buhovac 2014; Hussain et al. 2016).

Sustainability has brought pressures from various stakeholders to adopt sustainability practices. In addition, due to the prominence of its role in the field of organizational development, it has attracted great attention from academia and business world (Cerin and Karlson 2002). In this context, many organizations adopt different sustainability strategies to increase their competitive advantage (Flint and Golicic 2009).

Sustainability in the business world means meeting the current needs of the existing organization and stakeholders (such as customers, staff, and communities) without risking future stakeholder needs. In this context, management theory finds it important to focus on three issues that help the organization meet stakeholder needs now and in the future. These issues are economic, environmental, and social sustainability (Dyllick and Hockerts 2002).

Today's organizations have added social responsibility practices as a new component of their business models, besides their policies and strategies. In this context, organizations take into account environmental, economic, and social sustainability issues in their business models that they implement in order to meet the expectations of their stakeholders (Rupp et al. 2011). In this context, the prominent sustainability initiatives are improving workplace conditions in relation to ethical practices in employment, developing cooperation and communication with local people in line with the products and policies of the enterprise, investing in the establishment of social infrastructure, contributing to the provision of cleaner and sustainable environmental conditions, and providing support to economic development within the scope of corporate governance (Alameeri et al. 2017).

10.3.1 Sustainability in Airport

Sustainability has become a part of social and corporate culture today. Culture is a dynamic concept that includes all the dynamics of social life, determines the approaches of nations and institutions to the world and phenomena, and is also constantly changing. In this context, all stakeholders operating in the aviation industry also have their goals, perspectives, values, principles, and their own cultural characteristics. These values manifest themselves in the adopted sustainability practices.

While the conceptual debates on sustainable aviation emerged with the publication of the IPCC (Intergovernmental Panel on Climate Change) Special Report on the impacts of climate change in aviation in 1999, the public was also introduced to the term "sustainable aviation" (IPCC 1999; Sledsens 1998).

Sustainability, which can be briefly expressed as an approach that takes into account the environment and social sensitivity in economic activities, also means that the aviation sector stakeholders have social and environmental responsibilities while carrying out their activities and their inclusion in all business processes and decision-making mechanisms. In this context, factors such as continuity of economic growth, corporate worthiness, product and service quality, and customer loyalty come to the fore for aviation companies.

Aviation sector stakeholders should not neglect the areas of environmental awareness and social responsibility while striving toward their basic economic goals such as profitability and efficiency. The success to be achieved in these three main areas will enable the achievement of sustainability goals.

The importance of sustainability is gradually increasing due to the rapid growth of the aviation industry. The excessive increase in demand for air transport has

increased the number of planes and flights; as a natural consequence of this, fossil fuel use and carbon dioxide emissions have increased enormously. On the other hand, due to the increasing demand, the increase of the airport user has made it necessary to increase the physical capacities of the airport, which has been observed to cause many environmental problems.

Airports are considered to be the heart of air transport, as they are the common area where all stakeholders of the aviation industry carry out their activities. In this context, airports are the center of the sector in terms of sustainability concept in aviation. The relationship of airports with sustainability is evaluated from two sides. While airports have a negative impact on sustainability, air transport is also negatively affected by environmental impacts such as climate change. Sustainability issues considered to be affected by airports are the following: sea level rise, high rainfall and flooding, rising temperatures, extraordinary weather events, changing laws and regulations, changing expectations of investors, tourism trends and passengers' expectations, market and technology changes, and reputation (Learmonth 2020).

The excessive growth that emerges in the context of the efforts to expand the existing capacity and infrastructure at the airports of the world in order to meet the increasing demand for air transport brings with it some problems (Janic 2017). Poor management of airspaces causes additional noise and greenhouse gas emissions in and around the airport. The delays caused by the density of the airports and the increase in taxi times, as well as the excessive noise and carbon gas emission caused by the increasing urban airport connection traffic, increase the discontent among the airport users and local people (Guimaran et al. 2019).

10.4 Sustainability Practices at Airports

The place of airports in sustainability discussions is very important. Airports are therefore the places where sustainability practices benefit the most. All of the applications implemented constitute the concept of airport sustainability today. Airport sustainability is defined as “a holistic approach to managing an airport to ensure the economic viability, operational efficiency, protection of natural resources and integrity of social responsibility of the airport” according to ACI.

The sustainability practice at airports is very comprehensive due to the number of components and the variety of activities carried out, and it includes many types of initiatives. The main environmental impacts from airport operations and assets are based on discharges to water, air, and soil and fuel and electricity consumption. Global practices carried out in the name of sustainability especially focus on the environmental pollution created by airports. While the airport industry has long focused on improving noise, air, and light pollution for regulatory and health reasons, there is now an increasing focus on greenhouse gas management and climate change (Humphreys 1999). ACI aims to reduce the net carbon emission at airports to zero by 2050. The Airport Carbon Accreditation Program was established for this

purpose. Even when the technologies used today are more accessible and cheaper, more environmentally friendly technologies are increasingly involved in new investments. In this context, some environmentally friendly applications and technologies used in airport investments are as follows (Alameeri et al. 2017):

Ground support equipment and vehicles are equipped with electrically powered and smart technologies.

Energy is produced with wind and solar technologies that reduce energy costs.

It is seen that new technology aircraft provide fuel savings compared to old technology aircraft.

Technologies that provide energy efficiency and encourage savings are used in airport buildings.

As new smart building technologies are produced in a more environmentally friendly manner, energy efficiency has also been achieved in offices and additional buildings at airports and energy efficiency performance can be measured in real time.

Technologies that provide energy efficiency are also used in baggage handling systems and airport lighting systems.

Systems that generate energy from wastes started to be used and projects to reduce waste were also implemented.

It is possible to classify these exemplary sustainability practices at airports under various headings. It is possible to classify the components within the scope of sustainability practice at airports as follows (Torum and Yilmaz 2009):

- Efficient and effective use of natural resources and protection of the environment
- Addressing the needs and expectations of all stakeholders as a social process
- Monitoring and evaluation of economic performance data

In this classification, which is the general classification of the concept of sustainability, it is seen that social, economic, and environmental sustainability subtitles are used. International and/or national regulations should also be collected under these three main headings. In this context, for sustainability applications, obligations, incentives, priorities, and obstacles should be determined under these three main headings, because sustainability practices may conflict with the resource allocation priorities of stakeholders at airports and the importance that organizations attach to these three main topics differs.

The fact that airports are under the management of private companies with the aim of maximizing profit, within the scope of globalization and privatizations as a result of it, can create results that do not correspond to national sustainability efforts (Humphreys I.F. 1999). New airport investments required by the increasing passenger and aircraft traffic pushed the public authority avoiding high public expenditure to the background in the process. In this context, global businesses have come into play as suppliers of necessary financial funds and modern management knowledge. Bringing profit-oriented international businesses and national stakeholders together on the axis of economic, social, and environmental sustainability is not easy (Humphreys 1998).

The main topics focused on airport sustainability practices are effective environmental management policy, efficient and effective use of energy, waste management, reduction of carbon emissions, sustainable transportation system, and smart building practices. In this process, constraints on financing opportunities, restrictions on legislation, lack of qualified personnel, and the underdeveloped environmental culture of the society appear as the biggest obstacles to sustainability initiatives.

It is seen that social sustainability practices, which generally allocate the least resources for commercial reasons, are actually the most important topic for the residents around the airport. Activities carried out within the scope of the social dimension of sustainability practices at airports are generally focused on staff awareness and training. Beyond that, initiatives come to the fore less often in terms of preserving and promoting local culture and heritage. Considering the fact that airports play a key role in urban sustainability, it is important to establish alternative and effective transportation systems that directly affect urban sustainability in the context of airport sustainability practices.

10.5 Conclusion

With the emergence of the concept of sustainability since the 1980s, it was first defined by the United Nations in 1987 and subsequently became the subject of international research, especially due to environmental damage. The consequences of environmental damage adversely affect many countries and many industries in these countries. The aviation sector is one of the sectors that pollutes the environment the most and is most affected by environmental negativities.

In 1999, with the definition of ACI, aviation sustainability and then the concept of airport sustainability started to be discussed. Along with the fact that airports are responsible for most of the environmental impacts, the environments that will suffer the most from negative environmental impacts have increased the importance of aviation attaches to the concept of sustainability. It has been determined that the activities carried out with commercial concerns at the airports, which are the center of aviation operations, are not sustainable.

It has been observed that, first of all, airport operators and then all stakeholders in the sector adopt sustainability practices mainly due to national and international regulations. It has been determined that sustainability practices in aviation, which have a high need for investors worldwide, provide prestige to organizations. Thus, airport sustainability practices have become widespread. The opinions of countries and the importance they attach to practices on these issues are different from each other.

Although there are high-cost systems and technologies among airport sustainability practices, the cost of all applications is not high. It is seen that aviation organizations with environmental awareness become widespread with the feeling of the effects of sustainable practices in the organizational culture. For this reason, it is the

primary goal that all stakeholders in the aviation industry adopt sustainability. Therefore, sample applications should become widespread. In order for these practices to be adopted, they should be discussed and shared academically.

References

- Alameeri, A., Ajmal, M.M., Hussain, M., Helo, P.T.: Sustainability practices in the aviation sector: a study of UAE-based Airlines. *Int. J. Sustain. Soc.* **9**(2), 119–147 (2017)
- Cerin, P., Karlson, L.: Business incentives for sustainability: a property rights approach. *Ecol. Econ.* **40**, 13–22 (2002)
- Cui, Q., Li, Y.: Evaluating energy efficiency for airlines: an application of VFB-DEA. *J. Air Transp. Manage.* **44–45**, 34–41 (2015)
- Dyllick, T., Hockerts, K.: Beyond the business case for corporate sustainability. *Bus. Strategy Environ.* **11**, 130–141 (2002)
- Epstein, M.J., Buhovac, A.R.: *Making Sustainability Work: Best Practices in Managing and Measuring Corporate Social, Environmental, and Economic Impacts*, 2nd edn. Berrett-Koehler Publishers (2014)
- Flint, D.J., Golicic, S.L.: Searching for competitive advantage through sustainability A qualitative study in the New Zealand wine industry. *Int. J. Phys. Distrib. Logistics Manage.* **39**(10), 841–860 (2009)
- Grubestic, T.H., Matisziw, T.C.: World cities and airline networks. In: *The International Handbook of Globalization and World Cities*, pp. 7–116 (2012)
- Guimarans, D., Arias, P., Tomasella, M., Wu, C.: Chapter 4 – A review of sustainability in aviation: a multidimensional perspective. In: *Sustainable Transportation and Smart Logistics, Decision-Making Models and Solutions*, pp. 91–121. Elsevier, Amsterdam (2019)
- Humphreys, I.F.: Development and privatisation of Cardiff airport. *Contemp. Wales.* **10**, 81–102 (1998)
- Humphreys, I.F.: Privatisation and commercialisation: changes in UK airport ownership patterns. *J. Transp. Geogr.* **7**, 121–134 (1999)
- Hussain, M., Khan, M., Al-Aomar, R.: A framework for supply chain sustainability in service industry with Confirmatory Factor Analysis. *Renew. Sustain. Energy Rev.* **55**, 1301–1312 (2016)
- IPCC.: *IPCC Special Report. Aviation and the Global Atmosphere: Summary for Policymakers.* <http://www.ipcc.ch/pub/reports.htm> (1999)
- Janic, M.: Analysing and modelling some effects of solutions for matching the airport runway system capacity to demand. *J. Air Transp. Manage.* **65**, 166–180 (2017)
- Keles, R., Hamamci, C.: *Environmental Policy*, p. 237. Image Publishing House, Ankara (2005)
- Learmonth, I.: *Clean energy and infrastructure: Pathway to airport sustainability.* Clean energy report, AECOM Australia (2020)
- Morrell, S., Taylor, R., Lyle, D.: A review of health effects of aircraft noise. *Aust. N. Z. J. Public Health.* **21**(2), 221–236 (1997)
- Peace, H., Maughan, J., Owen, B., Raper, D.W.: Identifying the contribution of different airport related sources to local urban air quality. *Environ. Modell. Softw.* **21**(4), 532–538 (2006)
- Rupp, D.E., Williams, C.A., Aguilera, R.V.: Increasing corporate social responsibility through stakeholder value internalization (and the catalysing effect of new governance): an application of organizational justice, self-determination, and social influence theories. In: *Managerial Ethics: Managing the Psychology of Morality*, pp. 71–90 (2011)
- Schäfer, A.W., Waitz, I.A.: Air transport and the environment. *Transp. Policy.* **34** (2014)
- Sledsens, T.: *Sustainable aviation the need for European environmental aviation charge.* European Federation for Transport and Environment, T&E 98/1 (1998)

- Torum, O., Yılmaz, A.K.: Sustainability management in aviation: sustainability practices for research on airports in Turkey. *Aviat. Space Technol. J.* **2**, ss. 47–ss. 58 (2009)
- Turnbull, D.A., Bevan, J.R.: The impact of airport de-icing on a river: the case of the Ouseburn, Newcastle upon Tyne. *Environ. Pollut.* **88**(3), 321–332 (1995)
- Upham, P., Maughan, J., Raper, D., Thomas, C., (edt.), (2003), *Towards Sustainable Aviation*, Earthscan Publication Ltd
- Walker, S., Cook, M.: The contested concept of sustainable aviation. *Sustain. Dev.* **17**(6), 378–390 (2009)
- WCED.: Report of the World Commission on Environment and Development: Our Common Future, published in 1987 by the United Nations through the Oxford University Press (1987)
- World Environment and Development Commission: Our Common Future. EFT Publication, Oxford University Press (1992)

Index

A

Active bridge active clamp (ABAC), 125

Active flow control techniques

airfoils, 25

plasma actuators, 27, 28

suction and blowing, 25–27

Advisory Council of Aviation Research (ACARE), 115

Aerial vehicle aerodynamics, 181

Aerodynamic performance

airfoil, 19, 21

control techniques, 31

cross-flow component, 19

cross-flow effect, 20

drag of immersed bodies, 23–25

fluid, 21, 22

nondimensional forms, 22

optimal flight condition, 21

suction side, 22

three-dimensional boundary layer flows, 19, 20

time-dependent development, 22

time-dependent stages, 23

vortex structures, 22

Aeroelastic/aeroservoelastic structure, 53

Aircraft electric power system

aviation industry, 114

constant frequency distribution, 119

DC distribution, 120

electric aircraft technology, 115

electric machines, 135, 136

electric motors, 115

electric propulsion systems, 114

electrification approach, 118

environmental effects of aviation, 115–117

environmental impacts, 114

environmental sensitivity, 114

FC, 139

flywheels, 140

generator, 119

supercapacitors, 140

transformation, 119

VAC, 118

variable frequency distribution, 120

VDC, 118

Air cycle machine (ACM), 77–79

aircraft, 73

aircraft industry, 83

aviation industry, 84

characteristics, 81

component, 80, 95

compressor, 82, 94

computational tool, 82

conditioned air, 73

design process, 83

efficiency, 80

exergy analyses, 83

exergy analysis, 73, 83

exergy destruction ratio, 94, 97

exergy flow, 96

exergy values, 97

flight missions, 94

fluid stream temperature, 93

health monitoring, 81

mass flow rate, 92

operation conditions, 82

optimization, 80

parameters, 92

polytropic and isentropic efficiencies, 92

pressure values, 93

- Air cycle machine (ACM) (*cont.*)
 regulation effect, 94
 reverse Brayton cycle, 82
 source of energy, 73
 temperature evaluation, 94
 thermodynamic analysis, 73
 thermodynamic properties, 92
 turbine, 82, 92, 94
 water extraction, 92
- Air data computer (ADC), 75
- Airport sustainability
 air and environmental pollution, 191
 aviation industry, 191–193
 aviation sector stakeholders, 196
 business processes, 196
 characteristics, 191
 climate change, 191, 197
 corporate governance, 196
 culture, 196
 decision-making mechanisms, 196
 development, 194
 economic and social benefits, 191
 economic benefits, 192
 economic growth, 193
 economic models, 194
 economic operation, 193
 economic policies, 192, 193
 energy consumption, 191
 environment and social sensitivity, 196
 environmental and social costs, 191
 environmental policies, 195
 global economic functioning, 191
 global environmental events, 191
 growth-focused system, 193
 natural environment, 194
 noise and greenhouse gas emissions, 197
 organizations, 195, 196
 physical capacities, 197
 practices, 197–199
 principles, 194
 production and consumption processes, 195
 return on investment, 192
 sector, 192
 social efforts, 194
 stakeholders, 192, 195, 196
- All-electric aircraft (AEA), 117, 121, 136, 143
- All-electric systems, 120
- Autotransformer rectifier unit (ATRU), 119
- Autotransformer unit (ATU), 119
- Auxiliary power unit (APU), 75, 118, 119
- B**
- Battery
 air inlet temperatures, 3
 artificial neural networks, 3
 Bayesian regularization algorithm, 3
 computational fluid dynamics method, 3
 cooling, 2
 electric transport, 2
 electric vehicles, 2, 14
 electrochemical energy, 2
 energy density, 137
 energy storage system, 2, 137
 heat generation model, 2
 land and air transportation, 14
 lead-based, 137
 lithium-ion batteries, 136
 module, 11, 12, 14
 nickel-based, 137
 Nusselt number, 2
 storage systems, 137
 technologies, 137–139
 temperature analysis, 2
 temperature and electrical analysis, 15
 temperature changes, 2
 thermal analysis, 3, 4
 types, 137
- Battery pack model
 governing equations, 5–7
 numerical solution, 4, 5
- Bayesian regularization (BR), 7
- Brundtland Commission Report, 194
- Brushless doubly-fed machines (BDFM), 135
- C**
- Carbon Dioxide Information Analysis Center (CDIAC), 116
- Cascaded H-bridge multilevel inverter, 131
- Computational fluid dynamics (CFD), 169
- Control surfaces
 aerodynamic instability, 51
 aircraft, 51
 analysis, 55–57
 configuration, 52
 corrugation
 distance optimization, 63, 65
 height optimization, 61–63
 width optimization, 63
 corrugation design, 52–55
 experiences, 52
 flutter, 51–55
 modelling, 55–57
 number of corrugation optimization, 65, 66
 shape optimization
 curve-type corrugation, 59, 60
 natural frequency comparisons, 60
 simple plate, 57
 stiffness variations, 61

- trapezoidal corrugation, 59
- triangular corrugation, 58
- static analysis, 65, 66, 69
- type of flutter, 51

Corrugations, 55

Cost per available seat kilometers (CASK)

- functions, 152

Cycloconverter, 130

D

Drag reduction, 26, 28, 29, 31

Dual active bridge (DAB), 124

E

Economic sustainability, 196, 198

Elastic modulus, 56

Electric aircraft propulsion systems

- all-electric systems, 120
- hybrid systems, 121, 122
- turboelectric systems, 122, 123

Electric machines, 135, 136

Electrochemical energy, 2

Electromagnetic compatibility (EMC), 134

Electromagnetic interference (EMI), 134

Energy load, 106

Energy price, 110

Energy storage

- battery (*see* Battery)
- electric aircraft, 136

Energy storage systems, 2

Environmental control system (ECS)

- ACM, 77–79
- air cycle refrigeration cycle, 76
- air-conditioning system, 74
- aircraft industry, 73
- aircraft systems, 73
- APU, 75
- atmospheric ozone dissociation, 75
- bleed air, 74, 75
- cabin pressure, 75
- categories, 74
- design conditions, 73
- flight crew, 73
- flight operation, 74
- gas turbine engine compressor
 - stages, 74
- ozone concentration, 75
- pressurization, 75
- RBC, 79, 80

Environmental sustainability, 195, 198

Equivalent orthotropic model, 53

EU Environmental Noise Directive (END), 117

European Organization for Civil Aviation Equipment (EUROCAE), 134

Exergy analysis

- boundary conditions, 84–86
- method
 - bleed air, 88
 - chemical exergy, 88
 - components, 87
 - conventional air refrigeration
 - cycle, 86
 - exergy destruction ratio, 90
 - fluid stream, 89
 - fuel and product stream, 91
 - homogenous state, 87
 - molar basis, 88
 - molar composition, 87, 88
 - steady-state conditions, 87
 - system efficiency, 89
 - thermal capacity, 89
- system description, 84–86

F

Flat layers, 52

Flight management system (FMS), 75

Flow separation, 22, 23, 25, 26, 29, 31

Flying capacitor inverter, 129

Flywheels, 140

Fuel cells (FC), 139

G

Gallium nitride (GaN), 133

Glass facade systems, 102, 103, 107, 110

Greenhouse gas (GHG) emissions, 116

H

Heat exchangers, 73–77, 79, 80, 82, 84, 94, 97

Heat transfer, 102, 104, 105, 107, 110

Homogenization-based analytical

- model, 54

Hybrid systems, 121, 122

I

Induction motor (IM), 135

Integrated drive generators (IDG), 119

Interleaved boost with coupled inductors (IBCI), 125

International Energy Agency (IEA), 117

International standard atmosphere (ISA), 86

International Union for Conservation of Nature (IUCN), 194

L

- Laminar flow, 29
- Laminar model, 4
- Levenberg-Marquardt (LM), 7
- Life cycle cost (LCC)
 - acquisition costs, 159
 - activities, 148
 - aging, 147–150, 163
 - airline operating costs, 151, 152
 - analysis, 157
 - applications, 148
 - cost components, 158
 - cost functions, 155–157, 163
 - cost items, 154, 155, 159
 - cost parameters, 157
 - cost vs. fitness, 161, 162
 - development, 164
 - economic impact, 147
 - economic life, 147
 - economic values, 148
 - economical assessment, 148
 - economies, 149
 - external and internal factors, 150
 - implementation, 153
 - industry sustainability, 148
 - investment flexibility, 164
 - investment projects, 148
 - limitation, 164
 - methodology, 148, 150, 163
 - replacement scenarios, 153, 154
 - scenario analysis, 157
 - sensitivity analysis, 160, 161
 - structure, 149
- Life cycle energy assessment
 - airport terminal buildings, 102
 - cooling energy, 108
 - electricity price, 109
 - energy load, 106
 - fuel prices, 102
 - heat transfer coefficient, 104, 105, 107
 - heating energy load, 109
 - LCET, 106, 109
 - meteorological and geographical
 - features, 103
 - weather conditions, 102
- Life cycle energy total cost (LCET), 106, 109
- Li-ion battery
 - biological nervous system, 7
 - coefficient, 7
 - field of energy, 7
 - learning algorithms, 7
 - non-linear transfer function, 8
 - numerical systems, 7
 - thermal and electrical, 8, 10
- Lithium-ion batteries, 136

Lithium-sulfur (Li-S) batteries, 138

M

- Matrix converter (MC), 130
- Mean aerodynamic chord (MAC), 175
- Medium-altitude long-endurance (MALE), 168
- More electric aircraft (MEA), 117, 119, 136, 143
- Multiport topologies, 127

N

- NASA Research Announcement (NRA), 135
- National Advisory Committee for Aeronautics (NACA), 21
- National Aeronautics and Space Administration (NASA), 21, 115
- Neutral point clamped (NPC), 127, 131
- Newman, Tiedemann, Gu and Kim (NTGK), 4, 6
- Noise pollution, 116

P

- Parallel hybrid, 121
- Passive flow control techniques
 - cavity, 29
 - efficiency, 28
 - surface roughness, 29, 30
 - vortex generators, 28, 29
- Permanent magnet synchronous machines (PMSM), 135
- Power electronics circuits, 141
- Power electronics converters
 - AC-AC converters, 130
 - AC-DC converters, 130, 131
 - DC-AC converter, 127, 129, 130
 - DC-DC converters, 124, 125, 127
 - electrical/electronic systems, 124
 - multi-voltage level, 124
 - NASA, 124
 - semiconductor technology, 132–134
- Present worth factor (PWF), 106
- Pressure distribution, 176, 178

R

- Radio Technical Commission for Aeronautics (RCTA), 134
- Rayleigh distribution, 39
- Remote power distribution units (RPDU), 118
- Resonant converter, 125
- Reverse brayton cycle (RBC), 79, 80

Reynolds-averaged Navier-Stokes simulation (RANS) model, 174

S

Scaled conjugate gradient (SCG), 7
 Semiconductor technology, 132–134
 Semi-implicit method for pressure-linked equations (SIMPLE), 4
 Series hybrid, 122
 Series/parallel hybrid, 122
 Shear-stress transport (SST), 171, 175
 Silicon (Si), 133
 Social sustainability, 195, 196, 199
 Solid-state power controllers (SSPC), 118
 Supercapacitors, 140
 Synchronous reluctance machines (SRM), 135

T

Thermal management systems (TMS)
 batteries, 142
 electric propulsion system, 140
 heat, 140
 power electronics circuits, 141
 power electronics systems, 140
 supercooling, 140
 Three-phase DAB converter, 125
 Transformer rectifier unit (TRU), 119
 Transportation sector, 116
 T-type NPC (TNPC), 129
 T-type rectifiers, 131
 Turboelectric systems, 122, 123
 Turkish Aerospace Industries (TAI), 171
 Two-level rectifiers, 131

U

UN Conference on Environment and Development, 194
 Unmanned aerial vehicle (UAV)
 aerodynamic effects, 168, 169
 aerodynamic efficiency, 183
 aerodynamic performance, 181, 182
 aerodynamic study, 168
 analysis, 172, 173
 angle of attack, 184, 185
 Anka-like UAV models, 171
 boundary conditions, 174–176
 Boussinesq hypothesis, 170
 continuity equation, 169
 drag coefficient, 181
 dynamic similarity, 176, 177
 environmental conditions, 168

 experimental and numerical aerodynamic coefficients, 182
 experimental setup, 179, 180
 geometric parameters, 169
 geometries, 169
 grid independence, 173
 industry sector, 168
 load-carrying capacity, 168
 Navier-Stokes Equations, 169
 pressure distribution, 176, 178, 185
 single-rotor/multi-rotor drone, 168
 standard k- ϵ model, 171
 TURAC transition-flight mathematical model, 168
 turbulence model equations, 170
 vortex core regions, 185
 Wilcox k- ω model, 171
 wind tunnel, 169
 Unmanned aerial vehicles (UAVs), 52

V

Variable frequency generator (VFG), 119
 Vertical take-off and landing (VTOL)
 category, 121
 Vienna rectifier, 130
 Voltage Source Inverter (VSI), 127
 Volts alternating current (VAC), 118

W

Weibull distribution, 39
 Wideband range (WBG), 134
 Wind speed
 airport design, 35
 data, 37, 38
 goodness-of-fit evaluation, 39, 48
 marginal effects, 36
 measurement element, 35
 model, 39–42
 organization, 37
 orientation, 36
 runway design, 35
 three-dimensional seasonal models, 42, 45
 two-dimensional radial plane, 36
 wind rose, 46–48
 Wind tunnel test, 168, 169, 172, 176, 177, 182
 World Commission on Environment and Development, 194
 Wound field synchronous machine (WFSM), 135

Z

Z-source inverter, 127